Theoretical Notes

Note 350

10 March 1983

A Phenomenological Model of Soil Breakdown

Robert N. Carlile, Professor
and Marlene E. Righettini
Dept. of Electrical Engineering
University of Arizona
Tucson, Arizona 85721

ABSTRACT

This paper characterizes electrical soil breakdown by models which can be incorporated into computer codes. The evolution and decay of the corona is described. Parameters which characterize these processes are defined. Where possible, their numerical values are stated. The evolution within the corona of streamers is discussed and some of their properties are described.

Acknowledgments

The authors would like to thank the students at the University of Arizona who have contributed to this project: Rik E. Lantz, Peter J. McNellis, Robert D. Spencer, Lisa Smith, and Yit M. How. Thanks are also due to Susan Kinsey and Averell Jewett who went beyond the call of duty in typing the manuscript.

TABLE OF CONTENTS

1.0 Introduction

This paper describes the development of a model of soil breakdown based on a large number of soil breakdown experiments which were performed under the auspices of AFWL. The motivation for this work has been to characterize soil breakdown about buried conductors associated with an underground MX missile shelter when a SREMP induces a very large voltage on the conductors.

The first of the experiments supported by AFWL was performed in 1980 on small soil samples for breakdown times of the order of microseconds [1]. Recognizing that the induced voltage from an SREMP could persist for milliseconds, subsequent experiments were performed on this time scale.

Subsequently, Mission Research Corporation (MRC) at San Diego performed experiments on systems with cylindrical symmetry in 1981 [2]; concurrently JAYCOR of San Diego, CA, performed point-plane geometry experiments [3]. In both sets of experiments, the electrode spacing was of the order of 1 m. Since that time JAYCOR has performed combined drive experiments [4].

Starting in mid-1982, a large pulser became available, constructed by Maxwell Laboratories Inc., (MLI) of San Diego, CA. This pulser has potential parameters of 320 KV and 2 MJ. A second large pulser constructed by Physics International (PI), San Leandro, CA, with potential characteristics of 1 MV, 1 MJ is also available. To date (March 10, 1983), JAYCOR has performed experiments at a site within the MLI facility and also in a small test cell also at the MLI facility. One objective of these latter experiments is to do point-plane experiments with an emphasis on determining how far a streamer will propagate.

The purpose of this paper is to make use of this experimental data to develop a phenomenological model of soil breakdown suitable for use in a computer code. We have relied heavily on the experiments performed by MRC [2] because of the detail of spatial voltage variation in the presence of soil breakdown that was obtained. These workers inserted nonpurturbing voltage probes into their soil samples and were able to measure voltage vs. time at a large number of discreet points.

Soil breakdown characterized by corona formation and streamer propagation has been recognized for several decades. Petropoulous [5] postulated a corona forming about a buried electrode subjected to a large voltage pulse, and then predicted somewhat speculatively that streamers would form within the corona. Bellaschi et al. [6, 7] discussed corona. An excellent reference on both linear and nonlinear soil properties from this era is found in Sunde [8], a book which, unfortunately, is out of print. Liew, et al. [9] have more recently tried to model the decay of the corona as the pulser voltage relaxes.

In this paper, we have found that if the models of this early work are somewhat modified, they will fit the experimental data of Ref. 2. We have then proceeded to quantify these models in such a way that they can be used in computer codes.

The reader may find it useful to read Appendix A at this point before tackling the material of this paper. This Appendix is a description of the nature of soil from a geologist's point of view. This description defines the components of soil and then describes through Archie's Law how each component contributes to the linear ohmic conductivity of soil. This material provides a good basis on which to build an understanding of the nonlinear behavior of soil.

In Sec. 2 we discuss the relevant features of the experimental configurations which were used in the experiments that we draw upon to develop our model. In Sec. 3 is an overview of the model; Sec. 4 is a development of the electrostatic model while Sec. 5 develops the dynamic model of relaxation. Sec. 6 discusses streamers and Sec. 7 is a summary of the important points made in this paper, and recommendations for future experiments.

2.0 Experimental Systems

Nearly all the work in this paper is based on experiments which were performed by workers at MRC. Their work is reported in Ref. 2. This work was performed in two experimental configurations both of which contained cylindrical symmetry:

1. A cylindrical wedge of angle $\pi/2$. The thickness of the wedge was either .1 m or .3 m. and the radius was 0.5 m or 1.0 m. When an experiment is discussed in this paper, the wedge thickness and radius will be stated. Experiments performed in this configuration will henceforth be called Experiments A or Exp. A.

2. A full 2π cylinder. The length was 1 m and the radius .5 m was 1 m. Experiments performed in this configuration will be called Exp. B.

Exp. A were performed at Physics International, San Leandro, CA. The basic configuration is shown in Fig. 2.1.1. The soil sample is in the shape of a $\pi/2$ wedge with a center conductor of radius a, an outer conductor (a copper sheet) of radius b, and a thickness L. In some of the experiments, the outer conductor was connected to pulser ground through a resistor of 200 ohm. The top and bottom of the soil sample as well as the sides at 0 and $\pi/2$ radians were of an insulating material. The intervening space was filled with soil. For the experiments of interest in this paper, a = .01m, b = .5, 1.0 m, and L = .1, .3 m.

The center conductor was driven by a 30 - 100 KV, .9 μf pulser supplied by Physics International. The interesting feature about these experiments was that the voltage in the soil sample was measured at discreet points as a function of time by an array of voltage probes. A probe had a high impedance between its small spherical tip (in contact with soil) and ground. It hence drew little current. The probes were designed so that they would not purturb significantly the distribution of voltage in the soil sample.

The array of probe positions which were available are shown in Fig. 2.1.1. There were 10 data channels available. Nine of these were used for

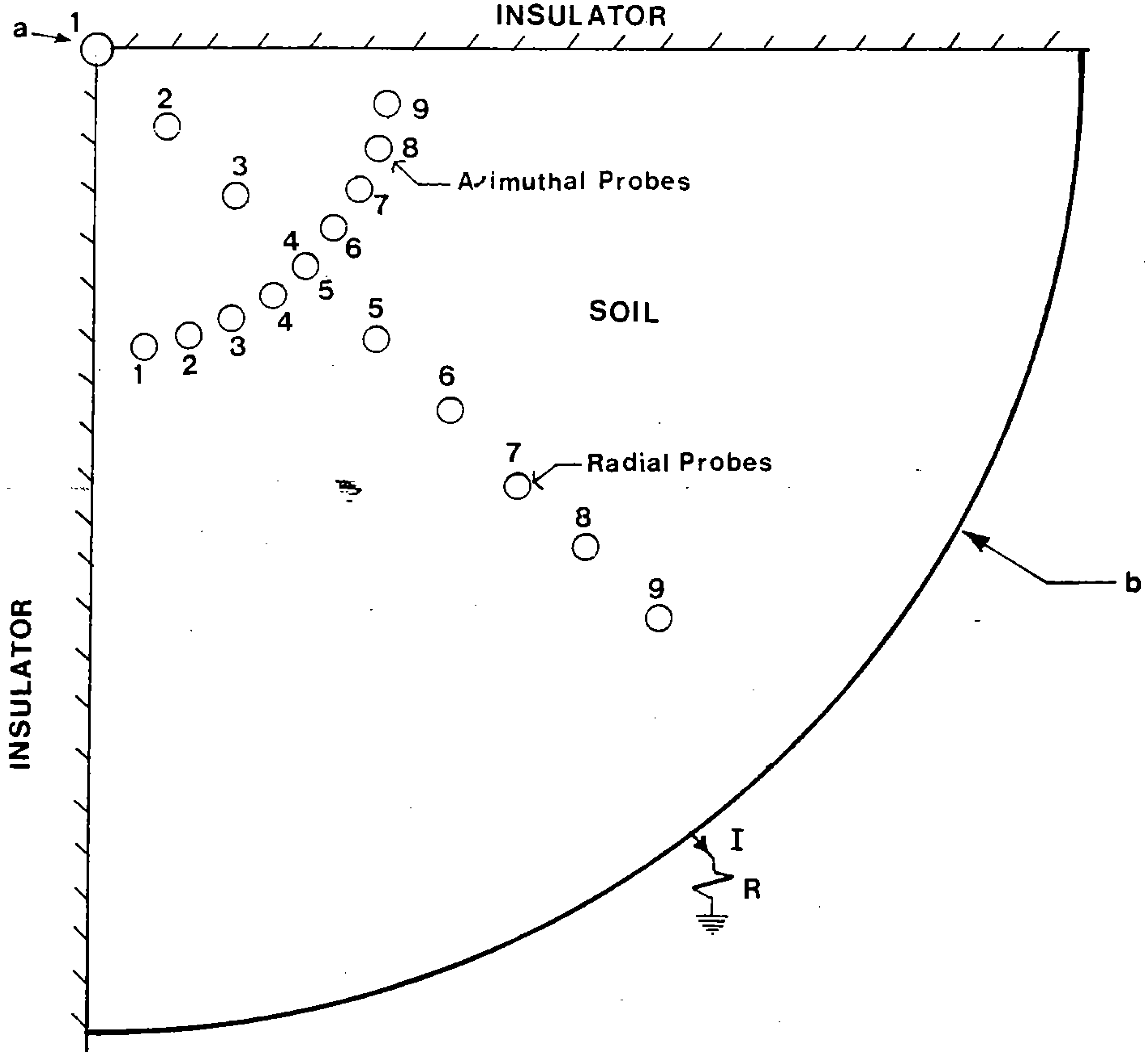

Figure 2.1.1 Radial and azimuthal probe arrays in $\pi/2$ cylindrical wedge soil sample used by Mission Research Corporation at Physics International. Wedge is .1 or .3 m. thick; radius a of center conductor is .01 m; radius b of outer conducter is .5 or 1.0 m. For details, see [2].

monitoring probe voltages while the tenth was used to monitor total current I through the sample. Thus, for a given discharge of the pulser (shot), nine probes could be monitored. The probes were either located in the nine radial positions in Fig. 2.1.1 or in the nine azimuthal positions.

The soil types used in Exp. A which are relevant to this paper are:

1. sand with an ohmic resistivity ρ_0 of about 150 to 2000 ohm-m;
2. a sand and gravel composite labeled MX-B; a typical ρ_0 is 130 ohm-m.

We hardly intend to give an exhaustive description of the details of the experiments here. For more information about these experiments, the reader is referred to Ref. 2 .

Exp. B were performed at the McDonnel-Douglas Lightning Facility (MCAIR) facilities in St. Louis, MO. The sample was a full 2π cylinder with a central conducting rod of radius a. The outer conductor was a standard steel culvert of radius b. The length of the system was L. The system had a top and bottom plate which were of an insulating material. The intervening space was filled with soil. For the experiments of interest in this paper, a = .01 m, b = .5m and L = 1 m.

The center conductor was driven by one or two five stage pulsers at the MCAIR facility. Each Marx pulser could be charged to 15 to 24 KV per stage with a total capacitance of 230 μf divided between the number of stages used. The same high impedance voltage probes were used in these experiments that were used in Exp. A. The probes were inserted into the soil through the top and bottom insulating plates in either a radial or azimuthal array. Of interest here is an azimuthal array described in more detail in Sec. 6.2. Twenty-six data channels were available. The soil of interest in this paper is 300 ohm-m sand.

Finally, there is a set of experiments called Exp. C. These were performed by Jaycor of San Diego, CA. at a site adjacent to Maxwell Laboratories, Inc., San Diego, CA. These were point plane experiments where the point was driven by a Marx type pulser supplied by MLI which had potential characteristics: 320 KV, 2 MJ. The soil resistivity was 50 Ω-m.

3.0 The Model, an Overview

The model that is adapted in this paper consists of two components: the corona and streamers. Although these components are in fact inseparable, in presenting an overview of the model, we shall discuss them individually.

3.1 The Corona

In discussing the corona, we shall make use of Exp. A described in Sec. 2.0. In Exp. A, the voltage V(r) with respect to ground was measured as a function of time by high impedance probes at the radial locations shown in the cylindrical wedge geometry shown in Fig. 2.1.1. Also measured was the total current I flowing through the wedge as a funciton of time. Thus, it is possible to plot the ratio V/I (the effective resistance between the location of the probe and ground) as a function of radial position r, or more conveniently, log r. For a typical shot, this plot is shown in Fig. 3.1.1.

If we assume cylindrical symmetry, we see from Fig. 3.1.1 that the cylindrical wedge is electrically divided into two regions. The division between the two regions occurs at a radius r_0, which for the parameters of Fig. 3.1.1 would be about .16 m. In each region, we see that V/I and hence V is nearly proportional to log r; since in this symmetrical case, $\bar{E} = \hat{r}\, E_r$, we are then lead to E_r being proportional to r^{-1} in each region, although the proportionality constants are different. If L is the thickness of the wedge, then the current density is

$$J_r = \frac{I}{2\pi\, r\, L} = \frac{E_r}{\rho} = \frac{A}{r\rho} \qquad (3.1.1)$$

where ρ is the soil resistivity and A is the proportionality constant for a region. Eq. (3.1.1) tells us that ρ is constant in each region and the difference in proportionality constants can be accounted for by the resistivity

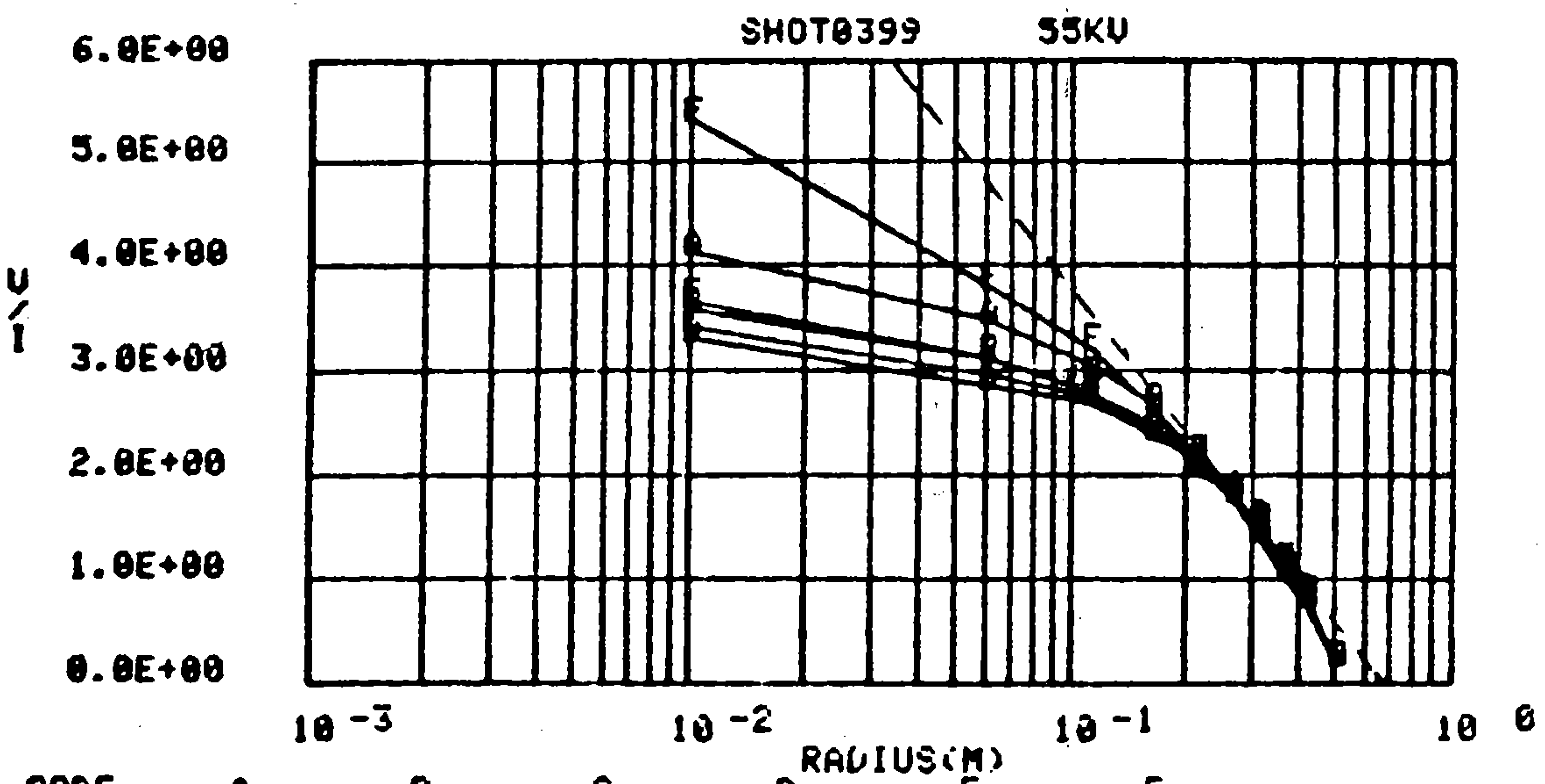

CODE	A	B	C	D	E	F
TIME	100US	200US	300US	500US	900US	1900US
CURRENT	14.00	15.25	15.00	14.00	10.75	5.00

Figure 3.1.1. Resistance (Kohm) for shott 399 at various times. Curve A, second from top; B, third; C, fifth; D, sixth; E, fourth; F, top curve. Total current through sample shown at botton (Fig. 3.3.3. of [2]).

being different in each region.

If, as in Fig. 2.1.1, a is the radius of the central high voltage conductor and b is the radius of the outer grounded cylinder, then we assume the following:

1. For $r_0 \leq r \leq b$, the soil is not broken down and is an ohmic state such that $\rho = \rho_0$, the ohmic value; furthermore, at $r = r_0$, $E_r = E_B$, a critical electric field above which the soil will break down but below which it will not; this is called the ohmic region.

2. For $a \leq r \leq r_0$, $E_r > E_B$ and the soil is broken down in some fashion; here, $\rho = \rho_1 < \rho_0$. This is called the corona region.

This two region description of soil breakdown we shall call the electrostatic model. A soil sample which is electrically stressed such that the electrostatic model applies is said to be in the electrostatic phase.

Although we have assumed that the corona will adapt the symmetry of the electrode system, e.g., cylindrical or spherical, assymetries in the soil or other perturbations, e.g. streamers, may cause the corona to depart from the symmetry of the electrode system. We may generalize the electrostatic model to be that in which the electrically stressed soil is still divided into two regions as illustrated in Fig. 3.1.2. In the region containing the high voltage electrode or the corona region, the resistivity is $\rho_1(\overline{r}) < \rho_0$. In the region containing the grounded electrode or the ohmic region, the soil is not broken down and the resistivity is just ρ_0. Furthermore, on the boundary between the two regions, in the ohmic region, the electric field is not necessarily normal to the boundary, but its magnitude is constant everywhere on the boundary and is E_B, the critical electric field. Finally, one can define a critical current density at the boundary in the ohmic region,

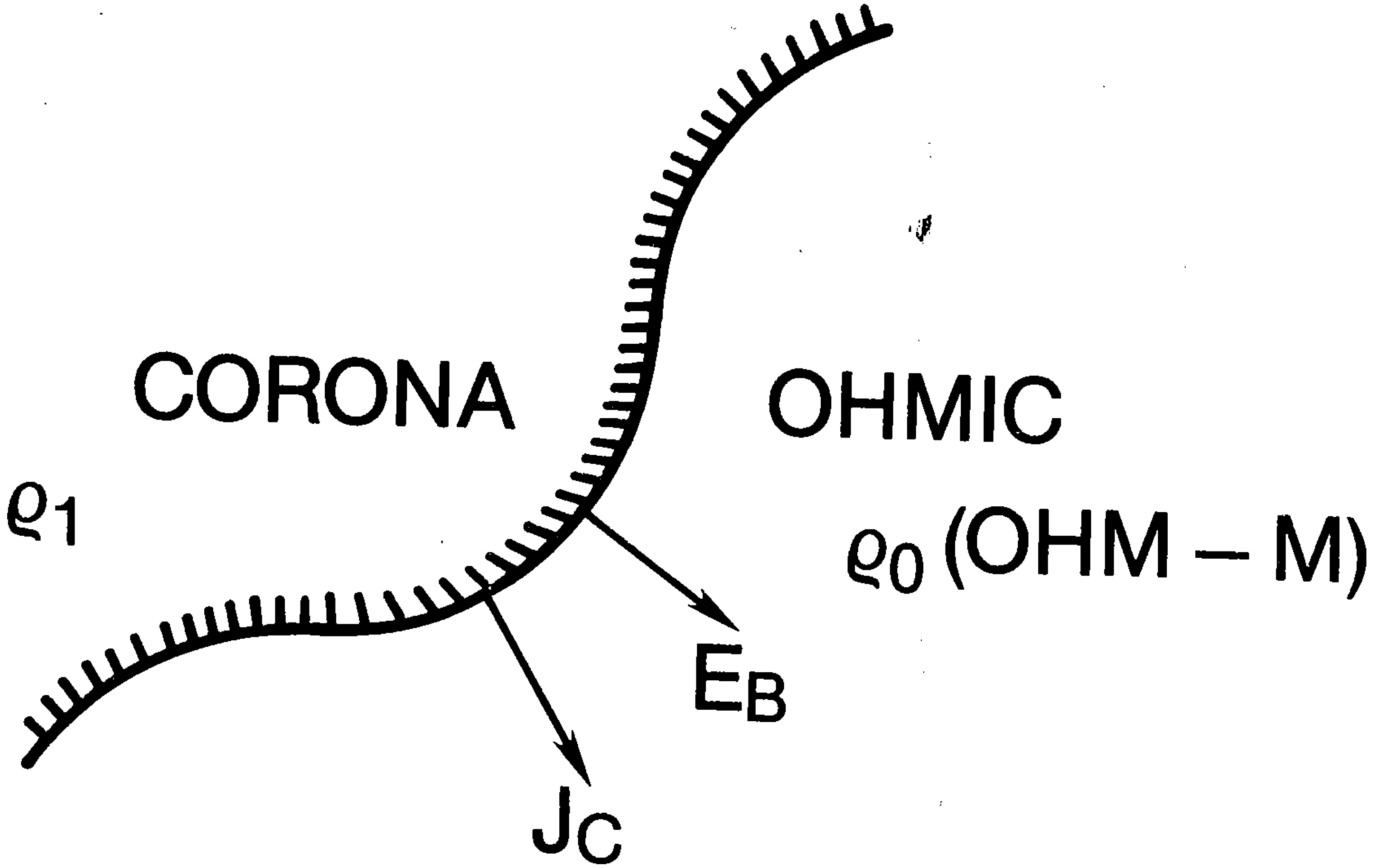

Figure 3.1.2. Boundary between a corona region and ohmic soil region; E_B is critical electric field and $J_c = E_B/\rho_o$.

$$\overline{J}_c = \overline{E}_B/\rho_0 \tag{3.1.2}$$

The magnitude of this current density is constant everywhere on the boundary.

It is of interest to see what precedes the electrostatic phase and how this phase decays as the voltage on the high voltage electrode decays. Call V_0 the voltage on the central high voltage electrode. As V_0 increases, the soil will remain ohmic until the electric field at the electrode $E_r(a) \equiv E_0$ approaches about 1 MV/m. Assuming a rise time of V_0 of the order of a microsecond, there will be a delay time t_i until the soil starts to break down and the soil remains ohmic. During this ohmic phase, it has been observed that the resistivity of the soil actually is larger than ρ_0. For example, in shot 012, while the ohmic resistance of the soil is 14.7 Kohm determined by low voltage measurements, during the prebreakdown phase, the resistance was measured to be 16.1 Kohm (Exp. A).

Once breakdown begins, the resistance of the soil drops rapidly in time as the total current through the sample I rises even though the V_0 is dropping. After a few tens of μs, r_0 begins to appear as the sample begins to enter the electrostatic phase. Two cases must be distinguished at this point. The first is that V_0 can be sufficiently large to cause the corona to extend all the way to the grounded conductor at $r = b$. We call this corona attachment. Then I will increase to a large value, and will only be limited by the low resistance of the soil. Corona attachment can occur if V_0 is so large that for a symmetric corona, $r_0 = b$, or r_0 exceeds a critical radius. Breakdown to the outer conductor can also occur by streamer attachment discussed in 3.2. The second case is that if V_0 is not large enough for any of these events to occur, the corona remains stable, I will increase to a maximum value, and then decline to zero as the voltage V_0 falls to zero. For a symmetric, stable corona, we may see in Figs. B.21 and B.22 in Appendix B how the current I rises as the voltage V_0 falls after the onset of breakdown for shot 399.

For shot 399 at 30μs, the ohmic region could be distinguished as we will see in Sec. 4.1 and there was indeed a region of corona where $\rho_1 < \rho_0$. The current reaches its maximum about 200μs. From 30 to 200μs, the electrostatic phase is clearly defined. Thus, it takes the order of 30μs fcr the electrostatic phase to be reached, which is typical for shots of Exp. A.

If $\overline{J}_c$ is nearly normal to the boundary separating the corona from the ohmic region, and since its magnitude is constant over this surface, then

$$I = \int \overline{J}_c \cdot \overline{dS} \approx \frac{E_B}{\rho_0} \pi r_0^2 \qquad (3.1.3)$$

so that for E_B being regarded as a constant, the surface of the boundary is a maximum when I is a maximum; for the symmetric corona, r_0 is a maximum when I is a maximum. Maximum I and r_0 should depend on maximum V_0, and indeed we have found this to be the case; as maximum or peak V_0 increases, so does maximum r_0.

As the current decays after reaching its maximum, then the symmetric corona enters what we shall call the dynamic phase. Modeling the decay of the corona after Liew, et al. [9], we postulate that a third region exists bounded by an inner radius r_1, where the current density is J_c, and an outer radius r_0, corresponding to r_0 at maximum I.

The three regions of the dynamic model are defined as follows:

Region 1: $a \leq r \leq r_1$, $J \geq J_c$ with $J = J_c$ at $r = r_1$; ρ_1 = const.

Region 2: $r_1 \leq r \leq r_0$, $J \leq J_c$ with ρ_2 dependent on r.

Region 3: $r_0 \leq r \leq b$, the ohmic region with $\rho = \rho_0$.

The dynamic model is discussed in Sec. 5.

3.2 Streamers.

It is well established that a second method of soil breakdown occurs in which narrow channels of high conductivity form at the high voltage electrode and proceed to grow outward at some velocity. These channels have been called streamers. We adopt a model proposed by Petropulous [5] in which a streamer is viewed as contained inside the corona as shown in Fig. 3.2.1. In this model, the corona forms first, and the streamer may initiate at some point on the high voltage electrode for reasons that are not understood. The streamer grows outward distorting the symmetry of the corona. In Fig. 3.2.1, a symmetric corona (dashed line) containing no streamers is contrasted with a corona containing one or more streamers. The streamers always stay inside the boundary of the corona and the electric field remains at E_B at the boundary of the corona.

This model is reasonable if one accepts that the resistivity of the streamer is very low. Then the voltage drop along the streamer will be small, and the potential of the streamer will approximate that of the high voltage electrode. Just as this electrode will cause soil breakdown some distance out from it, so the streamer, which must have a large electric field at its surface, will cause breakdown in the nearby surrounding soil. This model of a corona surrounding a streamer has been adopted by Longmire et al. [10].

These authors also predict that once a streamer is formed, the thermodynamics and electrical properties of the streamer tip will cause it to propagate outward with a predictable velocity. Eventually, the streamer will push the corona surrounding its tip out to the grounded electrode at

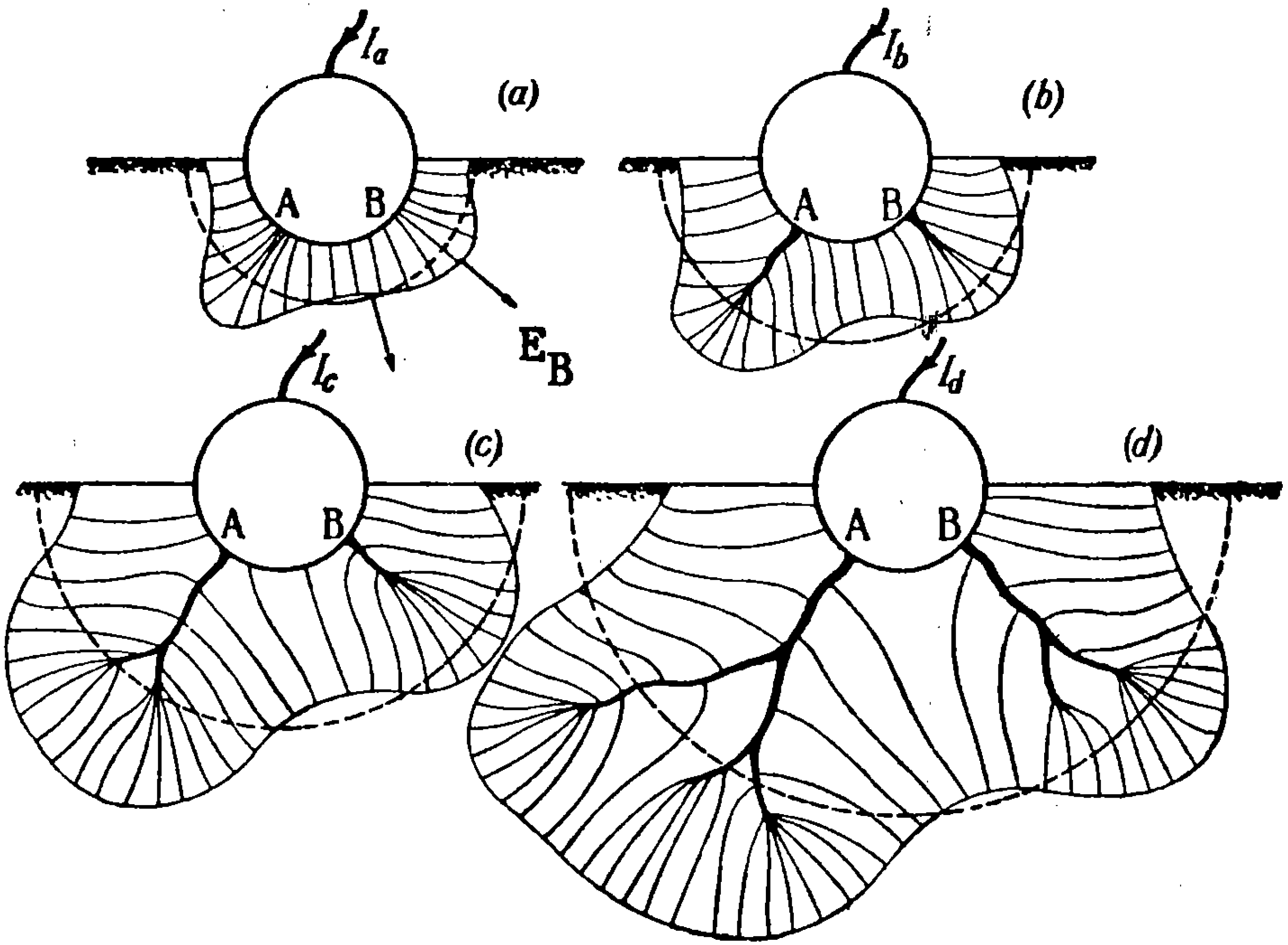

Figure 3.2.1. A buried spherical electrode with streamers propagating outward from points A and B. Streamers are embedded in corona (outer medium dark line). Dashed semicircle is corona boundary if streamers are absent. Current into electrode increases from (a) to (d) as does corona boundary surface. (Fig. 14 of [5]).

r = b, followed by the streamer itself attaching to this electrode. This form of breakdown to the grounded conductor is called streamer attachment.

In Sec. 6, we are able to make an estimate of the radius of a streamer that occured in a nearly symmetric corona. In that case, we found that the radius was about 1 centimeter.

4.0 The Electrostatic Model of the Corona

As we have seen in the preceeding section, the electrostatic model is the cornerstone of the corona model. In this section, we first discuss some other possible corona models and justify the use of the electrostatic model. We then present the details of the theory of the electrostatic model first for the symmetric cylindrical case and then for the symmetrical spherical case. Next, we characterize the electrostatic phase through experimental data. Finally, we show that the peak current can be very accurately predicted by the electrostatic model.

4.1 Other models

In referring to Fig. 3.1.1, we have said that since V(r) appears to vary in a manner proportional to log r in both the corona and ohmic regions, we conclude that in each region E_r is proportional to r^{-1}. We thus assume that

$$V(r) = V_0 - V_1 \log (r/a). \tag{4.1.1}$$

On the other hand, Longmire et al. [10] claim that the electric field in the corona is clamped to that required for electron avalanching to be just balanced by electron diffusion and attachment. They estimate this electric field to be about 1 MV/m. In any case, E_r is assumed to be independent of r, or E_r = const.

This would lead to a linear dependence of V(r) on r,

$$V(r) = V_0 + V_2 \left(1 - \frac{r}{a}\right) \tag{4.1.2}$$

We have tried to see if we could distinguish between these types of voltage variation in the corona by considering in detail the data from shot 399 of Exp. A. The raw data or data base from this shot is shown in Figs. B.1 through B.10 in Appendix B. In Figs. 4.1.1 through 4.1.4, we have plotted the data from the radial probes at the locations shown in Fig. 2.1.1 versus log r at two early

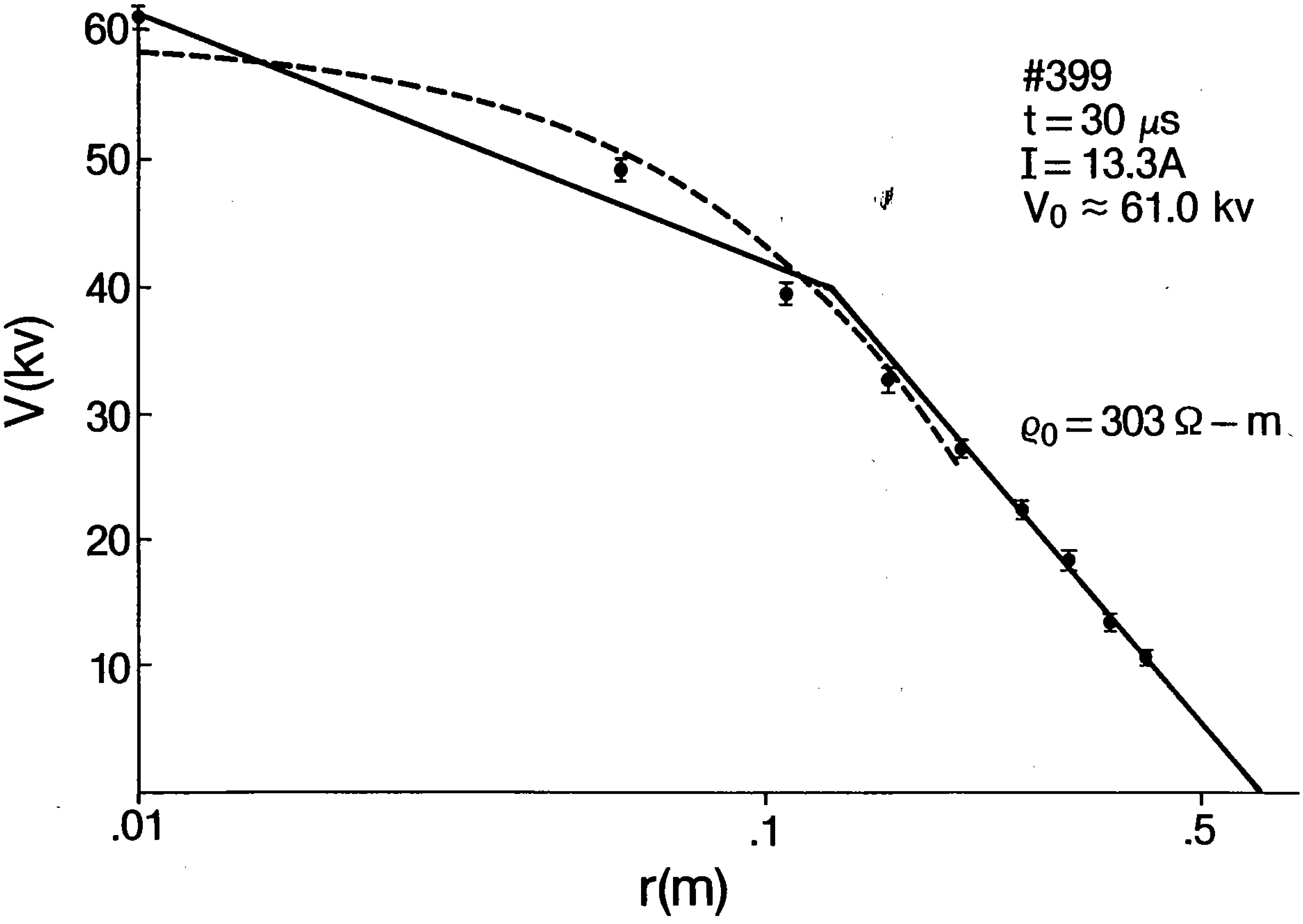

Figure 4.1.1. Log r (solid line) and linear r (dashed line) fit to radial voltage probe data for shot 399; $t = 30$ μs.

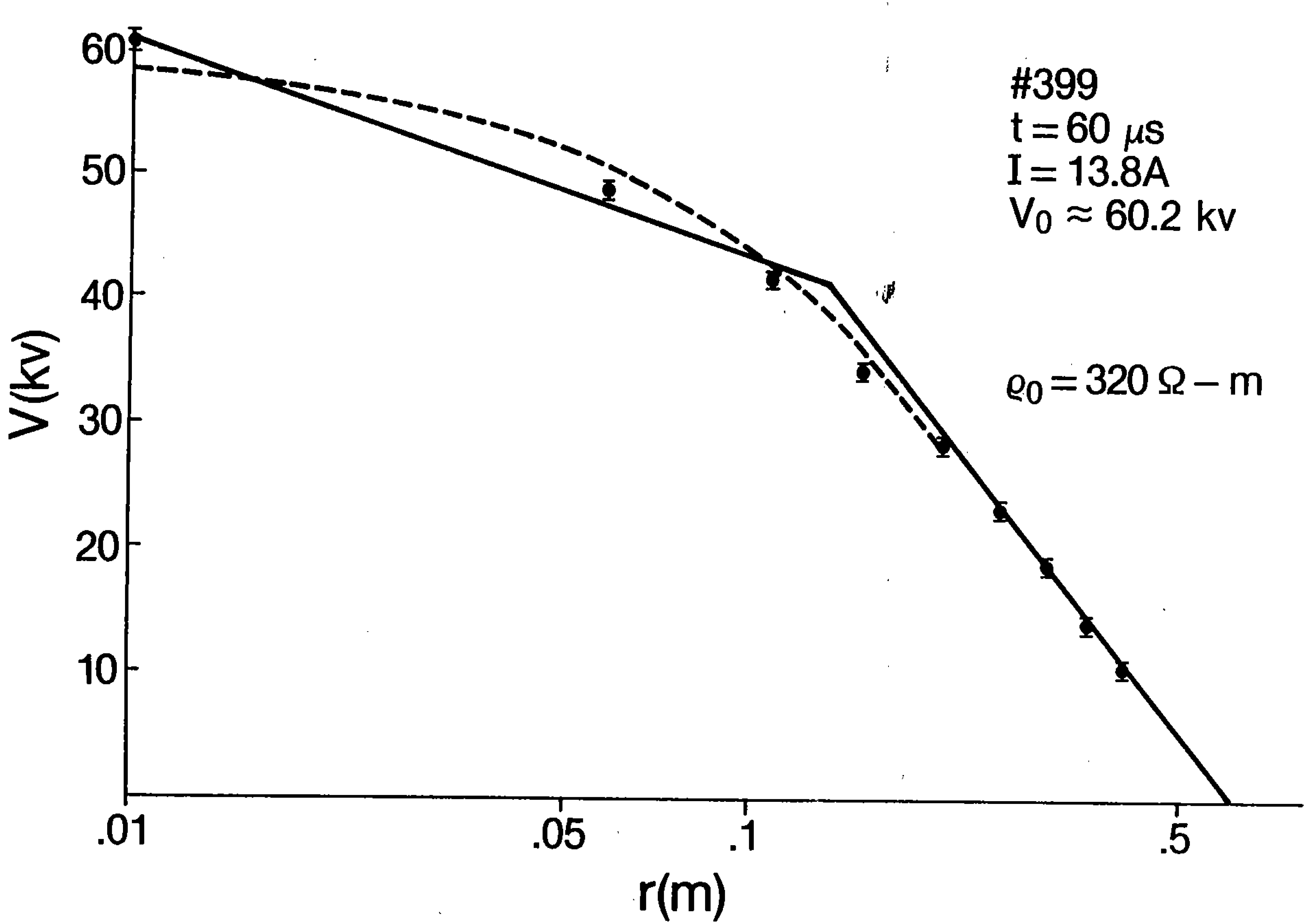

Figure 4.1.2. Log r (solid line) and linear r (dashed line) fit to radial voltage probe data for shot 399; t = 60 μs.

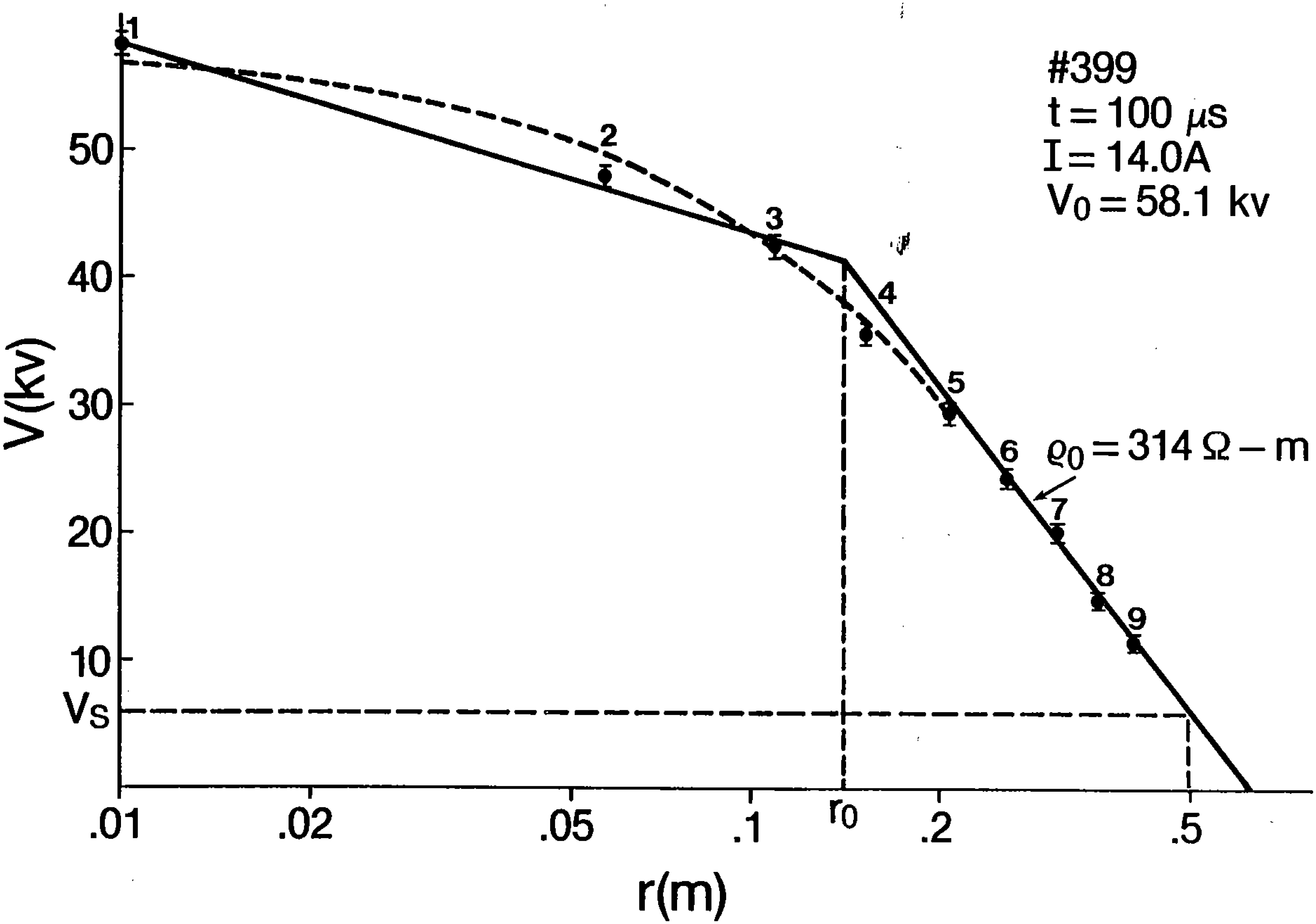

Figure 4.1.3. Log r (solid line) and linear r (dashed line) fit to radial voltage probe data for shot 399; t = 100 μs.

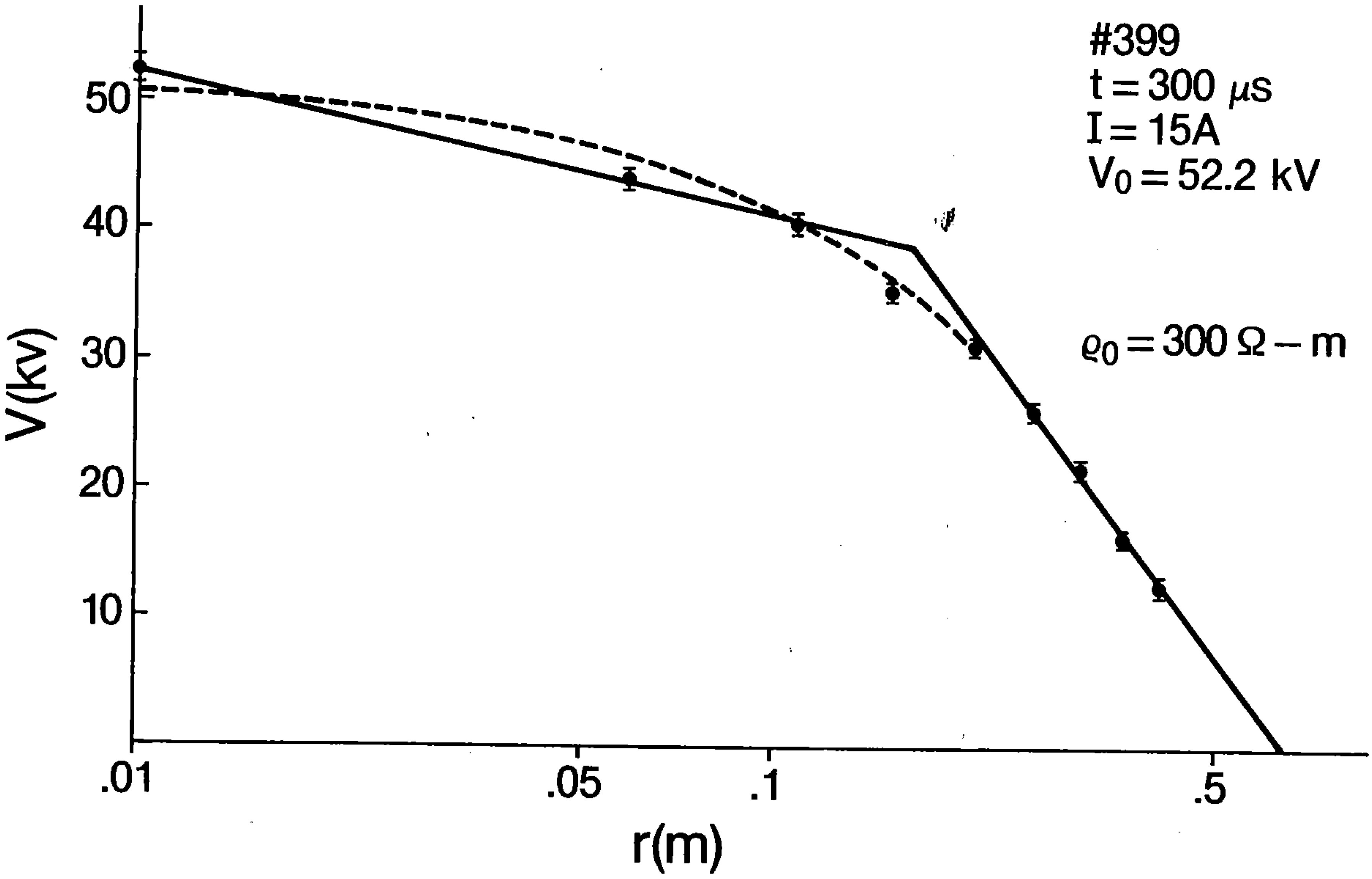

Figure 4.1.4. Log r (solid line) and linear r (dashed line) fit to radial voltage probe data for shot 399; t = 300 μs.

times, 30 and 60μs and at two times when the total current I was nearly its maximum, i.e., 100 and 300μs.

Consider Fig. 4.1.3 for 100μs. The probes in Fig. 2.1.1 are numbered 1 through 9 and the voltage at each probe is shown by a heavy dot in Fig. 4.1.3 with the number of the probe from which it was obtained shown above the point. The experimenters claim that the random error in a probe measurement had a standard deviation of 4% which we interpret to mean a random error of ± 2%. This error is shown by the errors bars on the data points.

We have done a least squares logrithmic regression fit of (4.1.1) on points 1, 2, and 3 and the resulting curve is shown as the solid curve in Fig. 4.1.3. We could only use these three points since these were the only probes in the corona region.

We also have done a least squares linear regression fit of (4.1.2) on points 1, 2, 3, 4, and 5 and the resulting curve is shown as dashed in Fig. 4.1.3. Although the error bars tend to support the log r dependence, this conclusion is somewhat tentative. It is unfortunate that there were only three probes in the corona region. Had there been more, a more certain conclusion might have been reached. Notice that to distinguish between the two types of voltage dependence on r, very precise measurements of V are required. A ± 2% error is the outside limit of what can be tolerated.

We have made the same kind of least squares fit of (4.1.1) and (4.1.2) on the same groupings of points in Figs. 4.1.1, 4.1.2, and 4.1.4 for 30, 60, and 300μs, respectively. At 30μs, neither dependence seems correct based on the error bars. At 60μs, the log r dependence gives a better fit than the linear fit as is the case at 100μs. At 300μs, the log r fit is nearly exact. Thus, as time proceeds toward I reaching its maximum, the log r fit gets progressively better.

In what follows, we shall assume a log r dependence. From the point of view of trying to develop a phenomenological model of the corona which is suitable for computer codes, whether on selects (4.1.1) or (4.1.2), certain important parameters would be predicted in either case. Voltage v.r would be satisfactorily predicted since the difference between the solid and dashed curves in the figures is not large. Also, the total current I and current density as well as r_0, the boundary between the two regions, would be predicted. What would be lost would be E_r and the dependence of ρ_1 on r.

In Figs. 4.1.1 through 4.1.4, we have performed a least squares logrithmic regression fit on points 5 through 9 in the ohmic region. There, as one would expect, the fit is excellent. The slope of this curve determines the ohmic resistivity. We see that there is a significant apparent variation of ρ_0 among the four times. We assume that this variation is not real, but reflects errors in measuring I, which was used in the computation of ρ_0.

The intersection of the log r curve for points in the ohmic region and the log r curve for points in the corona region determines r_0, as is shown in Fig. 4.1.3. Further, we see at each time, that at r = .5 m, which is the location of the grounded electrode, the voltage V(r) is not zero, but has some finite value, V_s. This is because there was a 200Ω resistor attached between this electrode and pulser ground.

4.2 The Cylindrically Symmetric Corona

In Fig. 4.2.1 is shown a diagram which will serve to illustrate both the cylindrically and spherically symmetric corona. It is assumed that the inner electrode of radius a is connected to a high voltage pulser which has negligible series inductance and resistance. The corona region, for which $a \leq r \leq r_0$, is characterized by a resistivity ρ_1 and permittivity ε_2. The ohmic region for $r_0 \leq r \leq b$ has an ohmic resistivity ρ_0 and a permittivity ε_2. The outer conductor of radius b is connected to pulser ground through a resistor R.

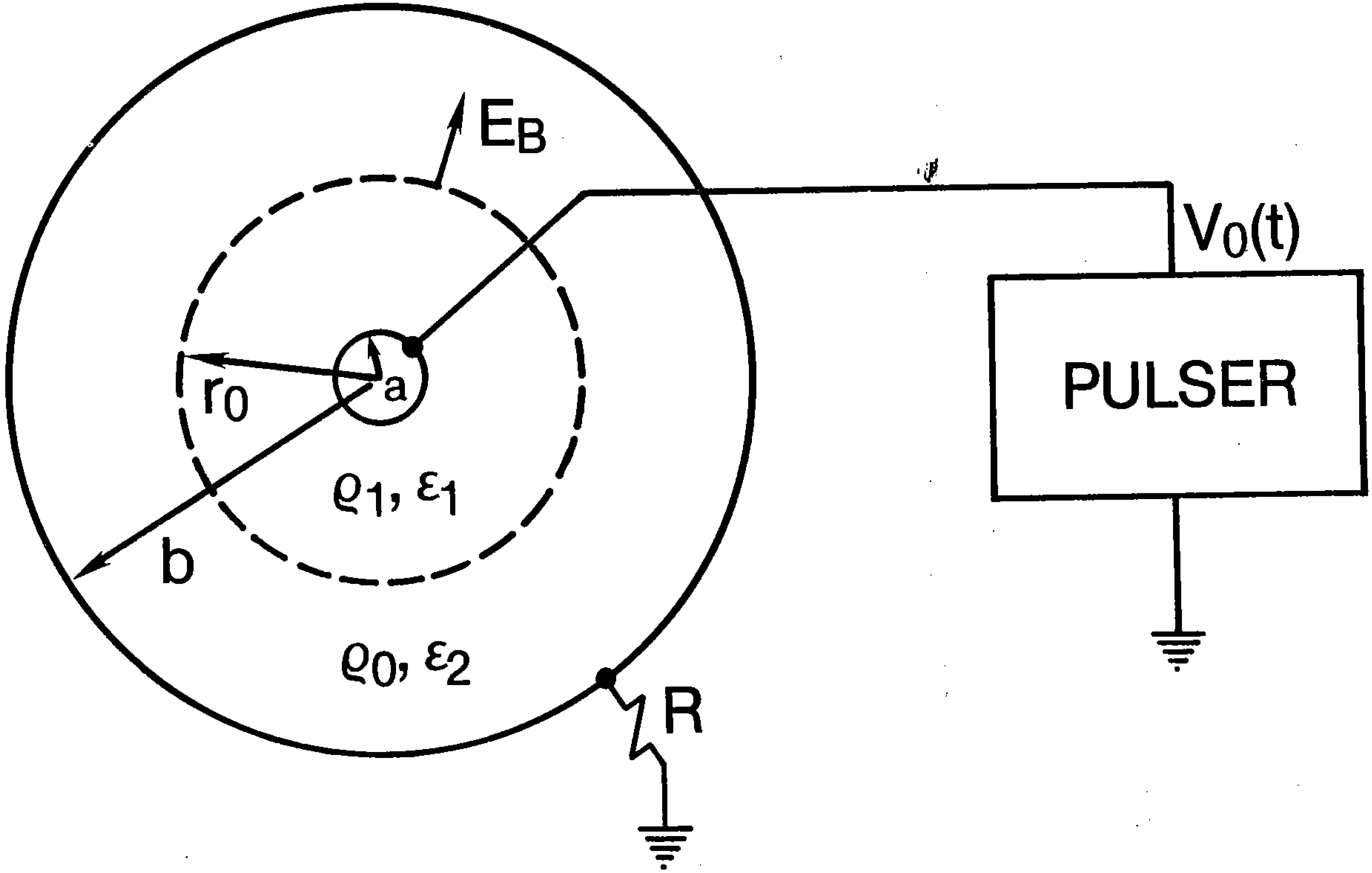

Figure 4.2.1. A cylindrical or sperhical soil sample in the electrostatic phase. $a \leq r \leq r_o$; corona region; $r_o \leq r \leq b$: ohmic region.

It is a simple matter to apply Gauss's Law to this system and the details will be omitted. We note, however, the following points:

1. By assumption, the electric field $\overline{E} = \hat{r}\ E\ (r)$ is radial and proportional to r^{-1} in both regions. This leads to $\nabla \cdot \overline{E} = 0$. Also, the resistivity is constant in each region.

2. The boundary condition at r_o is that the normal component of the current density is continuous across the boundary. This will require a charge on the boundary determined by the permittivity and resistivity of both regions.

3. If we express both the electric field E(r) and the voltage V(r) as a function of the voltage on the inner conductor V_o, the permittivities ε_1 and ε_2 will not explicitly appear in the expressions for either of these quantities.

4. The potential at r = b is V_s. This could be attributed to a resistor between this electrode and ground or to a contact potential at r = b.

With these comments, we have found that the expressions for E(r) and V(r) are:

$a \leq r \leq r_o$

$$V(r) = \frac{(V_o - V_s)}{D} \left[\ln \frac{b}{r_o} + \frac{\rho_1}{\rho_o} \ln \frac{r_o}{r} \right] + V_s \qquad (4.2.1)$$

$$E(r) = \frac{V_o - V_s}{D} \frac{\rho_1}{\rho_o} \frac{1}{r} \qquad (4.2.2)$$

$r_o \leq r \leq b$

$$V(r) = \frac{V_o - V_s}{D} \ln \frac{b}{r} + V_s \qquad (4.2.3)$$

$$E(r) = \frac{V_o - V_s}{D} \frac{1}{r} \qquad (4.2.4)$$

$$\text{where } D = \ln \frac{b}{r_o} + \frac{\rho_1}{\rho_o} \ln \frac{r_o}{a} \qquad (4.2.5)$$

We may obtain a number of useful expressions from the above equations.

E_B, the critical electric field may be obtained from (4.2.4) by setting $r = r_o$:

$$E_B = \frac{V_o - V_s}{D} \frac{1}{r_o}$$

$$= \frac{V_o - V_s}{r_o \left[\ell n \frac{b}{r_o} + \frac{\rho_1}{\rho_o} \ \ell n \ \frac{r_o}{a} \right]} \tag{4.2.6}$$

If α is the angle of the cylindrical wedge and L is its depth, then the total current through the sample I is

$$I = \alpha r_o L \frac{E_B}{r_o} = \frac{\alpha L}{\rho_o} \frac{V_o - V_s}{D} \tag{4.2.7}$$

Thus, from (4.2.3) and (4.2.7)

$$V(r) = \frac{\rho_o}{\alpha L} I \ \ell n \ \frac{b}{r} + V_s \tag{4.2.8}$$

and

$$\frac{\partial V}{\partial (\log r)} = - 2.303 \ I \ \frac{\rho_o}{\alpha L} \tag{4.2.9}$$

where ln 10 = 2.303. Thus, if we can obtain $\partial V/\partial$ (log r) and I from the experimental data, we may use (4.2.9) to calculate ρ_o.

From (4.2.1) and (4.2.3),

$$\frac{\partial V}{\partial \log r} = \begin{cases} K \dfrac{\rho_1}{\rho_o} & a \le r \le r_o \\ K & r_o \le r \le b \end{cases} \tag{4.2.10}$$

where $K = -2.303\ (V_o - V_s)/D$. Thus, the ratio of the slopes of the two solid curves in Figure 4.1.3 will give ρ_1/ρ_o.

Finally, it is of interest to define

$$x \equiv r_o/a \tag{4.2.11}$$

and

$$y \equiv (V_o - V_s)/a\ E_B. \tag{4.2.12}$$

Then we may rewrite (4.2.6) as

$$y = -x\ \ell n\ \frac{a}{b} x + \frac{\rho_1}{\rho_o}\ x\ \ell n x. \tag{4.2.13}$$

We have plotted y v. x with b/a = 50 and ρ_1/ρ_o as the parameter in Figure 4.2.2. For small ρ_1/ρ_o, y exhibits a maximum at some x. For example, for $\rho_1/\rho_o = 0$, the maximum will occur at $x = (b/a)e^{-1} = 18.4$ which corresponds to $r_o = b/e$. As V_o increases so that y increases with E_B assumed to be constant, r_o will increase. If V_o is so large that r_o or x reaches the point corresponding to the maximum, the system will become unstable and breakdown will occur all the way to r = b [11]. Thus, the corona will attach to the grounded conductor.

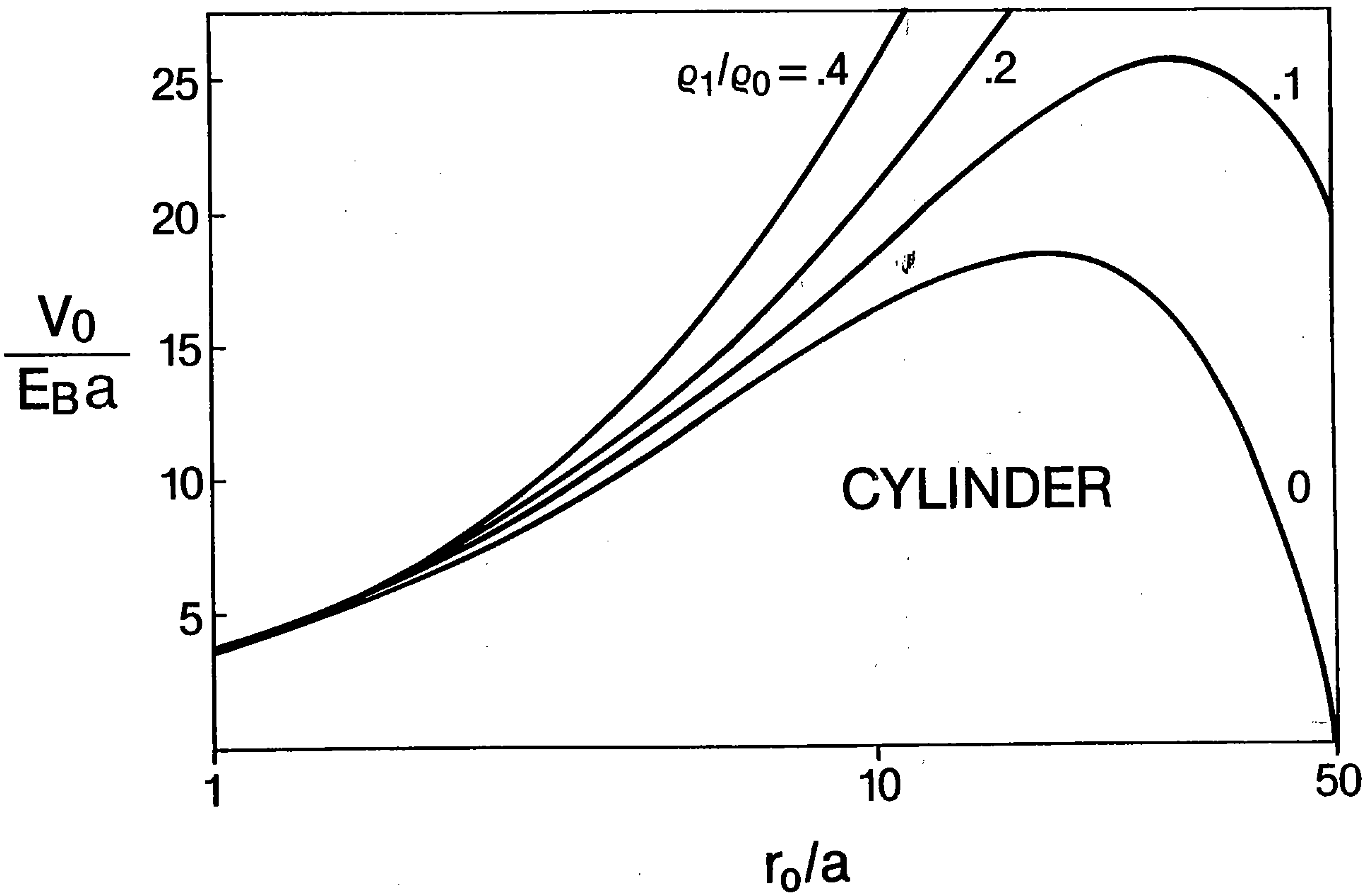

Figure 4.2.2. Stability curves for a cylindrical soil sample which is symmetrically broken down. V_0 on the ordinate is, in fact, V_0-V_s if there is a resistance between the soil and pulser ground; b/a = 50.

As ρ_1/ρ_0 increases from zero, the maximum moves to the right in Figure 4.2.2. At $\rho_1/\rho_0 = .203$, it has just arrived at x = 50, or r = b with y = 39.7. The system is therefore unconditionally stable for $\rho_1/\rho_0 > .203$ for b/a = 50.

The external resistance R in Figure 4.2.1 will also tend to stabilize the corona. Carlile [11] has shown that if a resistance of value

$$R_c = \rho_0/\alpha L \tag{4.2.14}$$

is inserted in series with the soil sample, the corona will be unconditionally stable. For a $\pi/2$ wedge with L = .1 m and ρ_0 = 350 ohm-m, R_c = 2229 ohm.

4.3. The Spherically Symmetric Corona.

Figure 4.2.1 suffices to describe this system. We assume here that $\overline{E}$ is again radial and proportional to r^{-2}. Once again, $\nabla \cdot \overline{E} = 0$ and ρ_1 is a constant. Points 2, 3, and 4 in the previous section once again apply. The expressions for V(r) and E(r) are:

$a \geq r \geq r_o$

$$V(r) = \frac{V_o - V_s}{D'}\left[\left(1 - \frac{\rho_1}{\rho_o}\right)\frac{1}{r_o} - \frac{1}{b} + \frac{\rho_1}{\rho_o}\ \frac{1}{r}\right] + V_s \tag{4.3.1}$$

$$E(r) = \frac{V_o - V_s}{D'}\ \frac{\rho_1}{\rho_o}\ \frac{1}{r^2} \tag{4.3.2}$$

$r_o \geq r \geq b$

$$V(r) = \frac{V_o - V_s}{D'}\ \left(\frac{1}{r} - \frac{1}{b}\right) + V_s \tag{4.3.3}$$

$$E(r) = \frac{V_o - V_s}{D'}\ \frac{1}{r^2} \tag{4.3.4}$$

where $D' = \left(1 - \frac{\rho_1}{\rho_0}\right)\frac{1}{r_0} - \frac{1}{b} + \frac{\rho_1}{\rho_0}\frac{1}{a}$ (4.3.5)

From (4.3.4)

$$\begin{aligned} E_B &= \frac{V_0 - V_s}{D'} \quad \frac{1}{r_0^{\,2}} \\ &= \frac{V_0 - V_s}{\left(1 - \frac{\rho_1}{\rho_0}\right)\frac{1}{r_0} - \frac{1}{b} + \frac{\rho_1}{\rho_0}\ \frac{1}{a}} \quad \frac{1}{r_0^{\,2}} \ . \end{aligned} \tag{4.3.6}$$

The total current I through the sample is

$$I = 4\pi r_0^{\,2} \ \frac{E_B}{\rho_0} \tag{4.3.7}$$

so that the total resistance from the high voltage electrode to r = b is:

$$R = \frac{V_0}{I} \approx \frac{\rho_0}{4\pi} \ D' \tag{4.3.8}$$

For the case, $b \to \infty$, $\rho_1/\rho_0 \to 0$, $D' = r_0^{\,-1}$, so that

$$R = \frac{\rho_0}{4\pi r_0} \tag{4.3.9}$$

If we define

$x = r_0/a$

and

$y = (V_0 - V_s)/aE_B$,

then (4.3.6) becomes

$$y = x^2\left[\left(1 - \frac{\rho_1}{\rho_0}\right)\frac{1}{x} - \frac{a}{b} + \frac{\rho_1}{\rho_0}\right] \tag{4.3.10}$$

The quantity y has been plotted v. x with b/a = 50 and ρ_1/ρ_0 as the parameter in Figure 4.3.1. We see that the system has an instability for $\rho_1/\rho_0 = 0$ at $r_0 = b/2$. However, it quickly stabilizes at small values of ρ_1/ρ_0. For example, the system is stable at $\rho_1/\rho_0 = .01$.

For the case $b \to \infty$, (4.3.10) becomes

$$y = \left(1 - \frac{\rho_1}{\rho_0}\right)x + \frac{\rho_1}{\rho_0}x^2 \tag{4.3.11}$$

and the system is unconditionally stable.

4.4. Evolution of the Electrostatic Phase.

Soil will break down at a metal-soil interface when the electric field is about 1 MV/m. For example, in Figure 4.4.1 for Exp. A where the electric field was initially 1.8 MV/m. (Fig. B.11), we see that the soil remains ohmic for about 10 μs, and then breaks down characterized by the current starting to rise. Call the delay until breakdown occurs, t_i, as shown in 4.4.1.

Breakdown is characterized by the formation of the corona, a subsequent lowering of the sample impedance, and an increase in the total sample current I as shown in Figure 4.4.2 with the accompanying voltage characteristic on the center conductor being illustrated in Figure 4.4.3. If the voltage is not large enough to push r_0 either to a radius where instability will occur

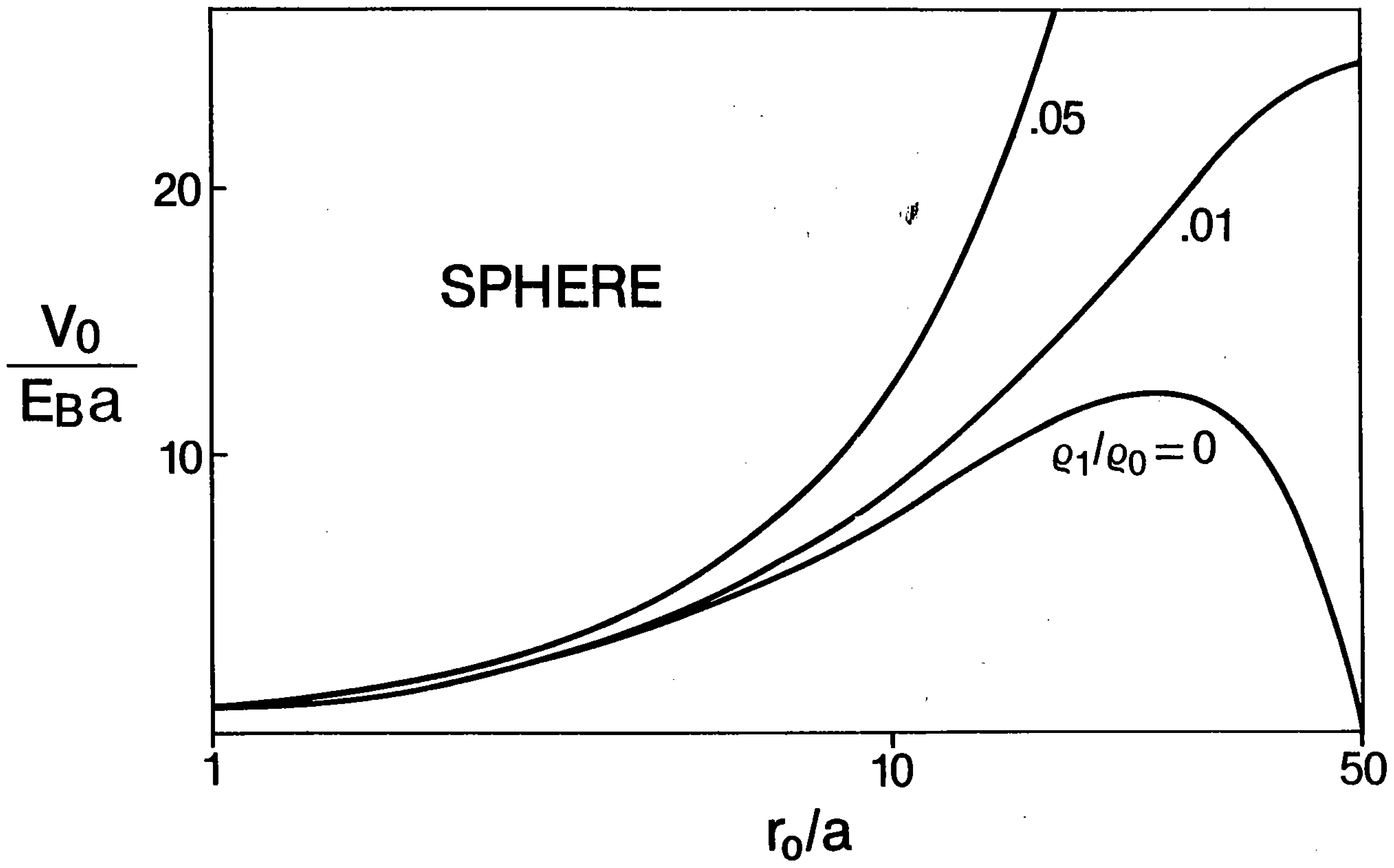

Figure 4.3.1. Stability curves for a spherical soil sample that is symmetrically broken down; b/a = 50.

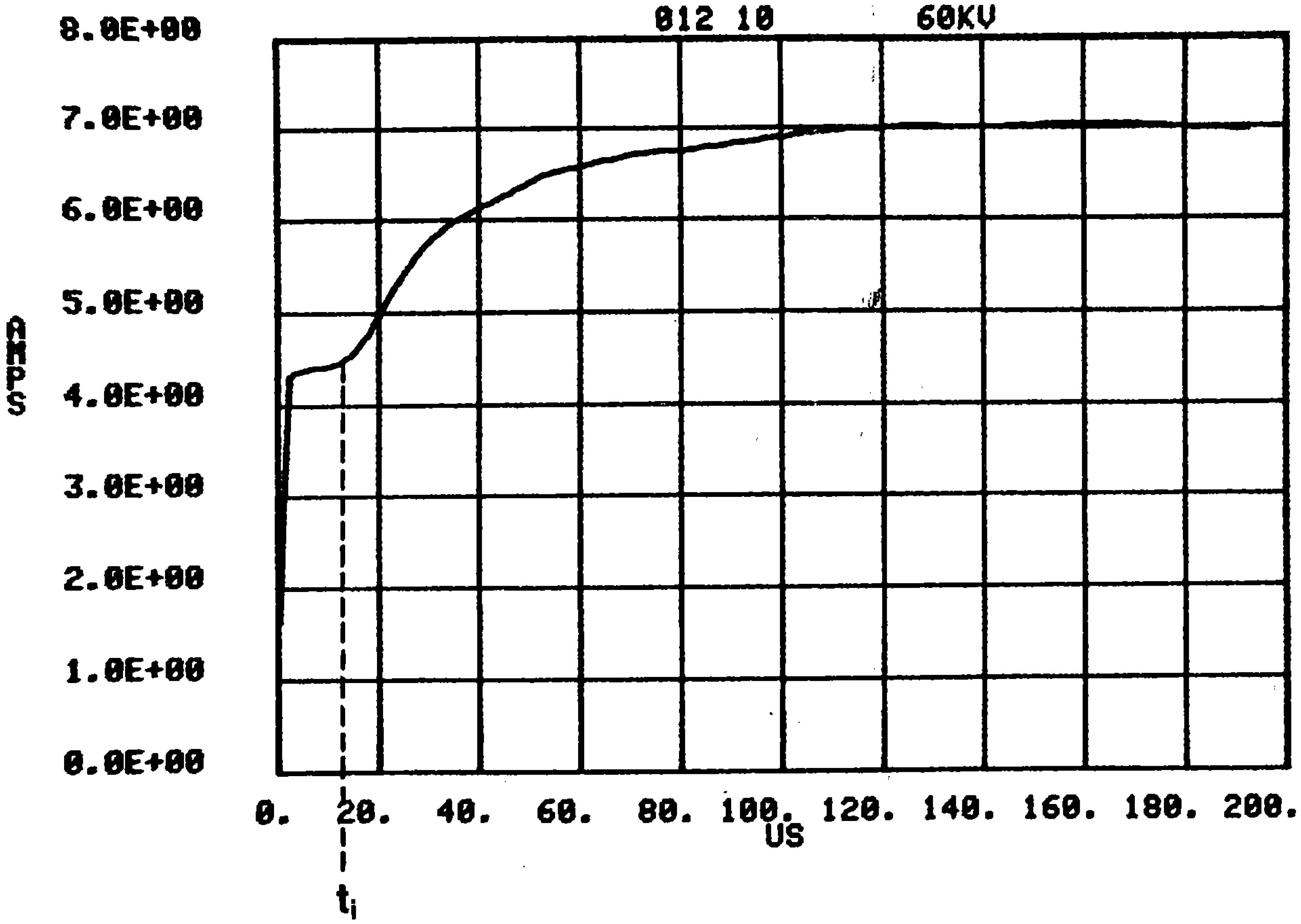

Figure 4.4.1. Current v. time for shot 012 (cylindrical wedge soil sample). The soil remains nearly ohmic until time t_i after the application of V_o.

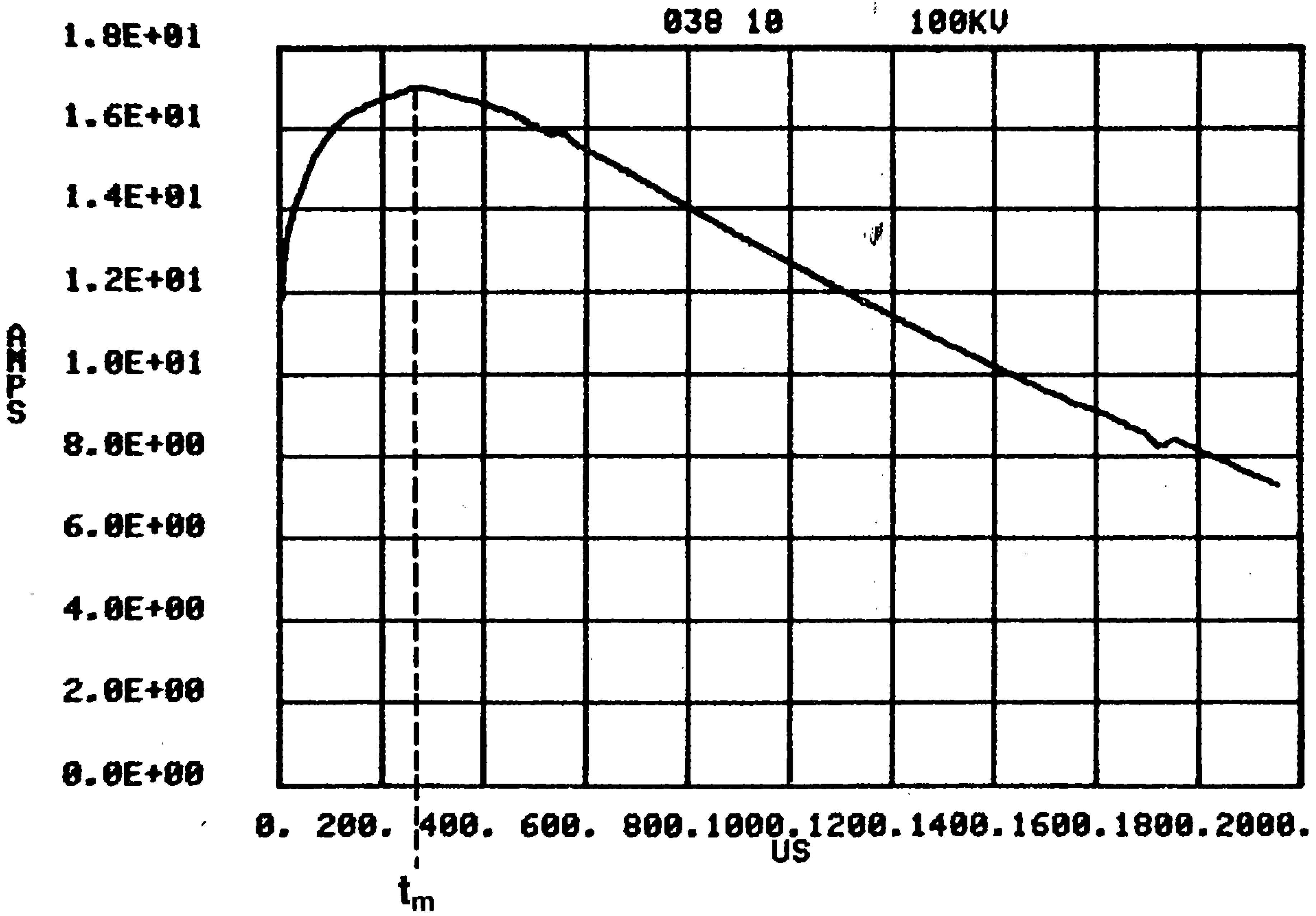

Figure 4.4.2. Current vs. time in shot 038 (cylindrical wedge soil sample). The current rises to a maximum at time t_m.

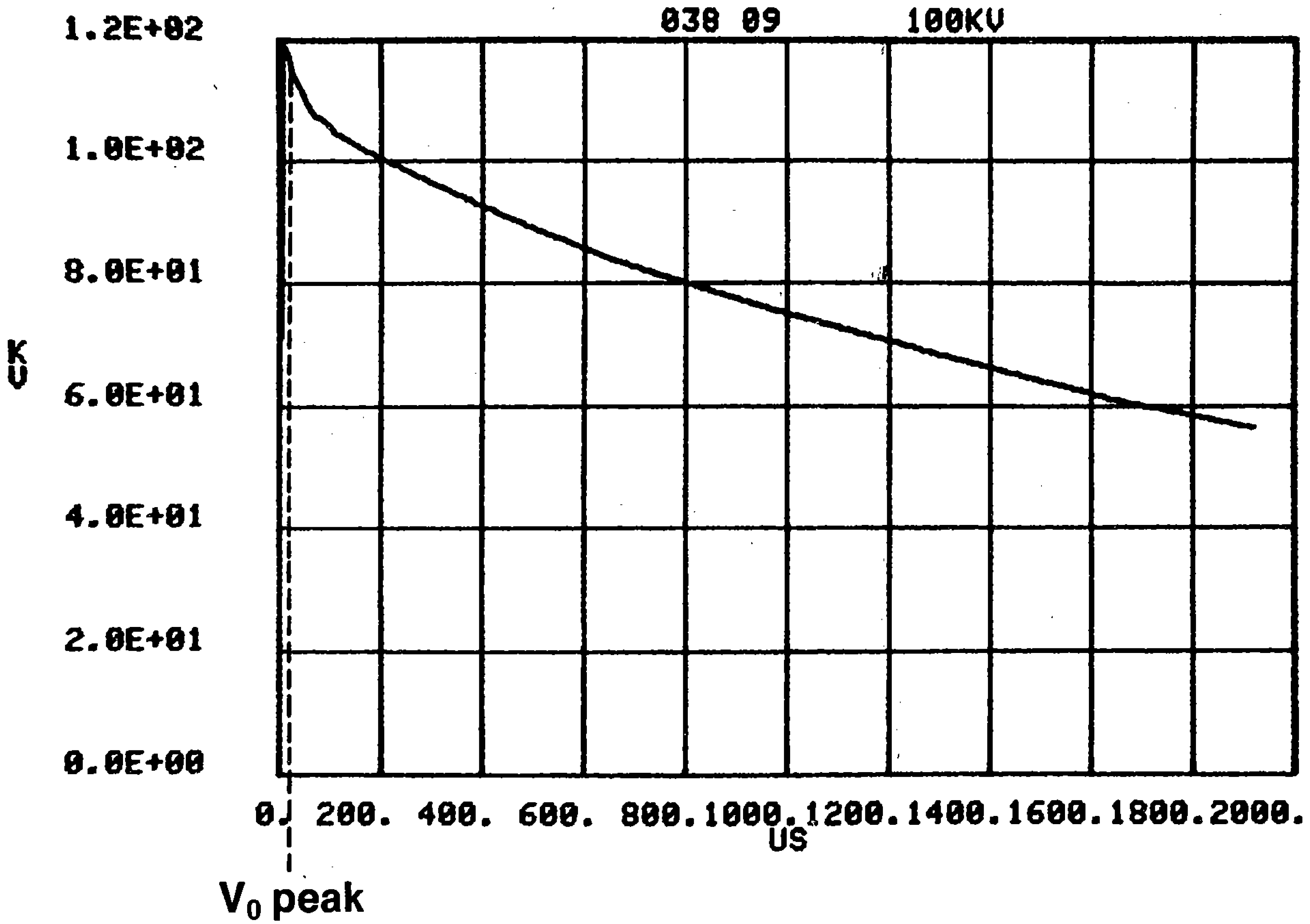

Figure 4.4.3. Voltage vs. time in shot 038 (cylindrical wedge soil sample).

or to the outer conductor, the current will reach a maximum at a time t_m as shown in Figure 4.4.2 and then will decline to zero. If, on the other hand, an instability radius is reached or the corona reaches $r = b$, then breakdown to the outer conductor at $r = b$ occurs, at some time t_B, and the current I will increase suddenly at t_B as shown in Figure 4.4.4.

In Figure 4.4.1, where $\rho_0 = 1500$ ohm-m, for $t < t_i$, $V_0/I = 16.1$ Kohm whereas the calculated ohmic resistance R_0 given by

$$R_0 = \frac{\rho_0 \ell n \, (b/a)}{\alpha L} , \tag{4.4.1}$$

is 14.7 Kohm. Van Lint, et al. [2] show that the measured resistance is characteristically larger than the bulk low voltage resistance due apparently to "a small increase in effective resistivity with increase in current density, a small increase in impedance near the small diameter center electrode, and a small increase with time of the contact impedance" at the center electrode [2]. They have treated this subject exhaustively, and the reader is referred to their paper for further details.

Also, these authors have shown experimentally the relationship between the applied electric field at the center conductor E_0 and the time of initiation of breakdown, t_i [2]. We repeat here two curves from their paper. In Figure 4.4.5, the dependence of t_i with E_0 is shown where the parameter is geometry and in Figure 4.4.6, the parameter is soil type. In all cases, t_i decreases as E_0 increases. Typically, t_i has dropped to about 1 μs if E_0 is greater than 2 MV/m. We will not pursue this matter further.

In the rest of this section, we shall consider only the stable case where breakdown does not reach $r = b$, and the current reaches a maximum as in

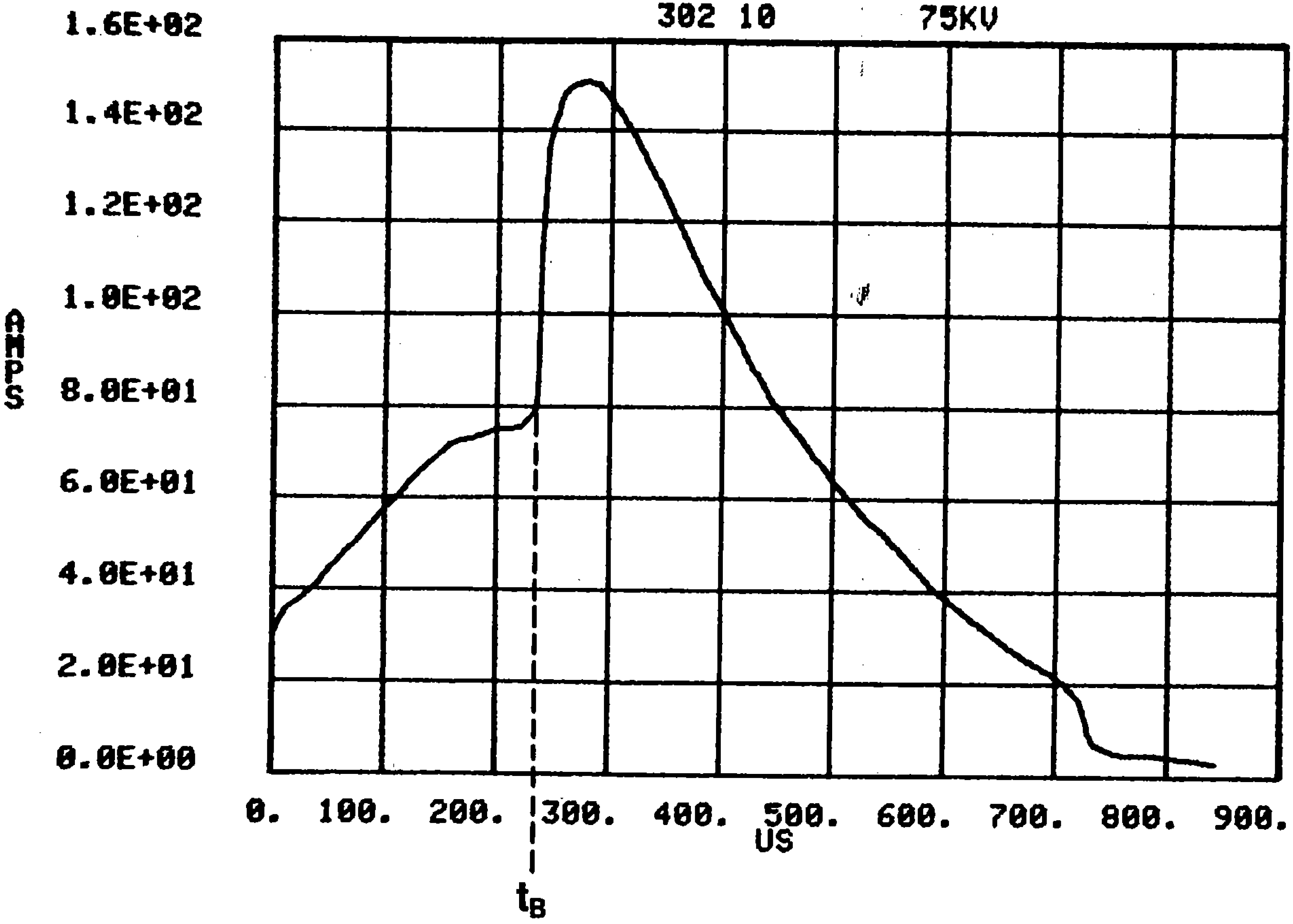

Figure 4.4.4. Current vs. time in shot 302 (cylindrical wedge soil sample). The current rises with time as if to a maximum, and then at t_B the sample breaks down to the outer conductor.

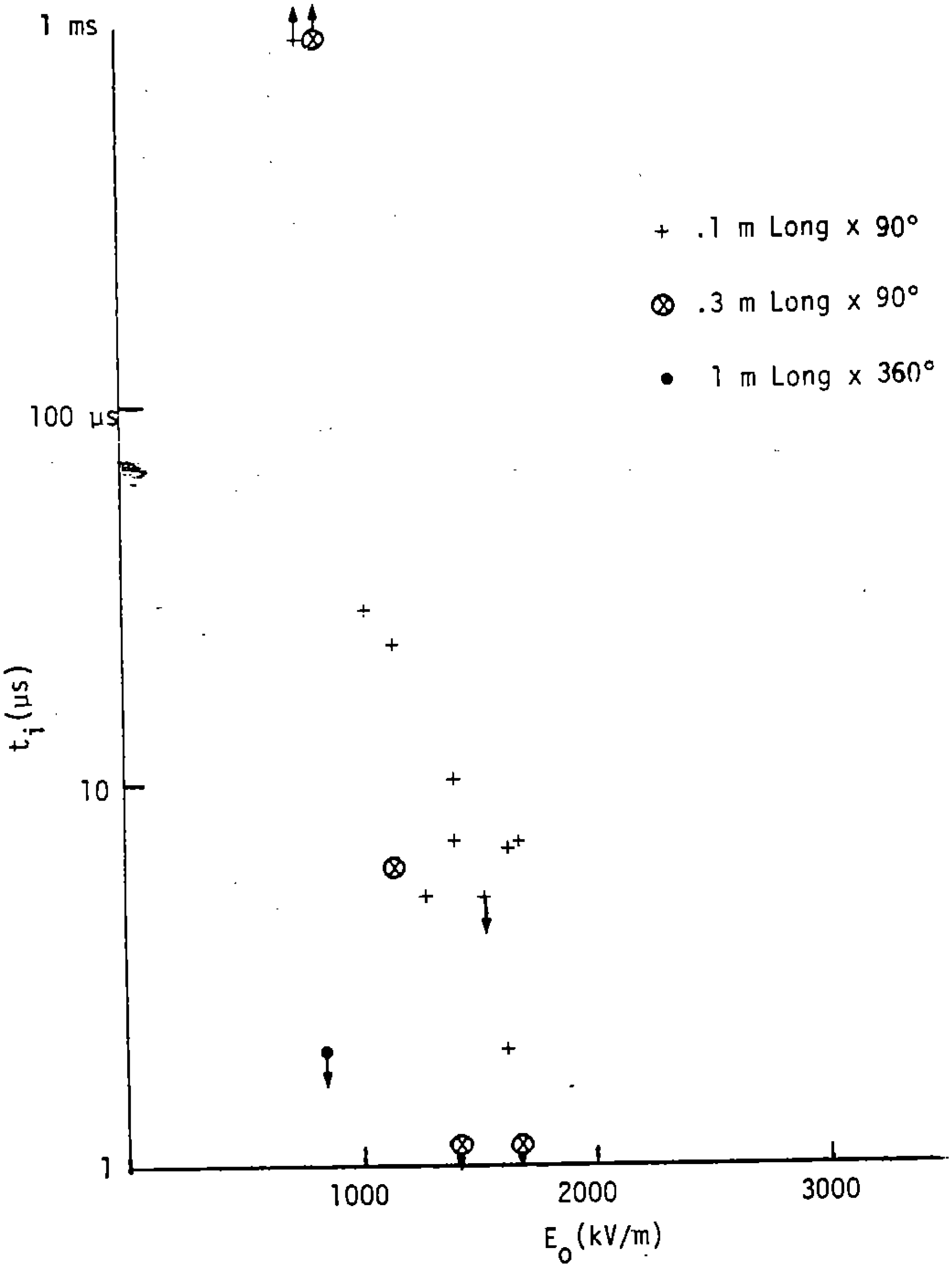

Figure 4.4.5. Time to breakdown t_i for three geometries (Fig. 3.2.4 of [2]).

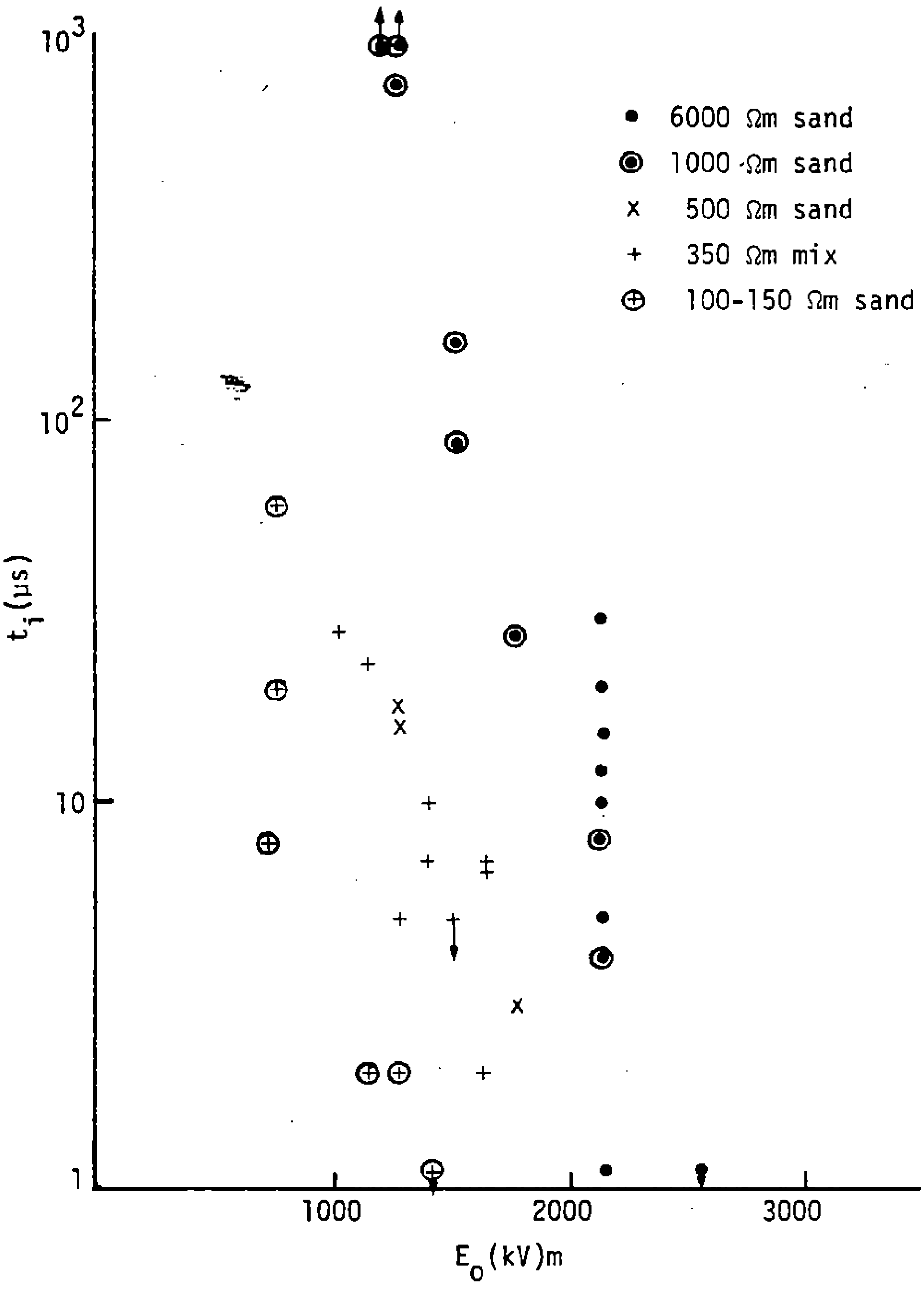

Figure 4.4.6. Time to breakdown t_i for various soil types (Fig. 3.2.5 of [2]).

Figure 4.4.2. We note that in Exp. A, t_m in Fig. 4.4.2 ranges from 100 to 100 μs. There is a rough correlation between t_m and the peak applied voltage: t_m increases with increasing V_o peak.

We have pointed out in Sec. 4.2. that given a plot of V(r) v. log r, as shown in Figure 4.1.3, we may obtain r_o from the intersection of the log r approximations to the ohmic region and the corona region. From the slopes of these two curves, ρ_1/ρ_o may be found from (4.2.10), and then E_B may be calculated from (4.2.6). There were a large number of shots obtained in the Exp. A in a 350 ohm-m sand mix which allows us to investigate these quantities in detail.

We shall use shot 399 as an example. Plots of V/I v. log r for this shot are shown in Figures 3.1.1, and V v. log r in Figures 4.1.1 to 4.1.4. Maximum current for this shot is 15.25 A occurring at 200 μs. From these figures, as time increases r_o increases and ρ_1/ρ_o decreases. At 30 μs: r_o = .127 m., ρ_1/ρ_o = .334; at 60 μs: r_o = .135 m., ρ_1/ρ_o = .28; at 100 μs, r_o = .141, ρ_1/ρ_o = .23; and at 200 μs, r_o = .16 m., ρ_1/ρ_o = .13. For time greater than 200 μs, we are in the dynamic region considered in Sec. 5.

In the other shots which have been investigated, we have found r_o, ρ_1/ρ_o, and E_B at current maximum. We find that for all these shots (12 in all, see Figs. B.1 through B.10 and B.12 through B.31) E_B ranges from about 100 to 250 KV/m. It is interesting that this range coincides with that found by Liew, et al. [9]. We have investigated the correlation between E_B and ρ_1/ρ_o with various parameters such as the total current I, the current density and the peak V_o. We find that these quantities correlate best with V_o peak. This may be justified by noting that the breakdown behavior of the soil may be determined by the initial value of the electric field at the center conductor. We note that this electric field E_o is related to V_o peak by

$$E_0 = \left(V_0 \text{ peak}\right) \Big/ \left(a \ \ell n \frac{b}{a}\right) \tag{4.4.2}$$

We have plotted E_B and ρ_1/ρ_0 v. E_0 in Figures 4.4.7 and 4.4.8. We have processed this data by the least squares linear regression method, which shows that the following linear relationships best fit the data:

$$E_B = 54.5 + 87.6\ E_0,\ R^2 = .69 \tag{4.4.3}$$

$$\rho_1/\rho_0 = .97 - .48\ E_0,\ R^2 = .87 \tag{4.4.4}$$

If E_0 is in MV/m., E_B will have the units of KV/m; similarly, E_0 should be in MV/m in (4.4.4). The coefficient of determination, R^2, is shown for each least squares linear fit. The range of E_0 for which this data is valid is $.5 \geq E_0 \geq 2.0$ MV/m.

In Exp. A, there was some data available such that we could obtain plots of E_B and ρ_1/ρ_0 v. E_0 for soils with other ohmic resistivities than 350 ohm-m (see Figs. B.32 through B.45). These are shown in Figures 4.4.9 through 4.4.14 for soils with resistivities of 200, 170 and 130 ohm-meter. These data should be used with caution because generally no more than four points were available to determine each curve, and some of the data points did not correspond to t_m when I is a maximum, but were obtained at an earlier time. With this qualification, these curves tend to show that E_B increases as the ohmic resistivity increases.

4.5 Calculation of Maximum Current.

One of the real achievements of the electrostatic model is its ability to predict the maximum value of the current through the sample. The maximum

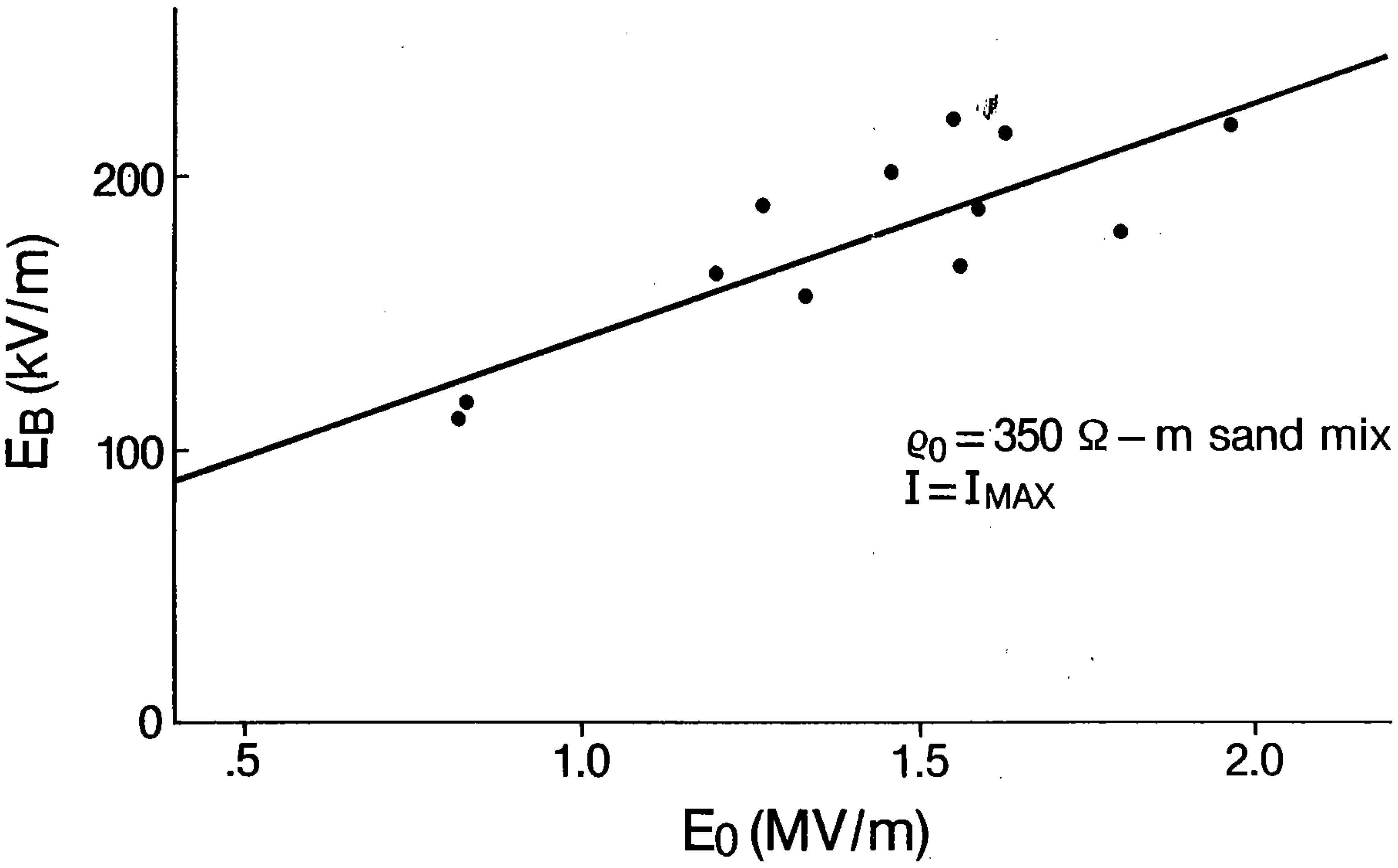

Figure 4.4.7. Linear regression of critical electric field at current maximum with peak electric field at center conductor. ρ_o = 350 ohm- m sand mix.

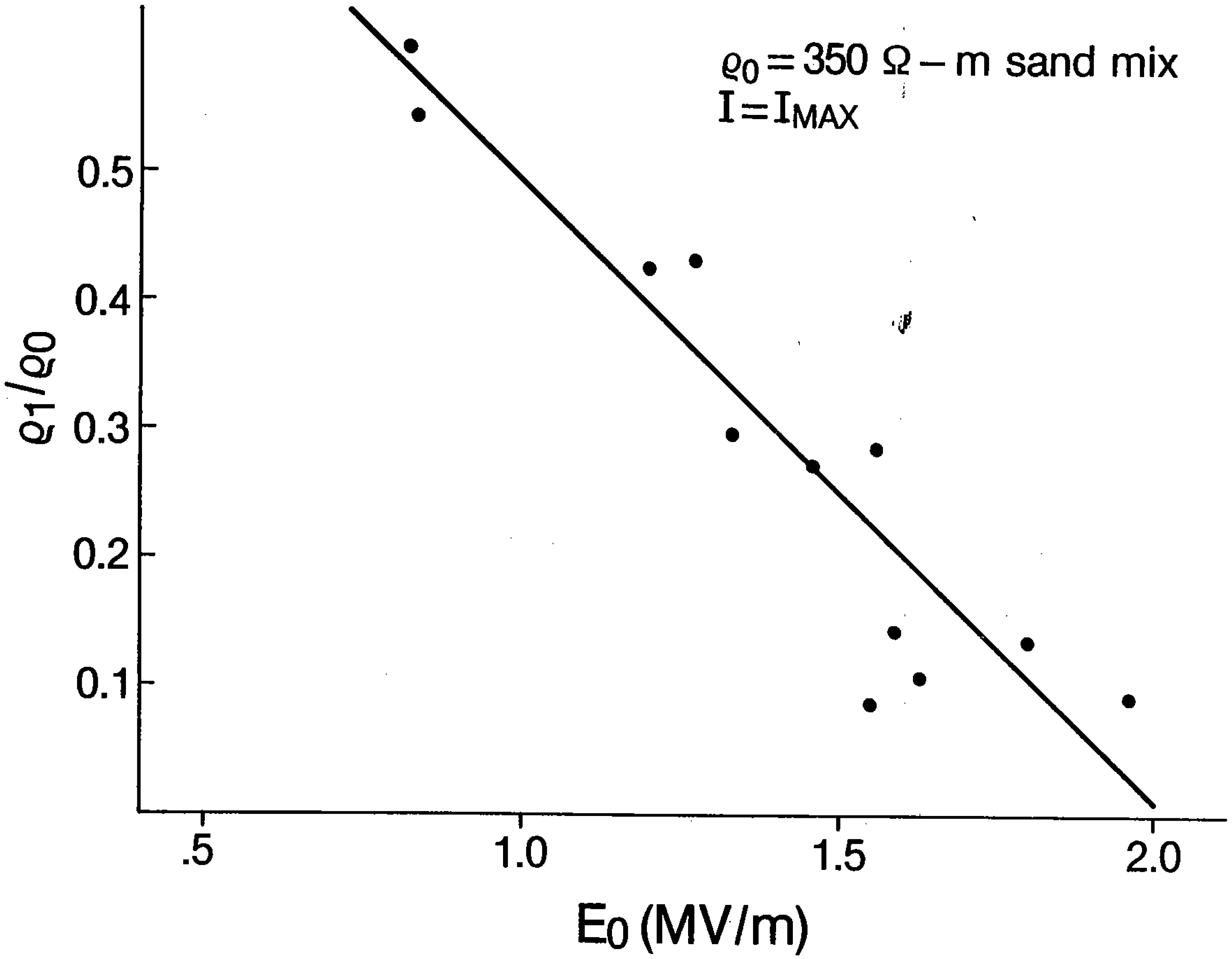

Figure 4.4.8. Linear regression of ρ_1/ρ_0 at current maximum with peak electric field at center conductor. ρ_0 = 350 ohm-m sand mix.

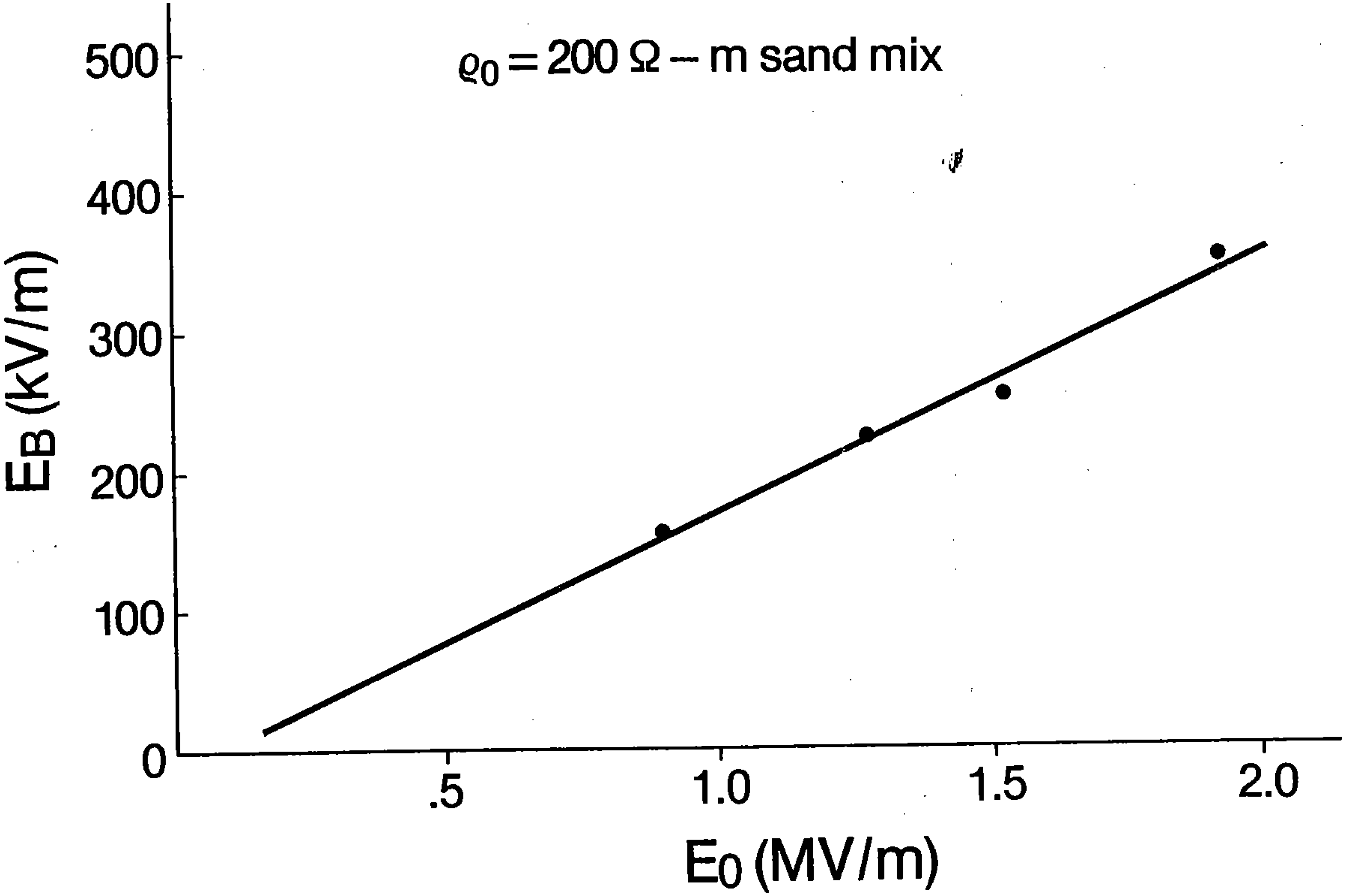

Figure 4.4.9. Linear regression of critical electric field at current maximum with peak electric field at center conductor. ρ_0 = 200 ohm-m sand mix.

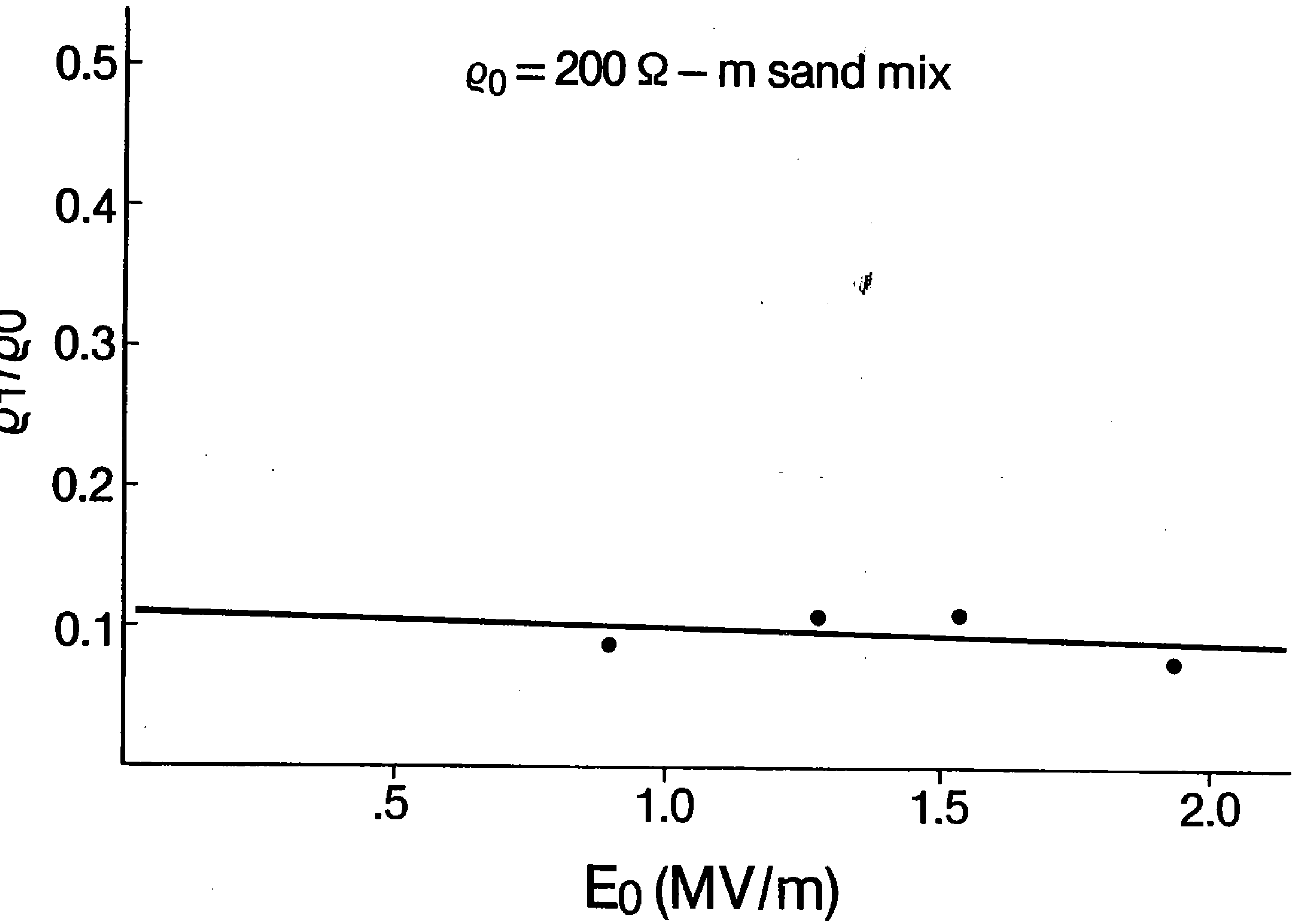

Figure 4.4.10. Linear regress of ρ_1/ρ_0 at current maximum with peak electric field at center conductor. ρ_0 = 200 ohm-m sand mix.

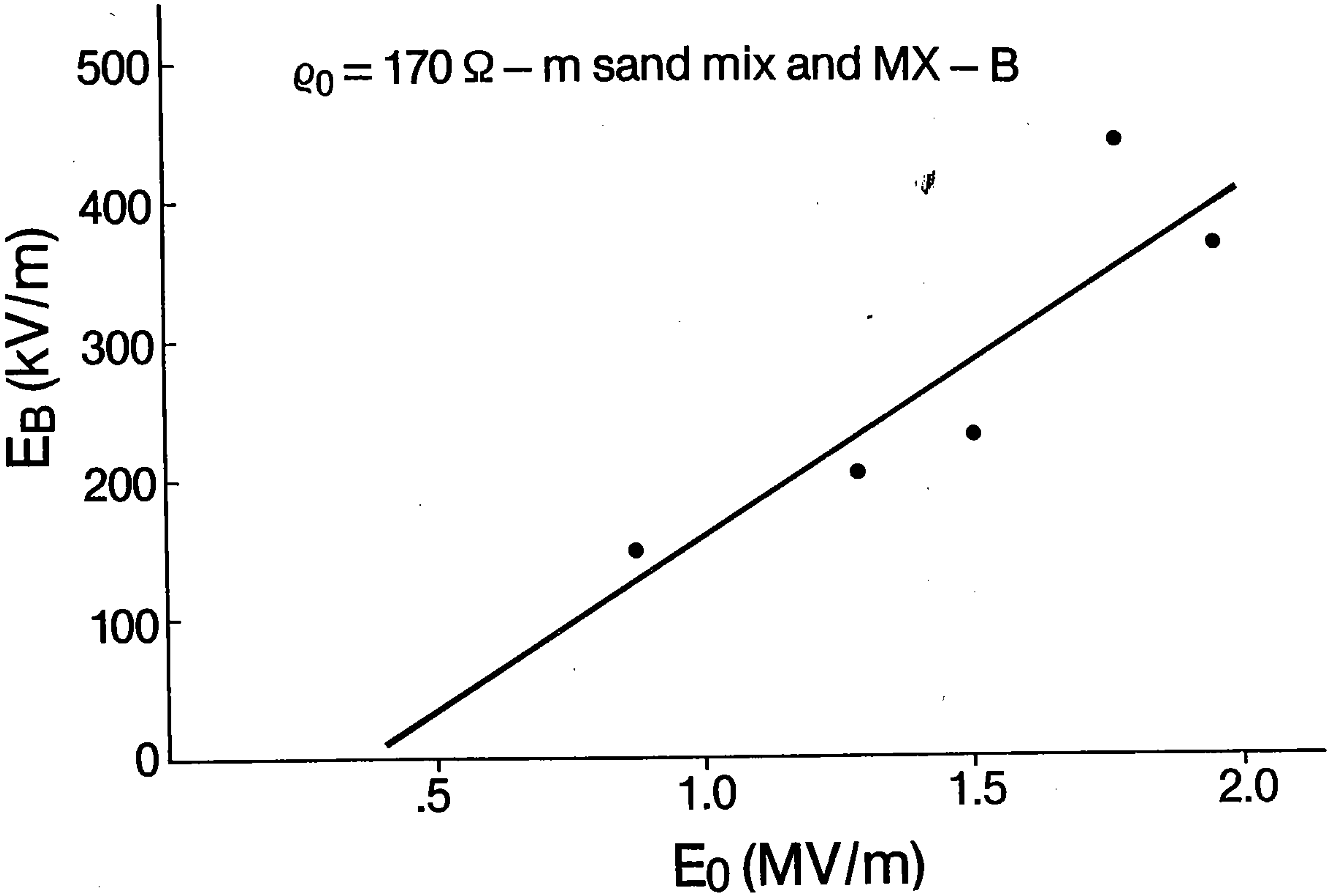

Figure 4.4.11. Linear regression of critical electric field at current maximum with peak electric field at center conductor, ρ_0 = 170 ohm-m sand mix and MX-B.

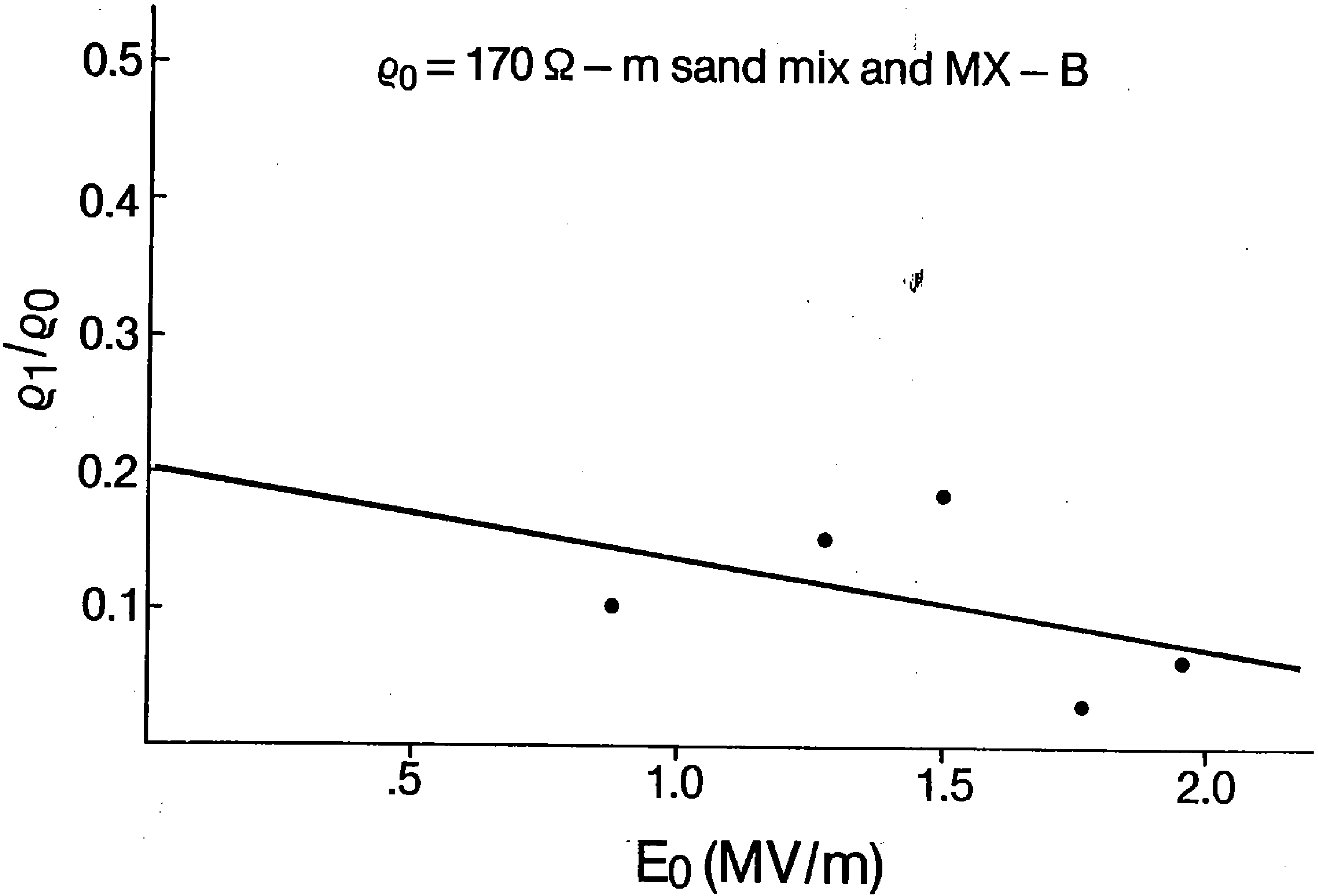

Figure 4.4.12. Linear regression of ρ_1/ρ_0 at current maximum with peak electric field at center conductor. ρ_o = 170 ohm-m sand mix a-d MX-B.

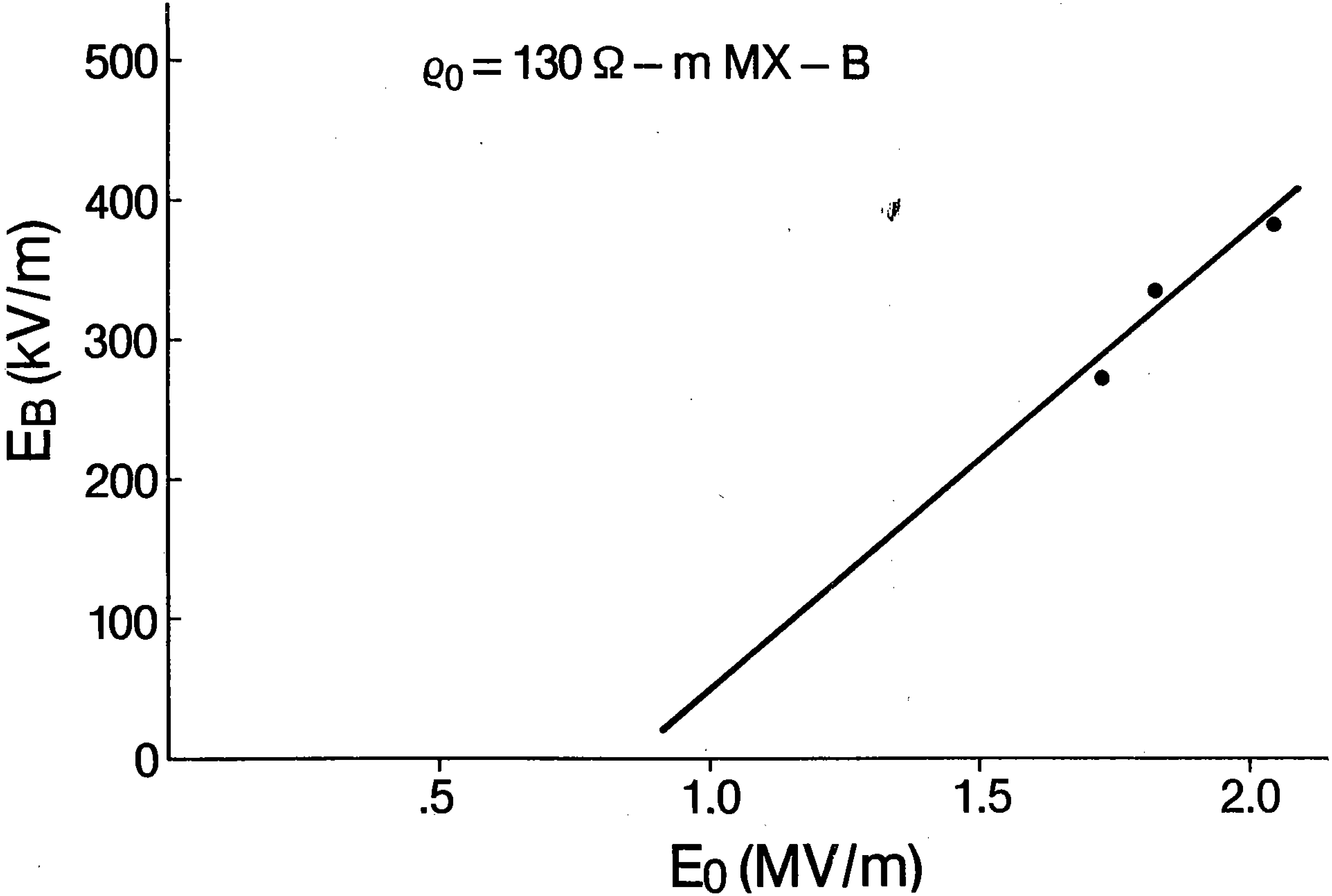

Figure 4.4.13. Linear regression of critical electric field at current maximum with peak electric field at center conductor, ρ_0 = 130 ohm-m MX-B.

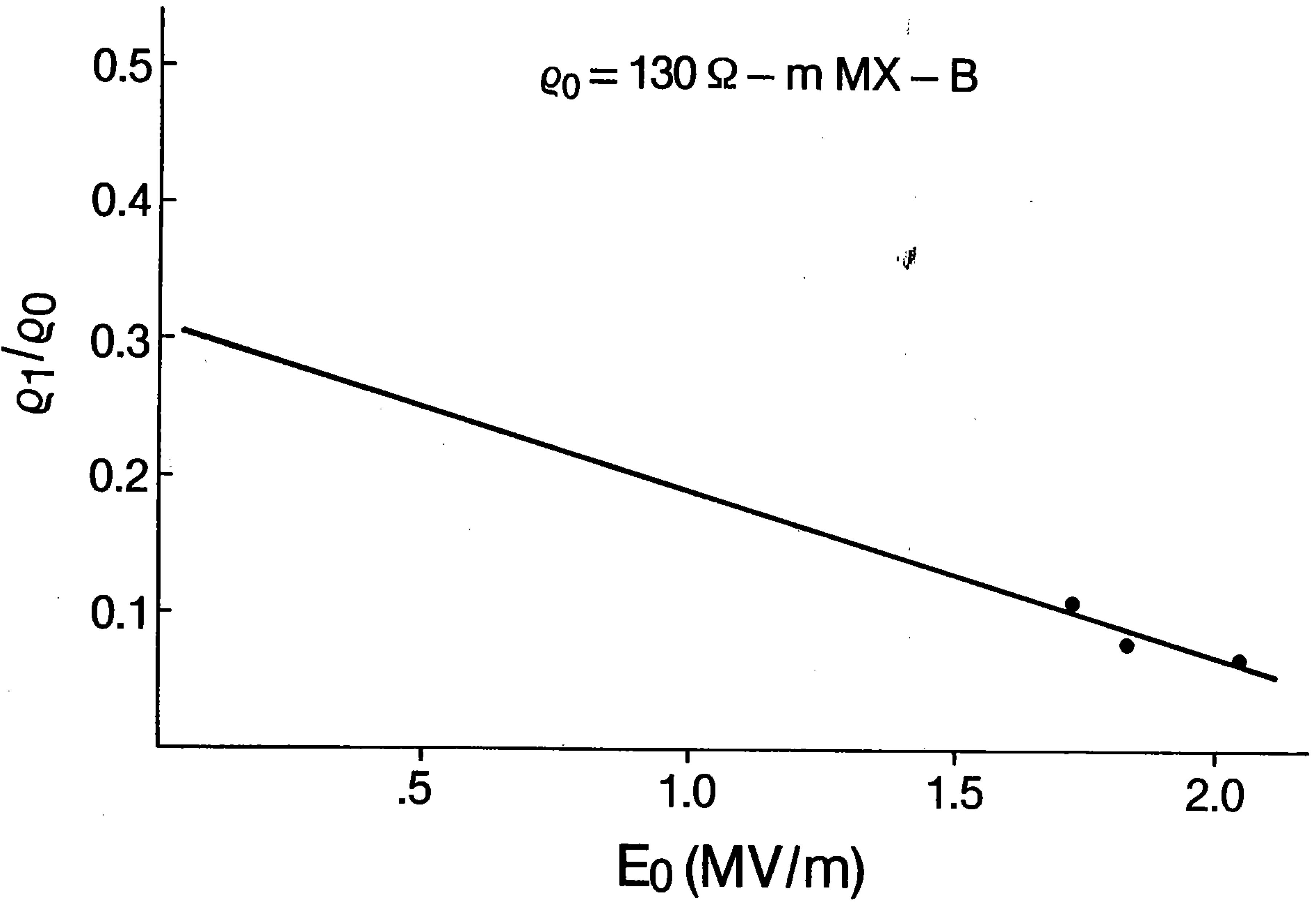

Figure 4.4.14. Linear regression of ρ_1/ρ_0 at current maximum with peak electric field at center conductor. ρ_0 = 130 ohm-m MX-B.

current, I_M, which is shown in Figure 4.4.2, has been measured for a number of shots for the 350 ohm-m sand mix.

The general expression for current through the sample is given by (4.2.27):

$$I = \frac{\alpha L r_o}{\rho_o} E_B \qquad (4.2.27)$$

If we use r_o and E_B at $I = I_M$, (4.2.27) should yield I_M. But, E_B for I_M is given in Figure 4.4.7 and r_o was also tabulated for this current.

In Figure 4.4.15, we have plotted the measured value of I_M v. V_o at t_m, i.e., the center conductor voltage at the time when the current is maximum. Of the 12 shots for ρ_o = 350 ohm-m, 4 were for a sample with L = .1 m. while 8 were for L = .3 m. The experimentally measured values of I_M are shown by the solid dots in Figure 4.4.15.

Alternately, we have used (4.2.27) to predict I_M, where we have used the actual r_o and E_B obtained for a shot. This prediction of I_M is shown by the open circles in Figure 4.4.15. The agreement is usually very close. The percentage differences are tabulated in Table I.

The most important conclusion to be drawn from the generally remarkable correspondence between the measured and calculated I_M is that the corona must be very azimuthally uniform. The radial probes which measure V, from which r_o and E_B are determined, lie at an angle of 45^o as shown in Figure 2.1.1. Thus, r_o and E_B are really only valid for this angle. If, for example, they were quite different at some other angle, then the current density would be azimuthally asymmetric and the total current could not be predicted by (4.2.27).

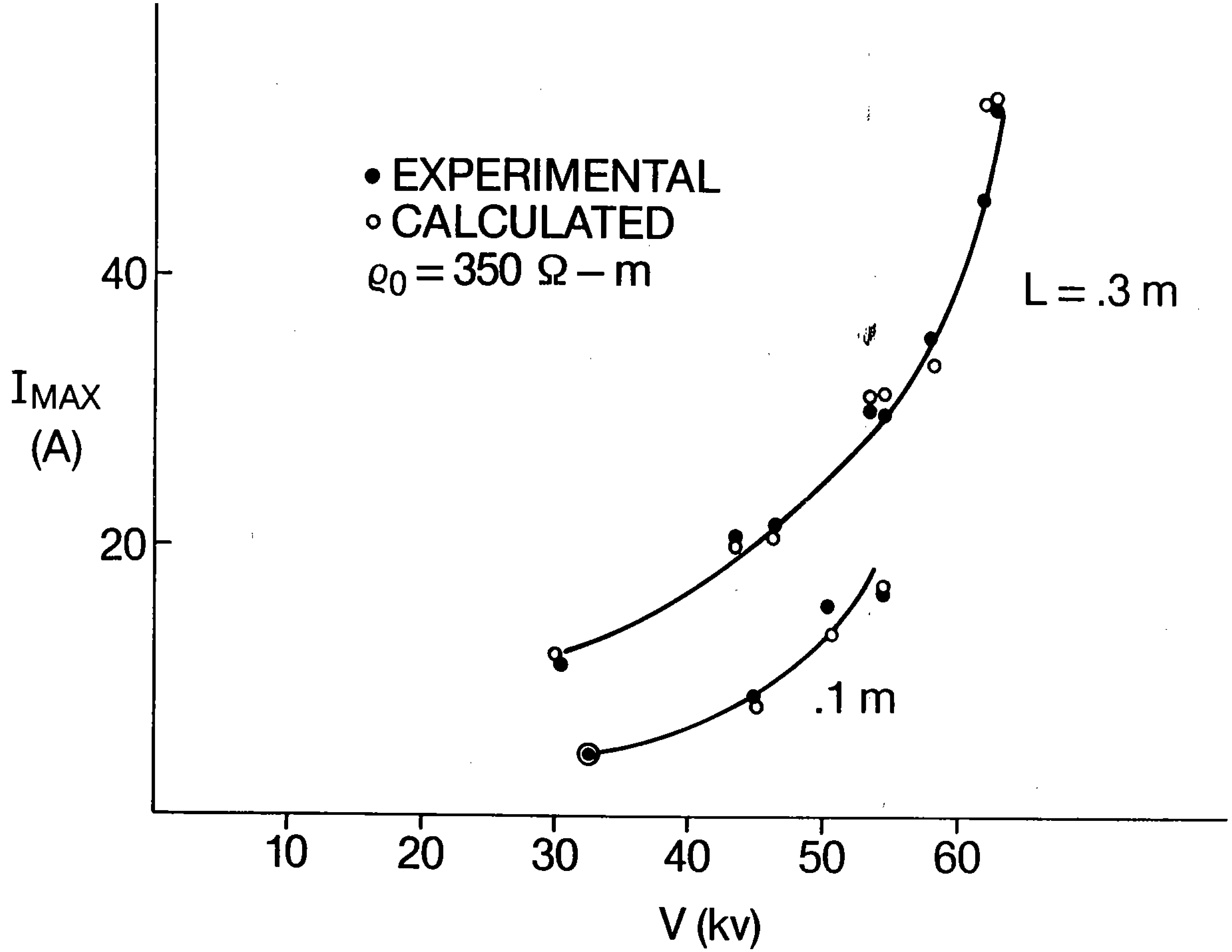

Figure 4.5.1. Max current v. voltage at center conductor. Dots: measured; open circles: calculated.

That may explain the discrepancies (15.5% and 21.1%) in shots 424 and 426. The fact that there is so little precent difference leads us to conclude that the corona is azimuthally symmetric and r_0 and E_B do not vary with azimuthal angle. The fact that electrical phenomena within the 90^0 cylindrical wedge sample must have exact images in the wedges constituting the other three quadrants of the circle, as well as in the wedges stacked on top and below, in order to satisfy the boundary conditions at the insulating walls of the wedge, may tend to preserve azimuthal symmetry.

TABLE I. Maximum Current I_M through 90^0 Wedge Sample.

Shot #	$I_M(A)$ (Measured)	$I_M(B)$ from (280)	% Difference
394	4.8	4.8	0
398	8.8	8.35	5.1
399	15.6	15.3	1.9
401	16.8	17.0	-1.1
419	11.3	12.0	-6.2
420	20.5	20.0	2.4
421	21.3	20.5	3.8
422	29.8	31.7	-6.3
423	30.0	31.3	-4.3
424	45.9	53.0	-15.5
426	55.4	43.7	21.1
427	52.8	53.3	-0.9

4.6 Spherical Case.

Referring to Figure 4.2.1, we consider a spherical geometry in which the spherical inner electrode has a radius a and the outer spherical shell will be removed to infinity, so that $b \to \infty$. Then, (4.3.26) may be written as:

$$E_B = \frac{V_o}{\left(1 - \rho_1/\rho_o\right)\frac{1}{r_o} + \left(\frac{\rho_1}{\rho_o}\right)\frac{1}{a}} \; \frac{1}{r_o^2} \qquad (4.6.1)$$

For the very high voltages used in Exp. C (point-plane experiments), e.g., about 200 KV, our estimate of ρ_1/ρ_o indicates that it will be less than .1. Therefore, if we set ρ_1/ρ_o equal to zero in (4.6.1), we get the very simple result that:

$$r_o = V_o/E_B \qquad (4.6.2)$$

By using E_B = 200 KV, and V_o = 200 KV, (4.6.2) indicates that r_o is about 1 meter.

As an indication of the validity of these calculations, it should be noted that Exp. C [12] have not yielded a direct measurement of the radius of the spherical corona region. Rather, what has been observed is that while the ohmic resistance from the high voltage electrode to infinite ground is about 200 ohms, when 200 KV is applied, the resistance initially at t = 0 is about 30 ohms and then declines to about 4 ohms. Subsequently, it drops to 1 ohm where it is believed that a streamer is propagating. If one postulates a spherical corona region which is growing in radius, one may thus account for the decreased resistance.

The total current flowing in the soil may be calculated by reference to Figure 4.2.1. At r_o, it is:

$$I = \frac{E_B}{\rho_o} 4\pi r_o^2.$$

Making use of (4.6.2), the resistance R to infinite ground is:

$$\frac{V_o}{I} = R = \frac{\rho_o}{4\pi} \frac{E_B}{V_o} \qquad (4.6.3)$$

For V_o having its peak value, 200 KV, and using the measured ohmic soil resistivity at the experimental site for experiments C,

$$\rho_o = 50 \text{ ohm-m},$$

we obtain:

$$R = 2.0 \times 10^{-2} E_B(\text{KV/m}) \text{ ohms}.$$

A resistance of 4Ω could be accounted for if E_B = 200 KV/m corresponding to r_o = 1 m.

5.0. Dynamic Theory of the Corona Region.

In Sec. 4, there was discussed the formation of the corona region about a high voltage electrode. The model is a simple one in which there are two regions: one adjacent to the high voltage electrode called the corona region and the second called the ohmic region. The corona region has radius r_o and resistivity ρ_1, while the ohmic region exists for $r \geq r_o$, and has the ohmic resistivity ρ_0. The corona region is in some fashion broken down electrically.

5.1 The Dynamic Model.

In 1974, Liew, et. al. [9] showed that if one considers the relaxation phase of the voltage pulse, i.e., the time after the current has reached its peak value and is declining to zero, then a third region could be identified with a resistivity ρ_2, which was dependent on the current density J, and was intermediate between ρ_1 and ρ_0. By introducing this third region, Liew, et. al., could phenomenologically predict their experimental results quite accurately. They referred to this model as a dynamic model of soil breakdown.

In a manner similar to that of Ref. 9, we propose the following model of corona relaxation. As the voltage rises at the high voltage electrode, we assume that the soil breaks down as described in Sec. 4, i.e., the soil breaks down out to a maximum radius r_0 determined by E_B, the peak applied voltage, ρ_1 for $r \leq r_0$, and ρ_0 for $r \geq r_0$. It should be noted that at r_0 in the ohmic region, there is a current density

$$J_c \equiv E_B / \rho_0 \qquad (5.1.1)$$

which has been called the critical current density.

As the applied voltage and current relaxes to zero, a new region forms. It is defined by $r_1 \leq r \leq r_0$, where r_0 is determined from the electrostatic phase. Call this region 2. The radius r_1 is defined such that at r_1, the current density is J_c . The resistivity in region 2, ρ_2, depends on J and therefore on r. Since ρ_2, does not equal ρ_o, the resistivity of this region undergoes hysteresis. Call this the relaxation phase.

During the relaxation phase, we can thus identify three soil regions which are shown in Figure 5.1.1. (This figure could represent either a cylindrical or spherical system.):

Region 1, corona region, $a \le r \le r_1$:

$\rho = \rho_1$, a constant; $J > J_c$.

Region 2, hysteresis region, $r_1 \le r \le r_o$:

$\rho = \rho_2(r)$; $J < J_c$ with $J = J_c$ at $r = r_1$.

Region 3, ohmic region: $r_o \le r \le b$.

$\rho = \rho_o$, a constant.

5.2. Relaxation Theory.

We shall consider a cylindrical system. We shall want to compare our calculations with the results of Shot 399, of Exp. A.

For region 2, we shall use

$$\rho_2 = \rho_1 + (\rho_o - \rho_1)(1 - J(r)/J_c)^2 \qquad (5.2.1)$$

which is approximately the expression that was empirically determined to give the best agreement between theory and experiment by Liew, et. al. [9]

Note that at r_1, $\rho_2 = \rho_1$ and the resistivity is continuous across the boundary between regions 1 and 2. From Eq. (3.1.1), E_r will be continuous (since J_r must be continuous), and there will be no charge on this boundary. At $r = r_o$, however, $\rho_2 \neq \rho_o$, so that the resistivity and E_r is discontinuous across the boundary between regions 2 and 3. There must be charge on this boundary.

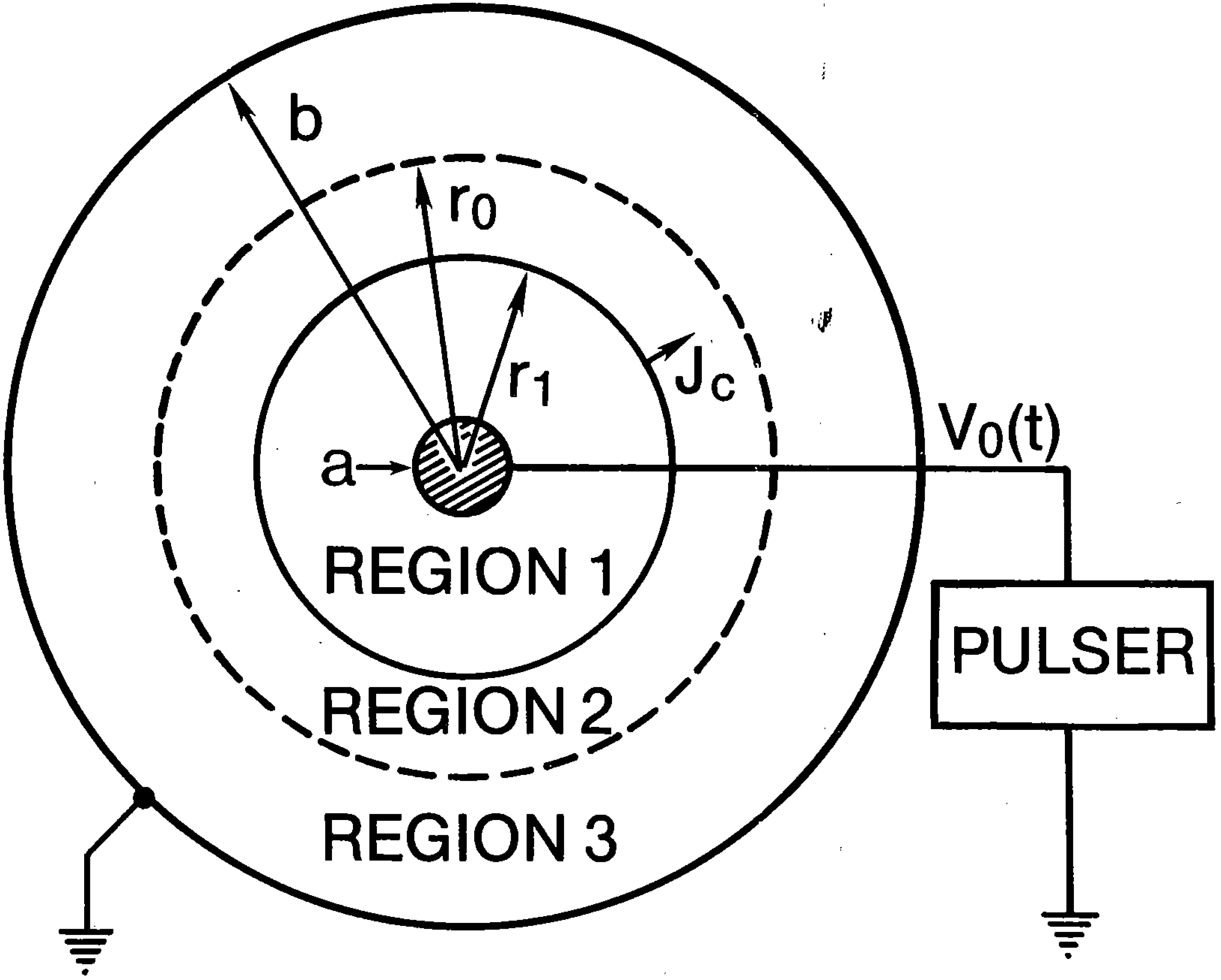

Figure 5.1.1. Cylindrical or spherical system for dynamic model. Region 1: corona; region 2: hysteresis; region 3: ohmic.

Let $V_0(t)$ be the applied voltage at the center electrode of radius a. Then a total current I(t) will flow, and

$$J(r,t) = I(t)\alpha r\ell \tag{5.2.2}$$

where α is the wedge angle and ℓ is the length of the cylindrical sample. For Figure 5.1.1, $\alpha = 2\pi$ rad.

We shall calculate the resistance of the system R(r) which we shall define as the resistance between radius r and the grounded electrode at r = b. By this definition, R(a) would be total resistance such that $I = V_0/R(a)$.

Consider two closely spaced cylindrical shells with the inner shell at radius r and the separation of the shells being dr. Then the resistance of the region between the shells is:

$$dR = \rho\frac{dr}{\alpha\ell r}$$

and

$$R(r) = \int_r^b \rho\,\frac{dr}{\alpha\ell\, r} \tag{5.2.3}$$

It is not difficult to obtain:

Region 3, $r_0 \le r \le b$

$$\left(\frac{\alpha\ell}{\rho_0}\right) R(r) = \ln\,(b/r) \tag{5.2.4}$$

Region 2, $r_1 \le r \le r_0$

$$\left(\frac{\alpha\ell}{\rho_0}\right) R(r) = \ln\,(b/r) - 2r_1\left(1 - \frac{\rho_1}{\rho_0}\right)\left(\frac{1}{r} - \frac{1}{r_0}\right) + \tfrac{1}{2}\left(1 - \frac{\rho_1}{\rho_0}\right) r_1^2\left(\frac{1}{r^2} - \frac{1}{r_0^2}\right) \tag{5.2.5}$$

Region 1, $a \le r \le r_1$

$$\left(\frac{\alpha\ell}{\rho_o}\right) R(r) = \ell n\,(b/r_1) + \frac{\rho_1}{\rho_o} \quad \ell n\,\frac{r_1}{r}$$

$$+ \left(1 - \frac{\rho_1}{\rho_o}\right)\left[\tfrac{1}{2} r_1^{\,2} \left(\frac{1}{r_1^{\,2}} - \frac{1}{r_o^{\,2}}\right)\right.$$

$$\left. - (2r_1) \left(\frac{1}{r_1} - \frac{1}{r_o}\right)\right] \tag{5.2.6}$$

where $r_1 = I/J_c\alpha\ell$ (5.2.7)

5.3. Results.

Shot 399 is reproduced in Figure 3.1.1 where the ordinate is just R(r) in Kohms and the abscissa is log r. For this shot, ρ_o = 350 ohm-meter, $\alpha = \pi/2$ radians, ℓ = 0.1 meter, a = 0.01 meter, and b = .5 meter. Each curve in Shot 399 is at a different time with curve A occurring at the earliest time and curve F at the latest time. The times for each curve are shown in Figure 3.1.1; also shown is the current I that was measured at each time.

Under the assumption that J_c is a constant, maximum radius r_o which marks the end of the electrostatic phase would occur when I is a maximum. This would correspond approximately for curve B at 200 μs. We may measure r_o directly by approximating curve B by two straight lines which are seen to intersect at r = .16 m. We take this value of r to be r_o. Using the techniques described in Sec. 4.4., we obtain ρ_1/ρ_o = .129 from which we may calculate E_B by the method described also in Sec. 4.4. to be 231.5 KV/m.

Alternately, since I was measured to be 15.25 amp. for curve B, at r_o = .16 m., J_c is 607 amp./m.^{2}, and from (5.1.1), E_B = 212.3 KV/m. This value of E_B is 8% lower than the value calculated using the techniques described in Sec. 4.4.

We now use J_c = 607 amp./m.^{2} and r_o = .16 m. to predict curves C, D, E, and F. We shall adjust ρ_1/ρ_0 as may be necessary. The results are shown in Figures 5.3.1 through 5.3.4 where we have made use of (5.2.4) through (5.2.7). The values of ρ_1/ρ_0 required are as follows:

Curve	I/A	ρ_1/ρ_0
C	15.00	.137
D	14.00	.121
E	10.75	.182
F	5.00	.409

Thus, one may get good agreement between the dynamic model and the experimental data, providing that one allows ρ_1/ρ_0 to increase as the total current decreases, not an unexpected result.

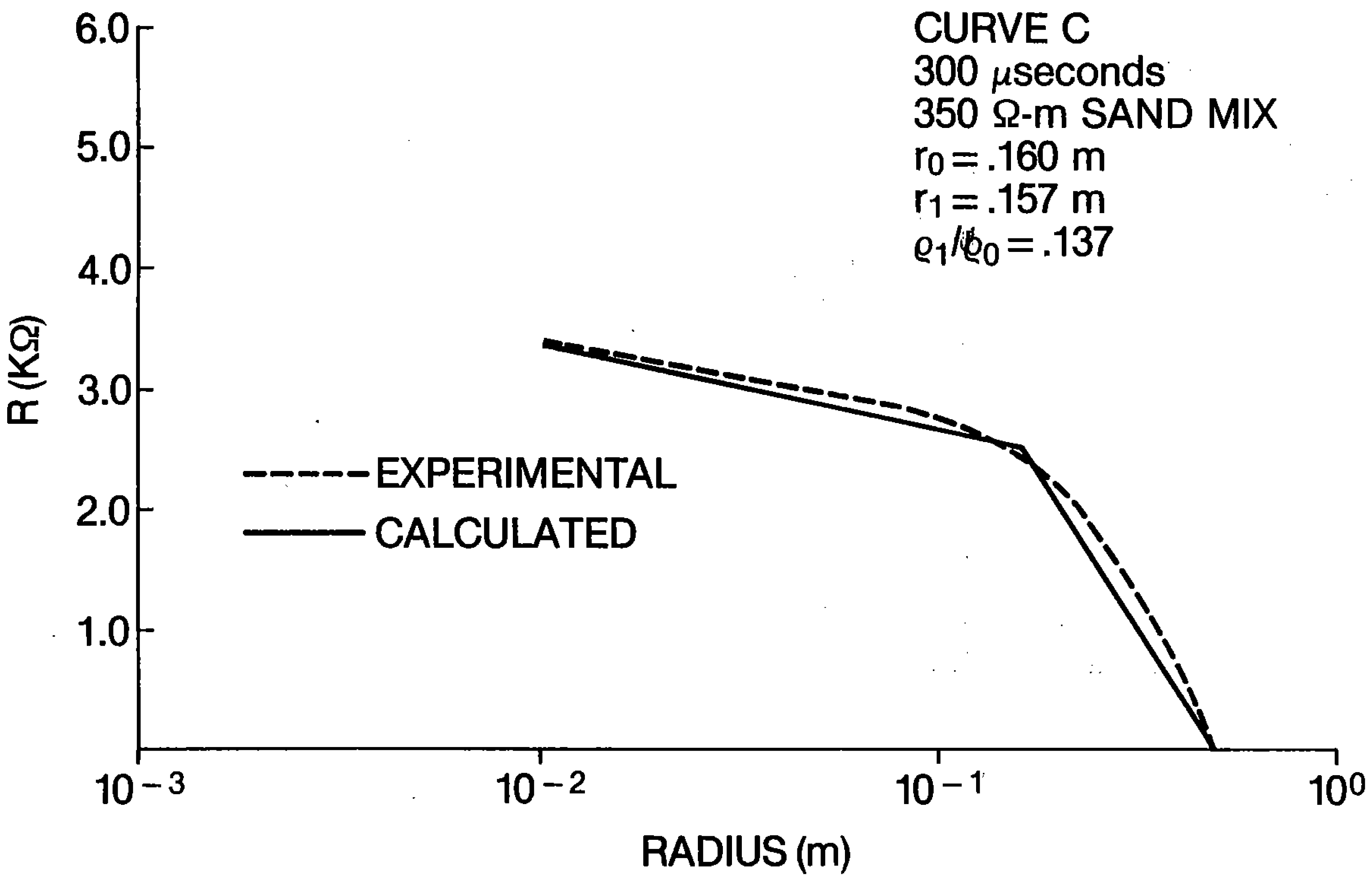

Figure 5.3.1. Dynamic model prediction (dashed line) of Curve C of Figure 3.1.1. ρ_1/ρ_o = .137.

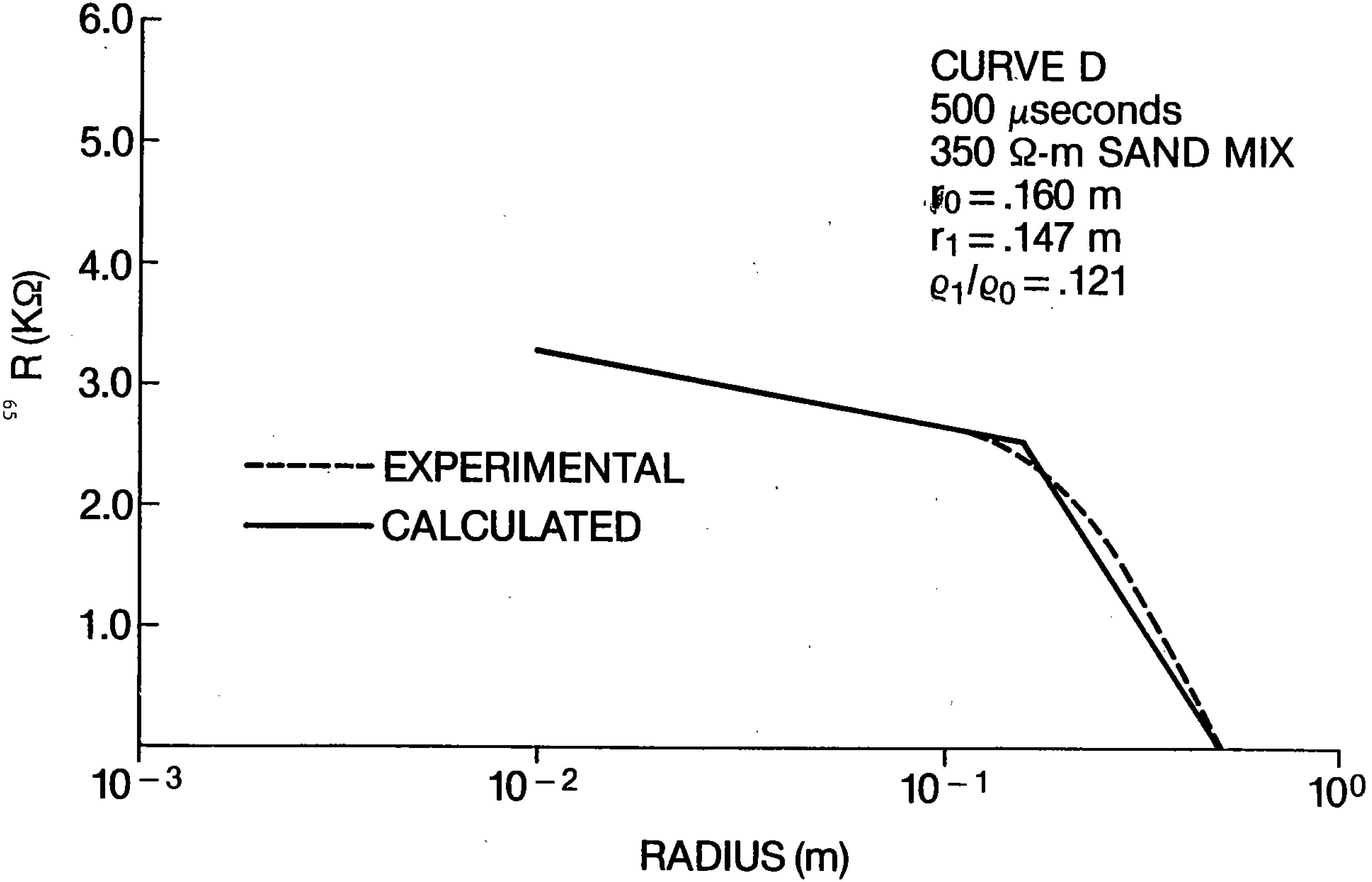

Figure 5.3.2. Dynamic model prediction (dashed line) of Curve D of Figure 3.1.1. $\rho_1/\rho_o = .121$.

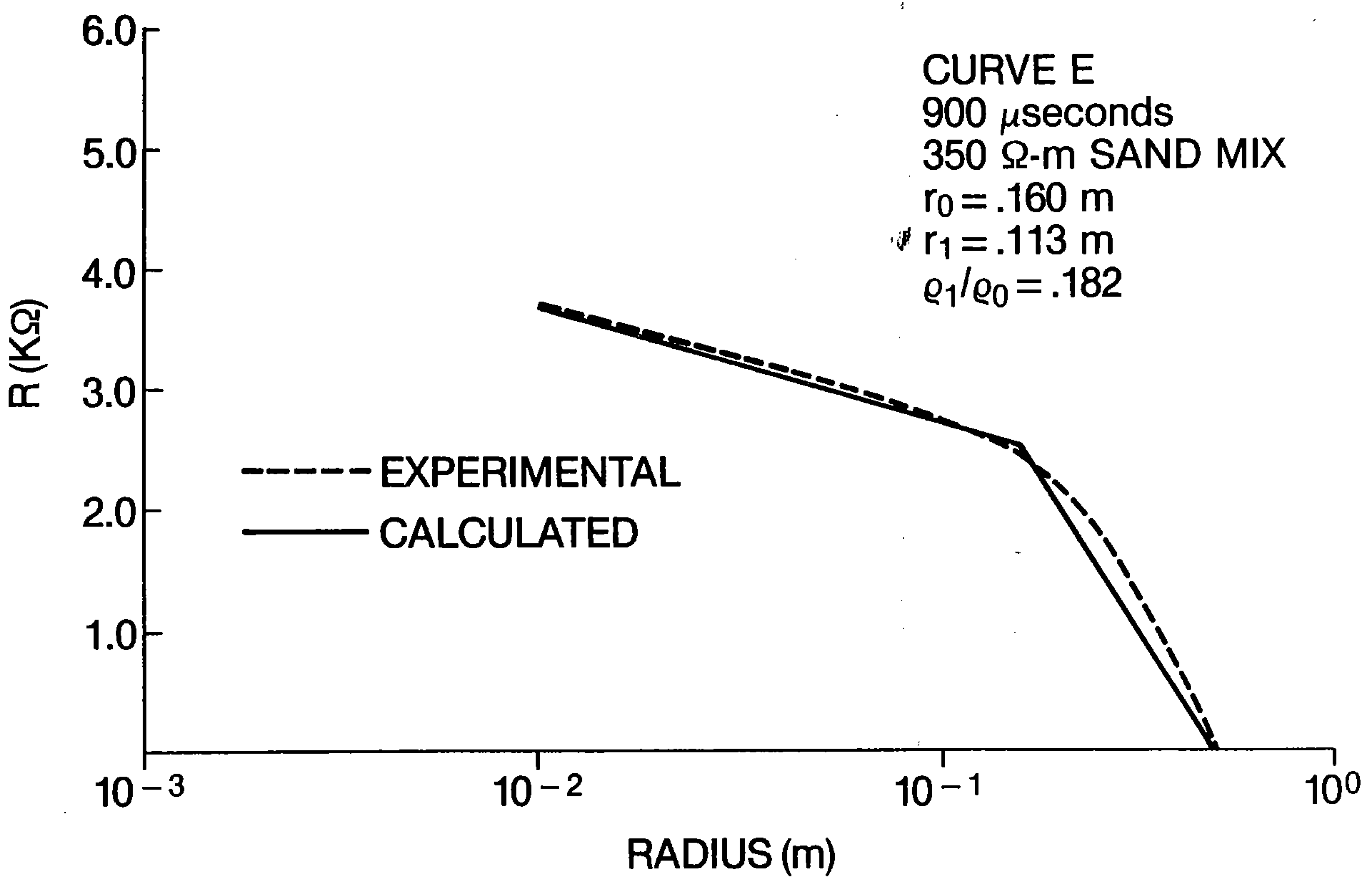

Figure 5.3.3. Dynamic model prediction (dashed line) of Curve E of Figure 3.1.1. ρ_1/ρ_o = .182.

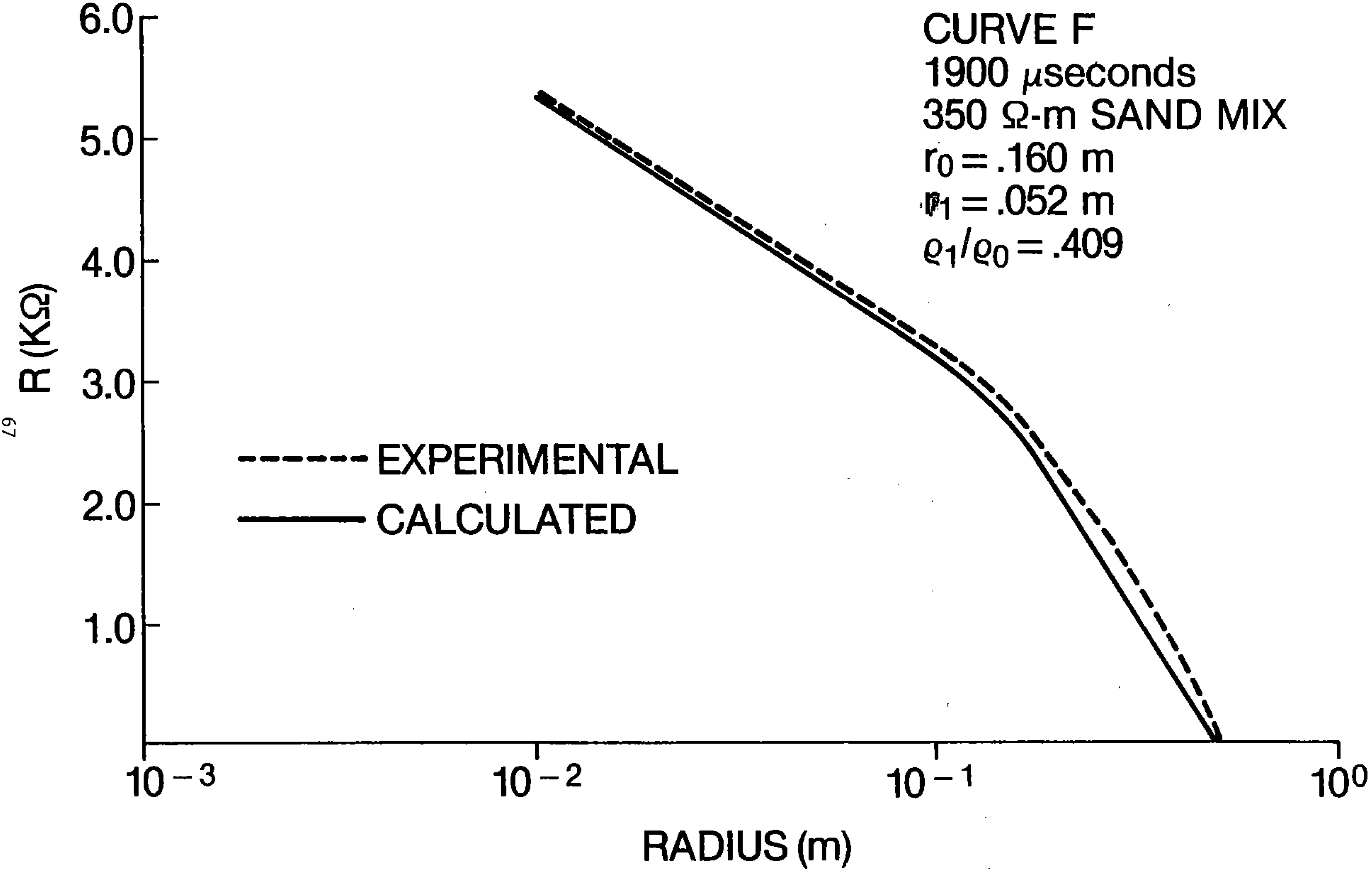

Figure 5.3.4. Dynamic model prediction (dashed line) of Curve F of Figure 3.1.1. $\rho_1/\rho_o = .409$.

6.0 Streamers.

If the voltage on the center conductor V_0 is large enough, the current through the sample will first start to rise, as if toward a maximum, but then will suddenly increase as is shown in Fig. 4.4.4. This sudden increase indicates that the broken down portion of the soil sample extends all the way to the grounded conductor, or that it has attached to the grounded conductor. We refer to this state as attached breakdown.

Attached breakdown can occur for the following reasons. If the corona is symmetric at its boundary as is the case in Fig. 4.5.1, the corona will attach if:

a) r_0 becomes large enough so that it equals the critical stability radius; if the system is stable, or the critical stability radius exceeds b, the corona will attach if V_0 is so large that:

b) $r_0 = b$.

The symmetric corona may contain streamers, but they apparently aren't dominant enough to significantly distort the boundary, so that the boundary retains the symmetry of the electrode system. We will see a case of corona attachment in Sec. 6.1 below.

On the other hand, streamers may dominate the corona. Then attachment occurs if:

c) the streamer propagates as described by Longmire, et al. [10] who characterize the streamer propagating outward with a velocity.

For this case, we envision the streamer pushing the corona ahead of it as shown in Fig. 3.2.1 so that the corona attaches first followed by streamer attachment. A case where streamer attachment occurs is discussed in Sec. 6.2.

For cases a) and b), when corona attachment occurs, we presume that the current is carried more or less uniformly by the corona. For cases c), when streamer attachment occurs, the current is presumed to be carried primarily by the streamer, which may benefit from attachment in the sense that its resistivity may decrease, its current increase, and its diameter increase. This, however, is speculation.

We have seen evidence in Fig. 4.5.1 that the corona in Exp. A is cylindrically symmetic. We would expect, therefore, that corona attachment of types a) or b) would occur in these Experiments. On the other hand, we will see in Sec. 6.2 that in Exp. B, streamers exist after attachment has occured. Thus, in these experiments, we would expect that attachment would be of type c), streamer attachment.

To strengthen these conclusions, refer to Fig. 6.0.1 which is a plot of attachment time t_B vs. V_o peak, the peak voltage on the center conductor. This data was obtained from both Exp. A and B [2]. The x's and open circles o are data from Exp. A. We see that, at least, for times t_B less than 1 millisecond, attachment does not occur for V_o below about 65 KV.

This data was obtained from a system in which a = .01 m and b = .5m. If we use the data for E_B and ρ_1/ρ_o for ρ_o = 350 ohm-m in Figs. 4.4.7 and 4.4.8, and Eq. 4.2.13, it is possible to show that the system is stable up to V_o = 65.7 KV. At that voltage, E_B = 190 KV/m and ρ_1/ρ_o = .17 leading to an instability radius of .4 m. The system continues to be unstable for V_o larger than 65.7 KV. This result is in accord with the observation above that in Fig. 6.0.1 attachment does not occur for Exp. A below 65 KV. This is further evidence that corona attachment is occuring in Exp. A.

On the other hand, data from Exp. B represented by the solid dots shows a correlation between V_o and t_B such that t_B clearly decreases as V_o increases.

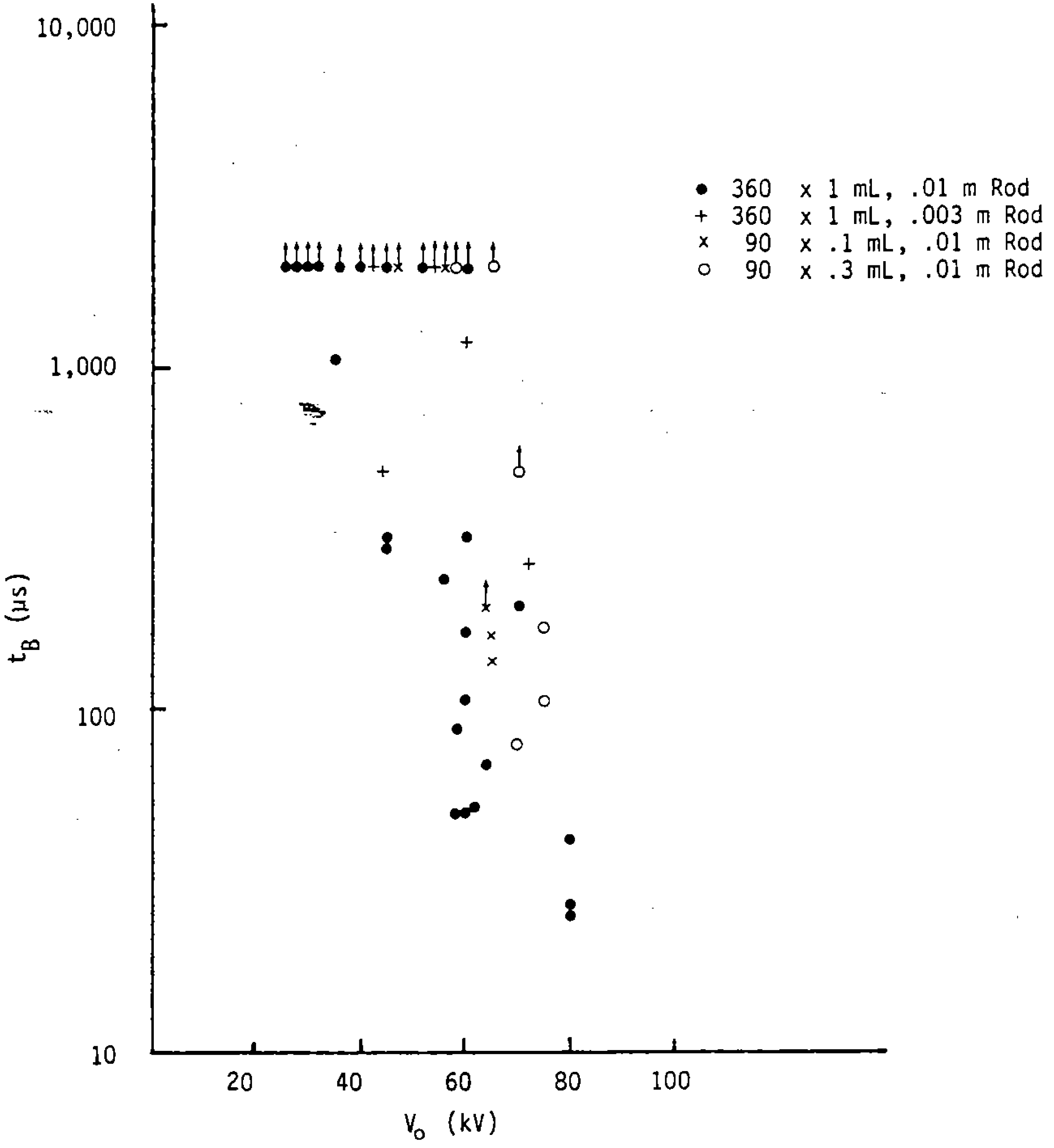

Figure 6.0.1. Time t_B for attachment to occur. x and o: corona attachment; · streamer attachment (Figure 3.3.13 of [2]).

with attachment occuring below 40 KV. This behavior is in accord with current theories of streamer attachment. For example, Smith * predicts a phenomenological dependence of V_0 and t_B of $V_0 t_B^n$ = const. where n is approximately 3/8.

6.1 Corona Attachment.

In shot 302 in Exp. A, the voltage on azimuthally located probes is measured (see Figs. B.46 through B.54). The location of the probes are shown in Fig. 2.1.1, where the radius of the probe arc is .144 m. Also, b = .5 m and a = .01 m, L = .1 m. Consider the probe arc in Fig. 2.1.1. A flattened-out view of this arc is shown in Fig. 6.1.1 where the x coordinate measures distance along the arc, and y measures distance down (in Fig. 2.1.1) into the soil sample. Since L = .1 m, $0 \leq y \leq .1$ m while x ranges from zero to $\pi/2 \times .144 = .226$ m. In Fig. 6.1.1 we see that the nine probes are of unequal depth.

In Fig. 6.1.2, data from these voltage probes is presented in the form of a resistance R_{eff} which is defined as:

$$R_{eff} = (V_o - V_n)/I \tag{6.1.1}$$

where V_n is the voltage at the nth probe and I is the total current through the sample. Thus, R_{eff} is the effective resistance between the center conductor and probe n if all the other probes were at the same potential as V_n. The smaller is R_{eff}, the closer is V_n to V_o. The voltages V_n v. time are given in Figs. B.12 through B.20.

---

* In a set of notes which have not been published, I. Smith predicts a phenomonological dependence among streamer closure distance d(cm) between a high voltage electrode and a ground plane, time for closure t (μs), and voltage V (kV) of the high voltage electrode, which is

$$\frac{v}{d} t^{3/8} d^{1/6} \approx 12$$

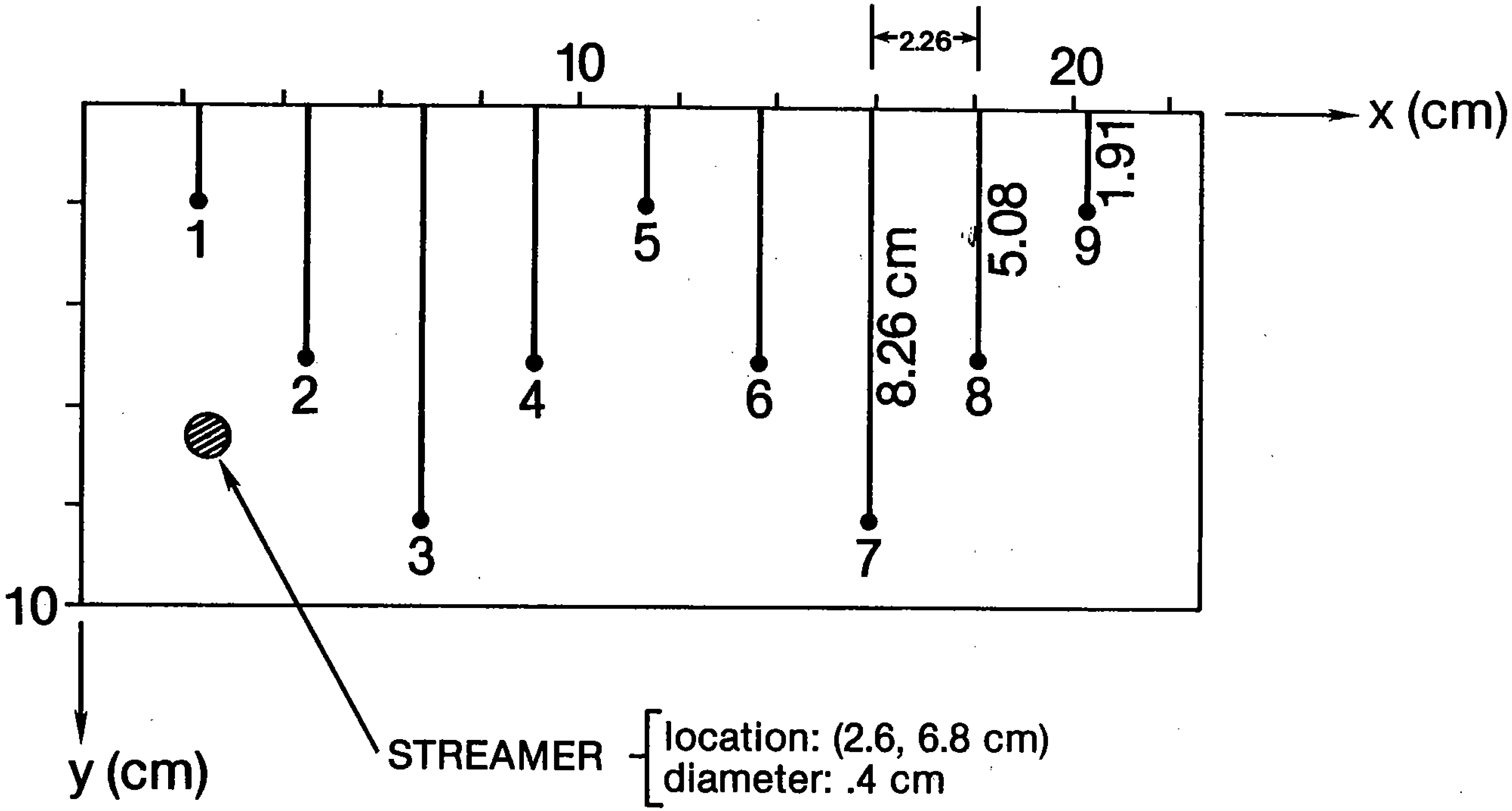

Figure 6.1.1. Location of azimuthal probes on probe arc of Figure 2.1.1. radius of probe arc: .144 m. x measures distance along arc, y into soil sample. Streamer location also shown.

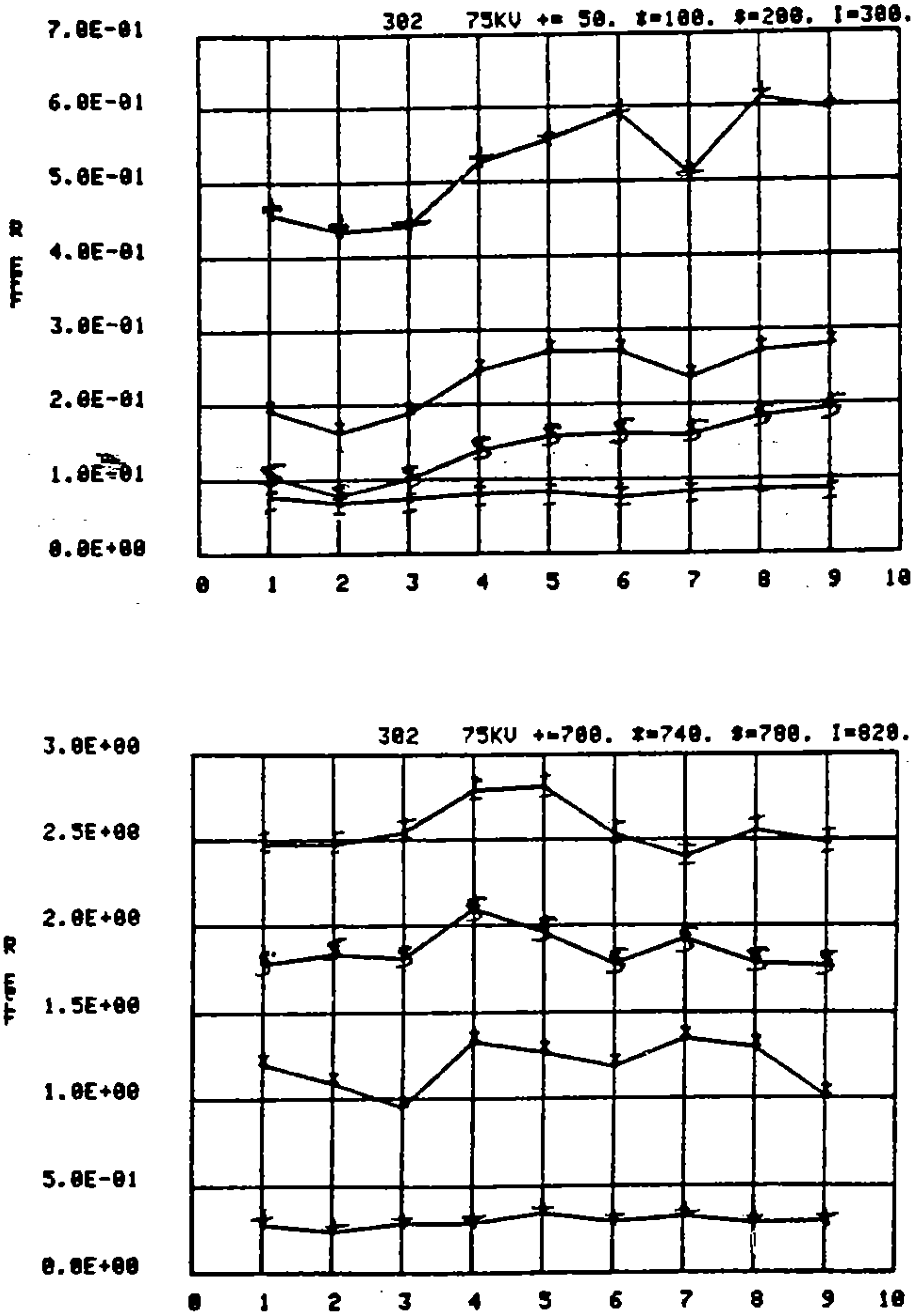

Figure 6.1.2. Resistance R_{eff} (Kohm) between center conductor and probe n for azimuthal probes. (Figure 3.4.7 of [2]).

The current I through the sample is shown in Fig. 4.4.4. We see that attachment occurs at about 240 μs and that from 300 μs to about 700 μs, the current rapidly decays. At time greater than about 730 μs, the soil is nearly ohmic.

From 6.1.2, during the current decay (curves for 300 μs and 700 μs) the voltages V_n are nearly equal, indicating a high degree of azimuthal symmetry of the voltage at .144 m. This symmetry strongly supports the idea that streamers are absent and that corona attachment has occured.

After attachment, the resistance of the sample, $R = V_0/I$, is shown in Fig. 6.1.3. We see that at 300 μs, it is about 400 ohm, and then increases slowing with time. Assuming corona attachment, we may calculate the resistivity of the broken down soil. Assuming that it is uniform, it is found to be 16.1 ohm-m. The ohmic resistivity of the soil sample (MX-B) is 130 ohm-m, so that the ratio of these resistivities is .123. From Fig. 4.4.14, this ratio is typical for this type of soil.

The complete picture of how the sample resistance R varies with time is shown in Fig. 6.1.4 for shot 403 (see Figs. B.55, B.56). The corresponding V_0 and I are shown in Figs. B.21 and B.22. The ohmic resistance of the sample is 8717 ohm. As the current starts to rise after t_i, R drops rapidly to below 2000 ohm. At about 150 μs, attachment occurs. R then drops below 400 ohm and recovers very slowly. Eventually it will revert to its ohmic value.

Returning to shot 302, it is of interest to examine the behavior of the sample before attachment. In Fig. 4.4.4 the current just prior to attachment (at 240 μs) is 75 amps. We may predict this current from Eq. 4.2.8 if we use as r_0 the instability radius. The peak V_0 is about 70 KV or $E = 1.8$ MV/m. From Fig. 4.4.14, this leads to $\rho_1/\rho_0 = .1$. From Fig. 4.2.2, we see that the instability radius is about .29 m. Thus, using E_B from Fig. 4.4.13, we

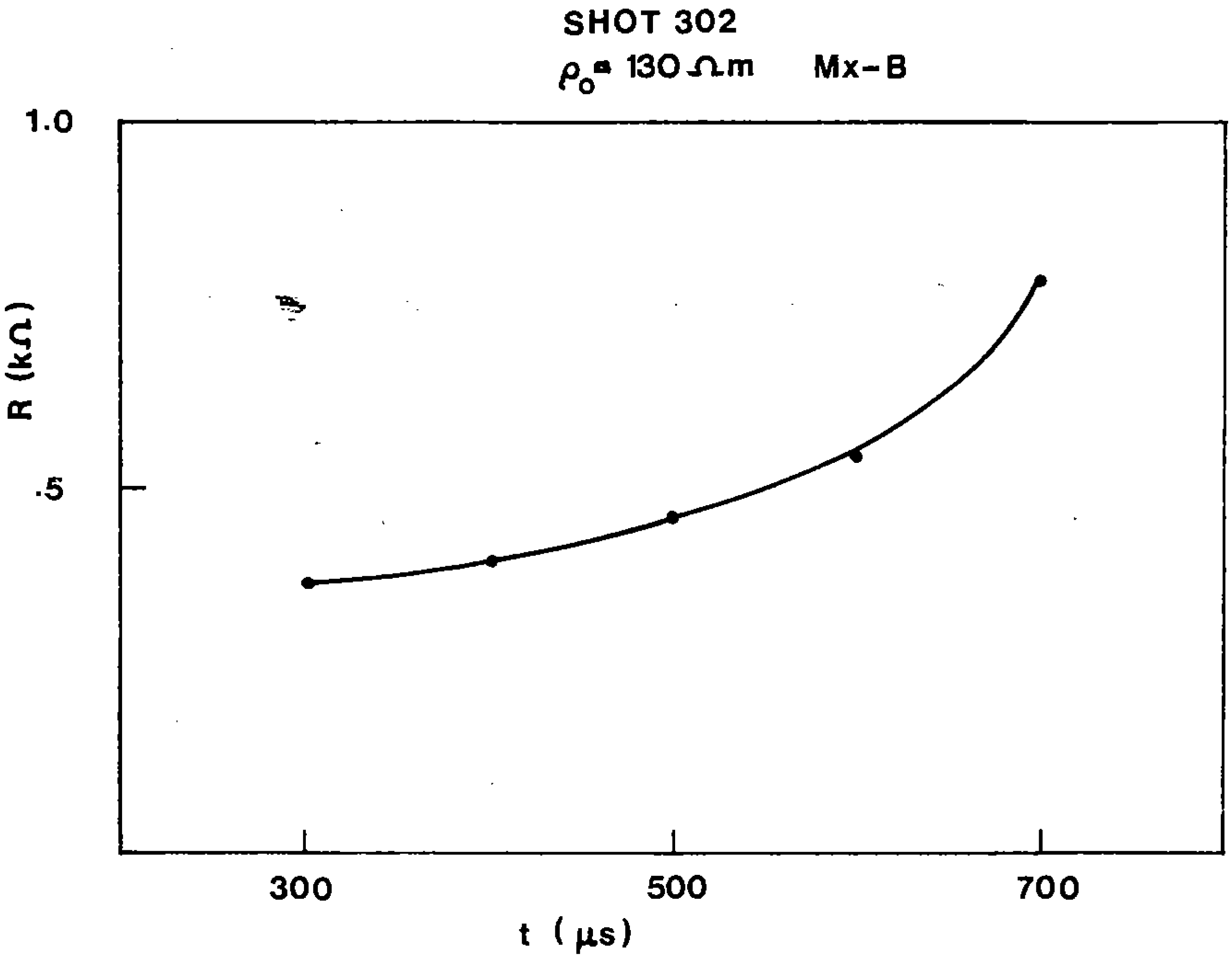

Figure 6.1.3. Resistance vs. time for shot 302 after corona attachment.

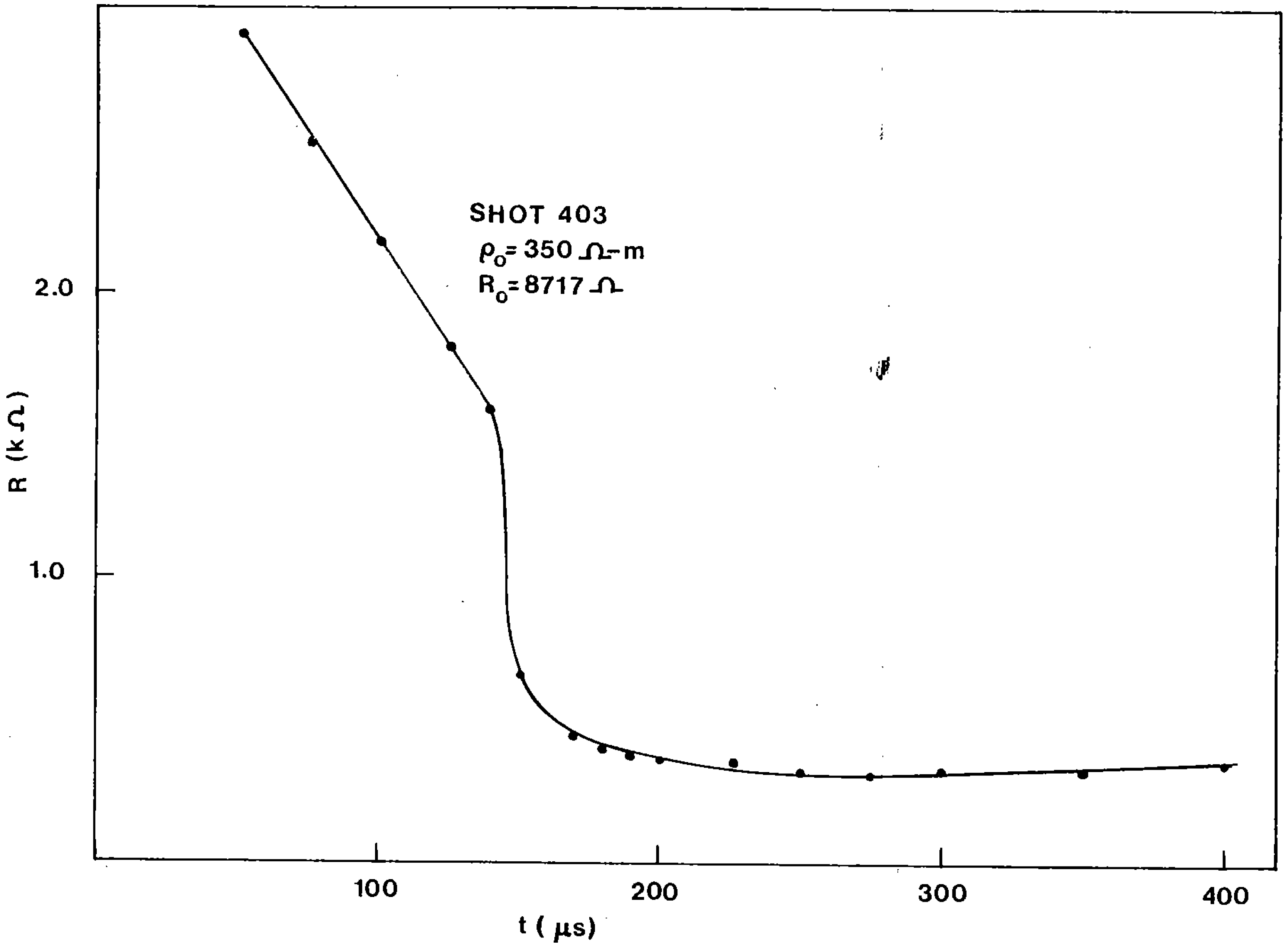

Figure 6.1.4. Resistance vs. time for shot 403.

calculate from Eq. 4.2.8 that I = 91 amp compared with measured 75 amp. Considering the error in E_B due to the few points available and other factors discussed above, the agreement is not bad.

In the above calculation, we assumed a symmetric corona. In Fig. 6.1.2, we see that just prior to attachment, at 200 μs, that R_{eff} is azimuthally varying, with a minimum occuring at probe 2. The actual voltages (at 200 μs) on the nine probes are shown in Fig. 6.1.5. V_0 at 200 μs is 65 KV.* This suggests that there may be a streamer near probe 2 which is causing its voltage to approach V_0.

A model for the corona and streamer is shown in Fig. 6.1.6 just prior to attachment. In this figure, the corona boundary has arrived at the instability radius, .29 m. A streamer has formed at the center conductor and has propagated out past the array of probes and is, perhaps, deforming the boundary. Corona attachment subsequently occurs. It is interesting that within the framework of this model that the streamer clearly disappears as is shown in Fig. 6.1.2 for 300 μs. One would speculate that the resistance to the outer conductor through the corona is lower than the resistance through the streamer. Thus, the corona drains current from the streamer and the streamer disappears!

It is possible to calculate approximately where the streamer is located and, as we shall see, estimate its radius. We use an extremely simple model of a streamer as shown in Fig. 6.1.7. The streamer is modeled as a cylinder of radius a_0 with a resistivity which is very low compared to the surrounding corona.

Let V_s be the potential at the surface of the streamer, assumed to not differ appreciably from the center conductor. Then if V_0' is the corona potential in the absence of the streamer, the potential V(r) in the vicinity of the

---

* This number was calculated from the data in Figs. 6.1.5 and 6.1.2. It is not clear how the experimenters [2] measured this voltage.

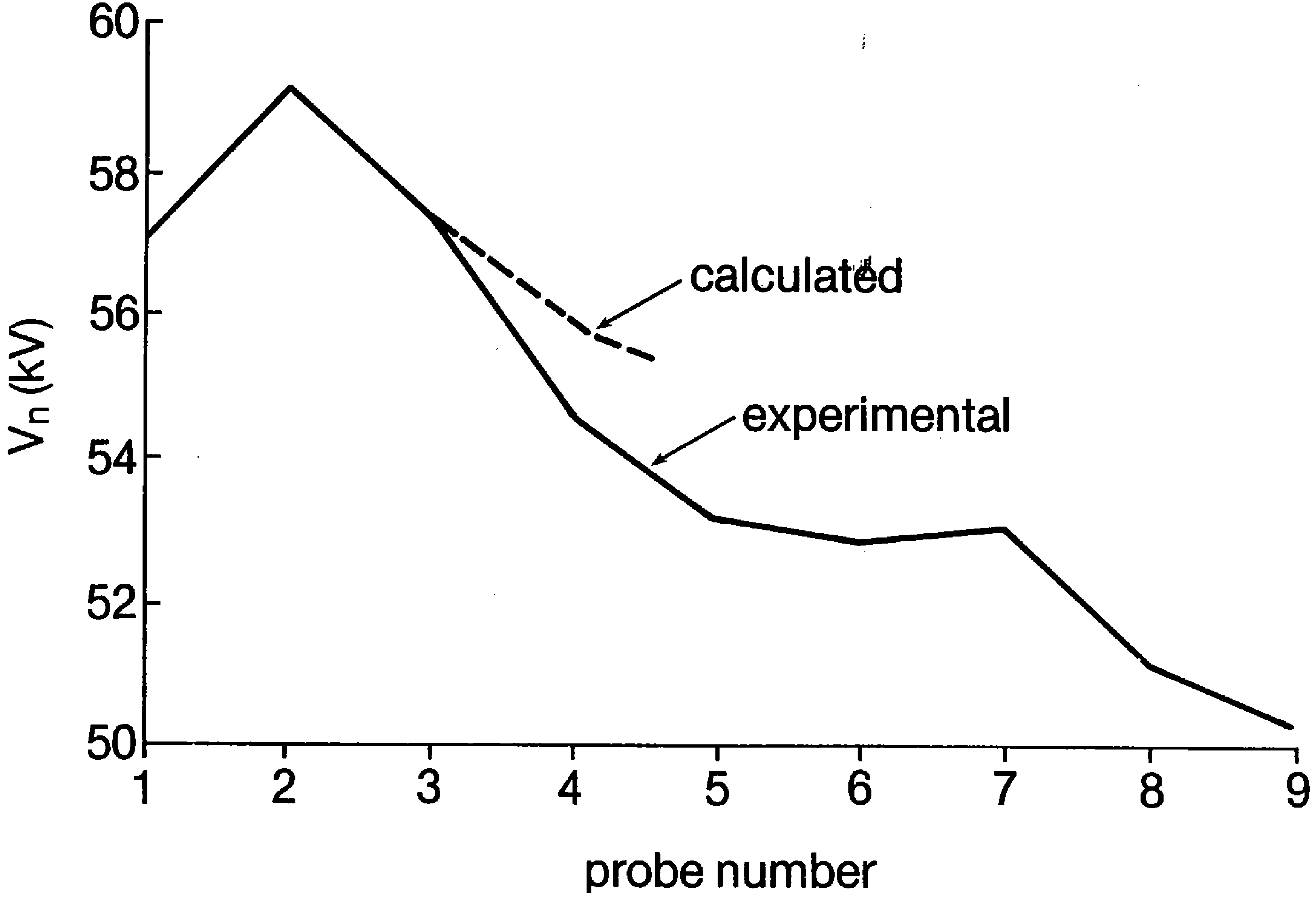

Figure 6.1.5. Voltage at azimuthal probe n for shot 302 at 200 μs.

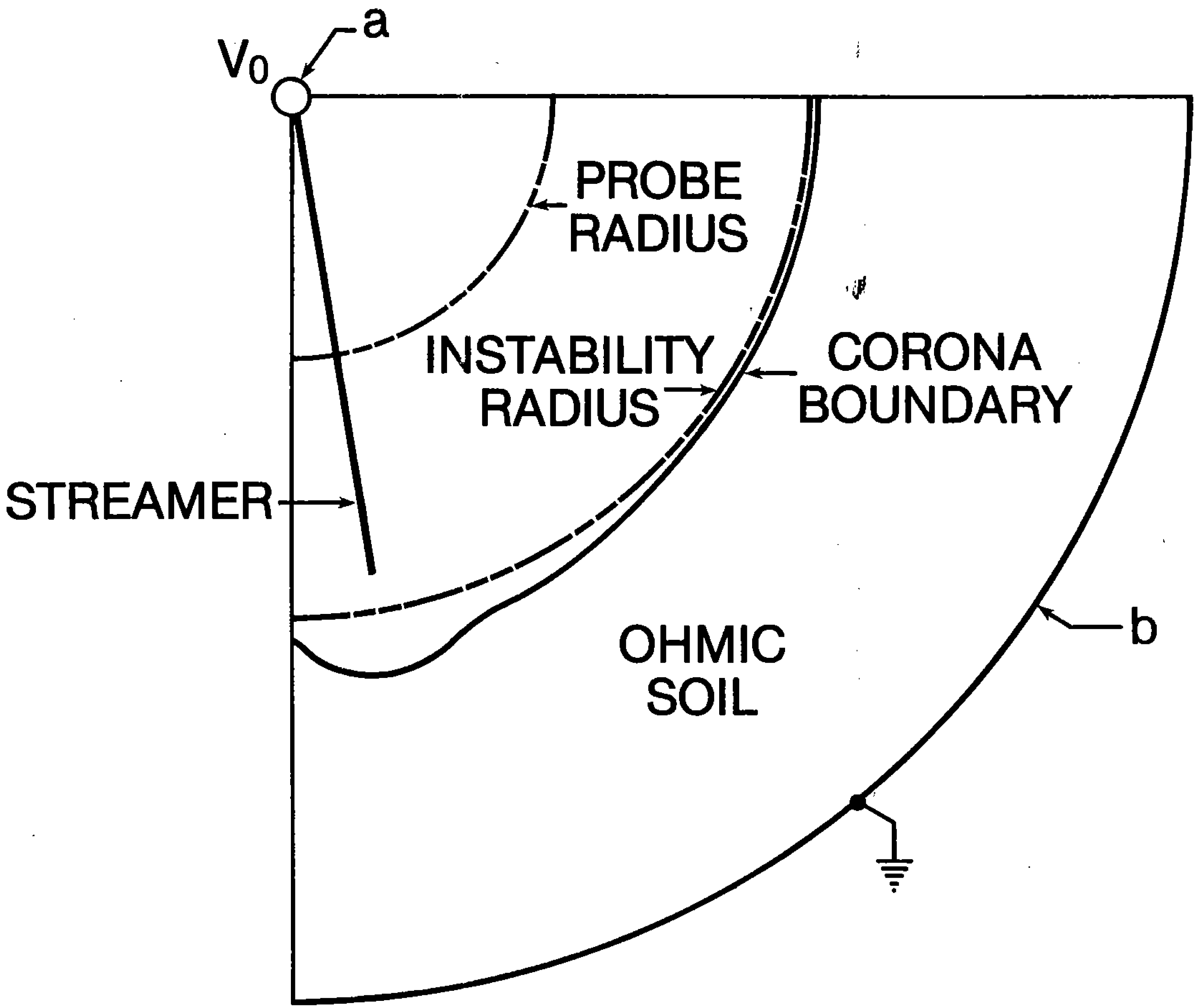

Figure 6.1.6. Speculation about corona boundary and streamer location in shot 302 just prior to corona attachment.

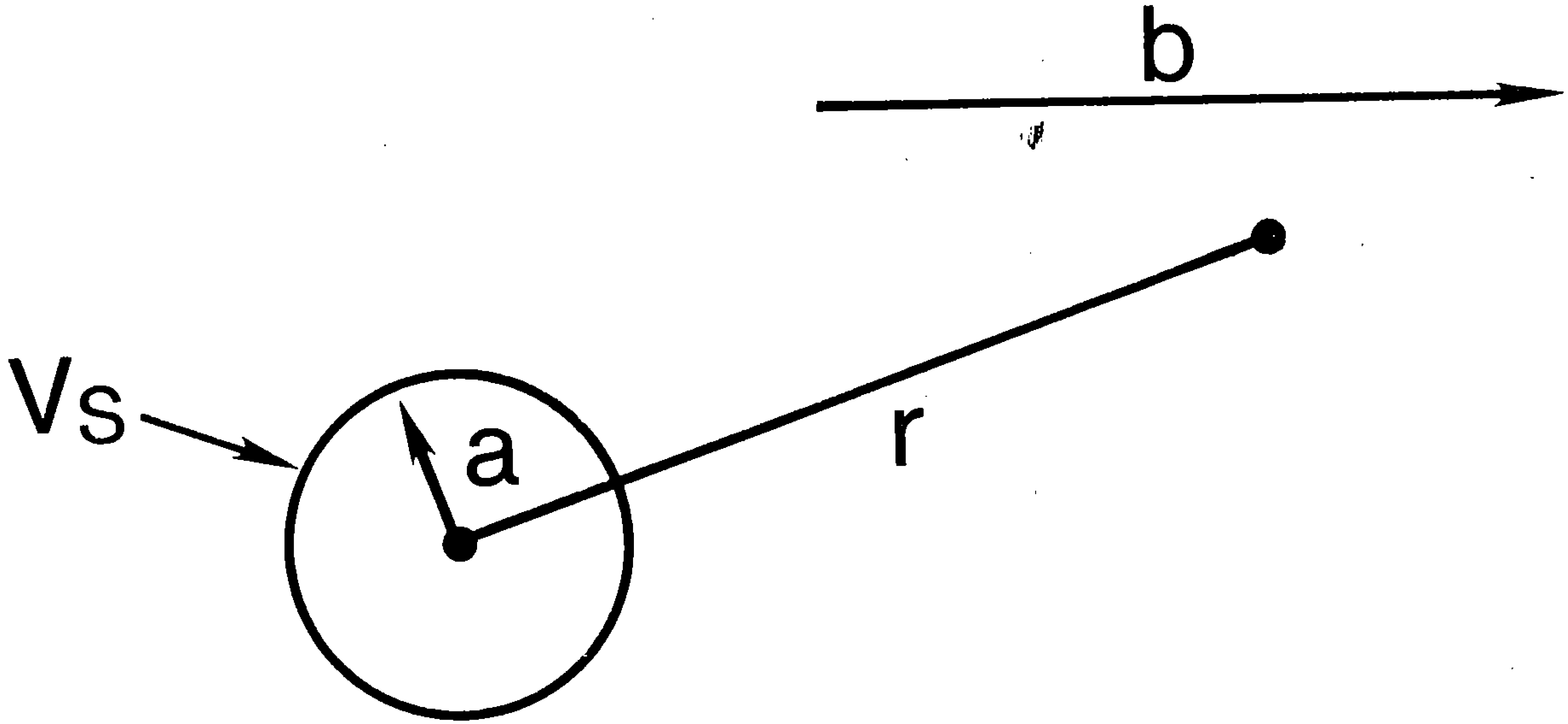

Figure 6.1.7. Streamer model.

streamer may be approximated as:

$$V(r) = \left(\frac{V_s - V_o'}{\ln \frac{b_o}{a_o}} \right) \ln \frac{b_o}{r} + V_o' \tag{6.1.2}$$

where r is the cylindrical coordinate radial distance from the streamer to the point where V(r) is being calculated, and b_o is some reference distance where the effect of the streamer is no longer flet.

Let V(r) be evaluated at probes 1, 2, and 3, which appear to be the closest to the streamer. Let

$$A = \frac{V_s - V_o'}{\ln \frac{b_o}{a_o}} \tag{6.1.3}$$

Then Eq. (6.1.2) becomes

$$V_n = A \ln(b_o/r_n) + V_o' \tag{6.1.4}$$

where r_n is the distance from the streamer to the nth probe, and n = 1,2,3.

Call (x,y) the location of the center of the streamer where it cuts the arc shown in Fig. 6.1.1. Then $r_n = r_n(x,y)$. Dividing the equation for V_1 and V_3 by the equation for V_2 (Eq. 6.1.4), we obtain two equations which do not contain A:

$$\frac{V_1 - V_o'}{V_2 - V_o'} = \frac{\ln(b_o/r_1)}{\ln(b_o/r_2)} \tag{6.1.5}$$

$$\frac{V_3 - V_o'}{V_2 - V_o'} = \frac{\ln(b_o/r_3)}{\ln(b_o/r_2)} \tag{6.1.6}$$

We know V_1, V_2, and V_3 from Fig. 6.1.5 and we estimate V_o' and b_o. Then we have two equations and two unknowns, x and y. Recognizing that r_n really depends on x_n' shown in FIg. 6.1.8 and not x_n, we have solved Eqs. (6.1.5) and (6.1.6) by a Newton-Raphson technique. We have used $V_o' = 50.5$ KV from Fig. 6.1.5 corresponding to V at a remove location (probe 9) and for b_o we selected the outer radius, i.e. $b_o = .5 - .144 = .356$ m. We then find that

$x = .26$ m, $\quad y = .68$ m.

The location of the streamer is shown in Fig. 6.1.1.

These values of x and y will guarantee that V_n, $n = 1,2,3$, where V_n is given by Eq.6.1.4, will have the values shown in Fig. 6.1.5. We may then use any one of these equations to find A: A = 3.2 KV. Letting $V_s \cong V_o =$ 65 KV, $\ln (b_o/a_o) = 4.53$, and for $b_o = .356$ m, $a_o = .0038$ m = .38 cm. Thus, we predict that the radius of the streamer is .38 cm.

It is clear that there are many sources of error in this calculation, e.g., we have neglected streamer images, and the value of b_o is unclear. Thus, we only make the point that this is an order of magnitude calculation. We do note, however, that the presence of streamers can be easily detected by probes that, as in Fig. 6.1.1, are about 4 cm apart.

6.2 Streamer Attachment

As an example of streamer attachment, we consider shot 525 from Exp. B (see Figs. B.57 through B. 90). In this shot, the parameters of the system are $a = .01$ m, $b = 1$ m, $L = 1$ m, and $\rho_o = 300$ ohm-m sand. The total current I through the sample and V_o are shown v. time in Figs. B.57 and B.58. In Fig. B.57 for I, an error occured in recording I between 120 μs and 240 μs so that the peak current is not available. The plot in Fig. B.57 is truncated during this time interval. We see that I first rises slowly until about $t_B = 80$ μs when attachment occurs. The current rises rapidly to its peak value (not recorded) and then decays

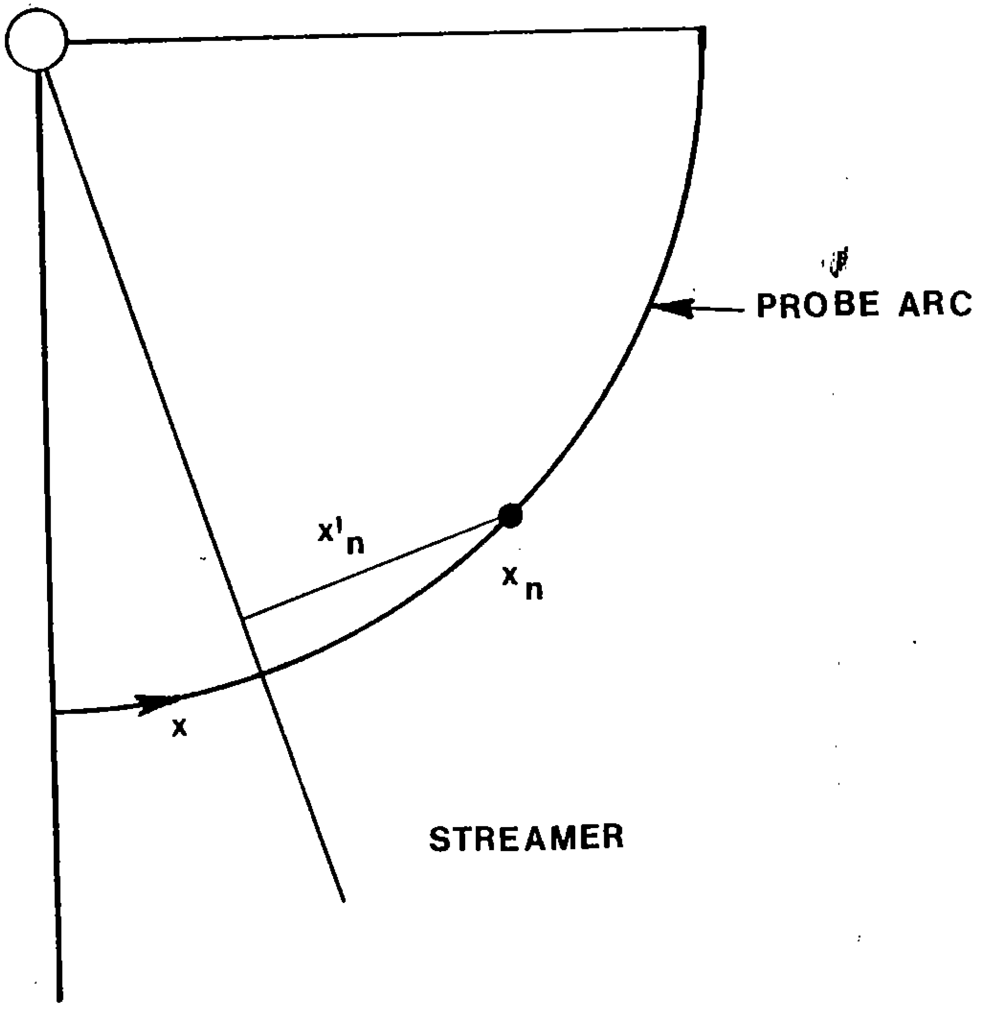

Figure 6.1.8. x_n is arc distance from streamer to probe n; x_n' is shortest distance.

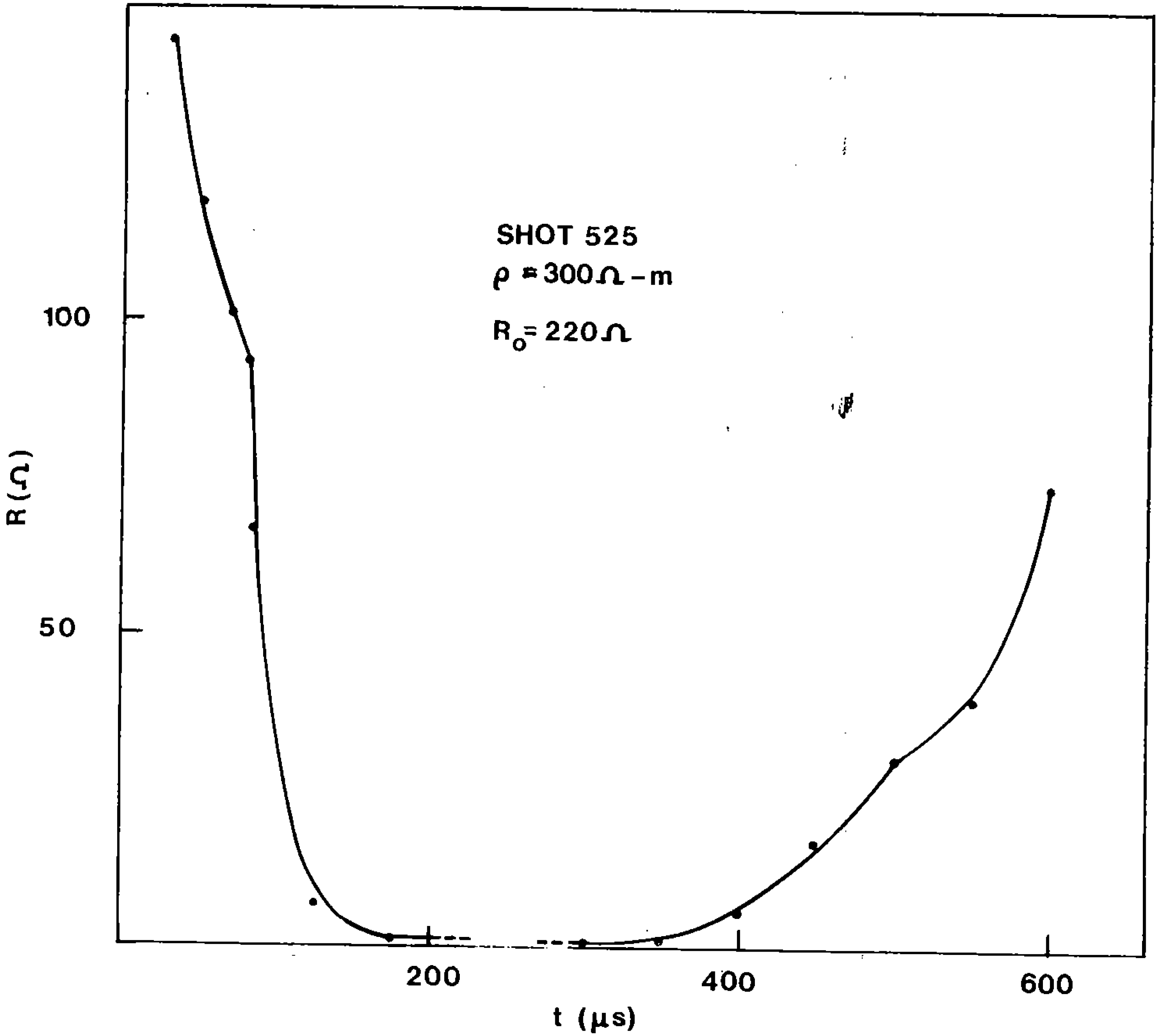

Figure 6.2.1. Resistance v. time for shot 525. R_o is ohmic resistance.

as the voltage decays. The resistance R of the sample is shown in Fig. 6.2.1. It drops from its ohmic value of 220 ohm to about 100 ohm at t_B, then drops rapidly during attachment to less than 10 ohm and then rises slowly as the soil recovers.

We have made a plot similar to Fig. 6.1.2 for shot 525, shown in Fig. 6.2.2. A set of azimuthally located voltage probes were located on an arc with a 6 inch radius at the top insulating plate of the system. The probes were separated by 11°; there were 19 probes covering 198°, approximately a semicircle. We have plotted the voltage on these probes versus angle at 50μs, prior to t_B; at 100 μs during the build-up of current during attachment; and at 200 μs when the voltage has decayed and the current is just starting to decay. This latter time would correspond to the time 300 μs in Fig. 6.1.2 when it was seen that the voltage was very uniform with angle. For shot 525, however, we see that at 200 μs, the voltage is not at all uniform. The voltage at the center conductor V_0 at 200 μs is 7.2 KV. There are three angles at which the probe voltage is very close to 7.2 KV: - 90°, -15° and 65°. We interpret this to mean that there is a streamer occuring at each of these angles. Since attachment occurs in the presence of streamers, this is streamer attachment. It is likely that the streamers carry the bulk of the current.

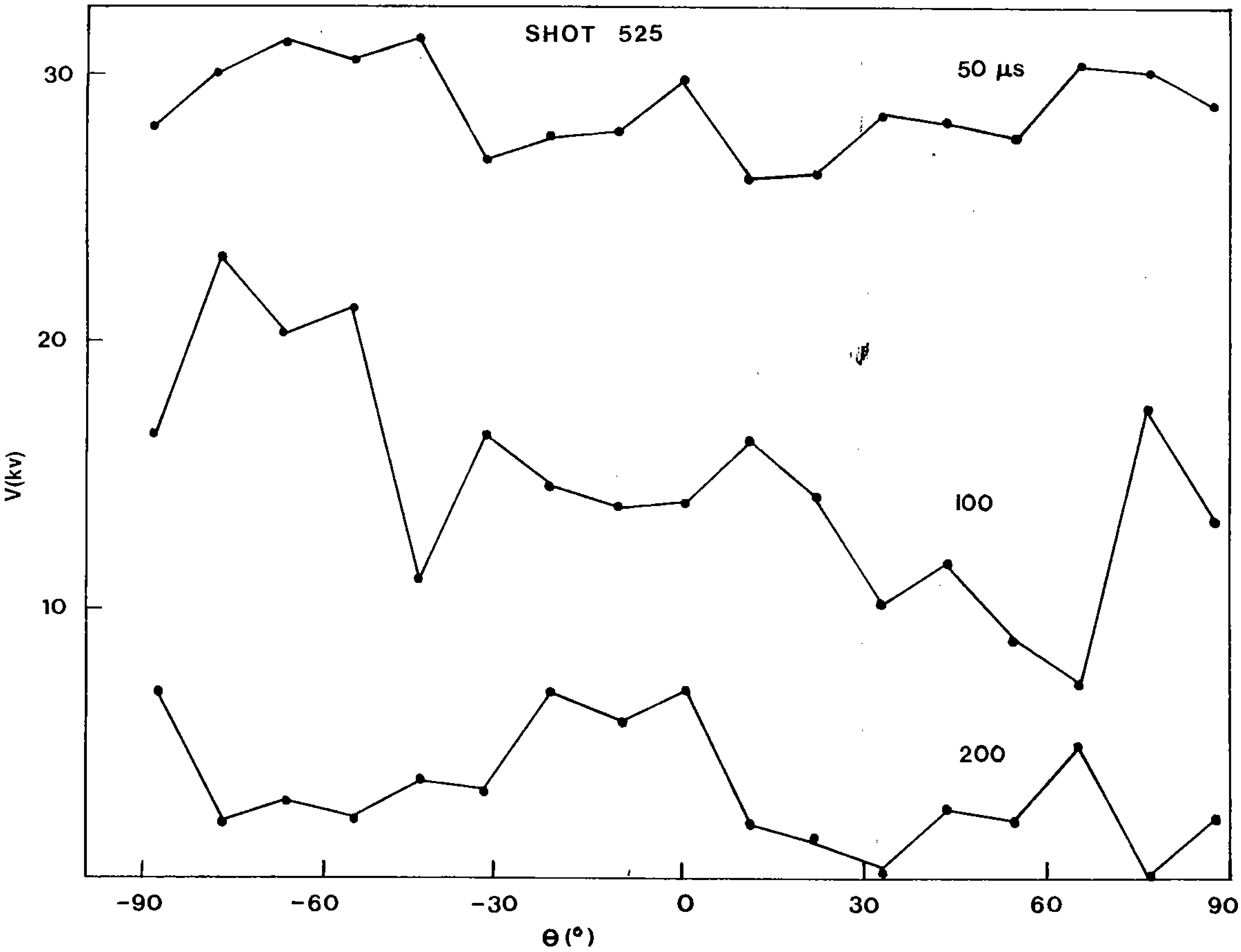

Figure 6.2.2. Voltage on 19 azimuthal probes (17 shown) located on 6-inch arc in top plate.

7.0 Summary, Discussion, and Recommendations for Future Experiments

7.1 Summary

The important points made in this paper are listed below. The electrode configuration is cylindrical.

1. The important features of the corona, including the location of maximum r_0, are defined by about 30 μs.

2. Sample current reaches a maximum or else attachment occurs in a symmetric corona in about 100 - 200 μs.

3. The corona can be defined by two parameters, E_B and ρ_1/ρ_0. We have tabulated these parameters here at maximum current and find that both parameters correlate well with peak V_0. Note that maximum r_0 which occurs at maximum I can be calculated from E_B and ρ_1/ρ_0. We find that E_B and ρ_1/ρ_0 depend on ρ_0. We have tabulated E_B and ρ_1/ρ_0 v. V_0 peak for four values of ρ_0.

4. For the cases examined here, $\rho_1/\rho_0 \approx .8-.1$ and E_B was 100 - 200 KV/m at maximum I.

5. For a symmetric corona, maximum I could very accurately be predicted from the model, requiring only that peak V_0 and ρ_0 be known.

6. The relaxation of the current through the sample as the voltage decayed was accurately predicted using a dynamic model in which a third region was introduced. It was required that ρ_1/ρ_0 increase slowly from its value at maximum I. No general data on this increase in ρ_1/ρ_0 is presented.

7. Attachment occurs by two different methods: corona attachment and streamer attachment.

8. Corona attachment is associated with a radius of instability in a cylindrical system. This radius can be calculated. Also, there is a voltage

which can be calculated below which the system is corona stable.

9. A spherical corona is inherently stable.

10. For the geometry investigated (b = .5 m), the time for corona attachment ranged from 100 to more than a few milliseconds in a random manner that showed no correlation with pulser voltage, V_o.

11. Streamer attachment time correlates with V_o.

12. The location of streamers can be predicted by voltage probes that are spaced 4 cm. apart. Probably larger probe spacings are possible.

13. A streamer radius is of the order of .4 cm.

7.2 Discussion of Corona Attachment

This is a phenomenon which has not been recognized previously. We have presented in this paper two independent pieces of evidence which support its existence. The conditions under which this type of attachment exists are more restricted than for streamer attachment, and we discuss these conditions below.

1. The corona must have a high degree of the symmetry of the initiating electrode system. This was the case in the $\pi/2$ wedge. We have theorized that the corona and streamer images in the other three quadrants of the circle, as well as in the image wedges stacked above and below the real wedge, contributed of a high degree of symmetry in the wedge. Van Lint, et al. [2] have pointed out that another way to bring about enhanced symmetry is to drive the center electrode at a voltage so high that the electric field at the surface of the electrode is well above the threshold value for metal-soil interface breakdown. The idea here is that if the corona really consists of a lot of small streamers, a large electric field will cause many of these to form, i.e., they occur with a high density, thus keeping the outer surface (corona

boundary) uniform. If, on the other hand, only a few little streamers form, the boundary is poorly defined, and there is no shielding of one little streamer from the next. Thus, one little streamer will start to propagate as described by Longmire, et al. [10], and it may evolve into a large streamer.

2. The grounded electrode must have an area large enough so that it intercepts a significant portion of the corona boundary and current will flow through a significant portion of the corona volume.

In conclusion, we note that if a symmetric corona arrives at a grounded electrode which has a small area relative to the corona boundary, we speculate that a streamer might form at the grounded electrode and propagate backwards toward the high voltage electrode. Also, we note that in most of the experiments reported to date, attachment of any sort has not occured over distances much larger than 1 m. Since coronas have been observed to have radii of this order of magnitude, they should not be ruled out as the main mechanism for attachment.

7.3 Suggestions for Future Experiments

1. Corona parameters. Since the corona and streamers are inseparable, and, in any case, corona determines current flow during early time before a streamer can form, its parameters should be tabulated. Reference here is to E_B and ρ_1/ρ_0. These parameters should be found for a wide variety of soils and possible center conductor radii. The experimental geometry is probably not important, so one may use the $\pi/2$ wedge. These parameters should be measured at I maximum as well as prior currents. ρ_1/ρ_0 during relaxation should be measured. The wedge experiments described in [2] should be revised somewhat. For example, more probes need to be introduced in the corona region

to confirm the dependence of V(r) on log r as well as the need for increased accuracy in measuring E_B and ρ_1/ρ_0.

2. Single streamer. The properties of a single streamer need to be investigated. It is proposed to use a spherical geometry. In fact, one could use a section of a regular polyhedron. For example, a good choice would be a section from a regular icosahedron which has 20 sides. This would represent a symmetric section of a sphere like the $\pi/2$ wedge is a symmetric section of a cylinder. Since the sphere is inherently stable, if its radius is large enough, corona attachment can be suppressed. Then a plate across the triangular bottom of the section could be grounded and streamer attachment from a portion of a sphere at the apex of the section to the plate would occur. This idea has been somewhat controversial in the past on the grounds that the image streamers would somehow shield the actual streamer. However, Longmire, et al. [10] have shown that according to their streamer model, it is the tip of the streamer that controls the propagation of the streamer. Thus, as long as a distance along the streamer from the tip to a few streamer diameters away from tip, is not shielded, the streamer should propagate without influence from the image streamers. This means that as long as the image is more than a few streamer diameters away, which should be generally the case, the actual streamer would propagate uneffected by the images.

We point out that this limited geometry affords the possibility of using an array of high impedance voltage probes that would tell much about the details of the streamer and for that matter the surrounding corona. It is recommended that data channels consisting of scopes whose traces are photographed be replaced by channels containing analog to digital converters (A/D converters). Each channel of this system would consist of a sample-hold circuit, and A/D converter and a memory.

This approach has the great advantage that many probes could be used, and one does not have to digitalize a large number of photos. We have found the following dismaying fact. If a photo is digitalized on two separate occasions by presumably two different people, the digitalized results may be 10% different. The reason for this is not known. It cannot be accounted for by the width of the line on the photo. We have determined that this difference constitutes a consistent (rather than random) error.

3. Number of streamers per meter. The last parameter that is needed to characterize streamers from the point of view of modeling in a computer code is to determine the number of streamers that emerges from a meter length of buried conductor, on the average. One could do this by burying, say, a 5 meter length of rod in a test cell, open circuit one end and drive the other with a pulser. One now needs some method of counting the number of streamers which originate on this rod.

One method might be to use a fast rise time microwave signal and propgate this signal along the rod. This constitutes a radar system or it is comparable to a well known piece of microwave test equipment called a time domain reflectometer. A microwave signal will propagate along a buried metal rod with the soil offering little attenuation. If it can be shown that the corona does not significantly attenuate the signal, and that, on the other hand, a streamer will cause a reflection, then this technique can be used to locate streamers. Obviously there are logistical problems that also must be solved.

APPENDIX A: LINEAR ELECTRICAL CONDUCTIVITY OF SOIL*

At low voltages, soil is known to exhibit electrical conductivity which is relatively independent of frequency below 10^5 Hz. The conductivity varies, however, from soil to soil and varies with time in a single soil. This suggests that the conductivity of a soil is a complex property dependent on a number of variables. The purpose of this Appendix is to discover what the variables are and to attempt to define them quantitatively. A literature search has shown that the variables of interest include the nature of the soil involved, the nature and amount of fluids held in the soil, and the temperature of the system. This Appendix will discuss these parameters and their interrelationship which determines the conductivity of a given soil.

In order to discuss soil conductivity, we must first define what is meant by 'soil'. A simplistic definition of soil is 'weathered rock', or rock that has been physically broken apart and chemically and biologically altered. The soil is a complex system which extends from the surface of the earth down to the unaltered rocks of the earth's curst, and consists of minerals, organic material, and voids between grains which may be filled with air or water. Soil has a diverse spectrum of compositions which vary both laterally and from the surface to extreme depths. In general, the soil close to the surface has a high proportion of organic material, such as decaying plant remains, organisms, and microorganisms, while the soil at large depth consists almost entirely of broken up bits of rock. The lower boundary of the soil is a point of debate among pedologists, most of whom

---

* The material in this Appendix was prepared by Mr. Rik E. Lantz, a graduate student in the Department of Geosciences at the University of Arizona. It was prepared as an individual studies project under the direction of one of the authors, and was completed in December, 1982.

claim that a soil must have at least some organic component in addition to mineral components to qualify as a soil, thus, excluding sand and gravel from the realm of soils. Similarly, pedologists may claim that lithified materials, that is, materials whose component grains have become cemented together by precipitation of chemicals carried in groundwater, have ceased to be soils and become rocks. From an electrical standpoint, however, these are philosophical matters, since neither organic material or cements have a pronounced effect on the electrical properties of the materials involved. For this discussion, the soil is simply a veneer on the earth's surface between the actual surface and unaltered rock at large depth.

The formation of soil from rock is a complex process, involving the physical cracking and disintegration of the rock to smaller grains, and chemical activity of groundwater, plants, and microorganisms on these grains. Physical breakdown occurs because of temperature variations at the surface, which induce stresses between grains due to differing coefficients of thermal expansion, as well as erosion by wind and water and a myriad of other mechanical processes. Chemical breakdown occurs because most rocks were formed at pressures and temperatures profoundly different from those at the surface. As a result, the mineral phases which were stable at the time of formation are not stable at surface temperatures and pressures, and with the aid of water, oxygen, and organic activity, they break down to more stable phases, notably clays. The fact that weathering begins at the surface and works its way downward has marked effects on soil formation. As mentioned previously, the soil near the surface may have a high proportion of organic material. Rainwater which falls on this organic matter may become acidic and begin percolating down through the soil, dissolving certain solids from the zone immediately below the organic matter. As the acidic water dissolves more and more solids, its pH changes, until a point may be reached where saturation in one or more ions occurs, and these will precipitate.

This is a very oversimplified sketch of the formation of soil horizons, but has been included here to introduce an important characteristic of soil, namely that it is exceptionally heterogeneous. Not only do compositions vary from one location to another, but they will vary with depth at a single location. The development of different horizons results in horizontal stratification of soil and may juxtapose two types of soil with contrasting electrical properties in a relatively short vertical distance. This anisotropy will have a complex effect on the behavior of electric fields in the soil which is difficult to define quantitatively. The following discussion has, therefore, been limited to an electrically homogeneous, isotropic soil, and the relationships discussed will apply only to this case. A single layer within a stratified soil is a close approximation to such a case, as are relatively simple porous media, such as loose sand and gravel.

Soil is made up of three components: mineral material, organic material, and voids which may or may not be filled with fluid. The conductivities of the overwhelming majority of minerals is very low (10^{-12} mhos/m for quartz, 0.5×10^{-12} mhos/m for calcite, 10^{-6} mhos/m for muscovite), as is the conductivity of dry organic matter. As a result, conductivity in the soil is dominated by the third component, the fluids in the voids. Pores in the soil may be filled to varying degrees with fluid, usually water with some dissolved solids. The conductivity of wet soil is much greater than the conductivity of dry soil. Conductivity of a slightly damp soil is somewhere in between. Put simply, the more water available to conduct electricity, the greater the conductivity of the soil as a whole. Conductivity is dependent on the amount of space available to be filled with water as well, so a porous garden soil will have a greater conductivity than a densely compacted chunk of clay. The conductivity of the fluid itself is another factor. Finally, conductivity is dependent on the distance the current has to travel. Soil with relatively straight water filled pores will have higher conductivity than the same soil with contorted water filled pores. The conductivity of soil, or of any porous medium, is described by a formula derived by G.E. Archie in 1941, which takes all of the above factors into account. This relationship, known as Archie's Law [13], is as follows:

$$\frac{1}{\sigma_\varepsilon} = \alpha\, \phi^{-m}\, s^{-n}\, \frac{1}{\sigma_\omega}$$

where σ_ε = overall conductivity of soil with fluid;

σ_ω = conductivity of pore filling fluid;

α = an empirically determined constant of proportionality: $0.5 < \alpha < 2.5$;

ϕ = porosity, the ratio of the volume of the voids between grains to total volume of soil: $0 \leq \phi \leq 1$;

m = an empirically determined constant which takes into account particle shape and pore geometry: $1.3 \leq m \leq 2.5$;

s = fraction of pore spaces filled with fluid: $0 \leq s \leq 1$;

n = an empirically determined constant $n \approx 2$.

As a specific case, Archie's Law for unconsolidated sand is given by:

$$\frac{1}{\sigma_\varepsilon} = 0.65\, \phi^{-1.5}\, s^{-2}\, \frac{1}{\sigma_\omega}$$

where $a = 0.65$ [14], $m = 1.5$ [15], and $n = 2$ [13].

Conduction of current through aqueous solutions is achieved by ions which carry charge. For this reason, a solution's conductivity is governed by the concentration and electrical affinity of these ions. Fig. A.1 shows the effect of concentration of various ionic solutions on resistivity. High ion concentrations have low resistance and high conductivity, and low concentrations have high resistance and low conductivity. In the southwest, the ion content of groundwater tends to be very high, so fluids in the soil here should have high conductivity. Solution conductivity is also governed by temperature. Low temperatures hinder the movement of ions in solution and, thus, the solution's capacity to carry current. A rough rule of thumb is that resistivity changes 2% per degree Centigrade [16].

The factor ϕ is the porosity of the soil, or the ratio of the volume of voids (pore spaces) to the total volume. Porosity ranges from 0 to about 0.75, and depends on a number of factors including grain size, range of grain sizes, grain shape, and packing. Coarse grained soils tend to have higher porosities than fine grained soils. A wide range of grain sizes will allow very small grains to occupy pore spaces and, thus, reduce porosity. Platy grains, such as clays, can be packed together more closely than nearly spherical grains, such as rounded quartz sand grains, implying that pure clay will have lower porosity than sand. Finally, it is obvious that a compacted soil will have lower porosity than an uncompacted soil. As an example, Blatt et al. [17] quote a porosity of 45% for freshly deposited River Sand. Middleton, et al. [18] give other examples of porosity values for various soil types which are shown in Table A1.

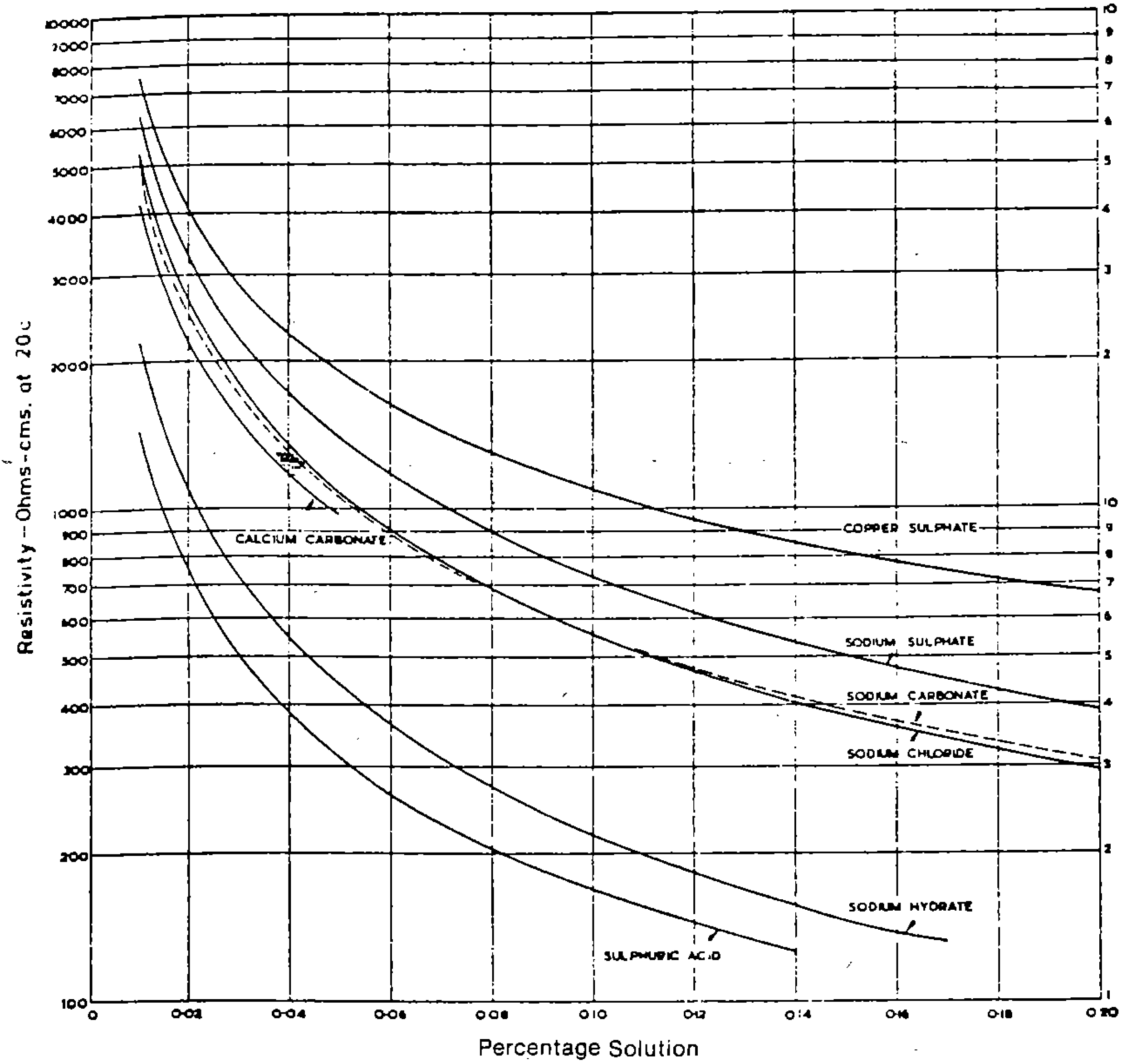

Fig. A.1 - Diagram showing relationship of concentration to resistivity for ionic solutions with different electrical affinities. (Fig. 1.2 from Tagg [19]).

TABLE A1

Type of Soil	depth	porposity (%)	depth (cm)	porosity (%)
Kirvin fine sandy loam Taylor, TX.	surface	29.7	76	53.4
Cecil sandy clay loam Statesville, NC	surface	44.0	69	52.0
Shelby silt loam Bethany, MO	surface	46.2	91	34.9
Houston black clay Temple, TX	surface	61.0	89	40.2

The factor m is an empirically determined constant related to the route the current travels through the rock, which is quantitatively defined as tortuosity. Tortuosity is the ratio of the actual length of a path through a medium to the linear distance between the starting point and ending point. The more tortuous or contorted a path, the greater the value of tortuosity. Due to the complex geometries of soil pores and the nature of electric fields in conductors, current can flow through a number of paths, as shown in Fig. A.2. The tortuosity in this case is simply the average path length the current flows through, divided by the shortest possible path (see Fig. A.2). Winsauer et al. [14] have devised a simple experimental method to determine tortuosity, τ, directly,* and have found that

---

* Winsauer et al. assume complete saturation, $s = 1$ and, in this case, Archie's Law reduces to $\phi^{-m} = \frac{\sigma_\omega}{\sigma_\varepsilon}$. They state in equation (9) that $\frac{\tau^{1.67}}{\phi} = \frac{\sigma_\omega}{\sigma_\varepsilon}$. Substituting ϕ^{-m} for $\frac{\sigma_\omega}{\sigma_\varepsilon}$, the equation $\tau^{1.67} = \phi^{1-m}$ is obtained.

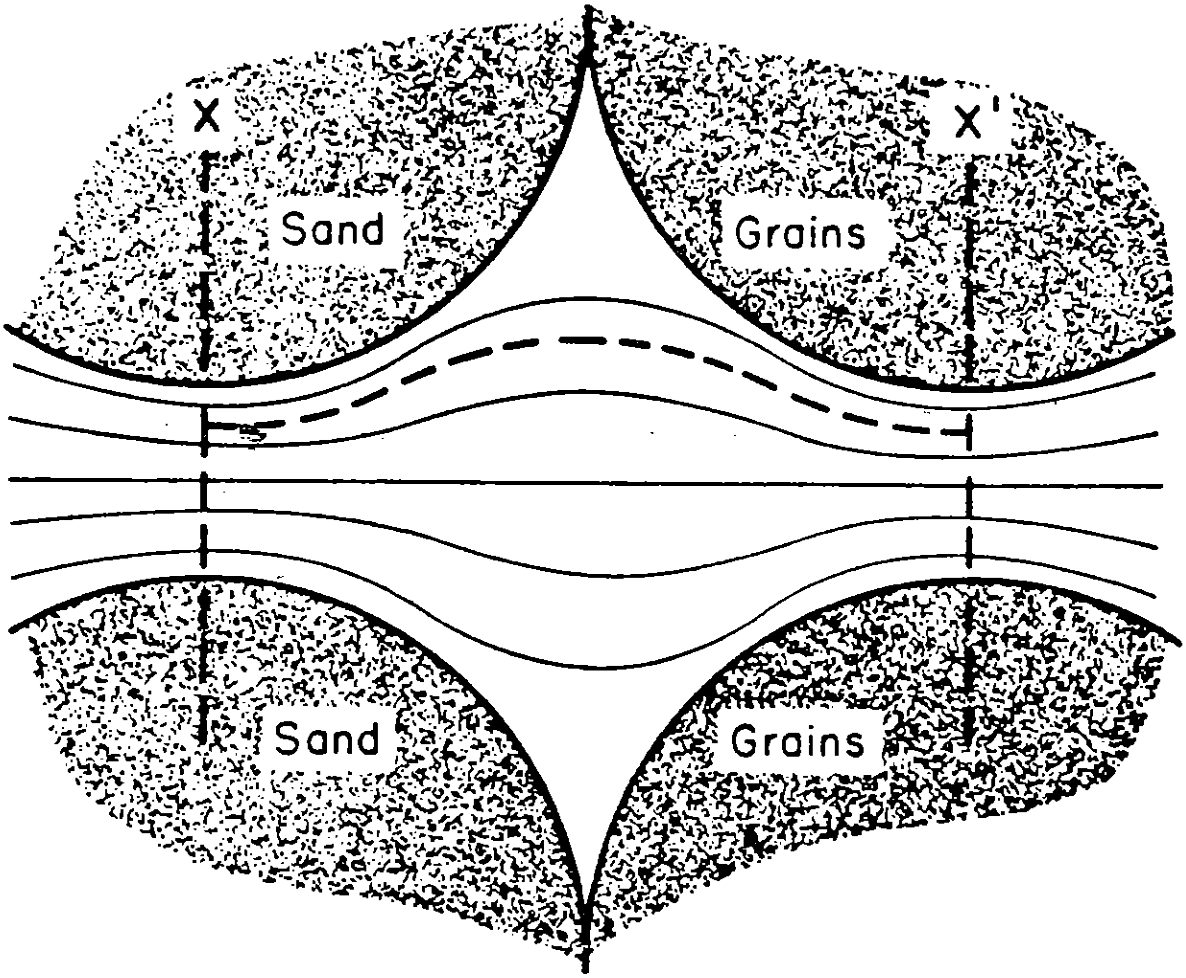

Fig. A.2 - Diagram illustrating the flow of current in pores. A relatively small amount of current flows through the straight path from A to A'. The average of all of the current paths is B to B', and the tortuosity is BB'/AA'. (Fig. 1 from Winsauer et al. [14]).

$$\tau^{1.67} = \phi^{1-m} \quad .$$

Measuring tortuosity and porosity allows empiric determination of m.

Tortuosity is, in part, a result of particle shape, and Jackson et al. [15] have attempted to evaluate the effect of particle shape on m. Their work has shown that particle shape and m are directly related, and that the more angular the particles, the greater the value of m. The result of their research is illustrated in Fig. A.3. The figure shows m = 1.2 for commercially produced glass spheres, m = 1.85 for extremely angular shell fragments of the same size, and intermediate values of m for intermediate grain shapes. Their experimental approach to empirical determination of m was to completely saturate their sands with fluids, decrease the porosity by successively compressing the samples, and determine m as the slope of the line when ϕ was plotted against $\frac{\sigma_\omega}{\sigma_\varepsilon}$. This method is probably more accurate than the method derived from Jackson's work because it is a more direct measurement.

The parameters take into account the amount of fluid actually held in the pore spaces. The parameter is a saturation factor ranging between 0 and 1, which is simply a ratio of the amount of pore space filled with fluid to the total pore space. The parameter is yet another empirically determined constant, which can be evaluated by determining all other constants and varying s. There are some physical constraints which in very dry conditions limit the values of s. One of these is the phenomenon of adsorption, which results from an electrical imbalance of minerals in the soil. Due to the nature of crystal growth, the surfaces of minerals often have unneutralized charges, which can attract one or more layers of dipolar water molecules (see Fig. A.4). Even when the mineral

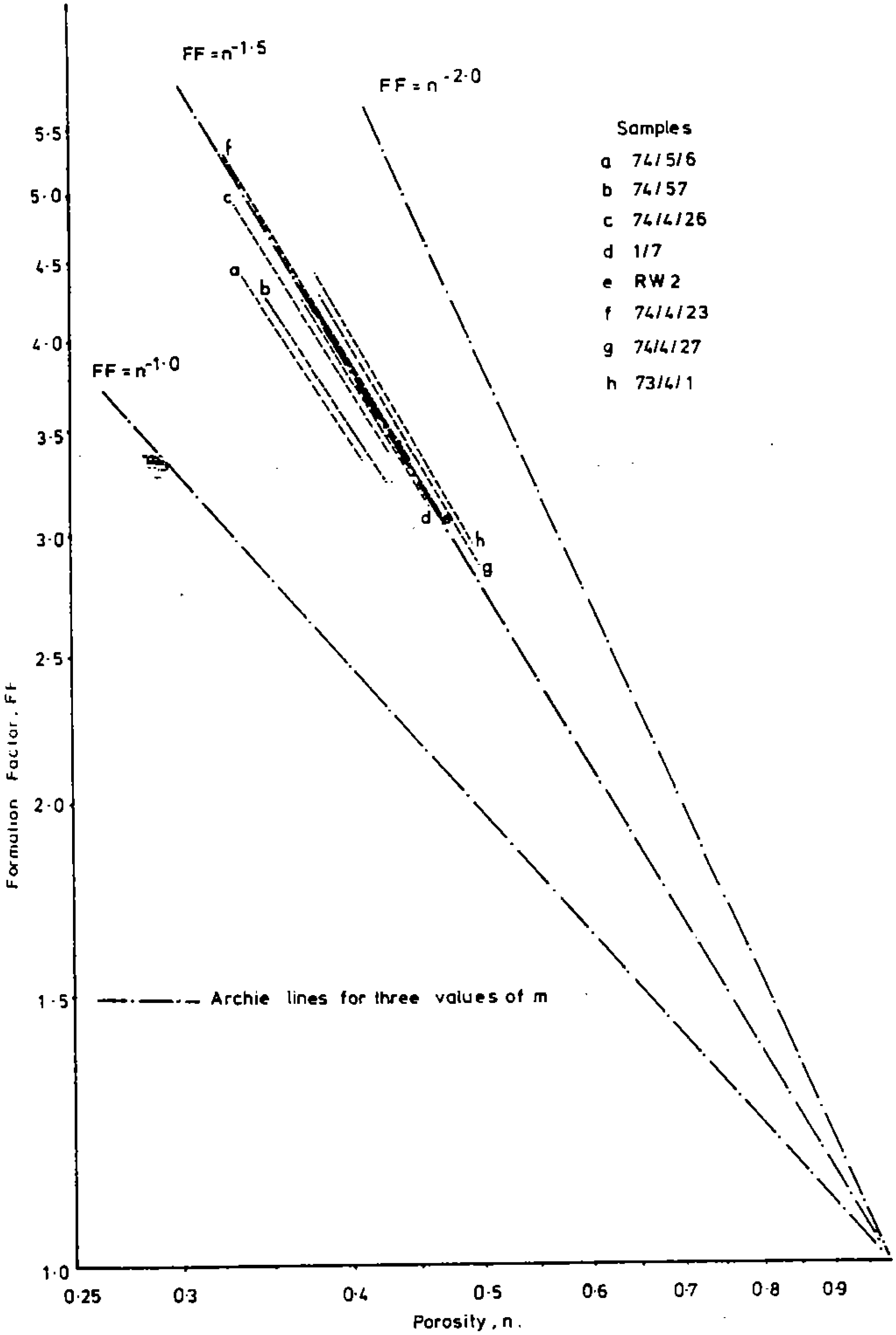

Fig. A.3 - Diagram showing the effect of particle shape on m. The particles are increasingly angular from A to E. The linear groups of points reflect successive decreases in porosity for each sample. Their notation has $\sigma_\omega/\sigma_\varepsilon$ = FF, and ϕ = n. (Fig. 6 from Jackson et al. [15].

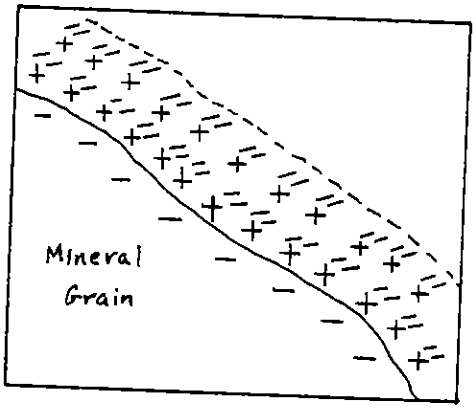

Fig. A.4 - Diagram showing charge distribution at the surface of a mineral crystal and two adsorped layers of water molecules. The symbol = + represents a dipolar water molecule.

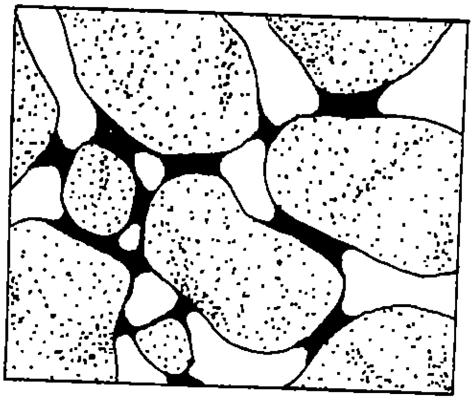

Fig. A.5 - Schematic illustration of meniscus contacts. Water is in black, grains are shaded, and air filled pore space is white. When the radius of curvature of the meniscus gets very small, surface tension forces are high, and the water will not evaporate.

is dried, the thin lamina of water remains and provides a path for current flow. This effect is especially pronounced in clays. Another phenomenon which keeps soil from drying completely is surface tension. At low fluid content, water is held very tightly in between grains in what are known as meniscus contacts due to surface tension (see Fig.A.5). A certain minimum value exists for each soil where surface tension forces are greater than the water's natural tendancy to evaporate, and the water held in these meniscus contacts will remain unless the soil is subjected to abnormal conditions. The result of these two physical constraints on saturation is that each soil contains a minimum amount of water and, therefore, should have a minimum conductivity. This minimum value can be significant, as shown in Fig. A.6, where the minimum value of s for a 'clay soil' is around 10 per cent.

In summary, then, it has been shown that soil conductivity for frequencies below about 100,000 Hz is described by the relatively simple relationship, Archie's Law. The form of Archie's Law indicates that the solid components of soil are more or less electrically inert, and that the parameters which govern soil conductivity are porosity, amount of pore fluids, ionic content of pore fluids, and grain shape. The soil is such a complex system that the law must be modified by several empirically determined constants which allow for compositional and geometric variations between soils in order to describe each individual case. After experimentally determining these constants, an equation can be written which accurately expresses the conductivity of a given soil, and the meaning of such an equation has been the object of this investigation.

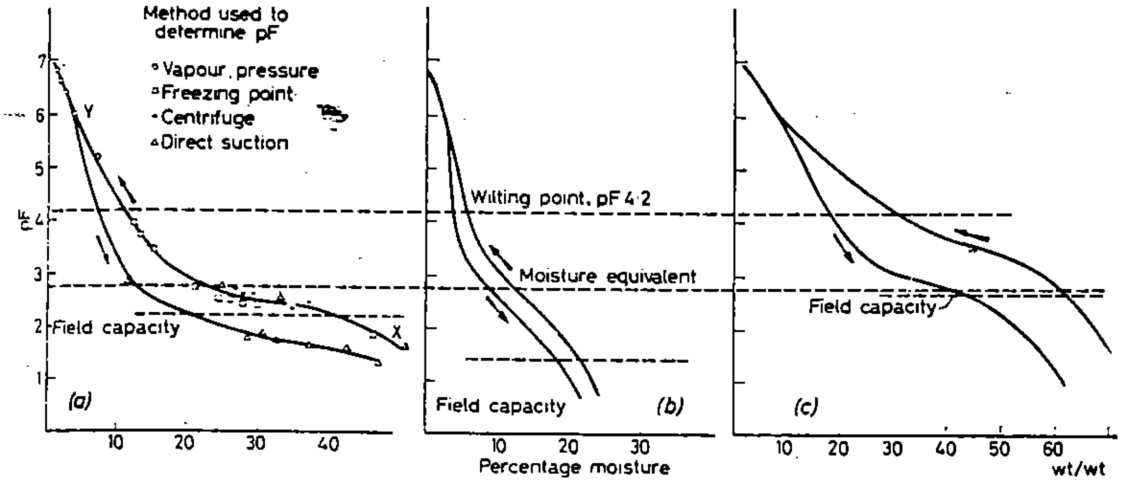

Fig. A.6 - Hysteresis curves showing per cent moisture vs. pF, a measure of the free energy of molecules of the water held in the soil, which is proportional to the amount of energy needed to get them out. Point Y represents 'air dryed' soil, and shows the associated minimum water content. a) Loam Soil; b) Sandy Soil; c) Heavy Clay Soil. (Fig. 4 from Ingram, [20]).

APPENDIX B

Data Base

Presented in this Appendix is the raw data from the experiments upon which many of the calculations in this paper are based. The data are digitilizations of polaroid photos and are presented as plots of voltage or current v. time.

In the figure captions, the first number is the shot number followed by a letter designating the group of experiments from which it was obtained. The second number is a, the radius of the center conductor; the third is b, the radius of the outer conductor. The fourth is L, the sample length, the fifth is ohmic resistivity in ohm-m. All distances are in meter. For example, 399A, .01, .5, .1, 350 sand-mix means shot 399 of Exp. A, with a = .01m, b = .5m, L = .1m, and ρ_0 = 350 ohm-m sand mix.

Also, V_0 indicates that the voltage on the center conductor in KV is being plotted v. time in μs; I means that total sample current in amp is being plotted. Finally, V indicates that a probe voltage is being plotted; and r is the radial position of a probe in meter; Θ is azimuthal angle of probe in degrees; and "bottom" or "top" indicates that a probe was near the bottom on top of the soil sample.

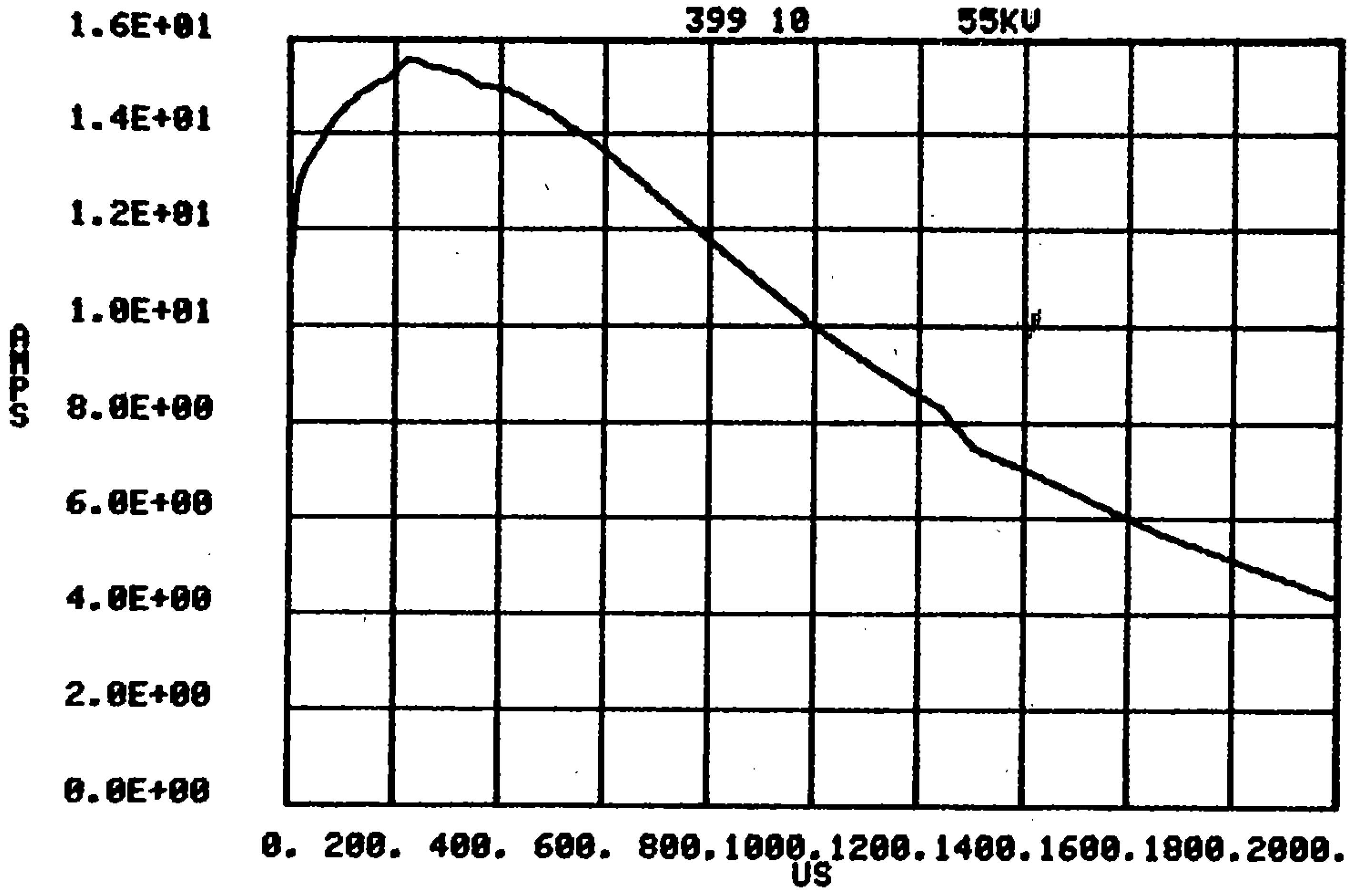

Figure B.1. 399A, .01, .1., .5, .1, 350 sand-mix; I.

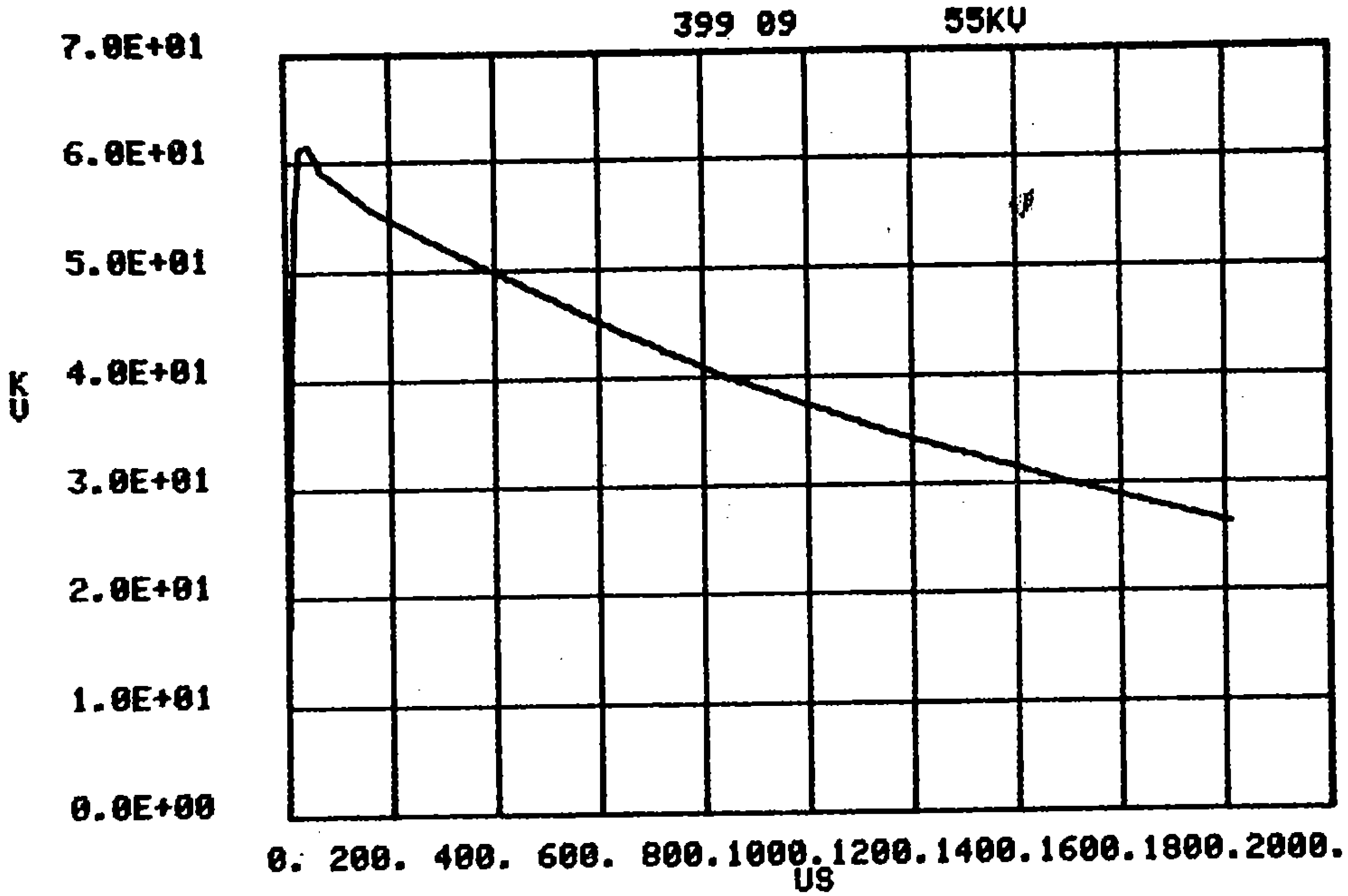

Figure B.2. 399A, .01, .1, .5, .1, 350 sand-mix; V_o; r = .01 m.

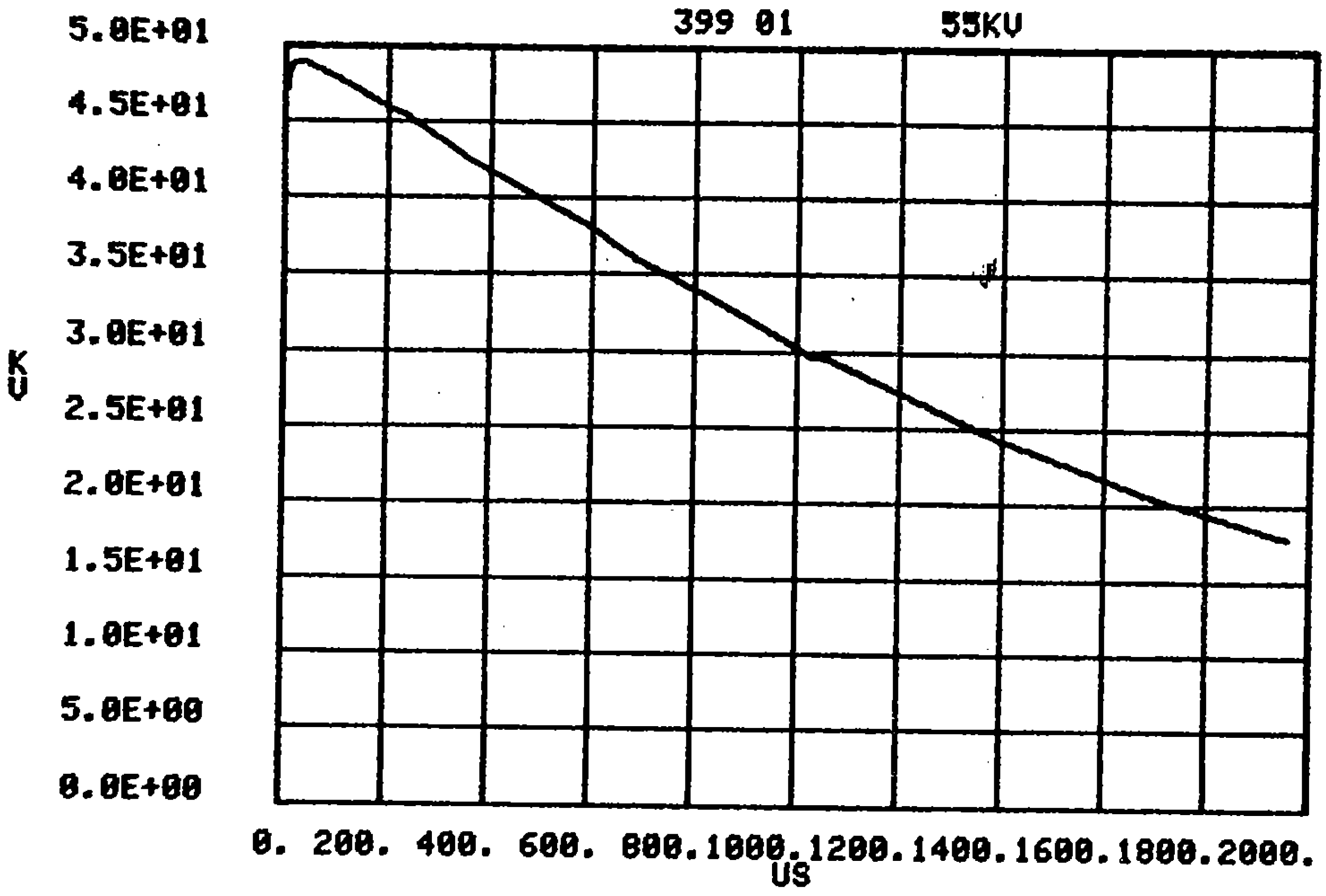

Figure B.3. 399A, .01, .1, .5, .1, 350 sand-mix; V at radial position 2; r = .059 m.

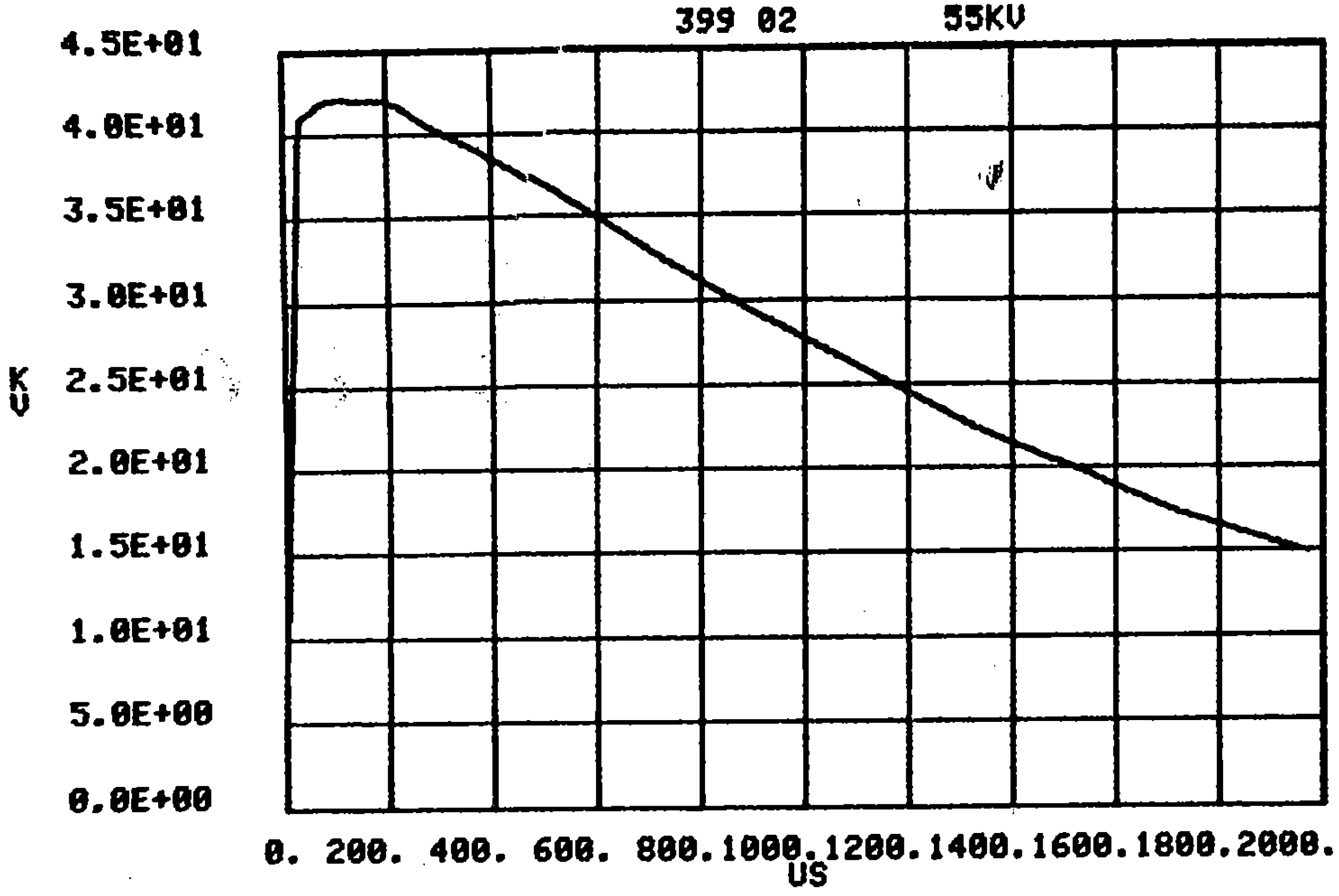

Figure B.4. 399A, .01, .1, .5, .1, 350 sand-mix; V at radial position 3; r = .109 m.

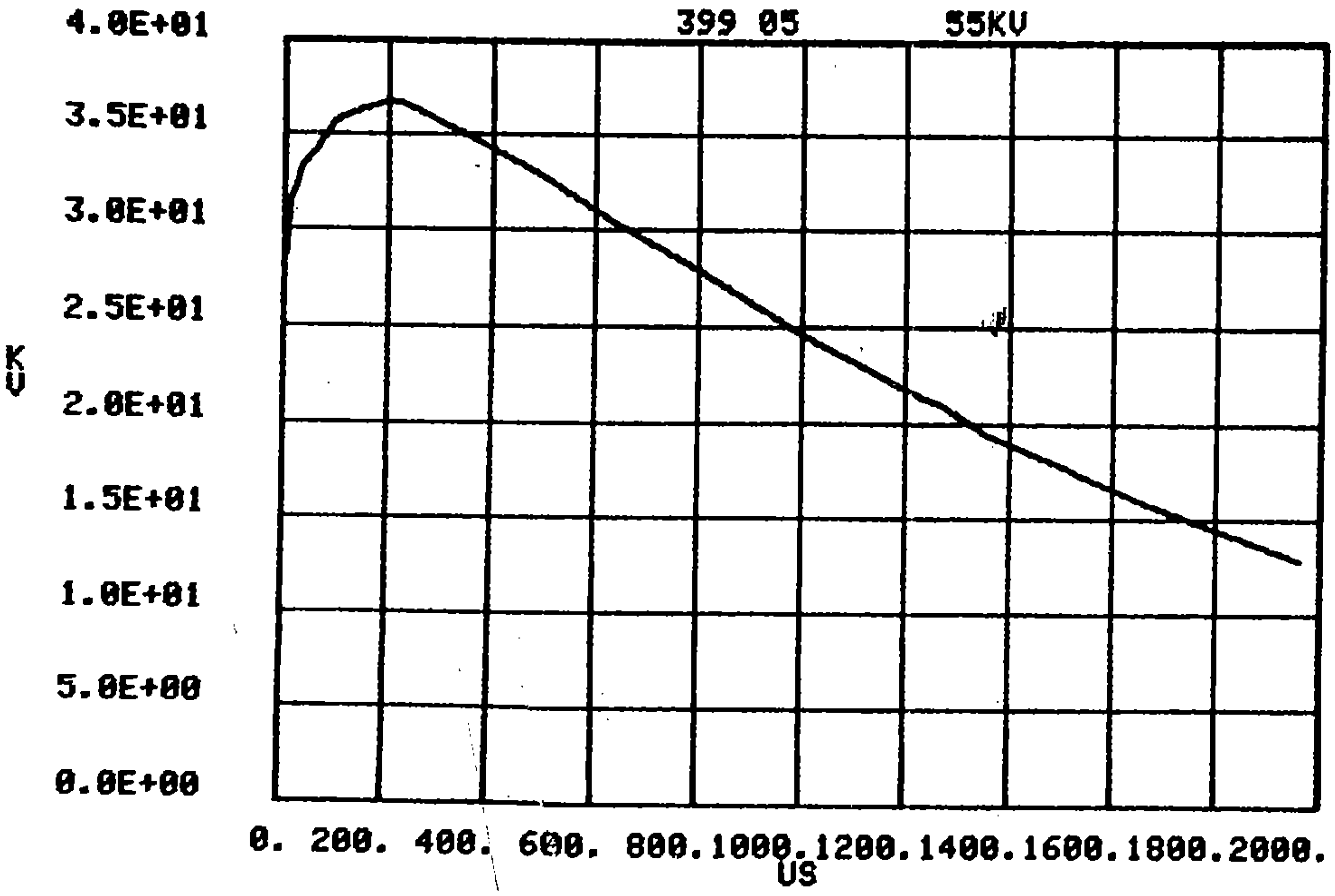

Figure B.5. 399A, .01, .1, .5, .1, 350 sand-mix; V at radial position 4; r = .159 m.

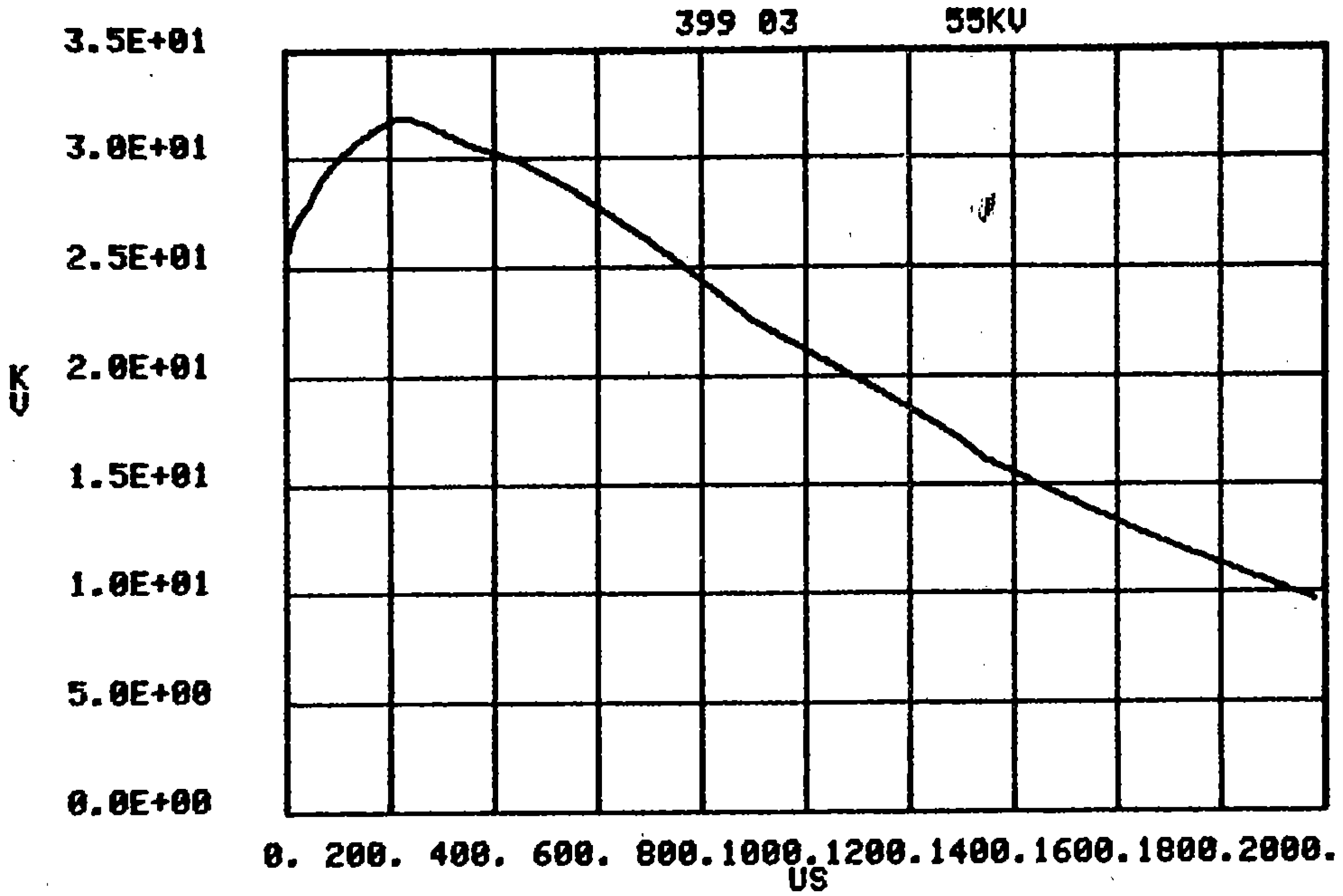

Figure B.6. 399A, .01, .1, .5, .1, 350 sand-mix; V at radial position 5; r = .209 m.

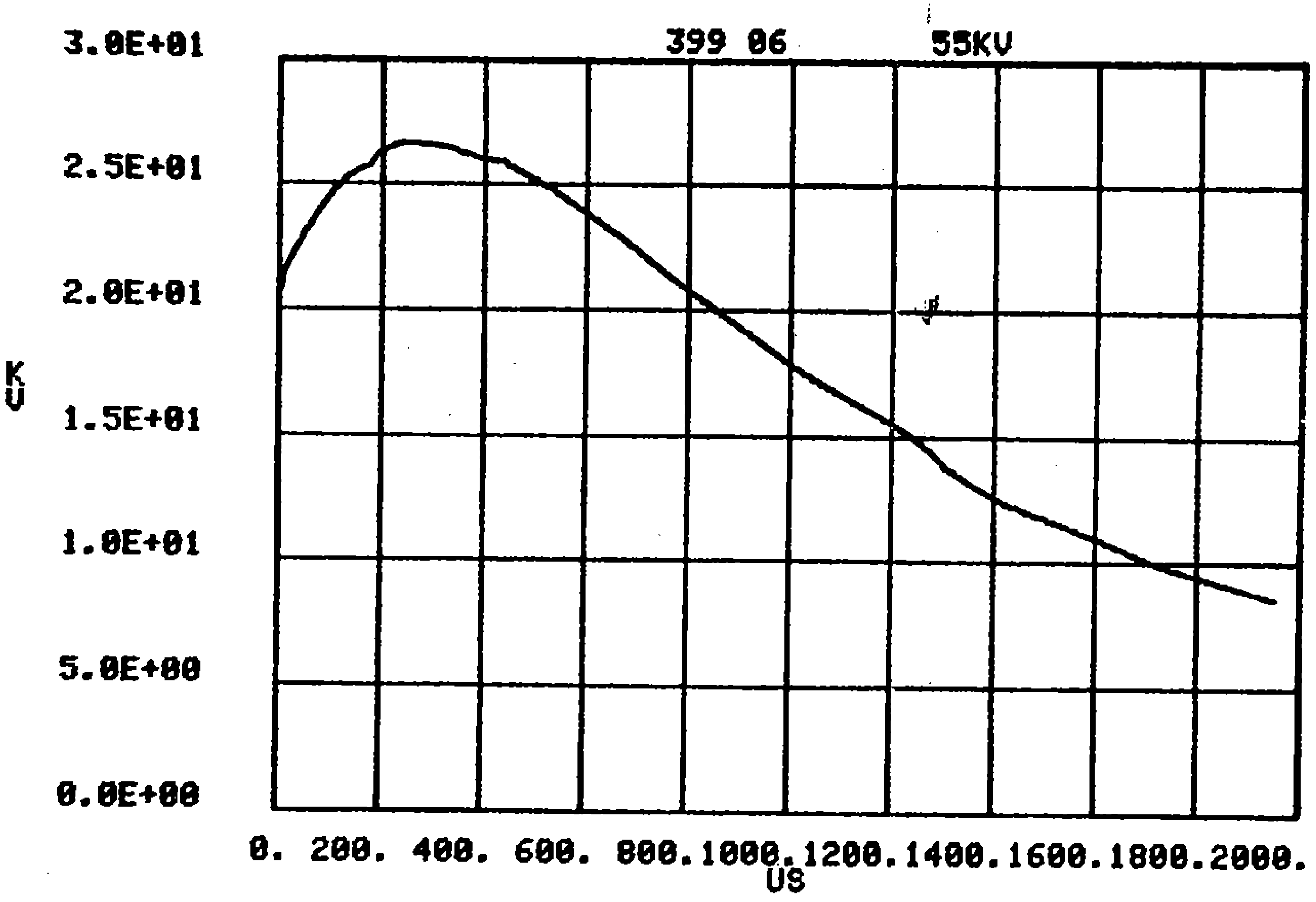

Figure B.7. 399A, .01, .1, .5, .1, 350 sand-mix; V at radial position 6; r = .259 m.

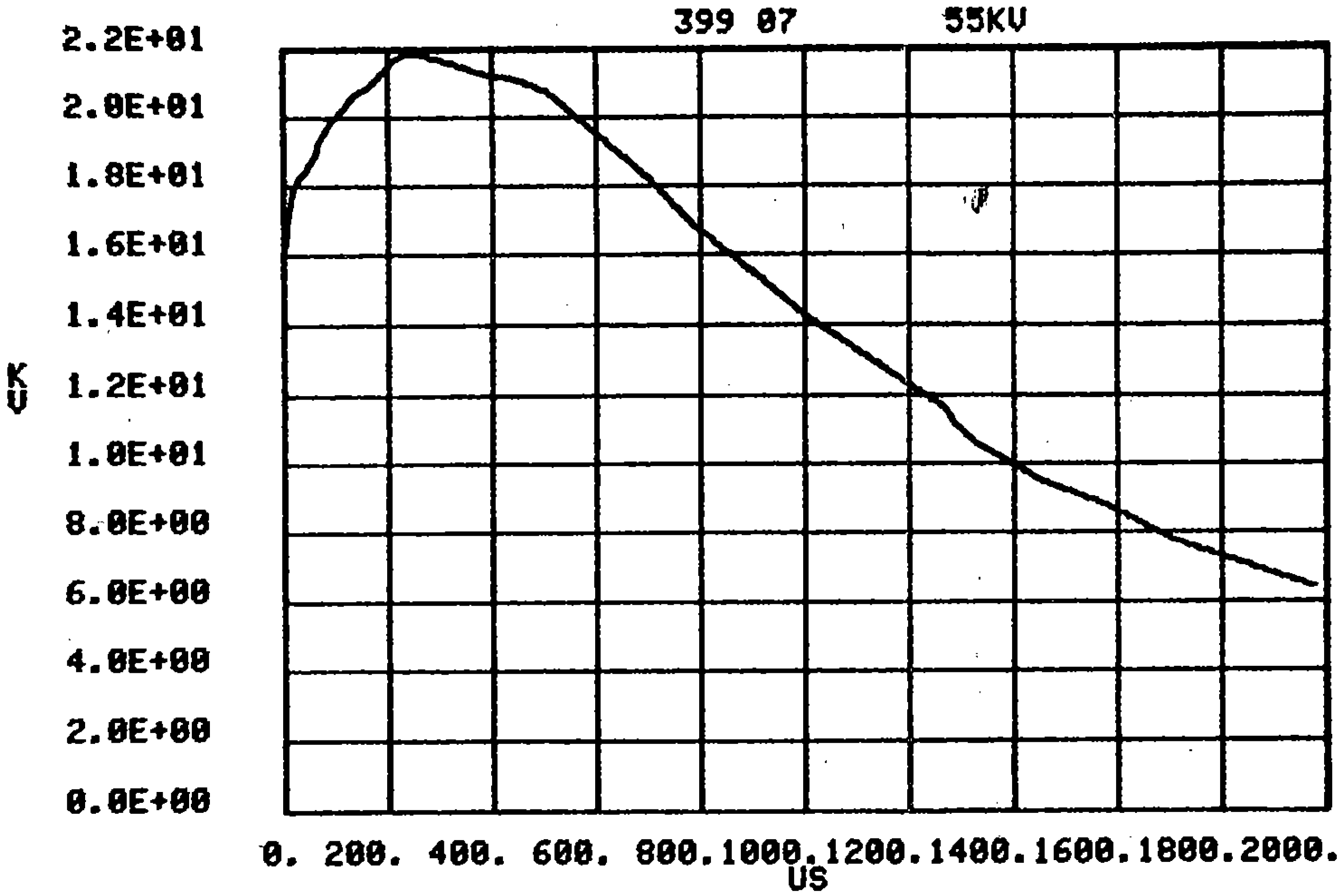

Figure B.8. 399A, .01, .1, .5, .1, 350 sand-mix; V at radial position 7; r = .309 m.

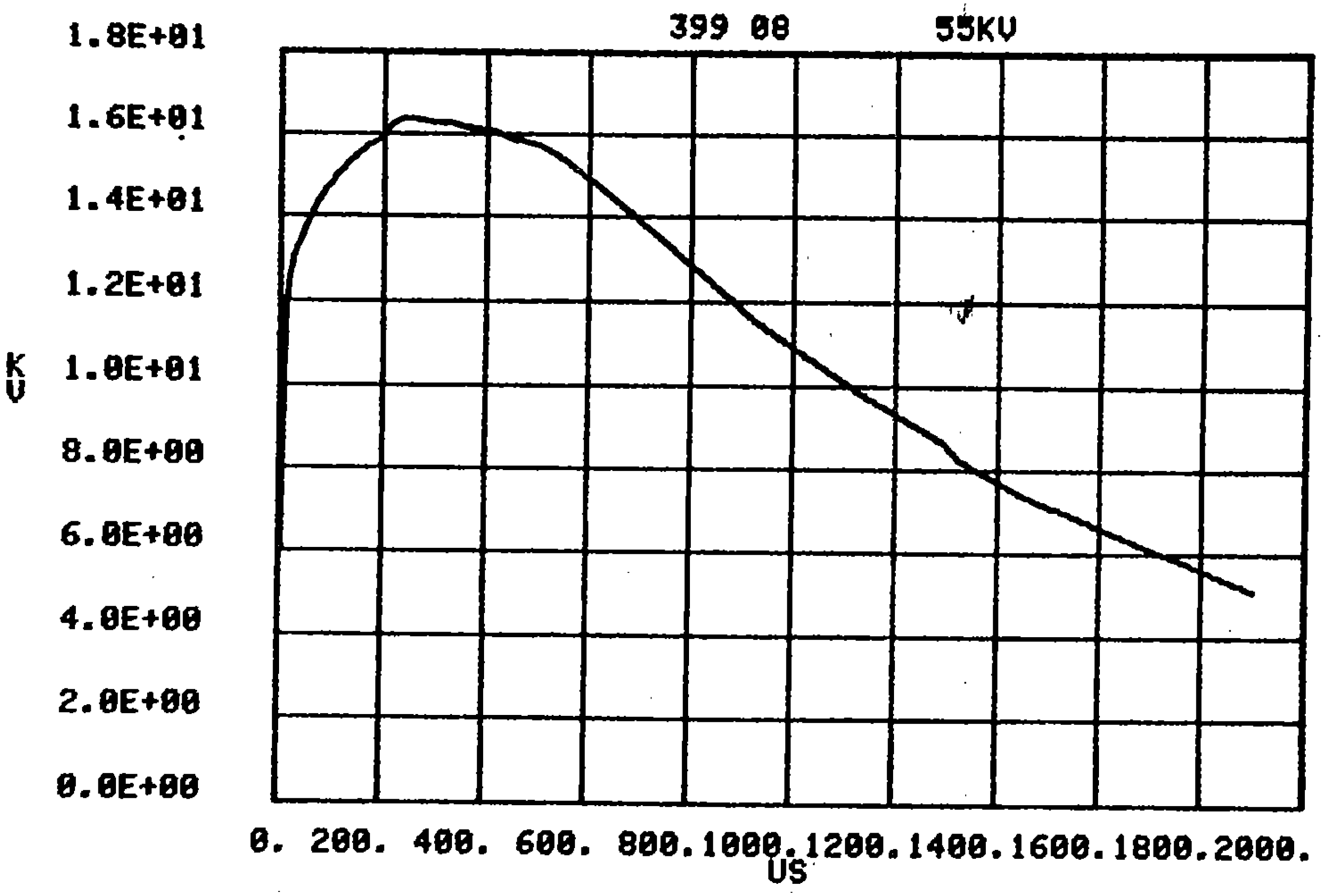

Figure B.9. 399A, .01, .1, .5, .1, 350 sand-mix; V at radial position 8; r = .359 m.

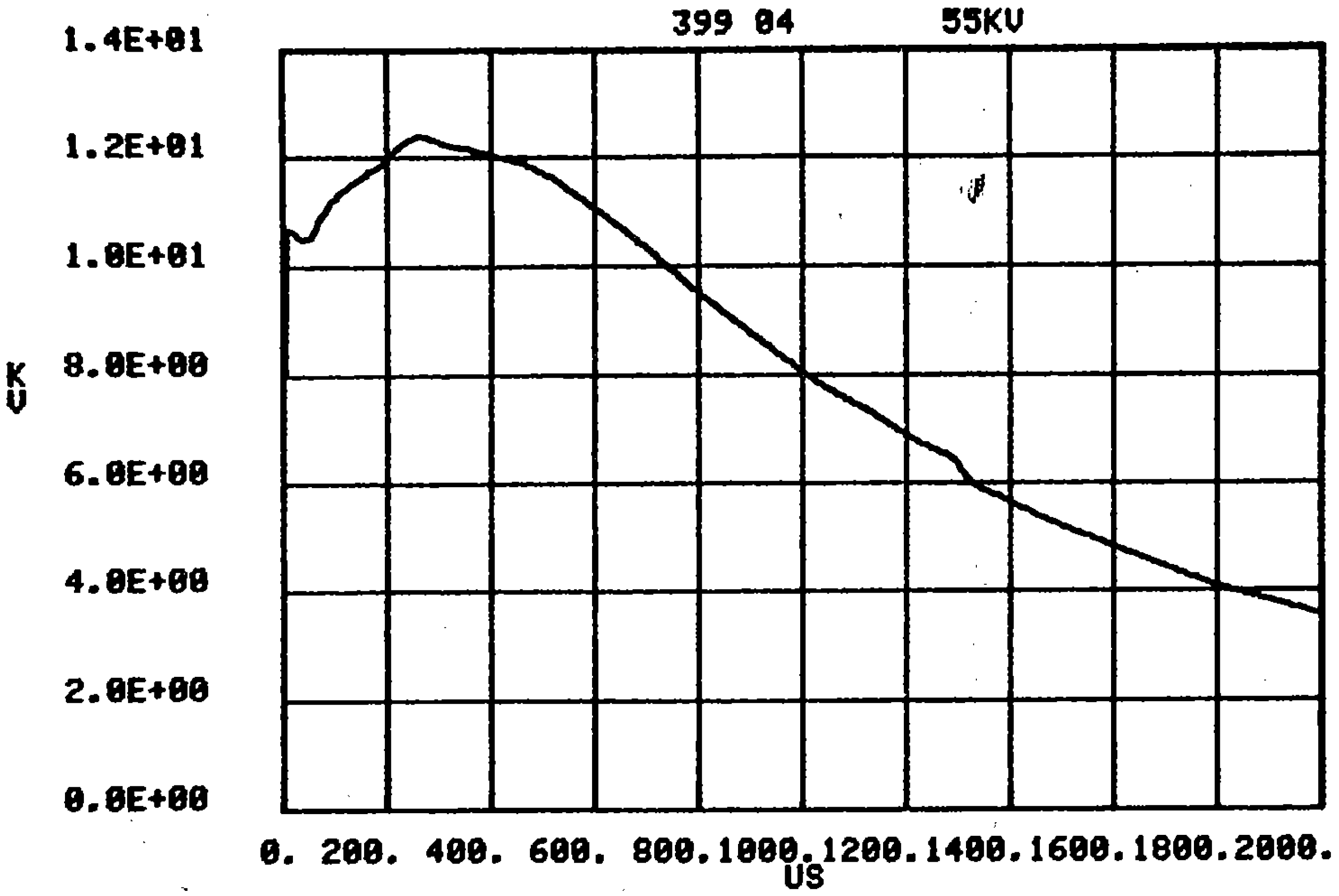

Figure B.10. 399A, .01, .1, .5, .1, 350 sand-mix; V at radial position 9; r = .409 m.

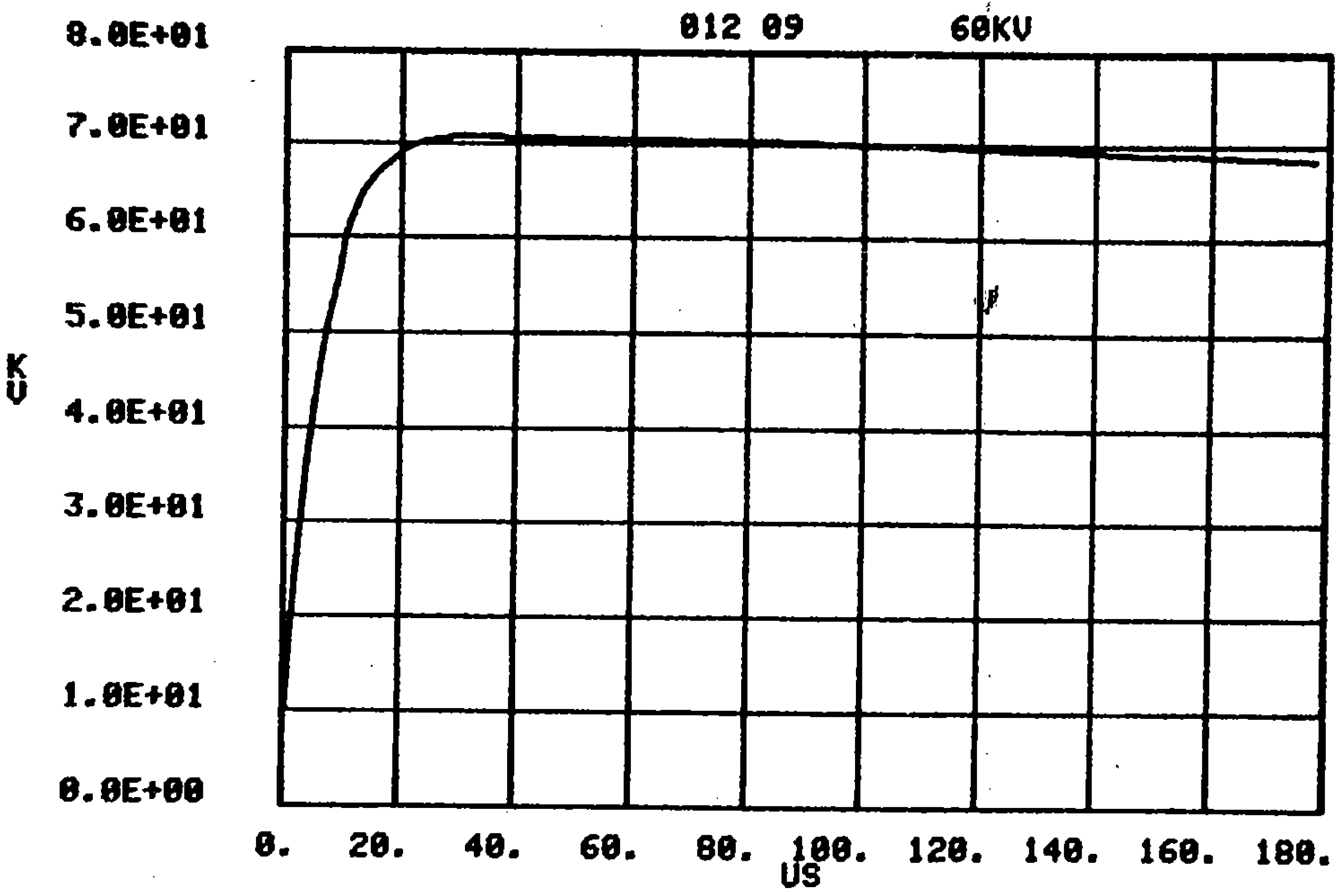

Figure B.11. 012A, .01, 1.0, .3, 1500 sand; V_0.

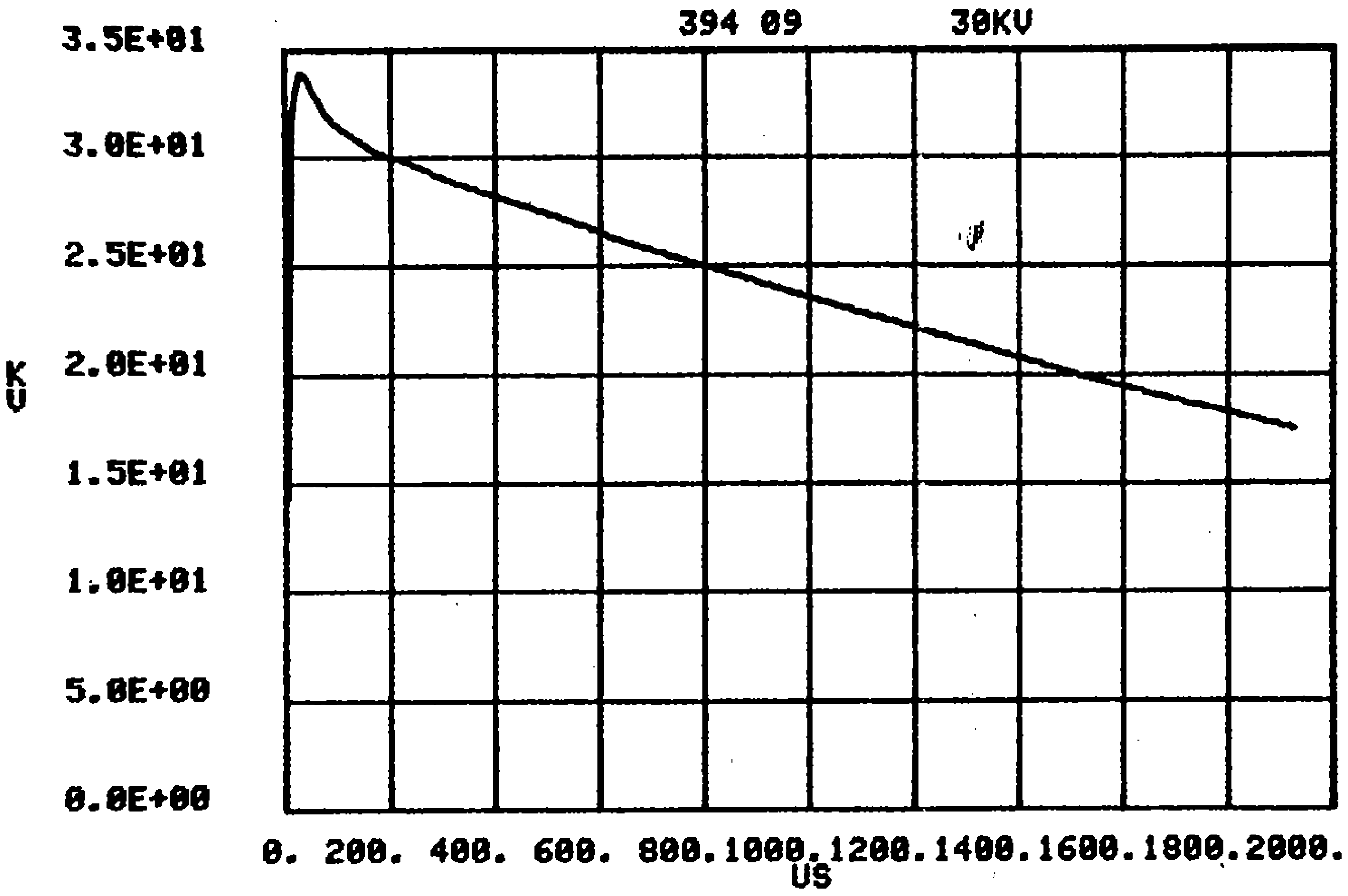

Figure B.12. 394A, .01, .5, .1, 350 sand mix; V_0.

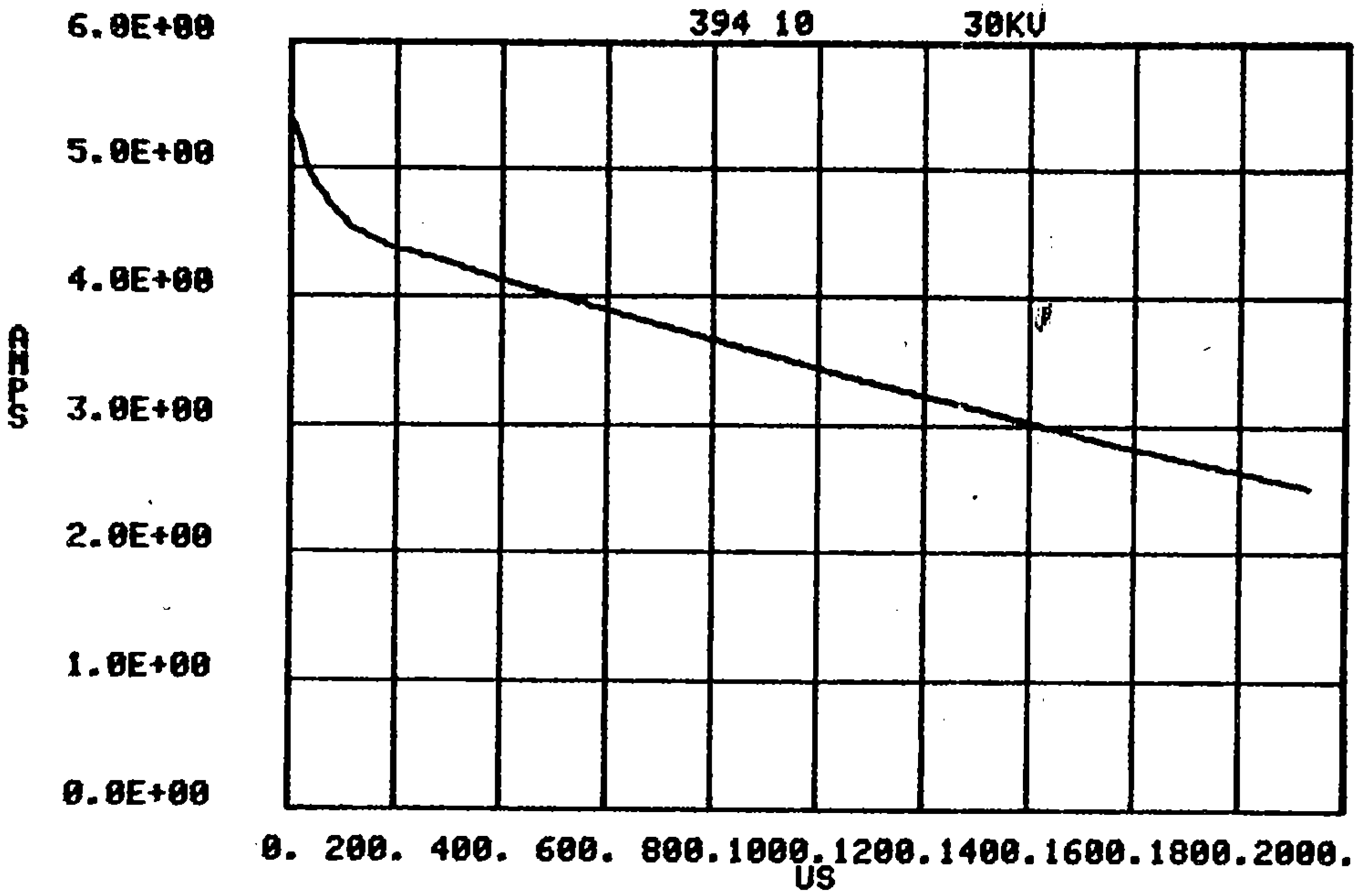

Figure B.13. 394A, .01, .5, .1, 350 sand mix; I.

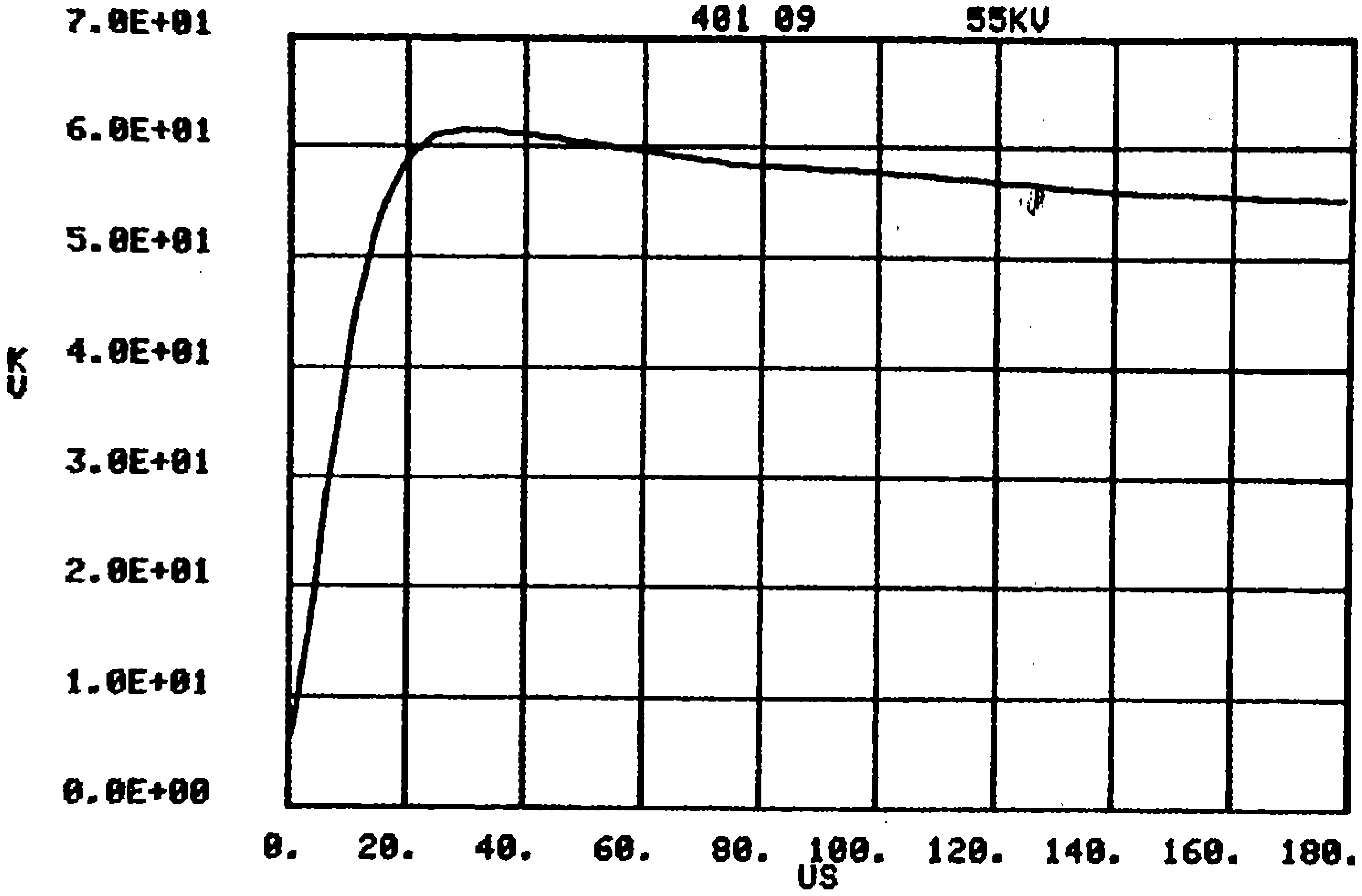

Figure B.14. 401A, .01, .5, .1, 350 sand mix; V_o.

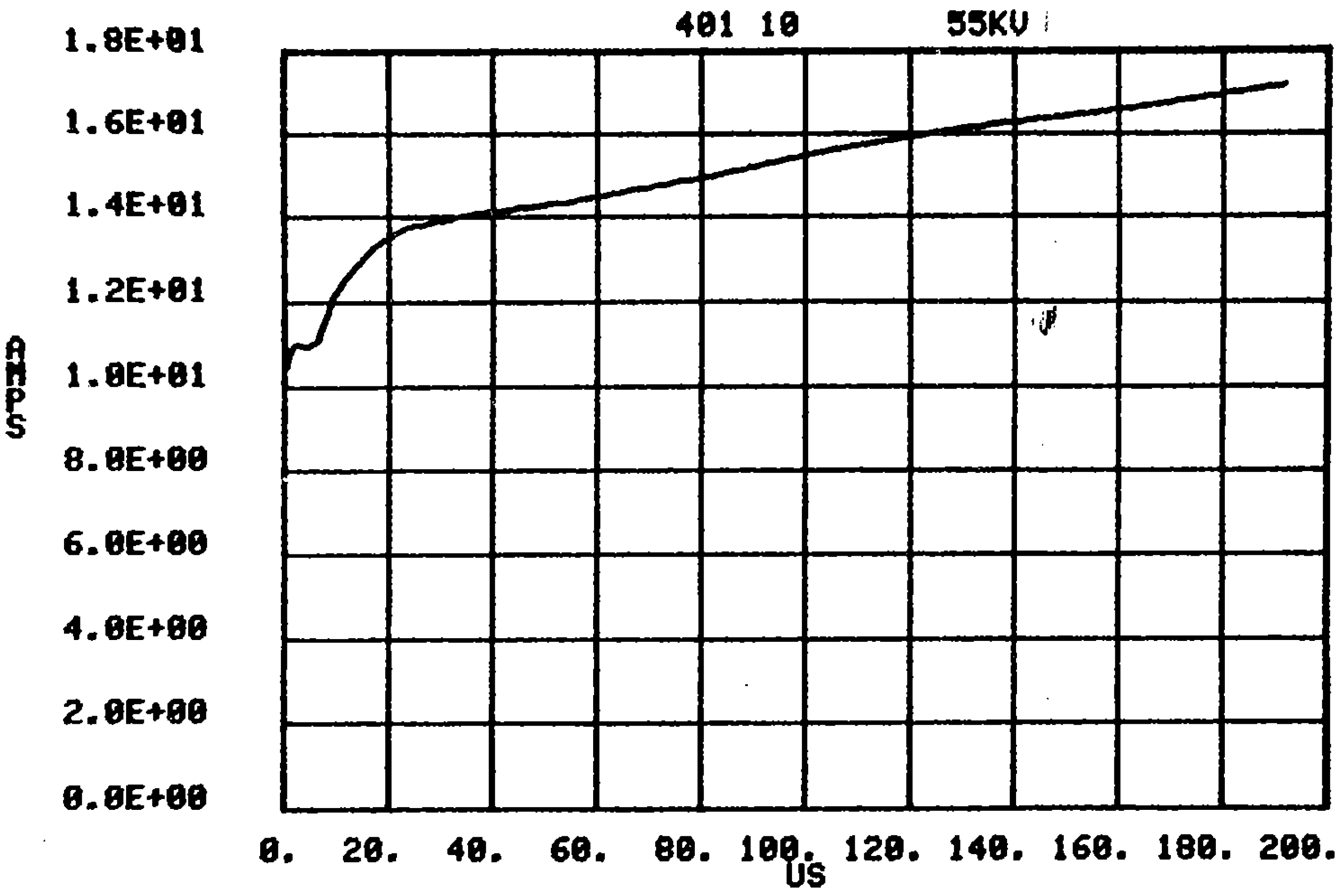

Figure B.15. 401A, .01, .5, .1, 350 sand mix; I.

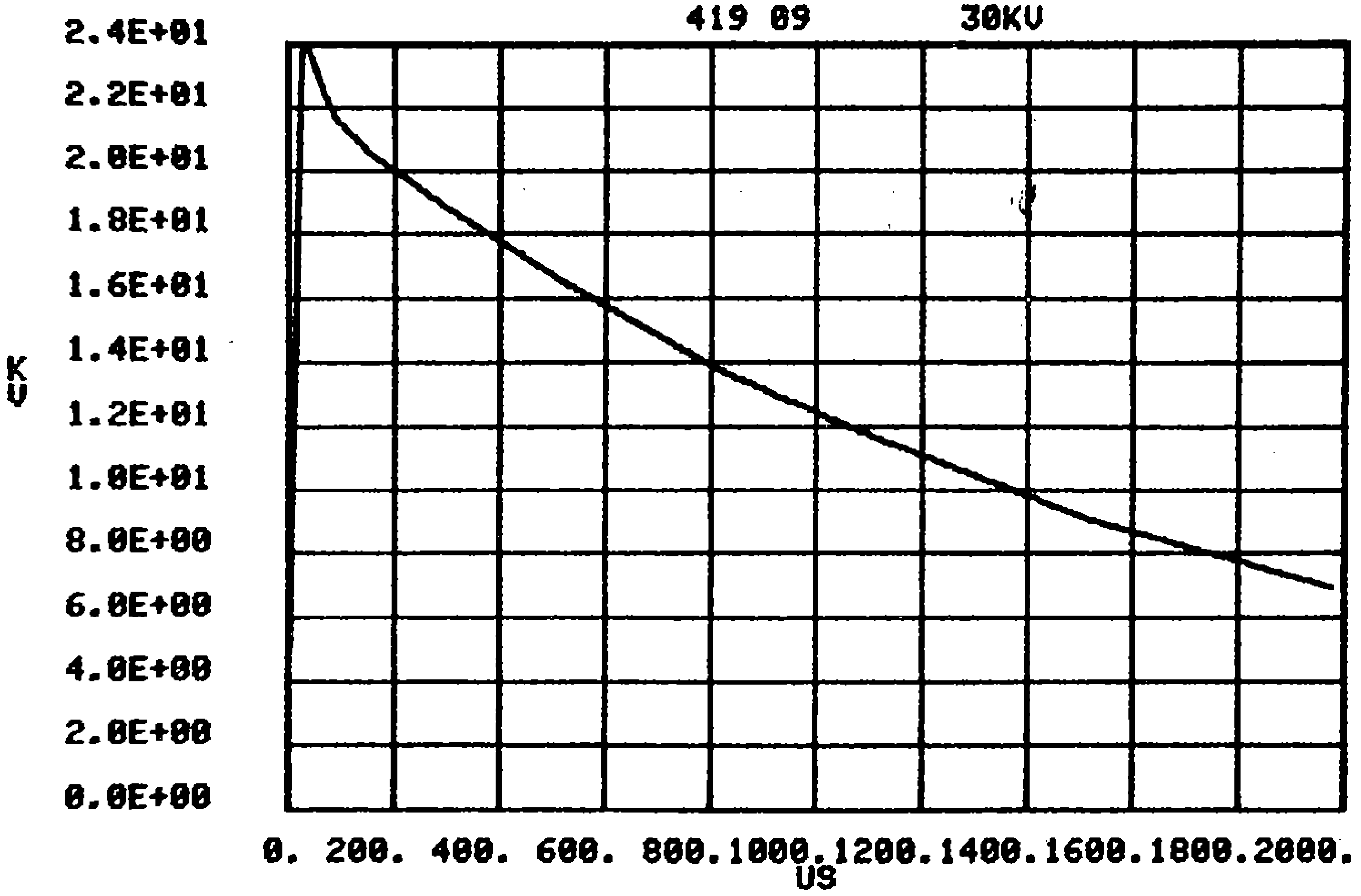

Figure B.16. 419A, .01, .5, .3, 350 sand mix; V_o.

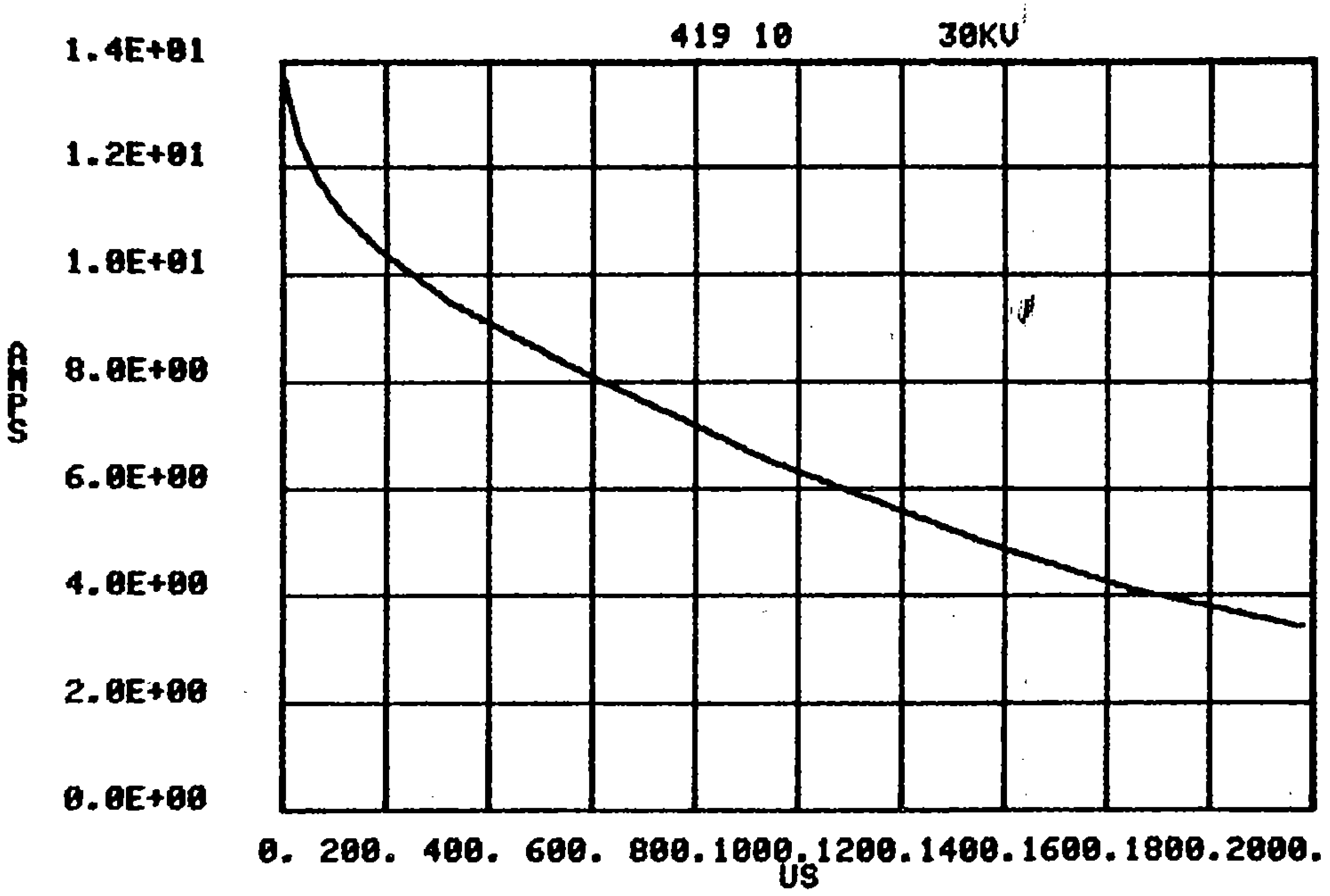

Figure B.17. 419A, .01, .5, .3, 350 sand mix; I.

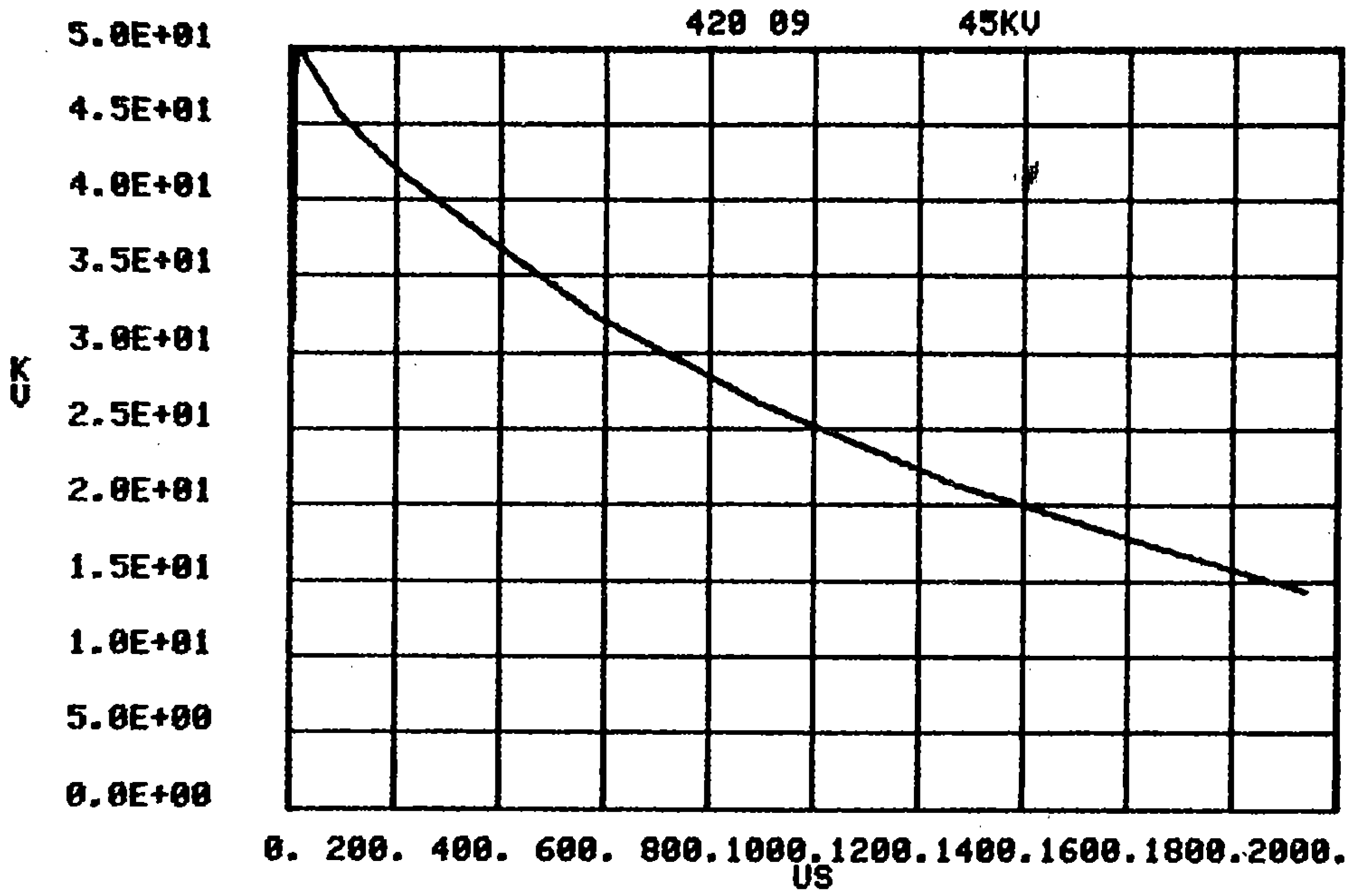

Figure B.18. 420A, .01, .5, .3, 350 sand mix; V_o.

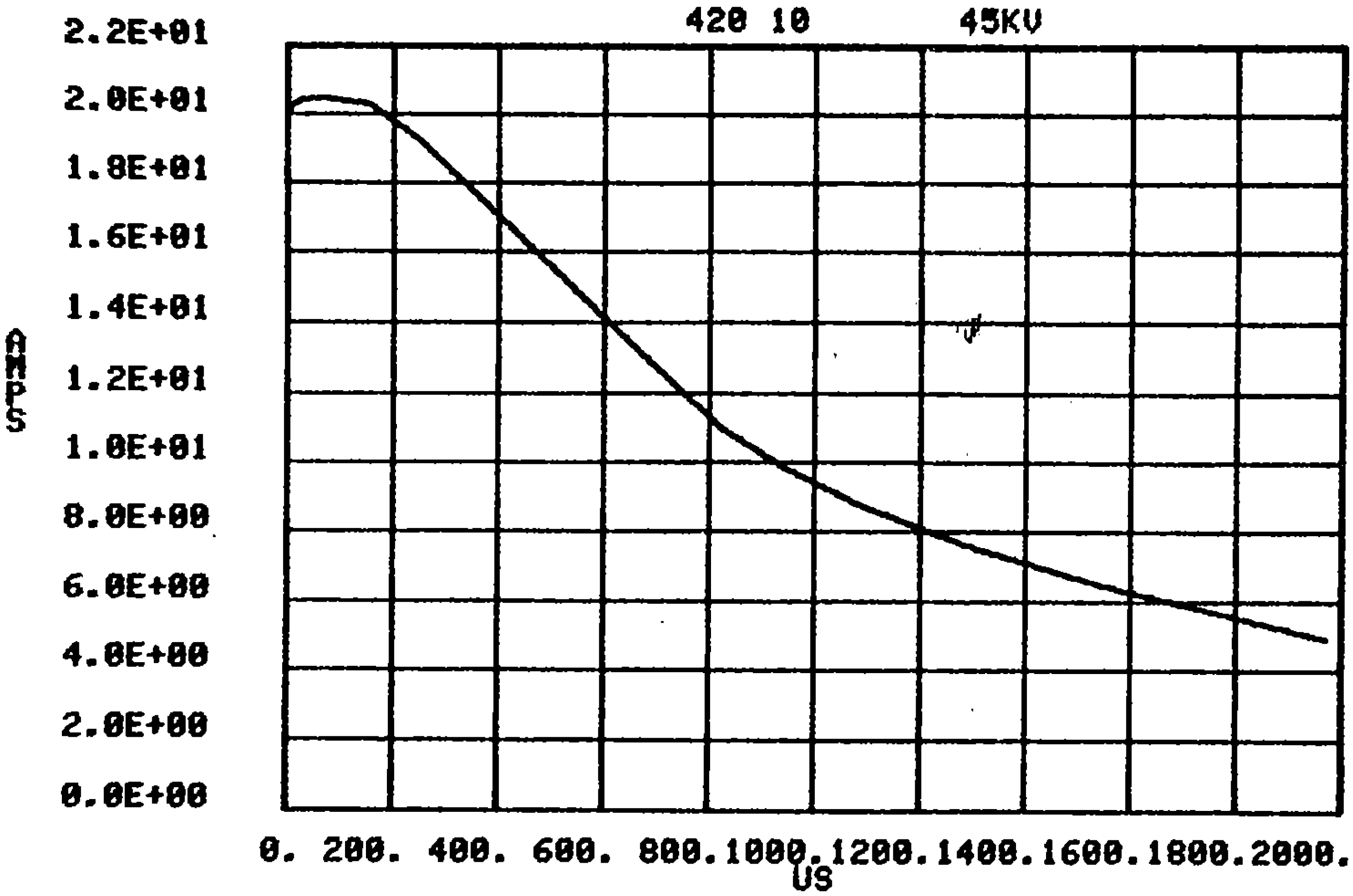

Figure B.19. 420A, .01, .5, .3, 350 sand mix; I.

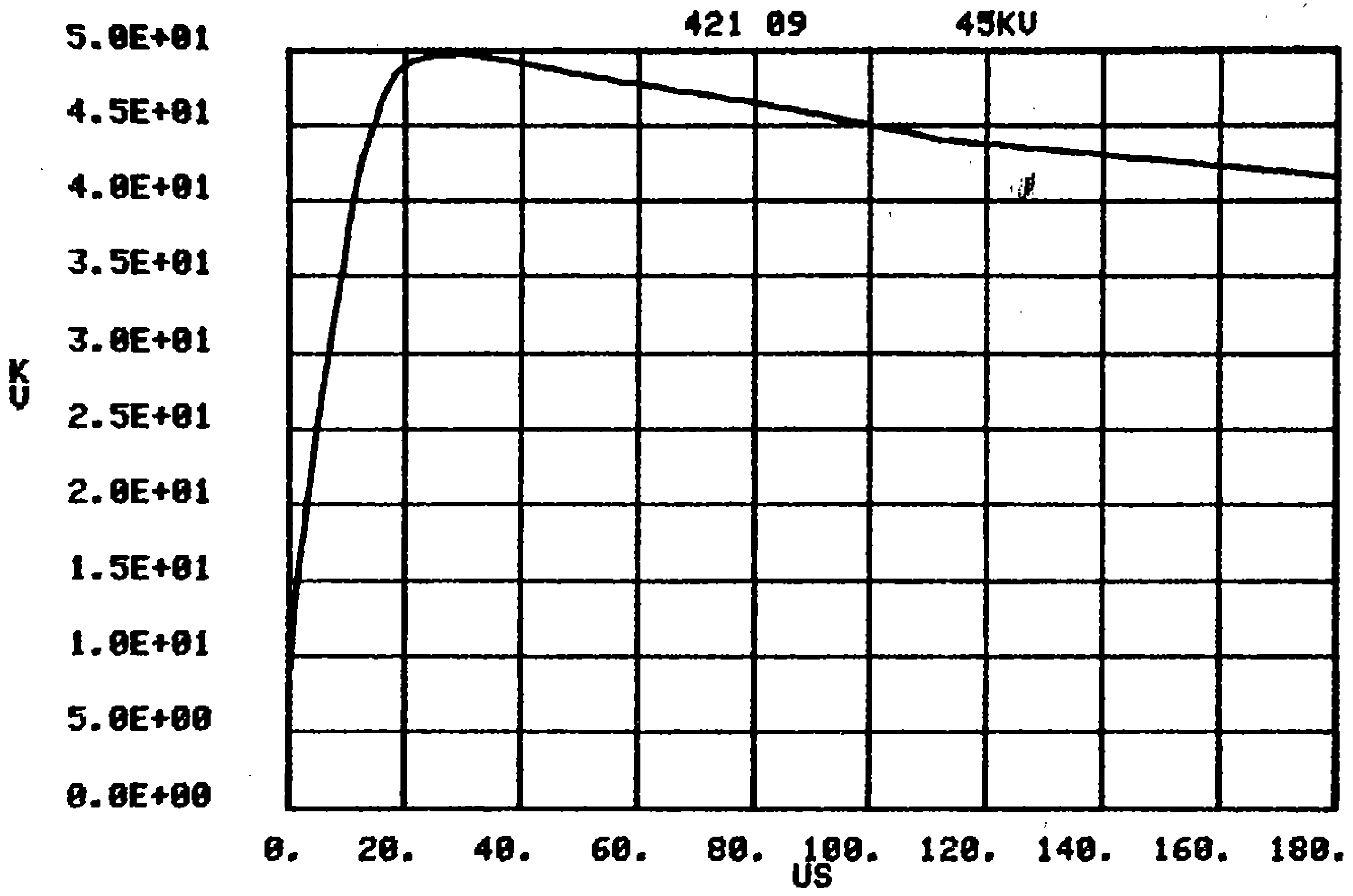

Figure B.20. 421A, .01, .5, .3, 350 sand mix; V_o.

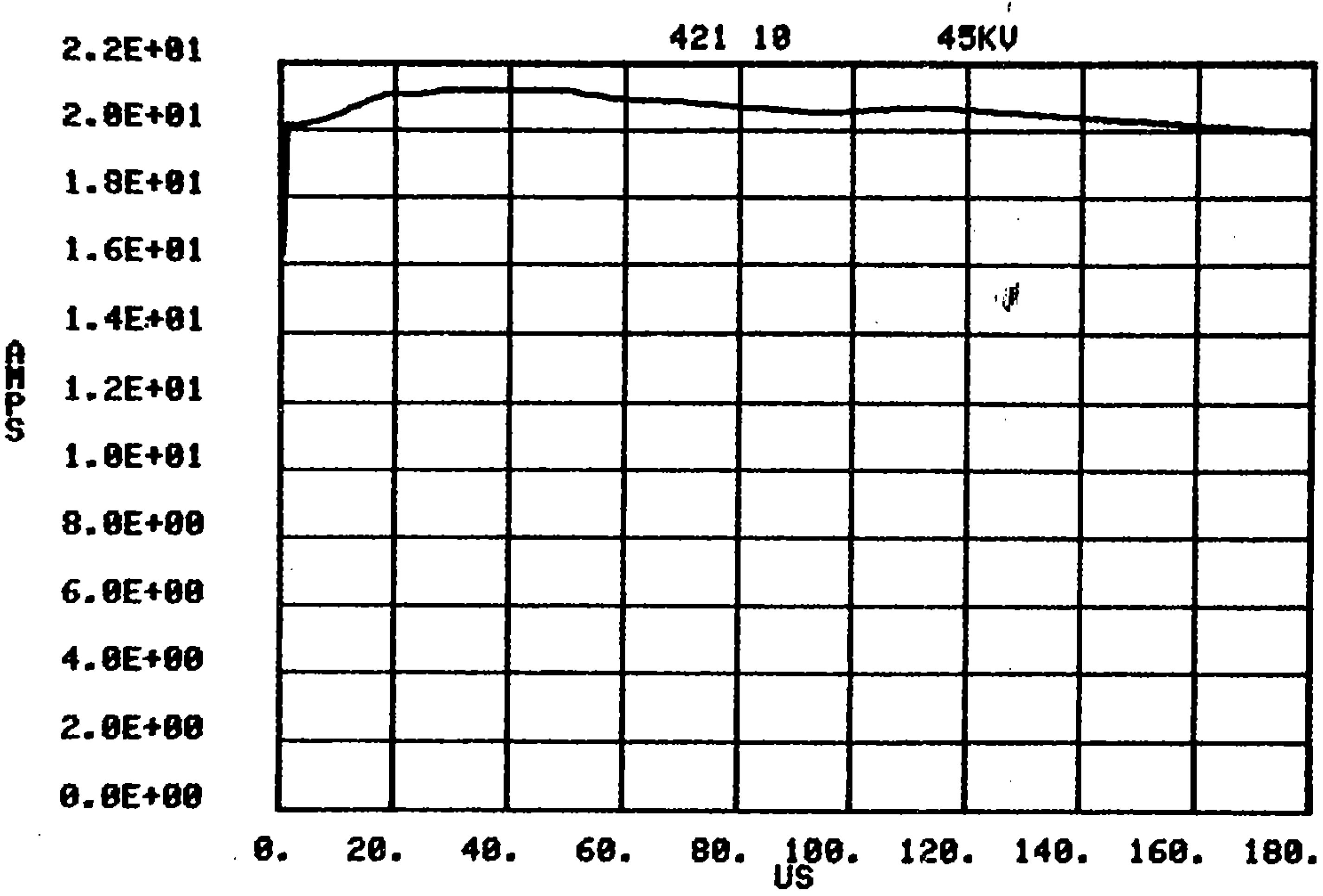

Figure B.21. 421A, .01, .5, .3, 350 sand mix; I.

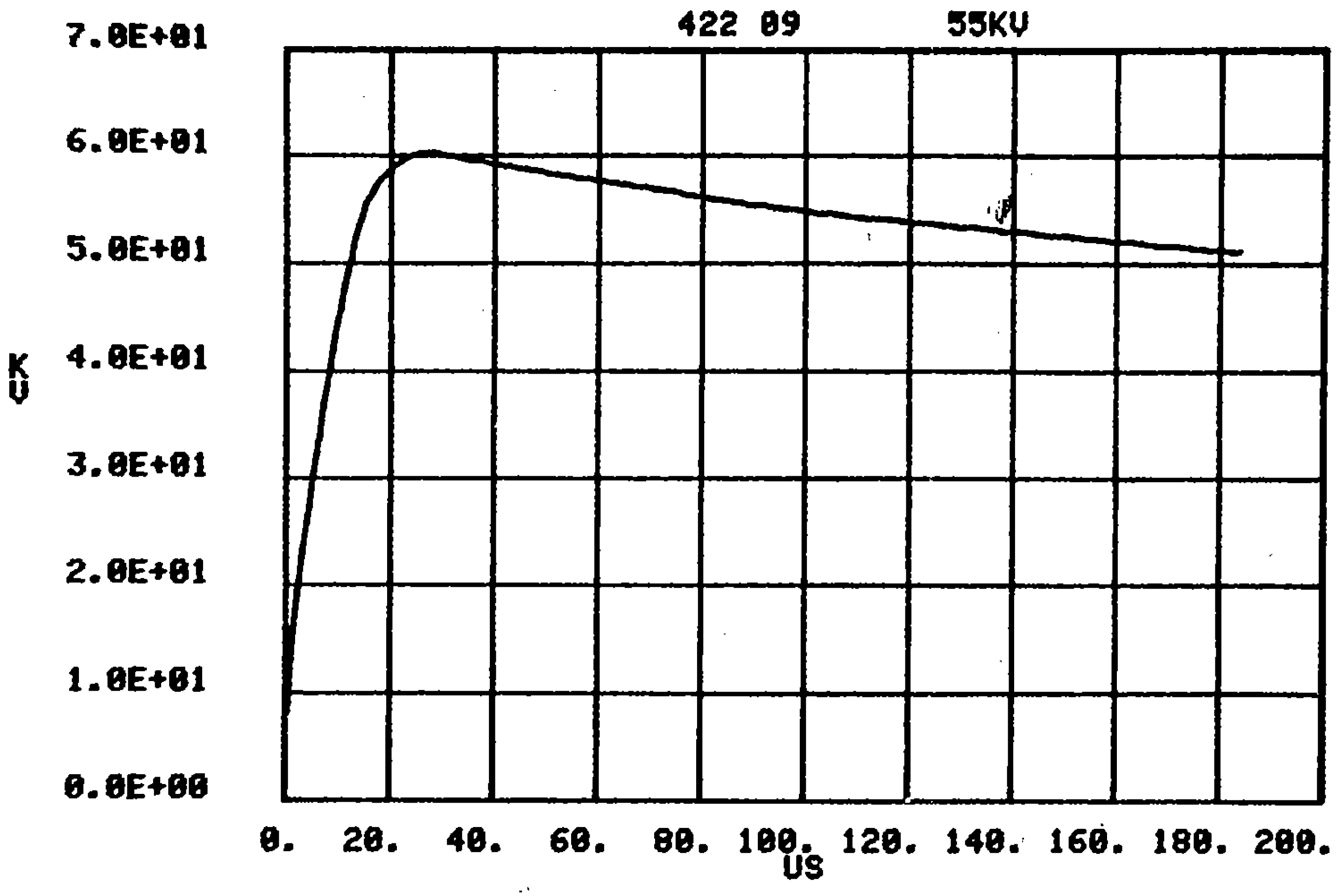

Figure B.22. 422A, .01, .5, .3, 350 sand mix; V_o.

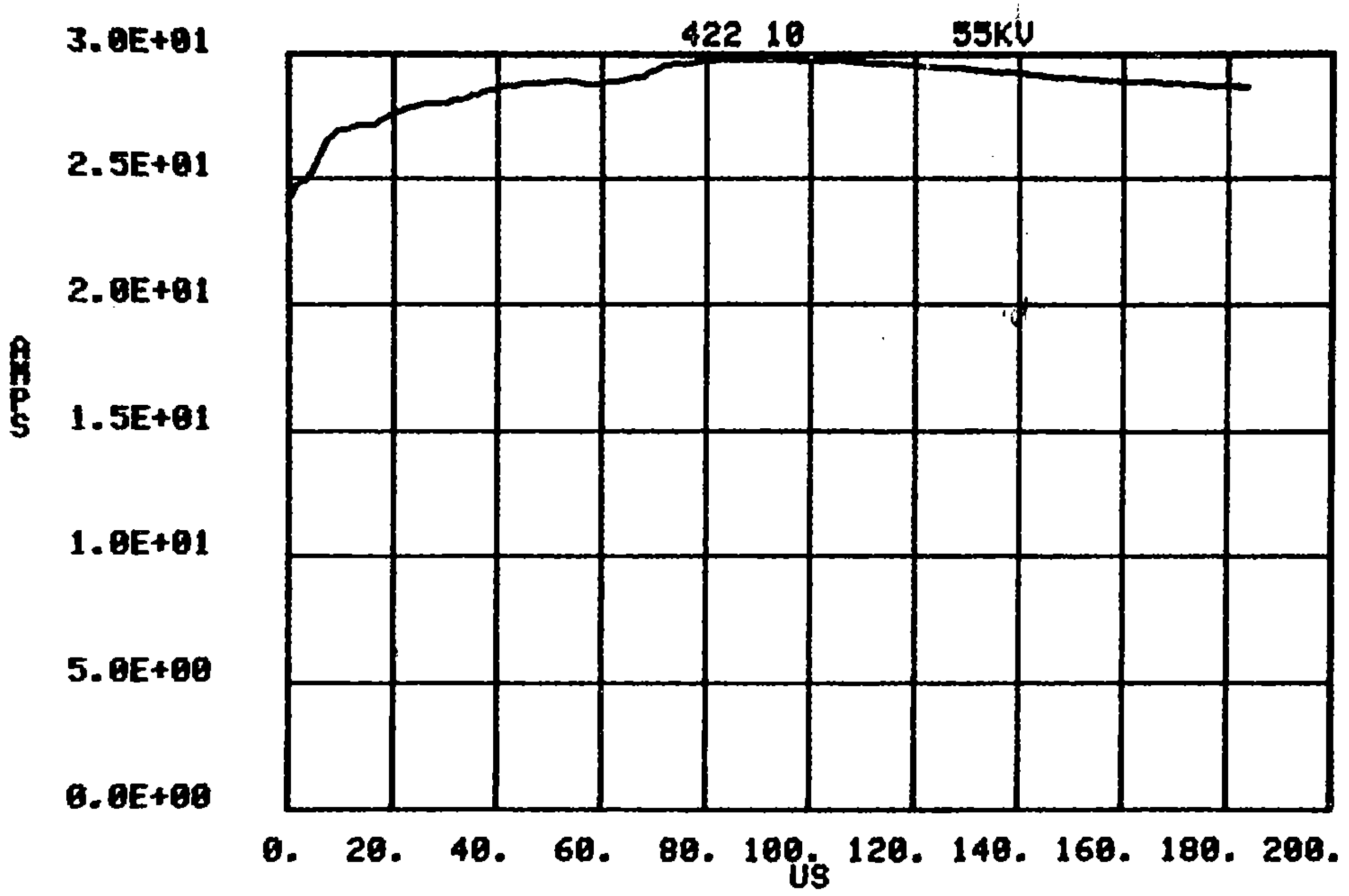

Figure B.23. 422, .01, .5, .3, 350 sand mix; I.

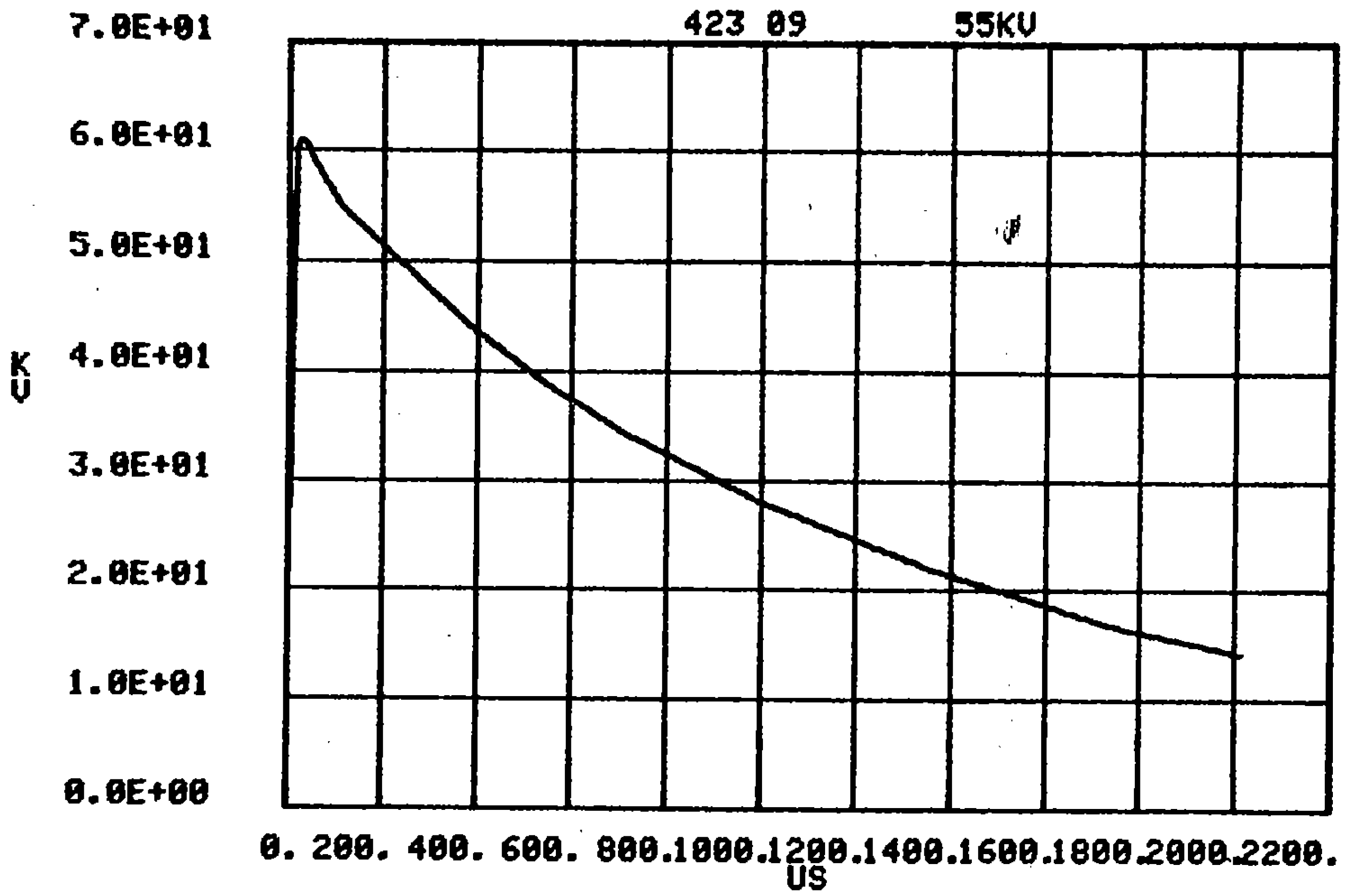

Figure B.24. 423A, .01, .5, .3, 350 sand mix; V_o.

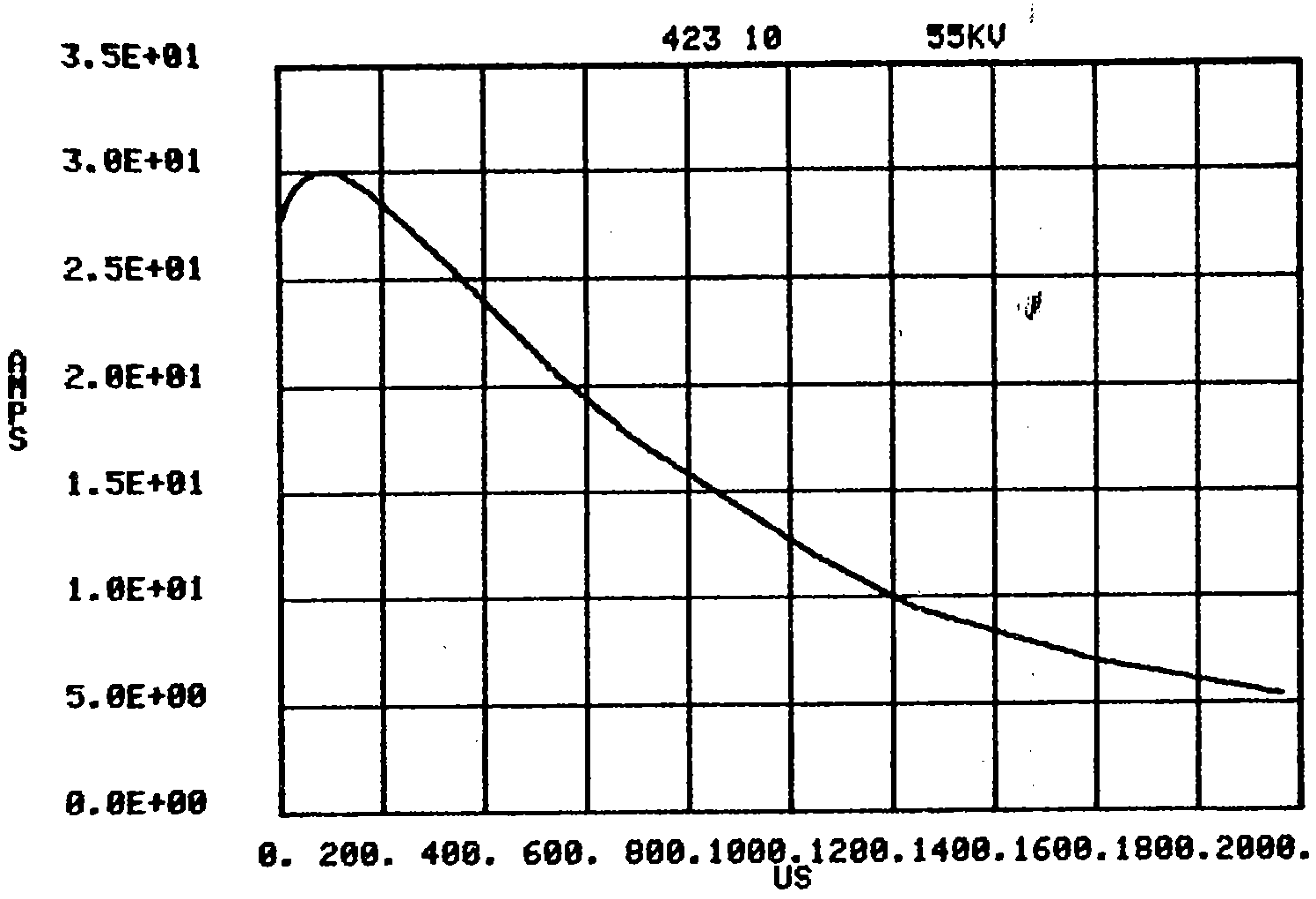

Figure B.25. 423A, .01, .5, .3, 350 sand mix; I.

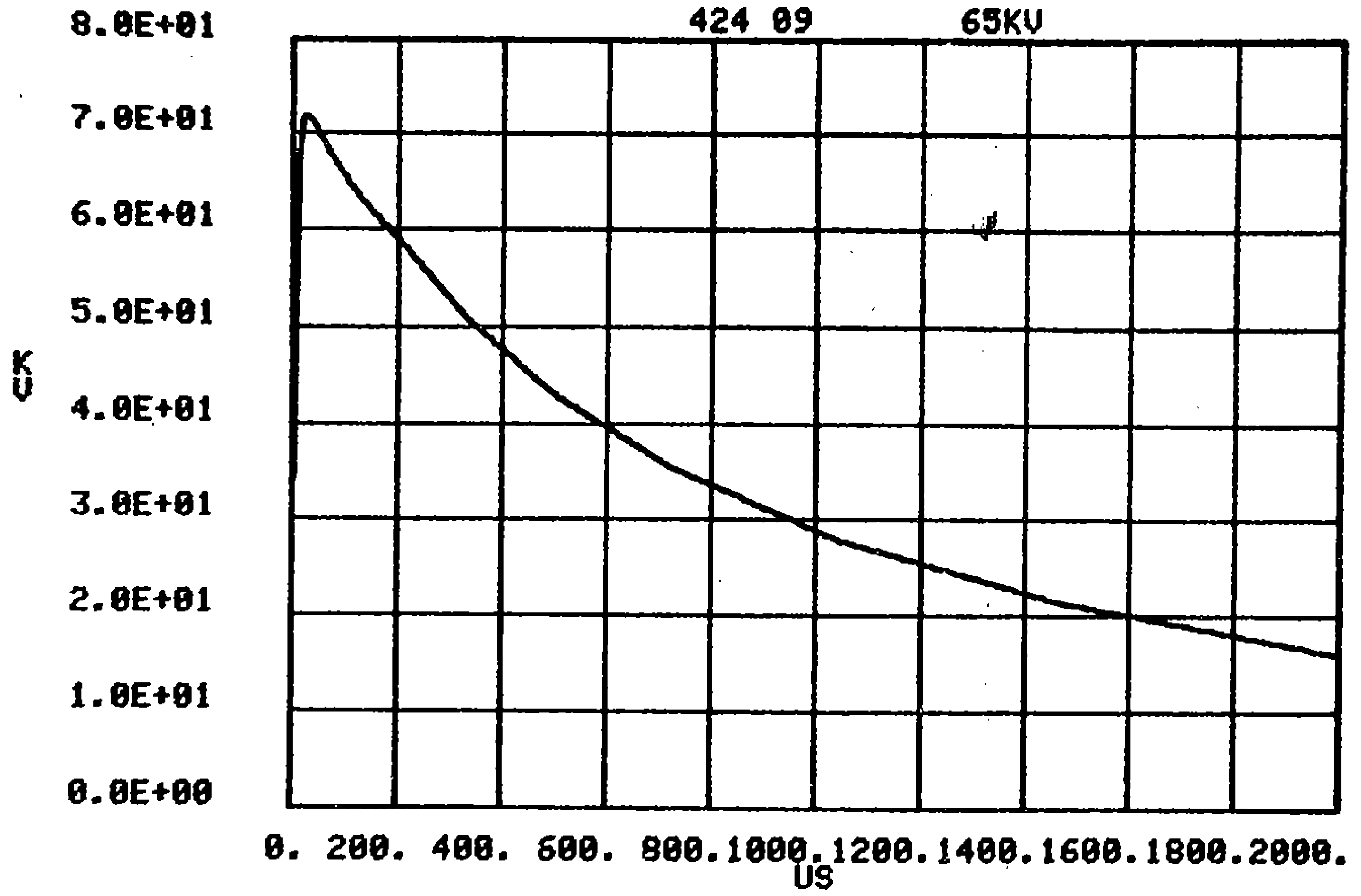

Figure B.26. 424A, .01, .5, .3, 350 sand mix; V_o.

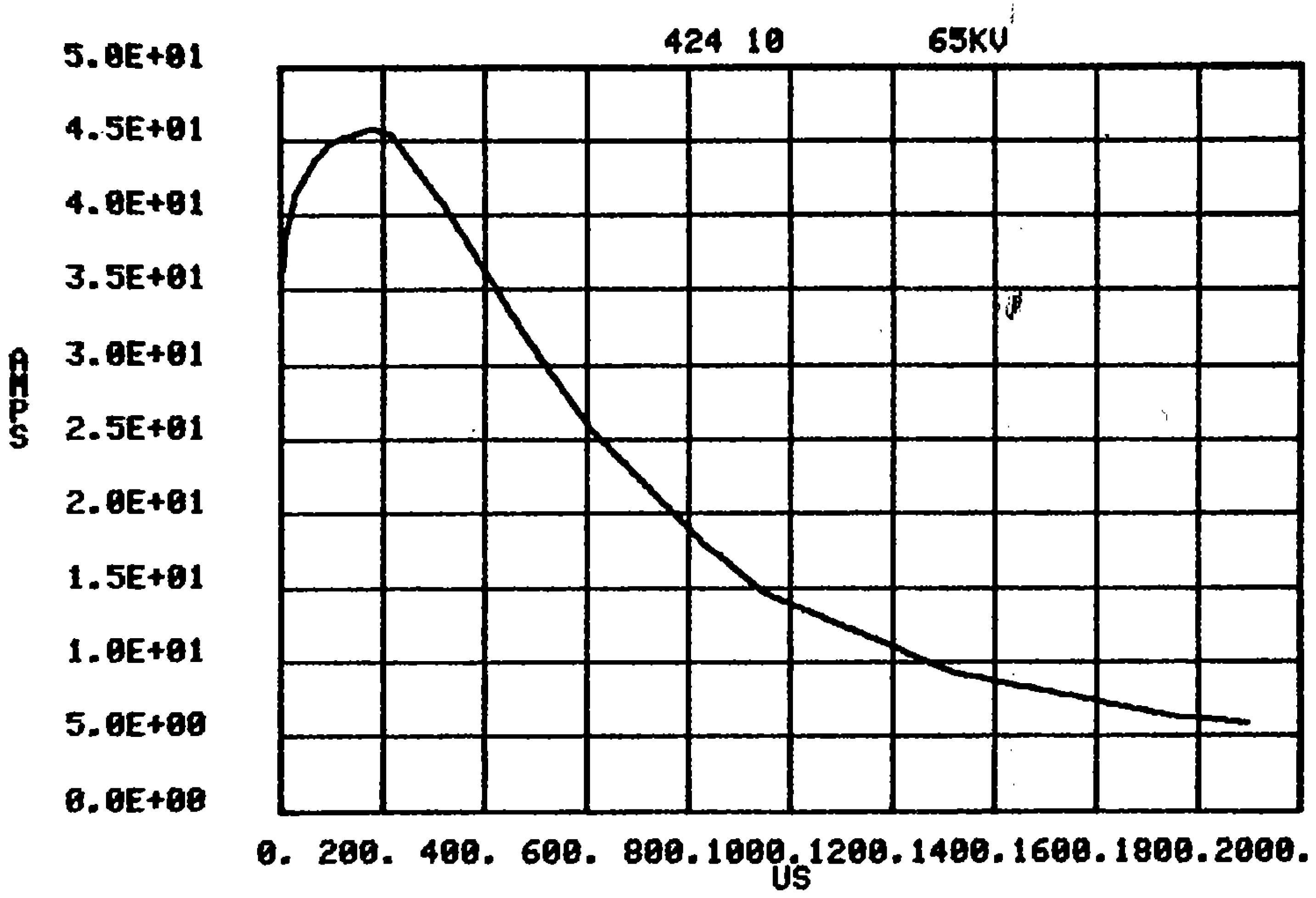

Figure B.27. 424A, .01, .5, .3, 350 sand mix; I.

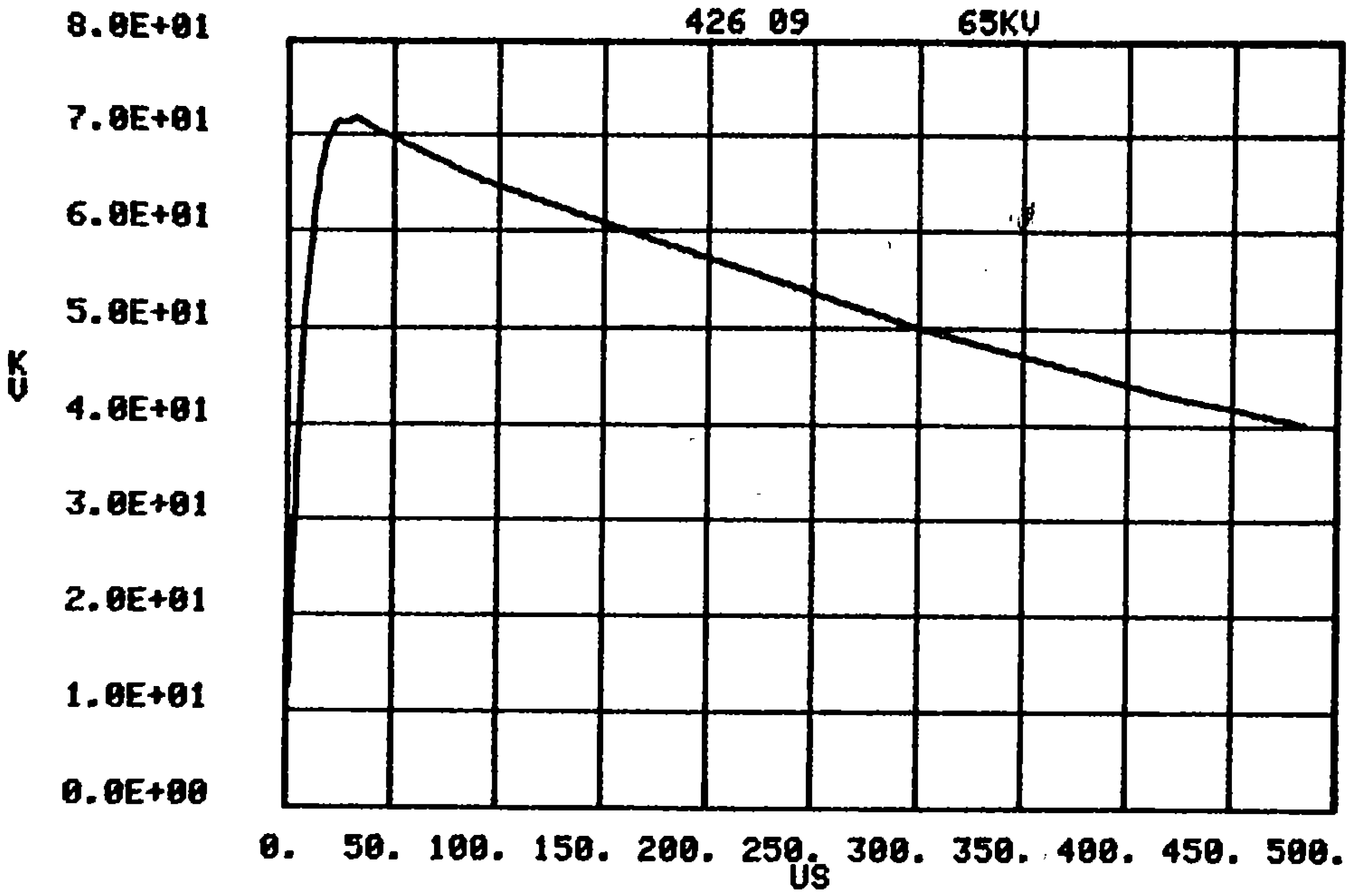

Figure B.28. 426A, .01, .5, .3, 350 sand mix; V_o.

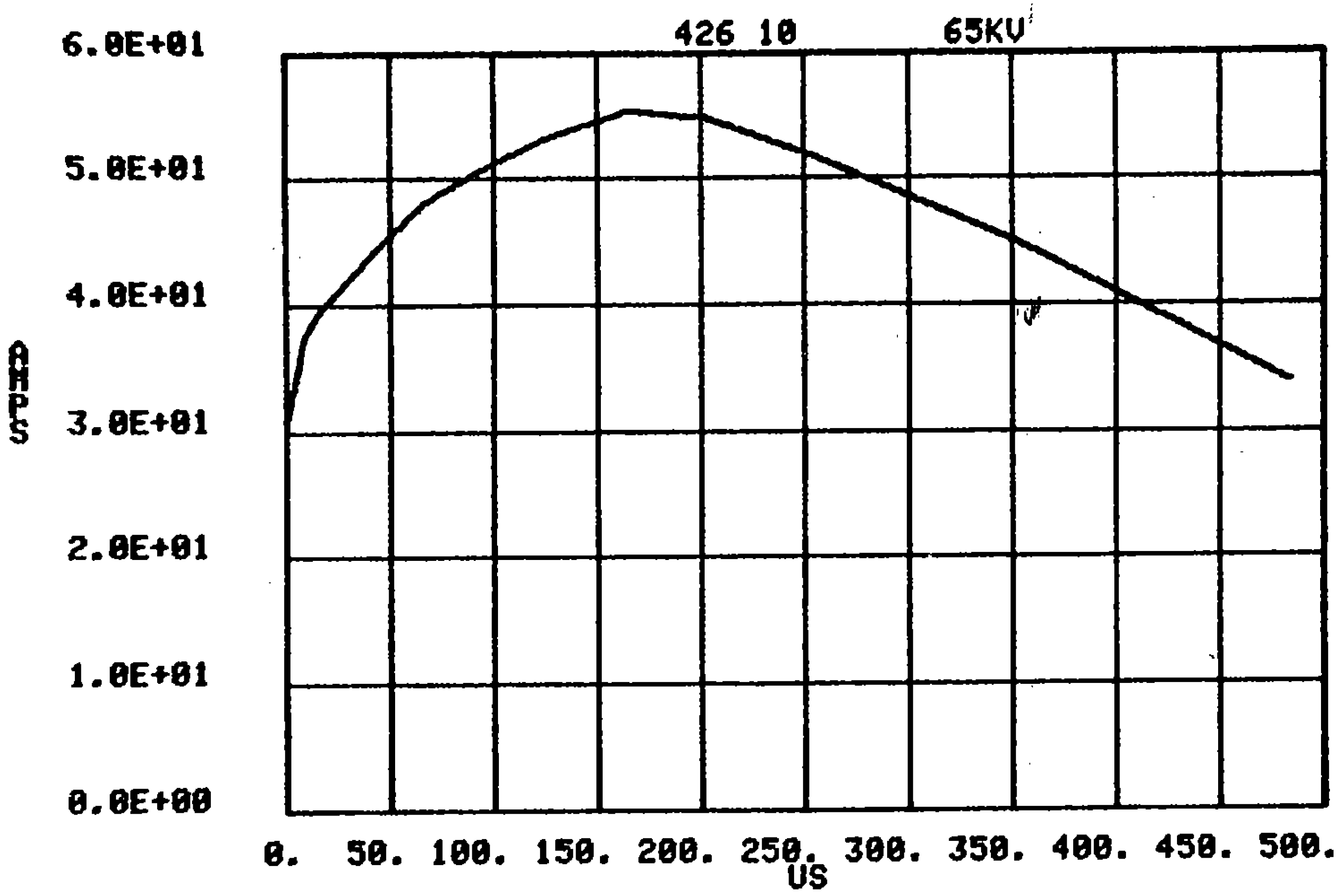

Figure B.29. 426A, .01, .5, .3, 350 sand mix; I.

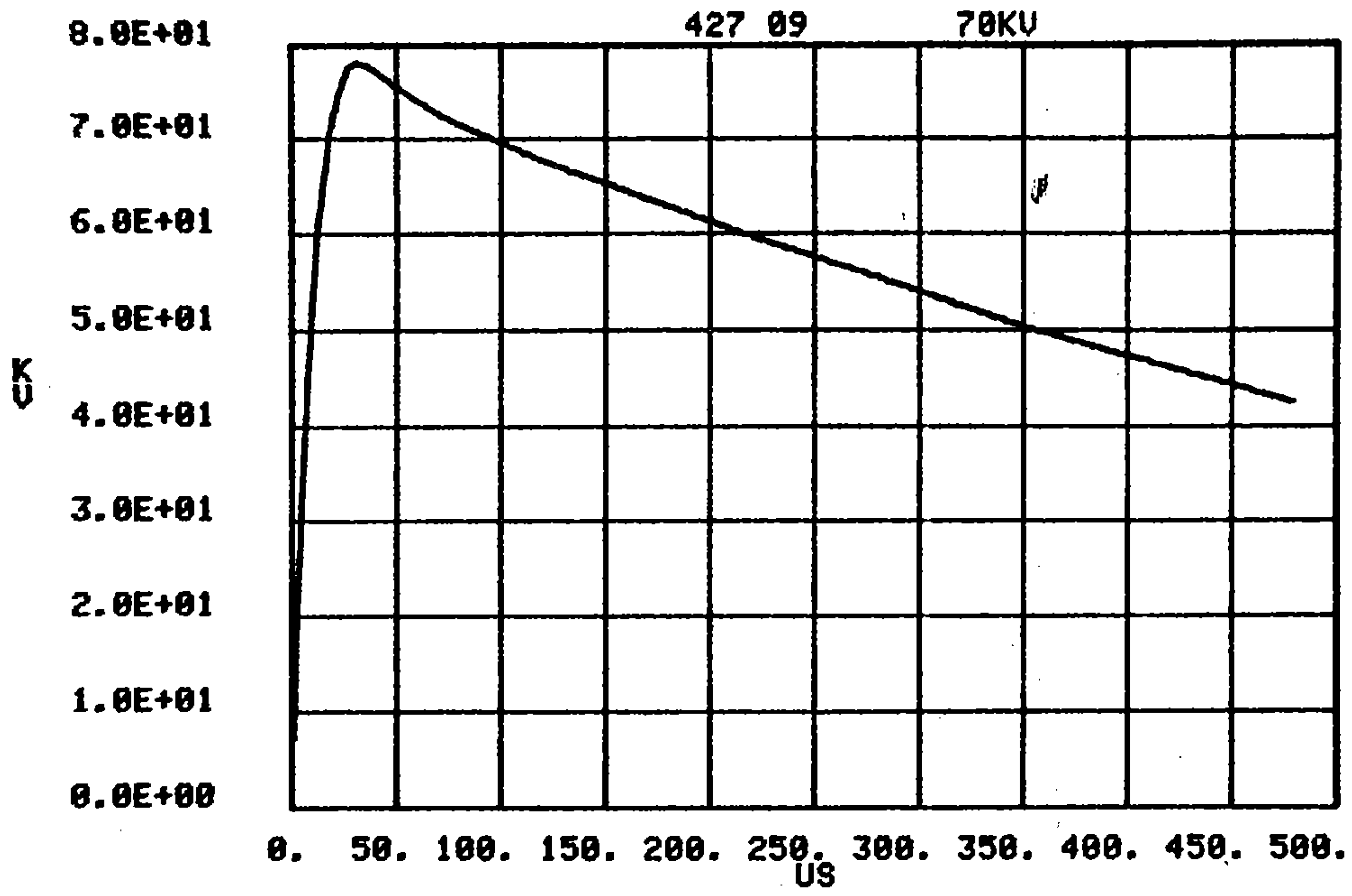

Figure B.30. 427A, .01, .5, .3, 350 sand mix; V_0.

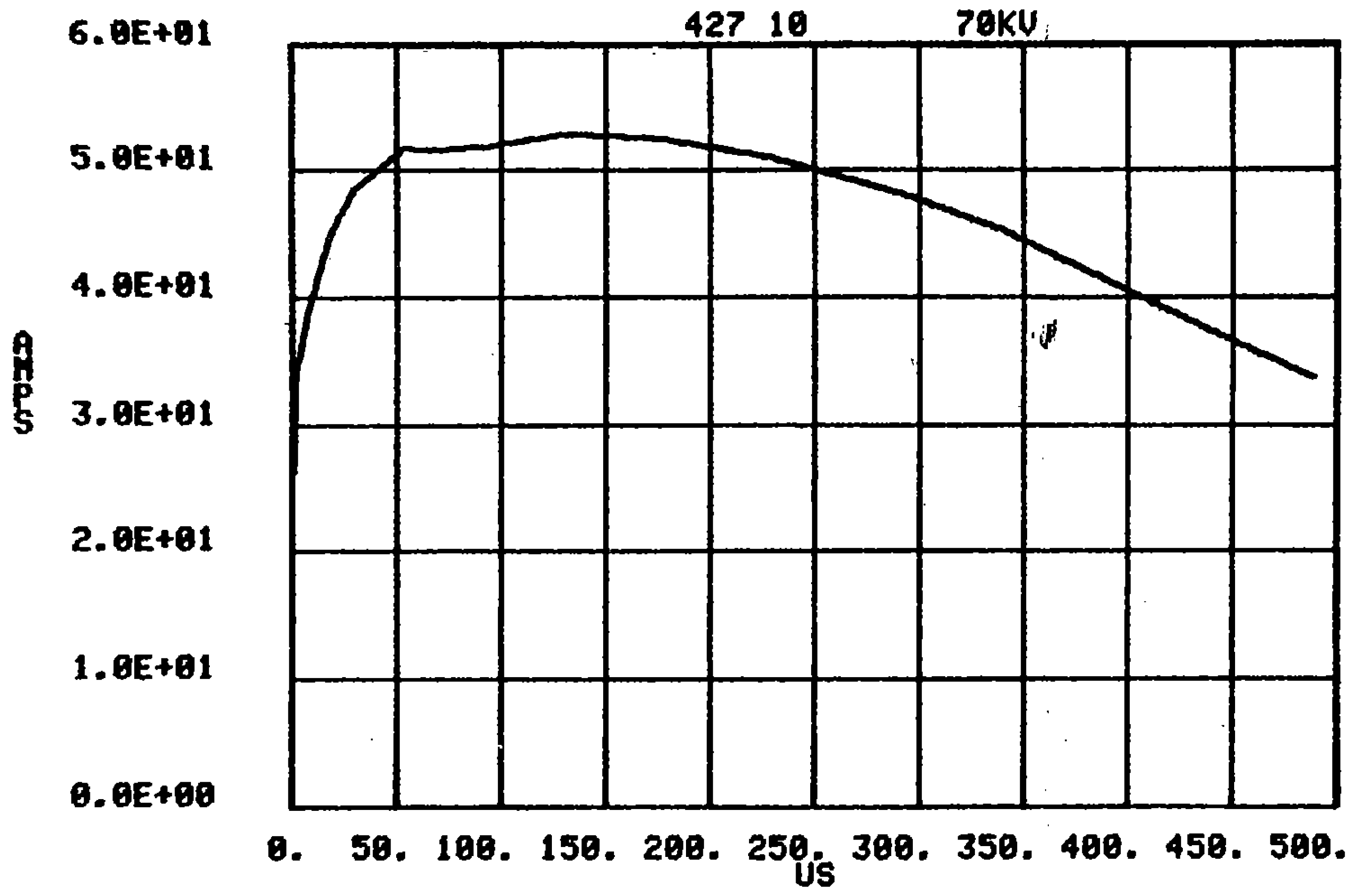

Figure B.31. 427A, .01, .5, .3, 350 sand mix; I.

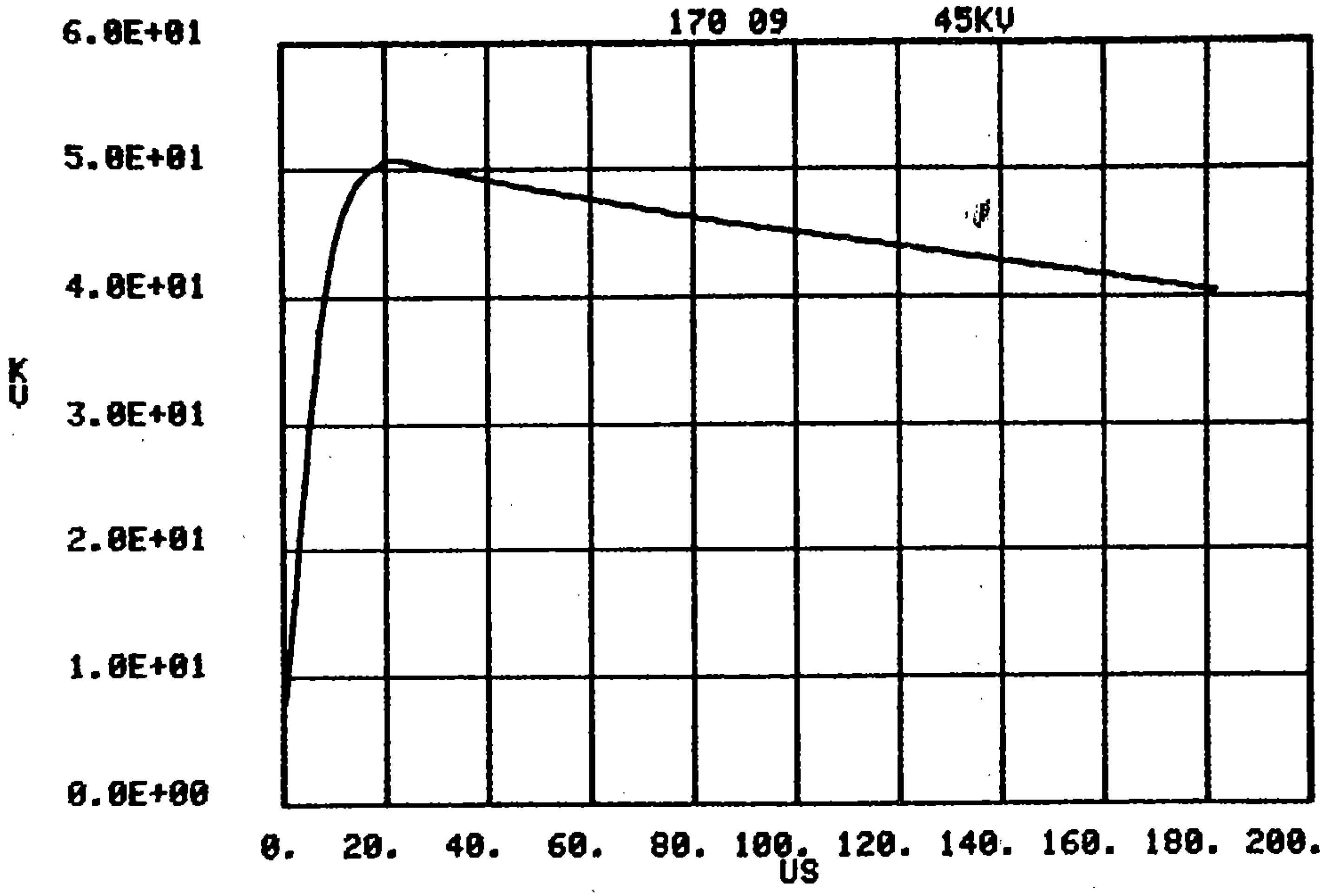

Figure B.32. 170A, .01, .5, .1, 200 sand; V_o.

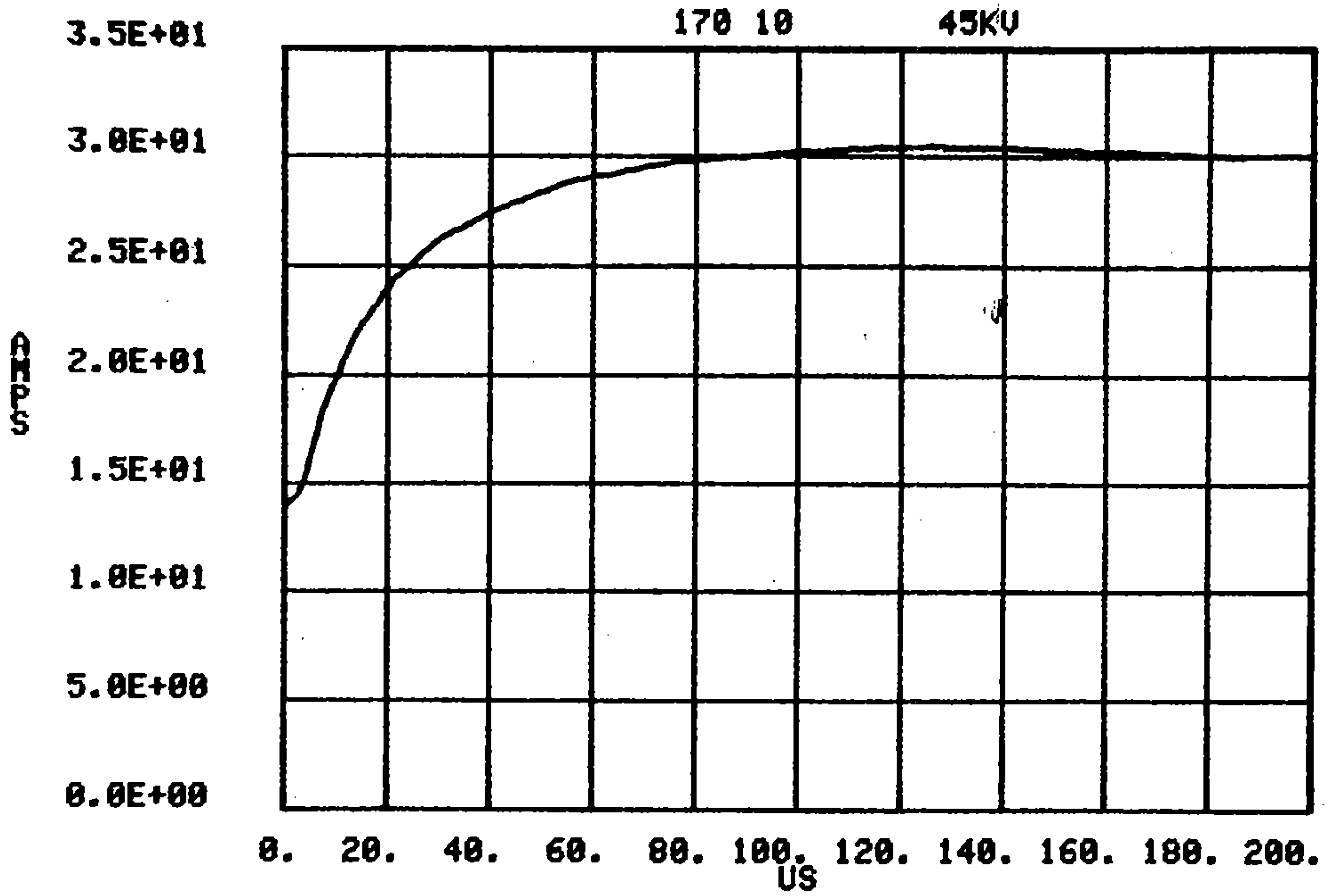

Figure B.33. 170A, .01, .5, .1, 200 sand; I.

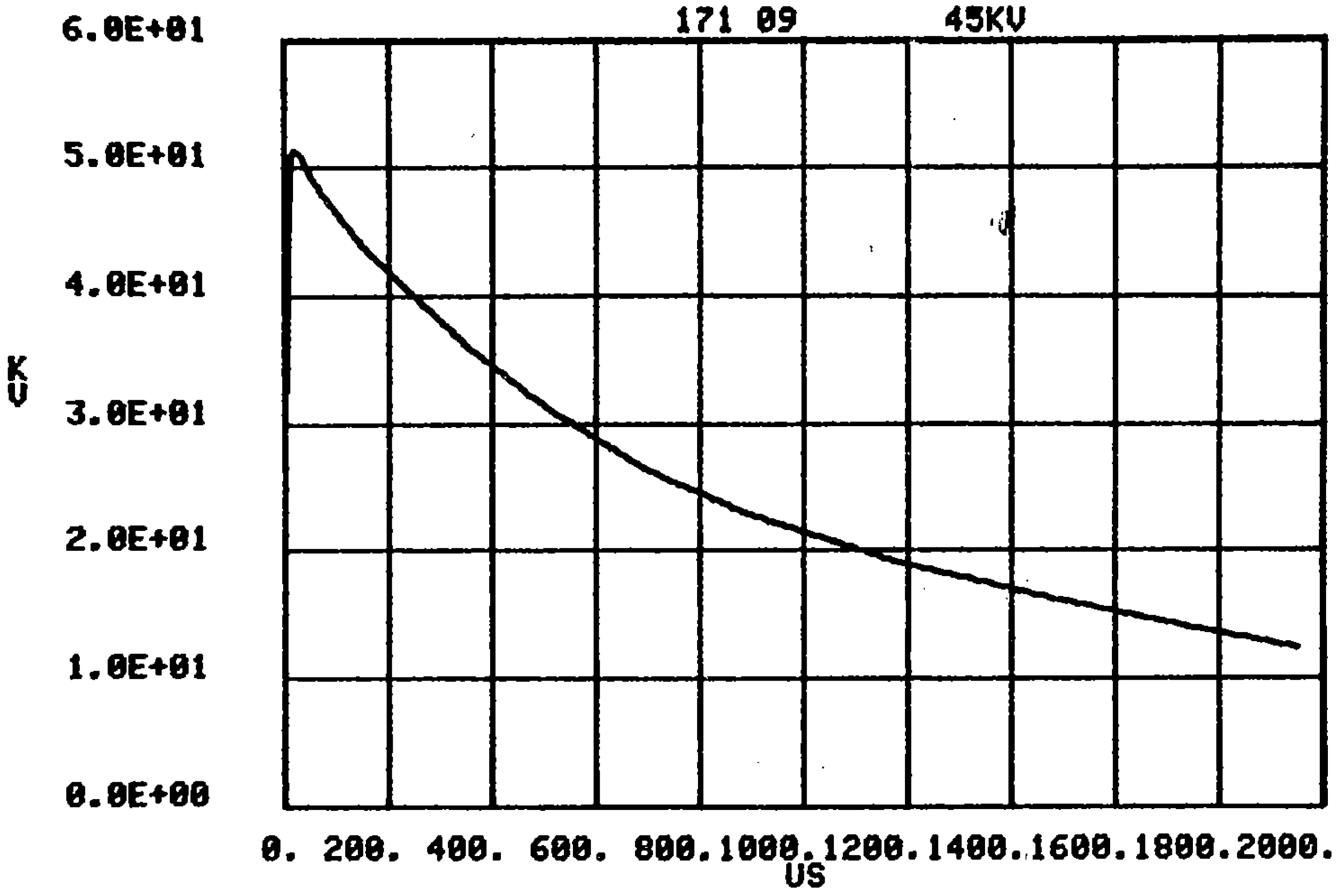

Figure B.34. 171A, .01, .5, .1, 200 sand; V_o.

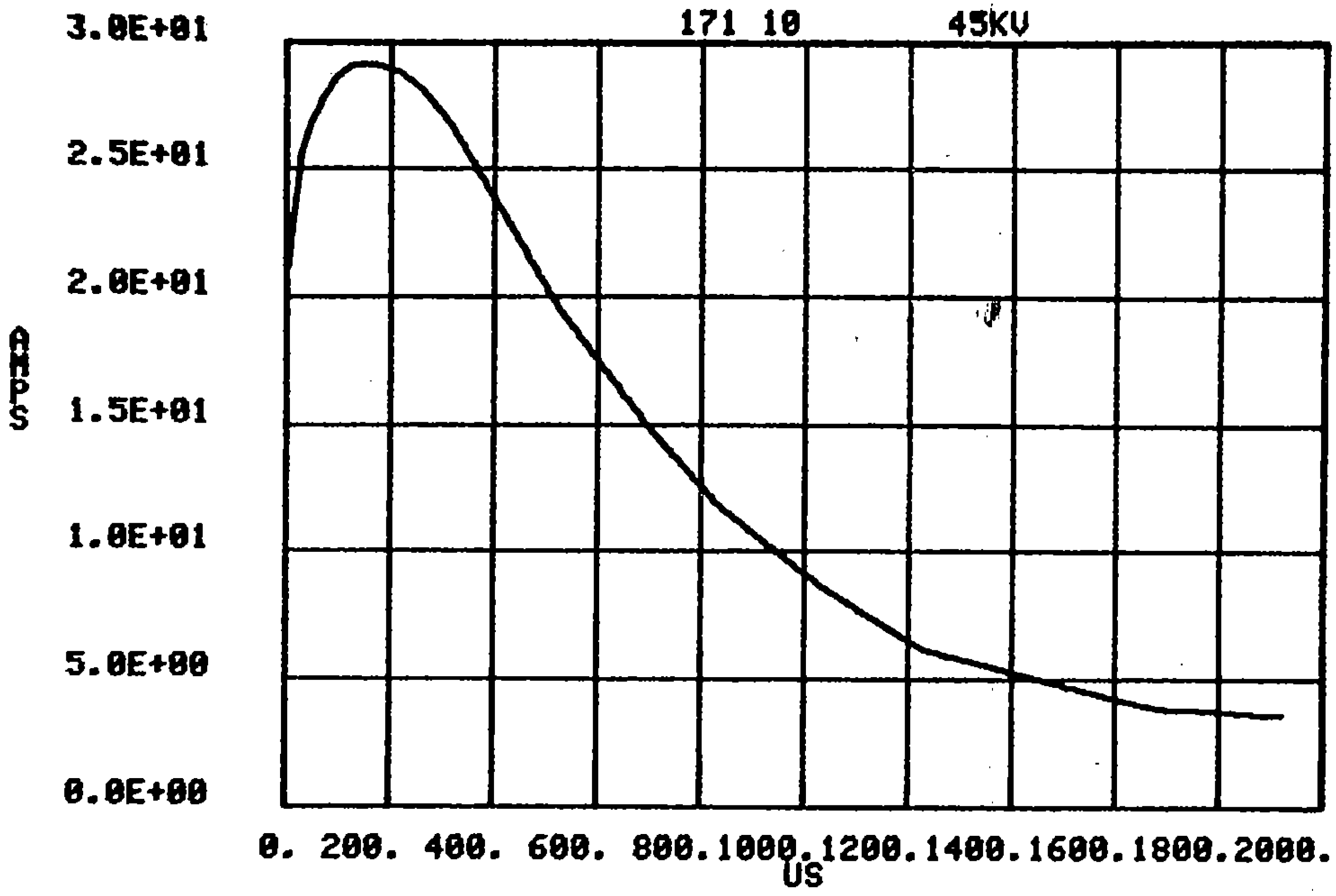

Figure B.35. 171A, .01, .5, .1, 200 sand; I.

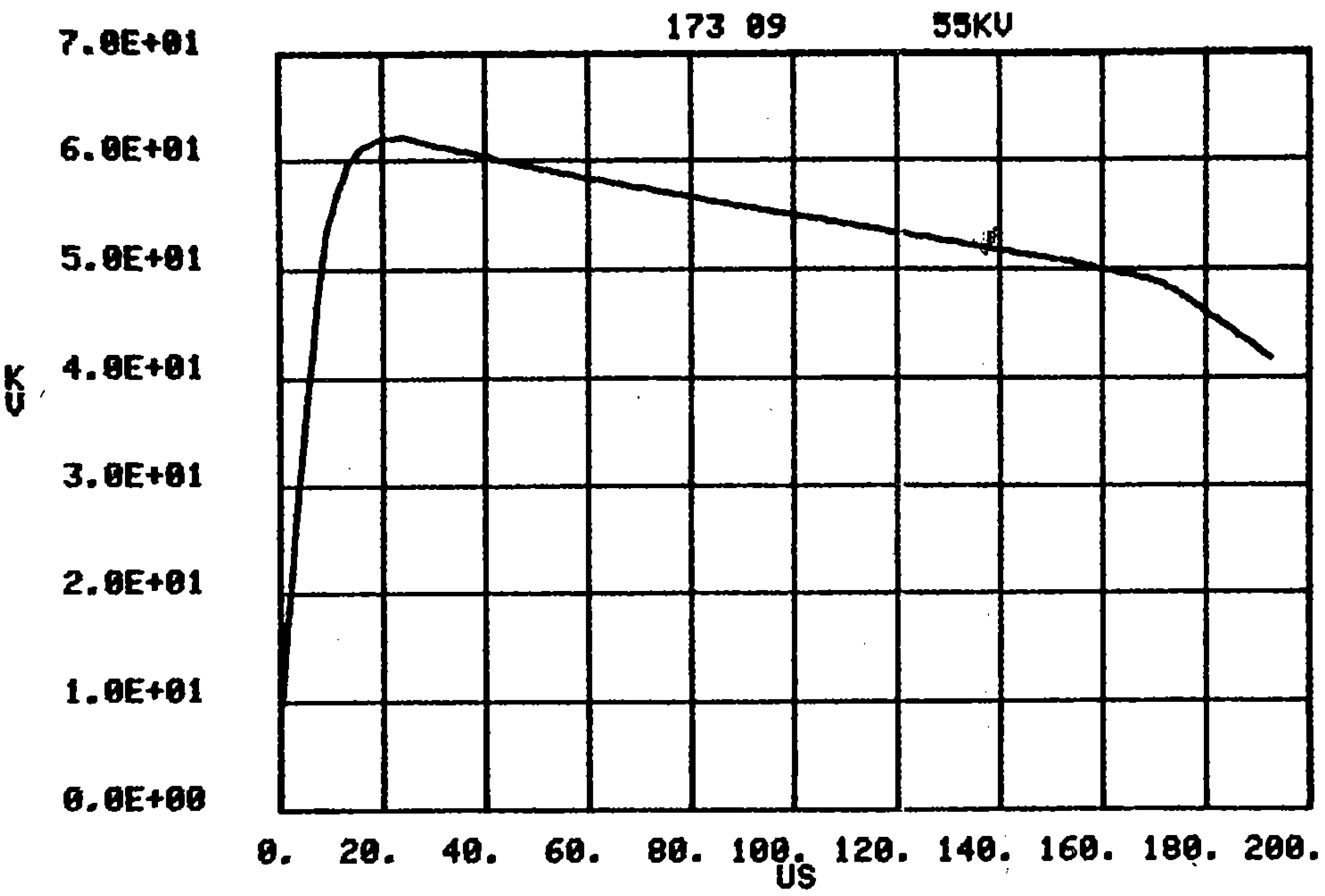

Figure B.36. 173A, .01, .5, .1, 200 sand; V_o.

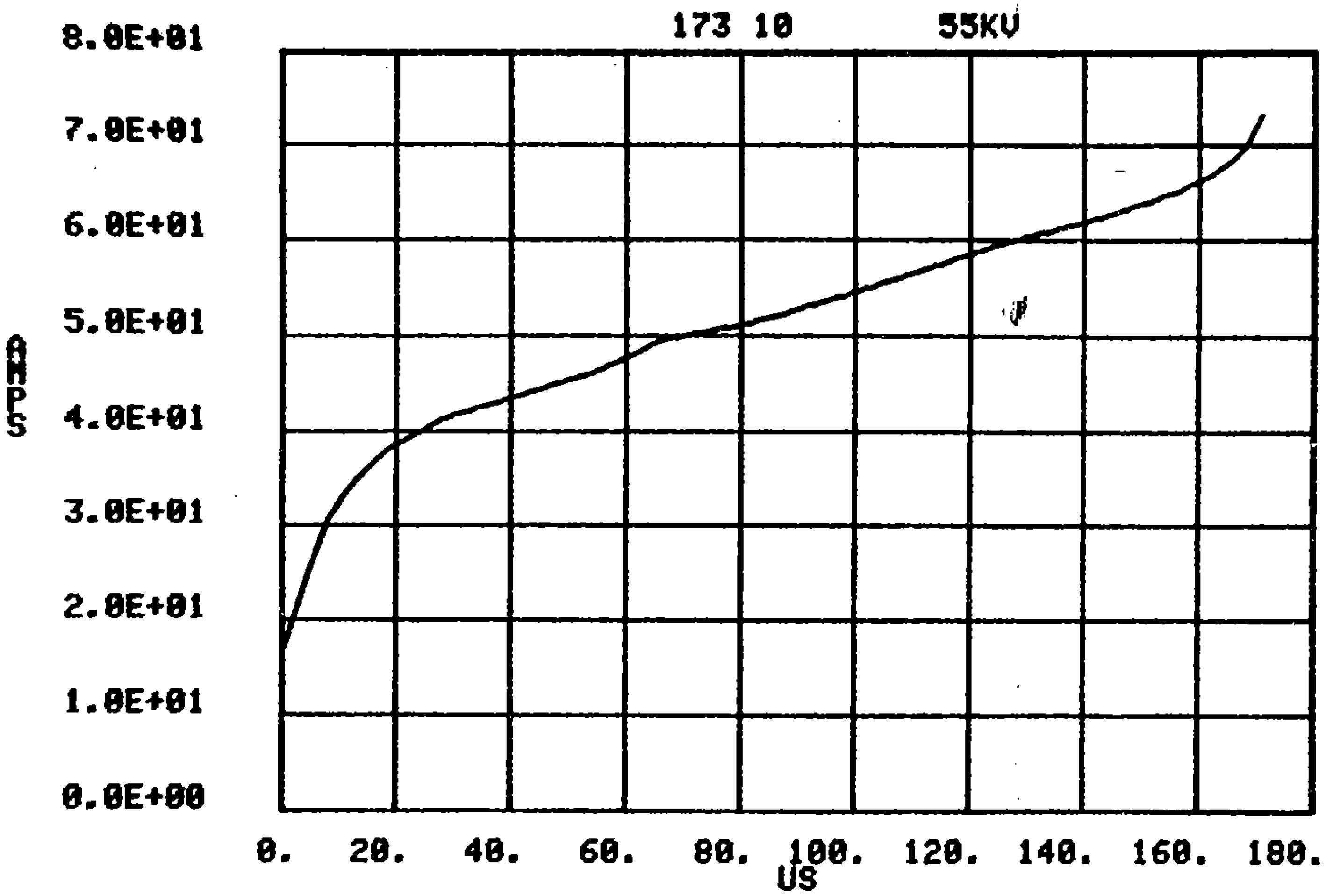

Figure B.37. 173A, .01, .5, .1, 200 sand; I.

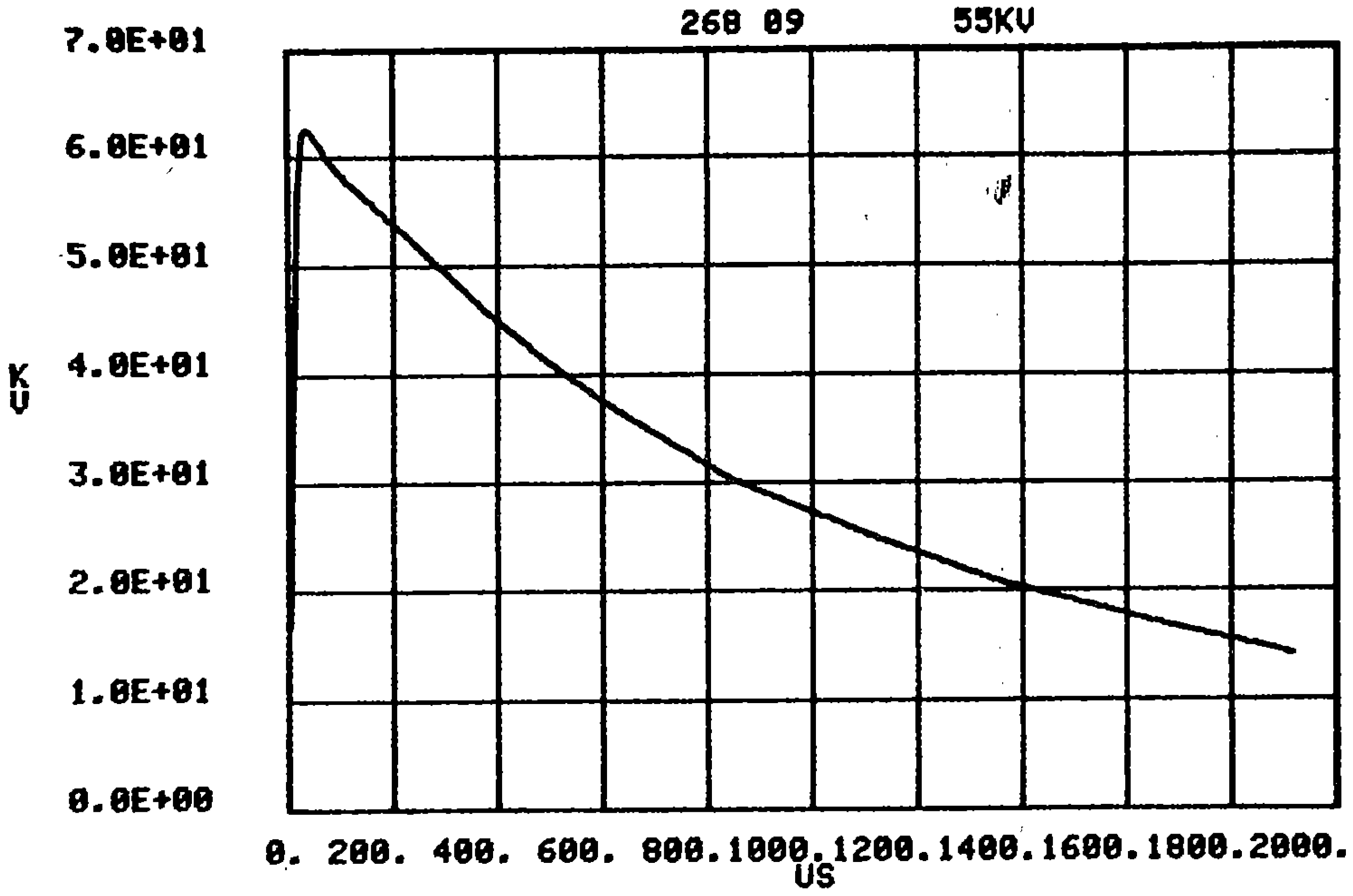

Figure B.38. 268A, .01, .5, .1, 170 MX-B; V_o.

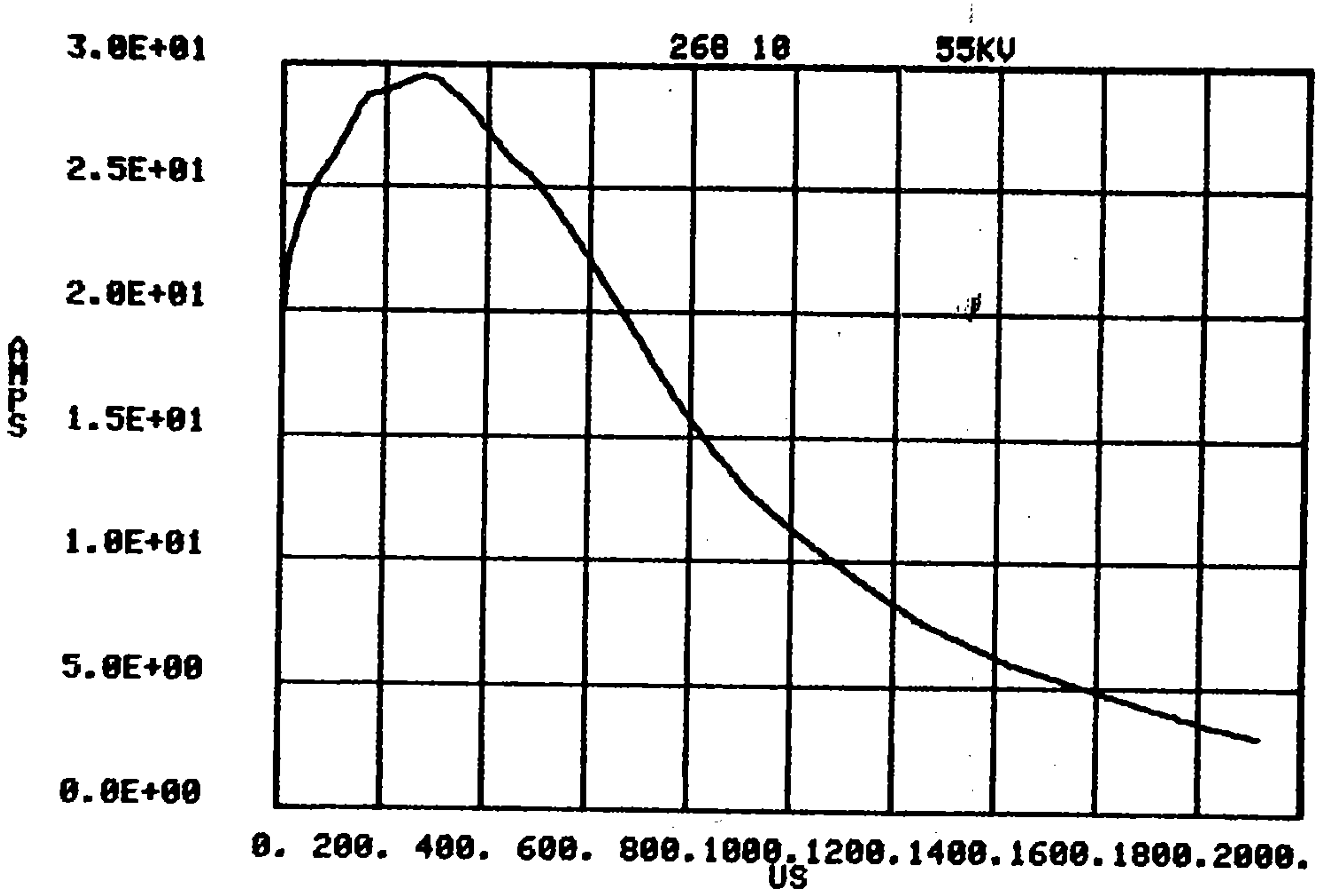

Figure B.39. 268A, .01, .5, .1, 170 MX-B; I.

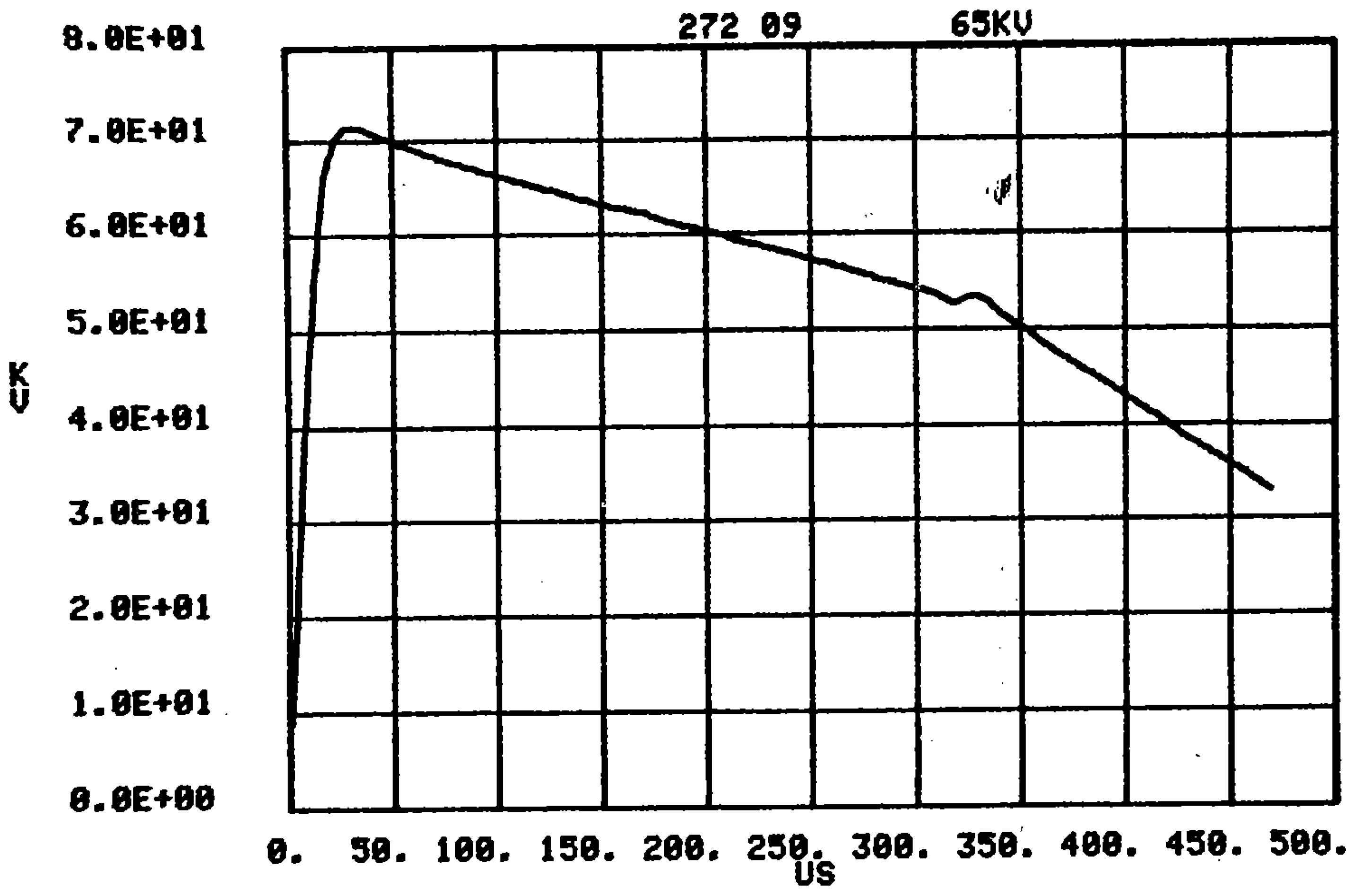

Figure B.40. 272A, .01, .5, .1, 170 MX-B; V_0.

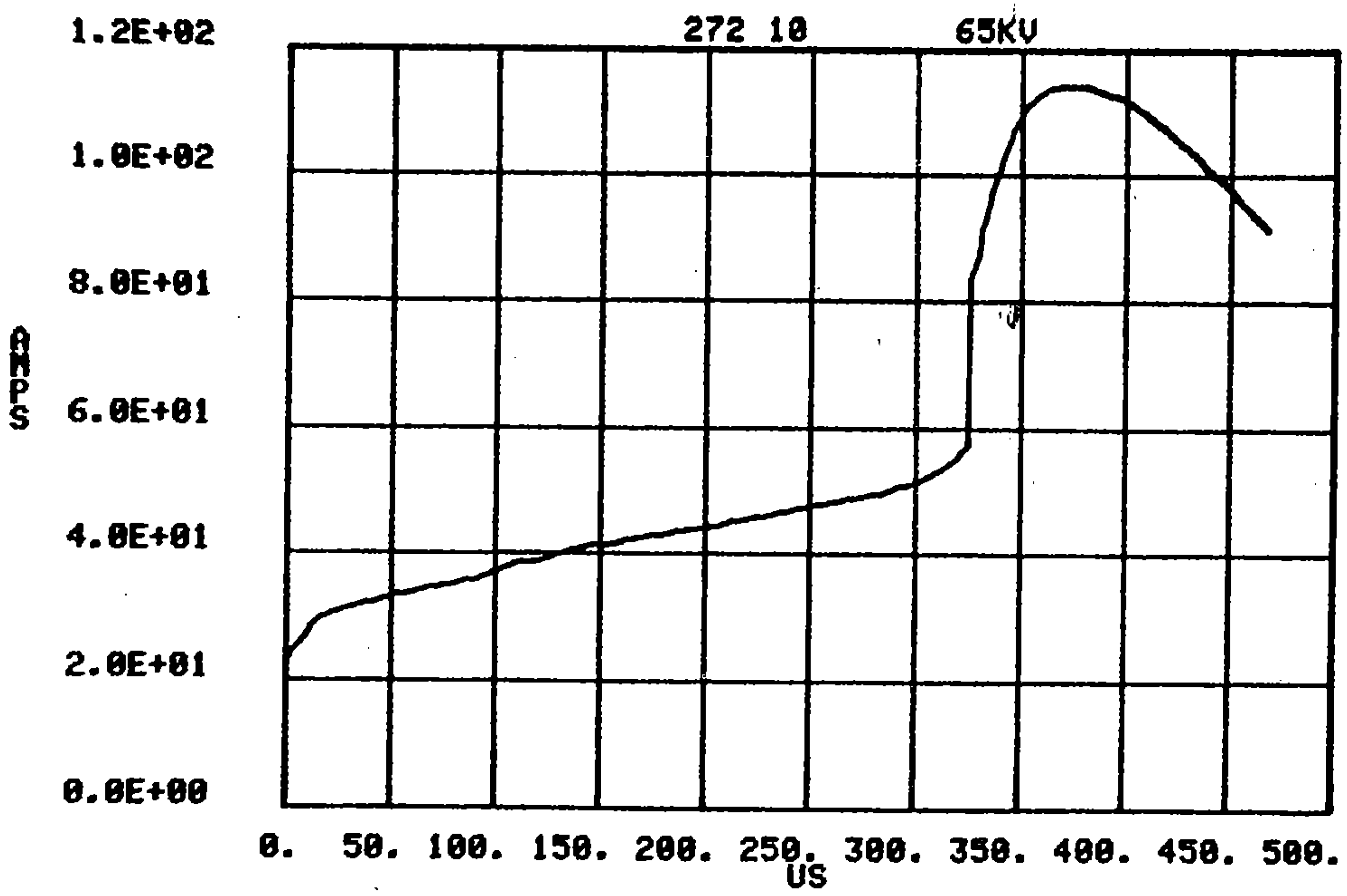

Figure B.41. 272A, .01, .5, .1, 170 MX-B; I.

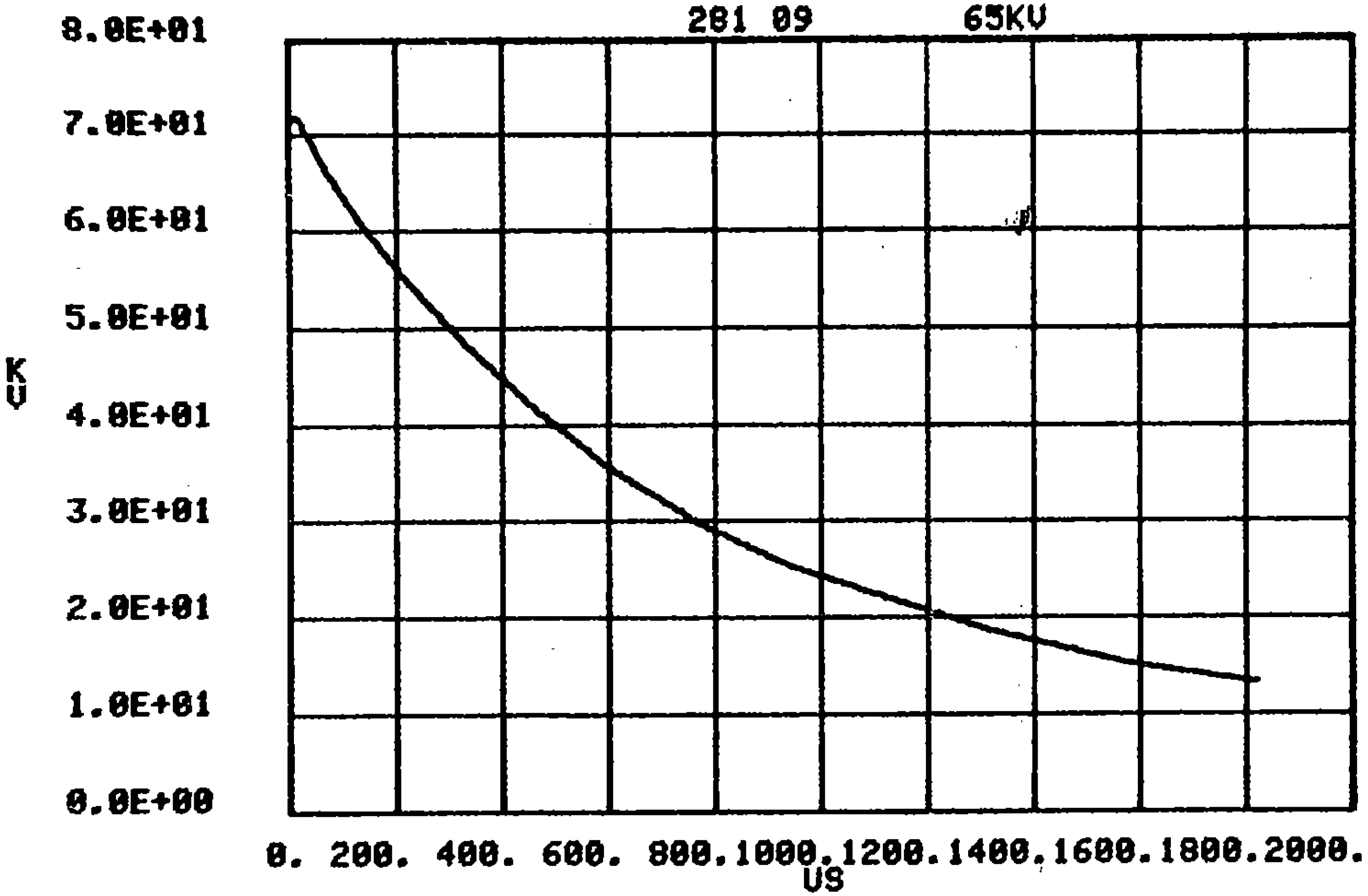

Figure B.42. 281A, .01, .5, .1, 130 MX-B; V_o.

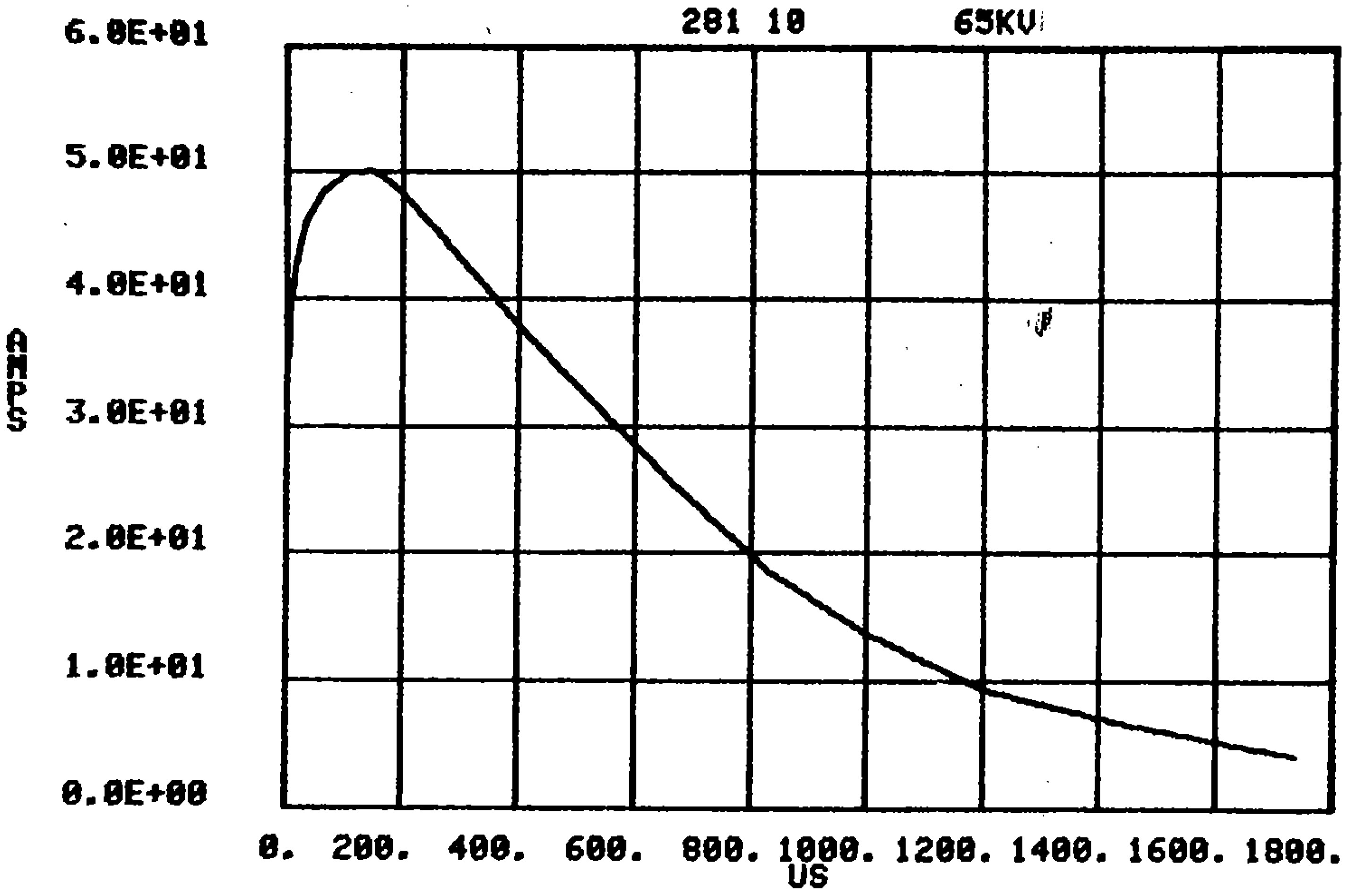

Figure B.43. 281A, .01, .5, .1, 130 MX-B, I.

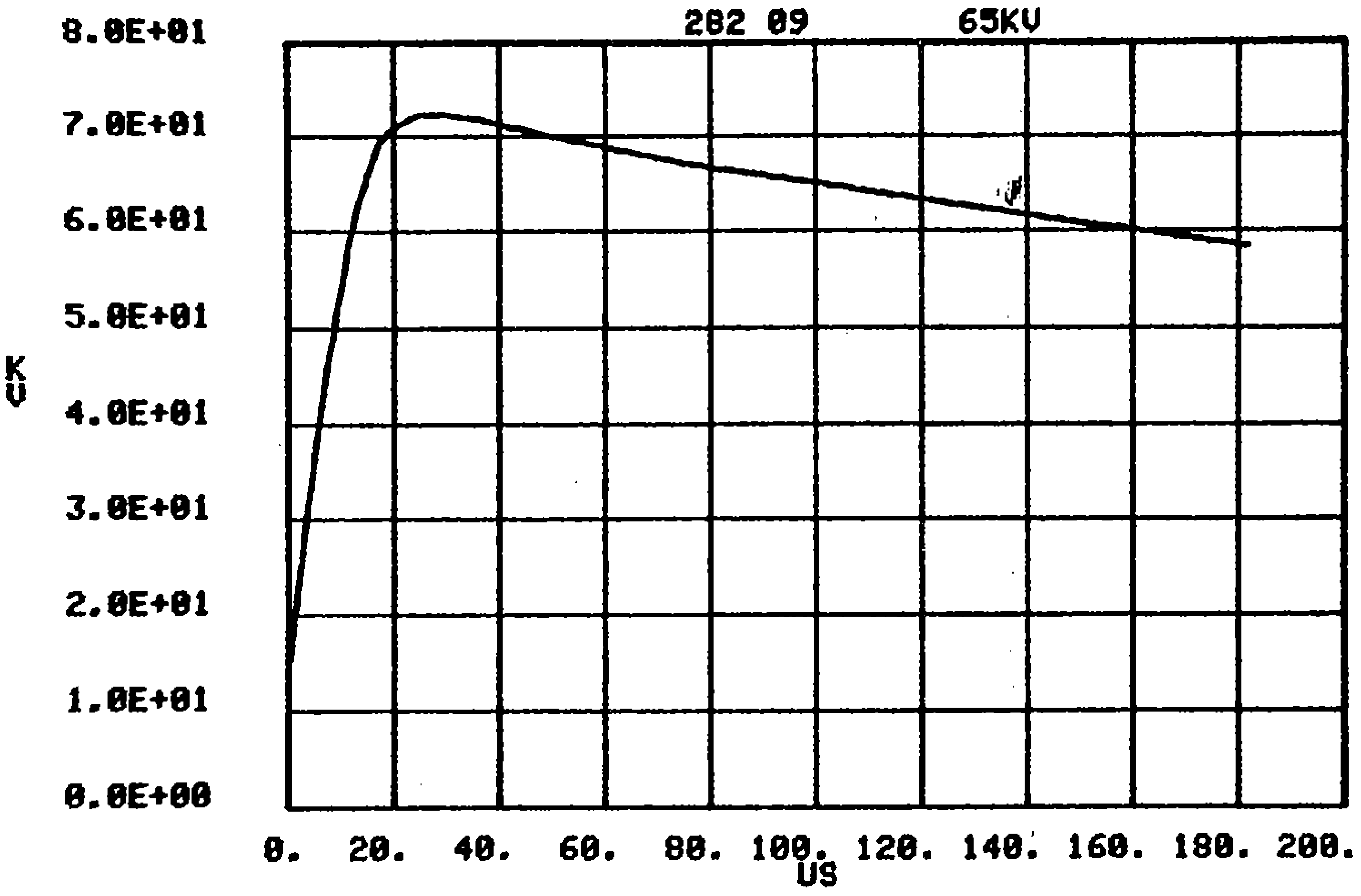

Figure B.44. 282A, .01, .5, .1, 130 MX-B; V_o.

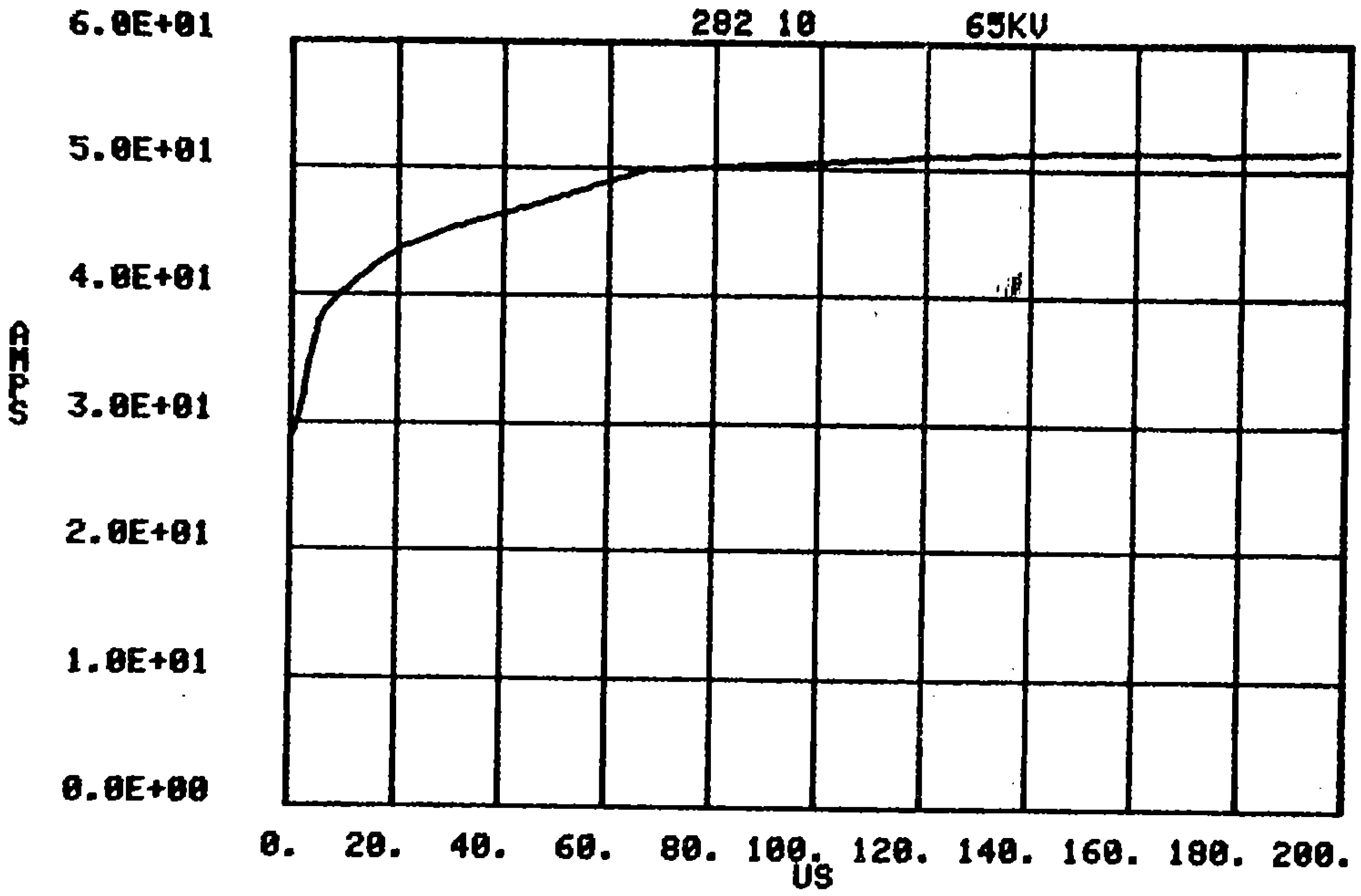

Figure B.45. 282A, .01, .5, .1, 130 MX-B, I.

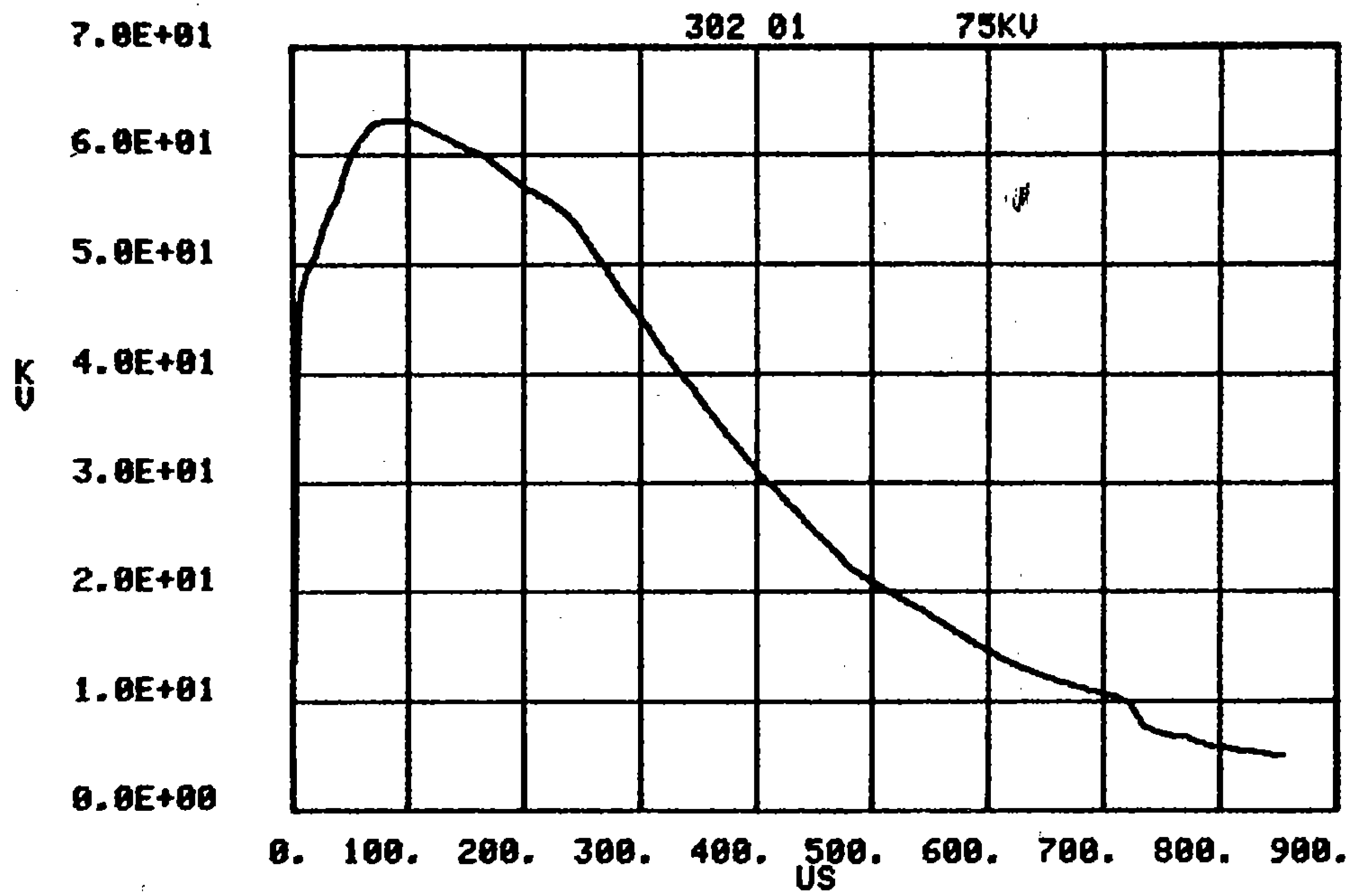

Figure B.46. 302A, :01, .5, .1, 130 MX-B; V at azimuthal position 1.

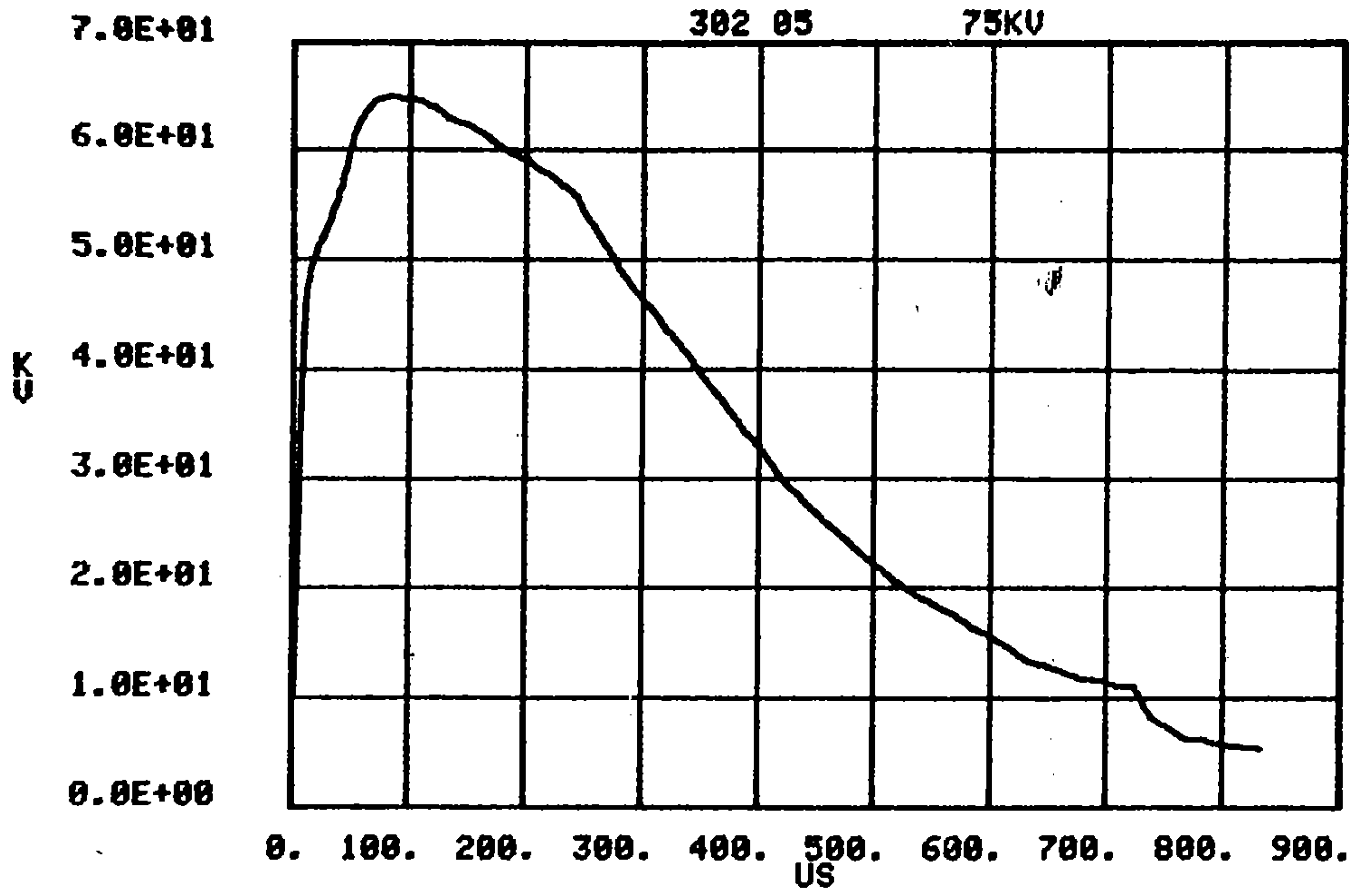

Figure B.47. 302A, .01, .5, .1, 130 MX-B; V at azimuthal position 2.

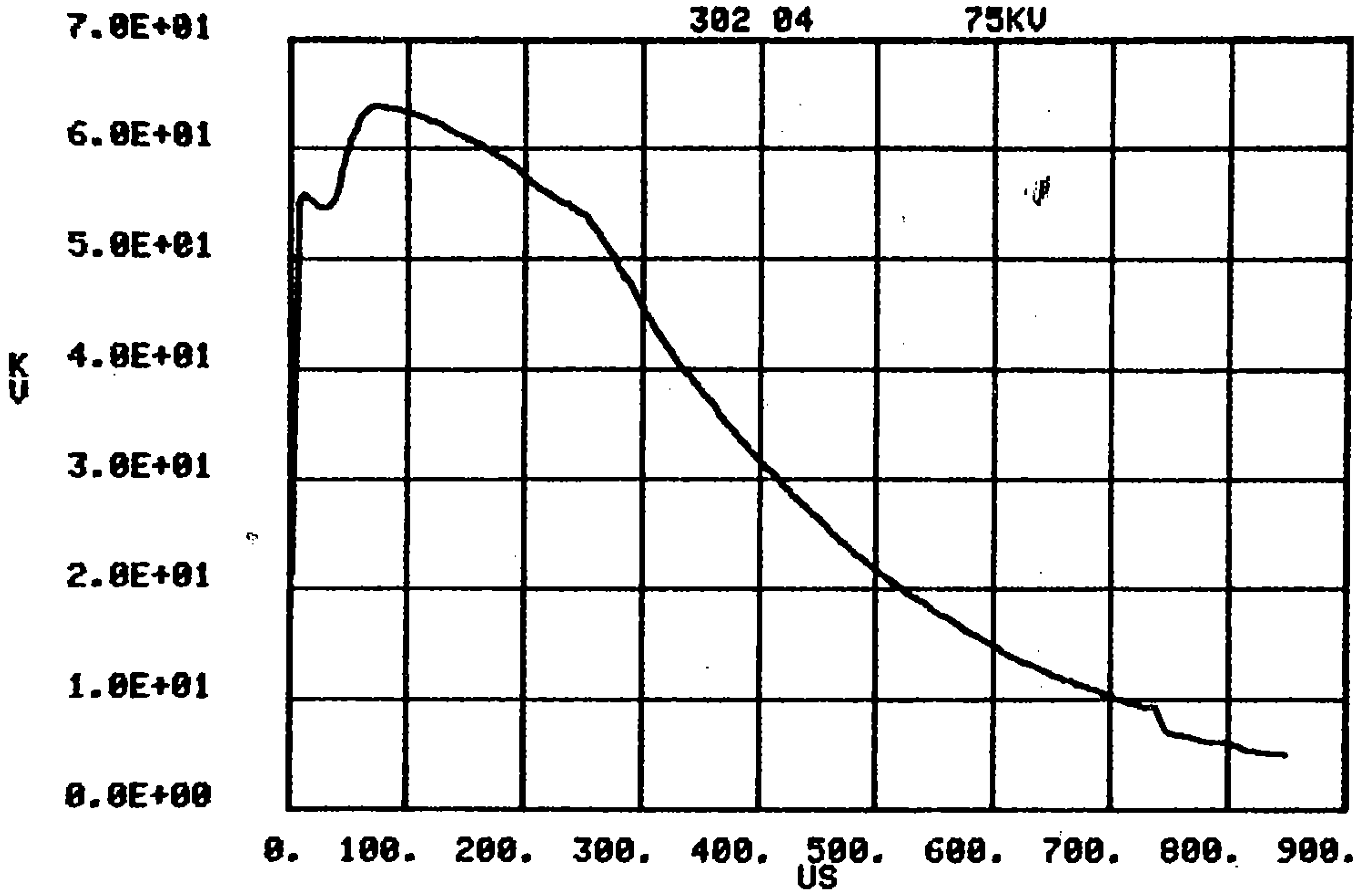

Figure B.48. 302A, .01, .5, .1, 130 MX-B; V at azimuthal position 3.

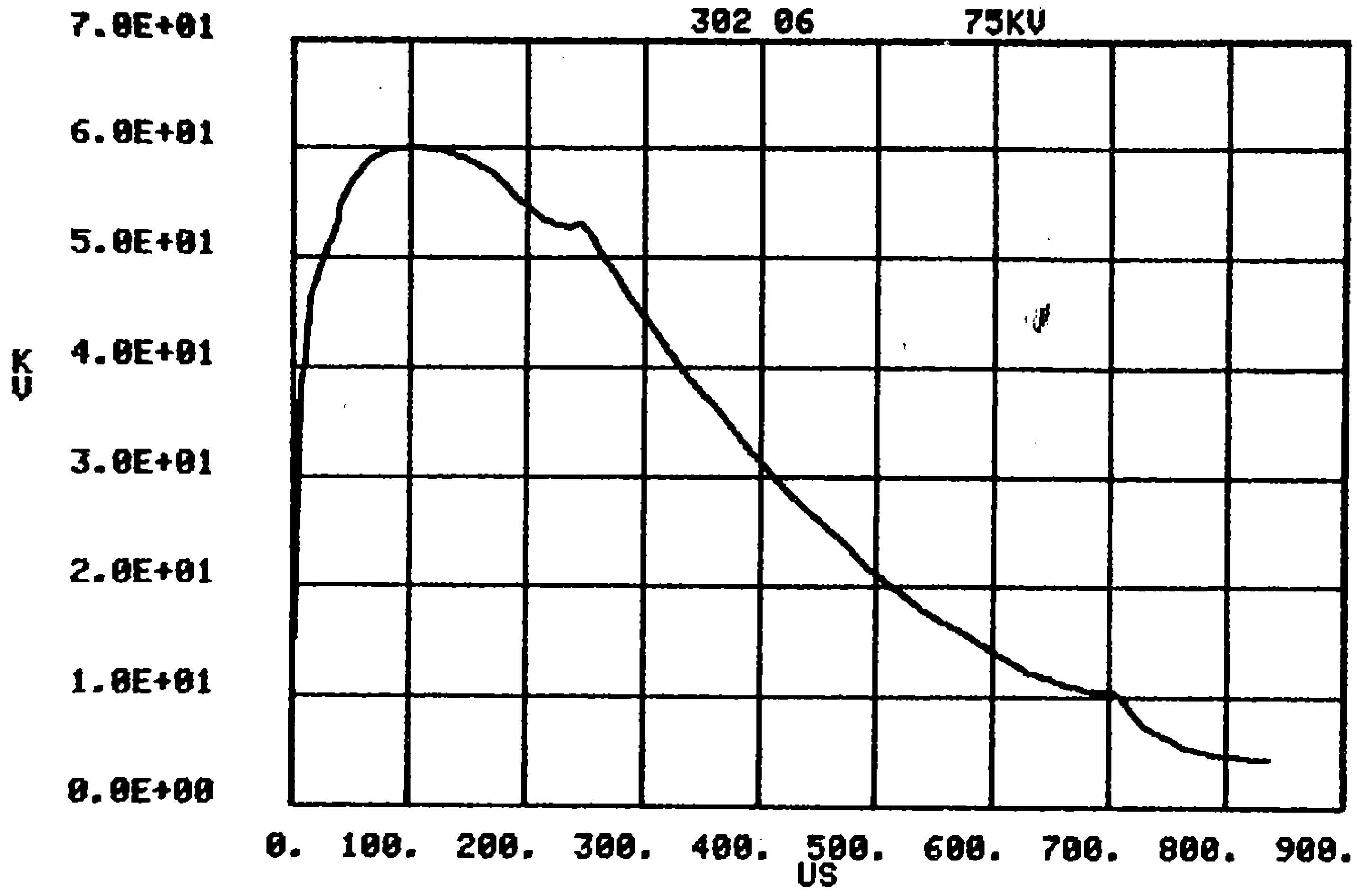

Figure B.49. 302A, .01, .5, .1, 130 MX-B; V at azimuthal position 4.

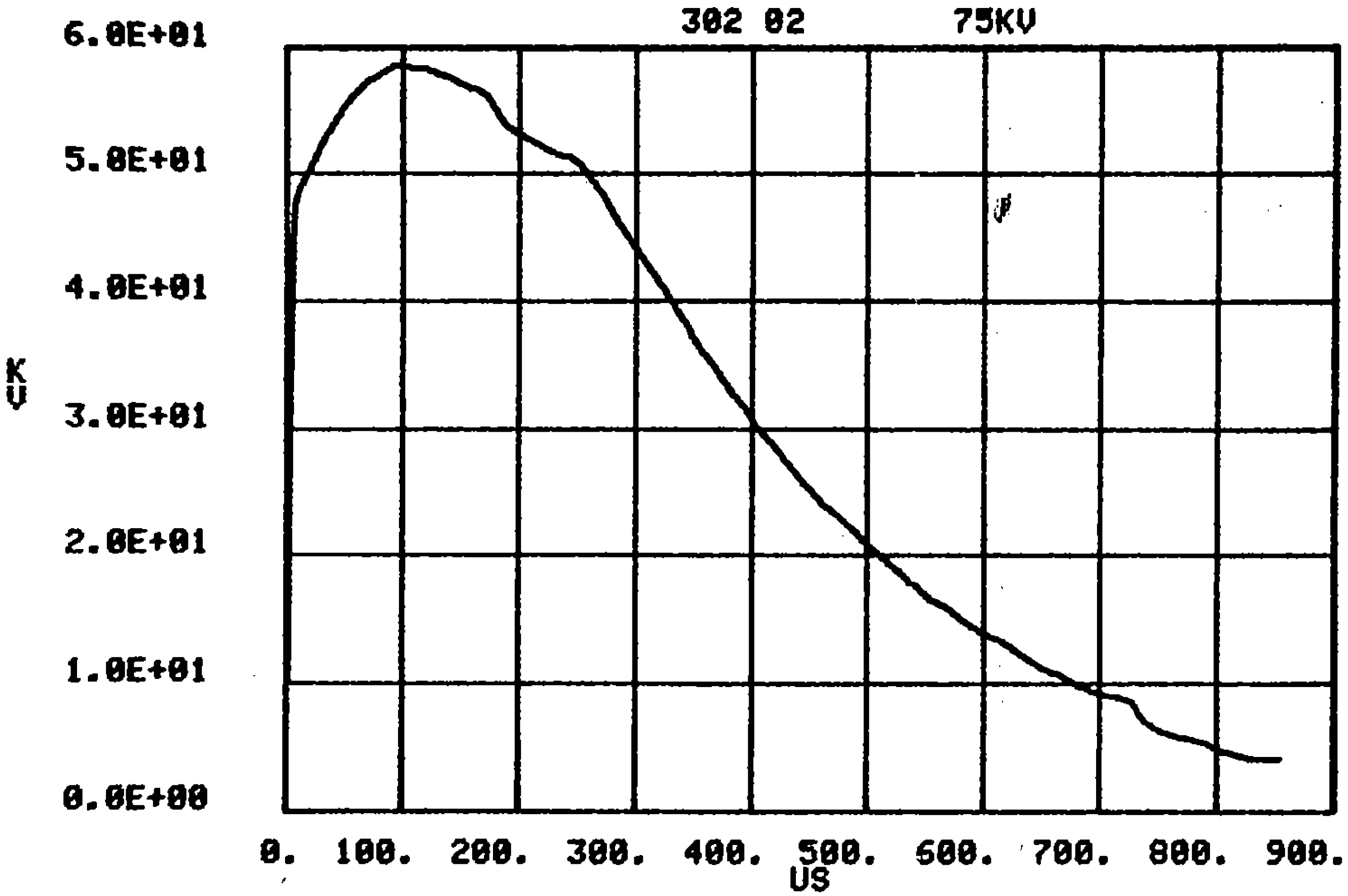

Figure B.50. 302A, .01, .5, .1, 130 MX-B; V at azimuthal position 5.

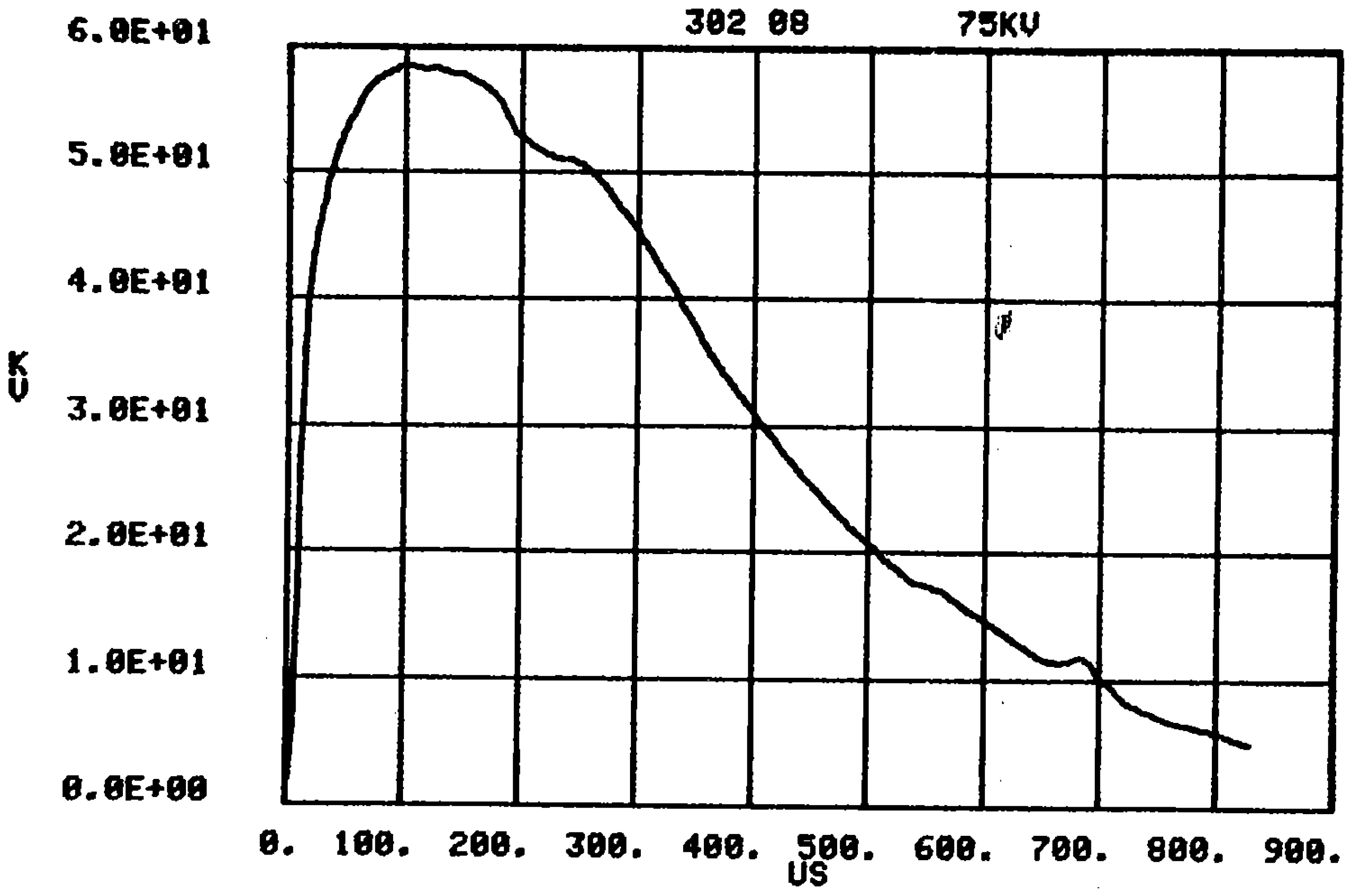

Figure B.51. 302A, .01, .5, .1, 130 MX-B; V at azimuthal position 6.

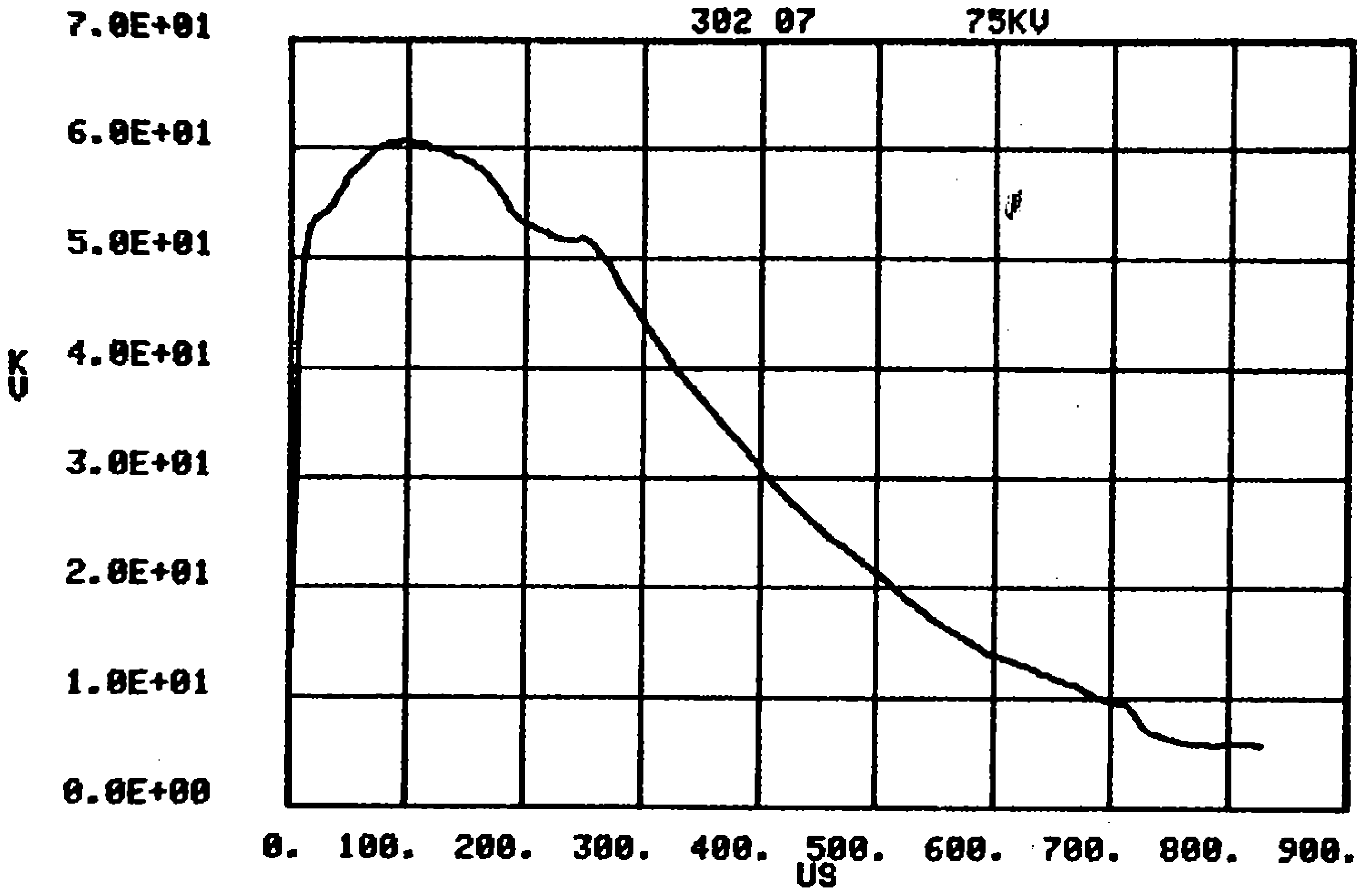

Figure B.52. 302A, .01, .5, .1, 130 MX-B; V at azimuthal position 7.

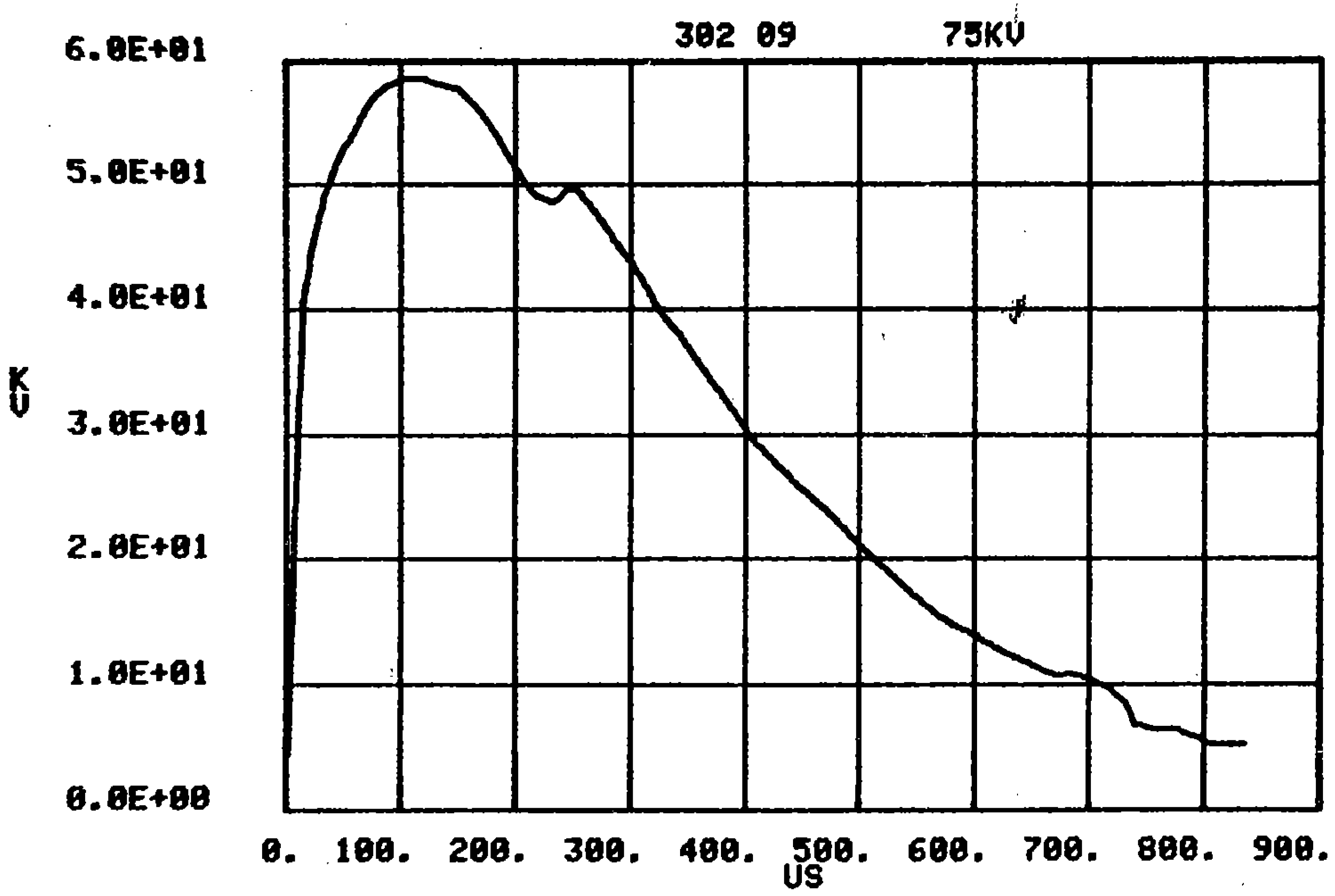

Figure B.53. 302A, .01, .5, .1, 130 MX-B; V at azimuthal position 8.

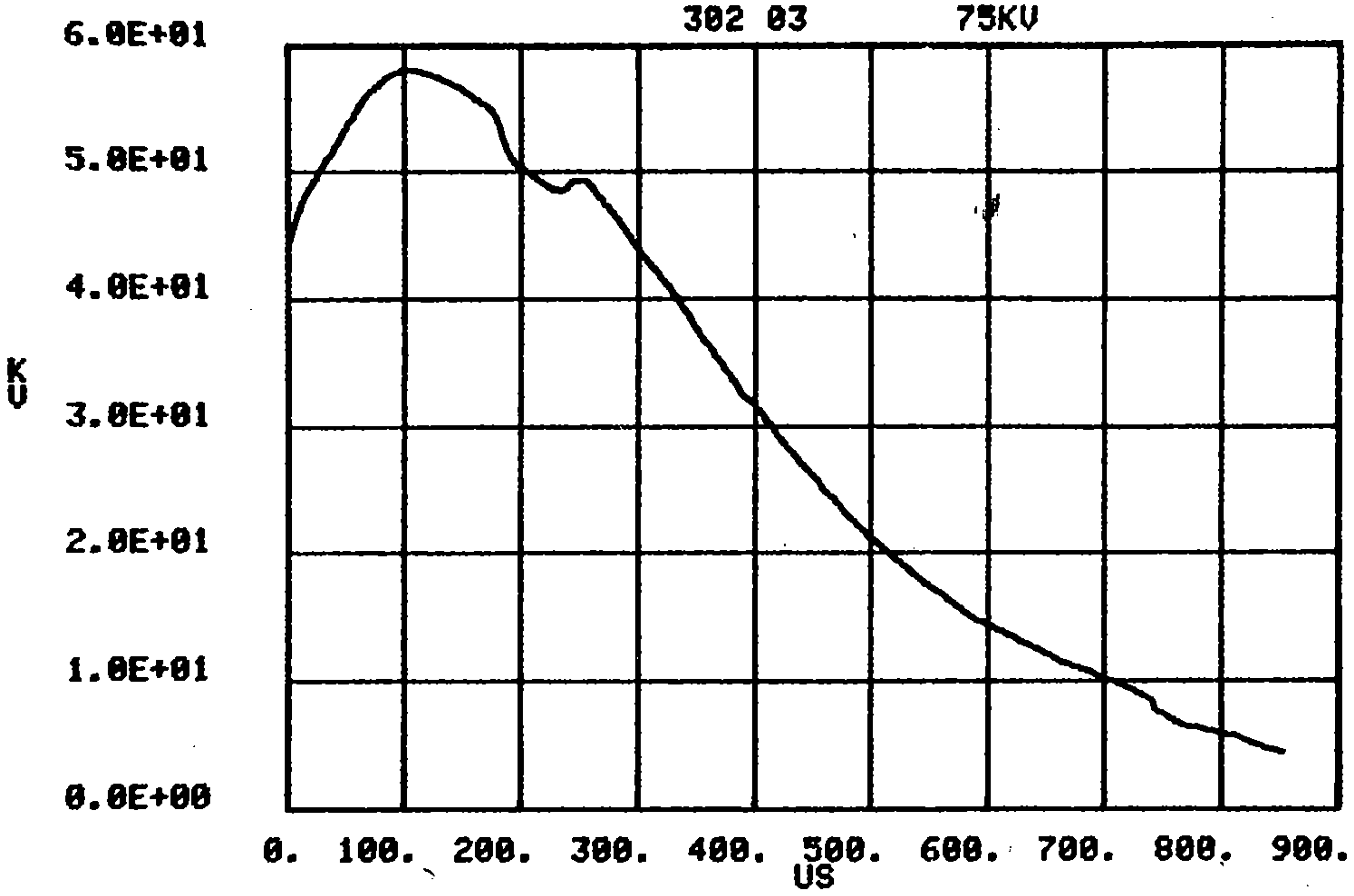

Figure B.54. 302A, .01, .5, .1, 130 MX-B; V at azimuthal position 9.

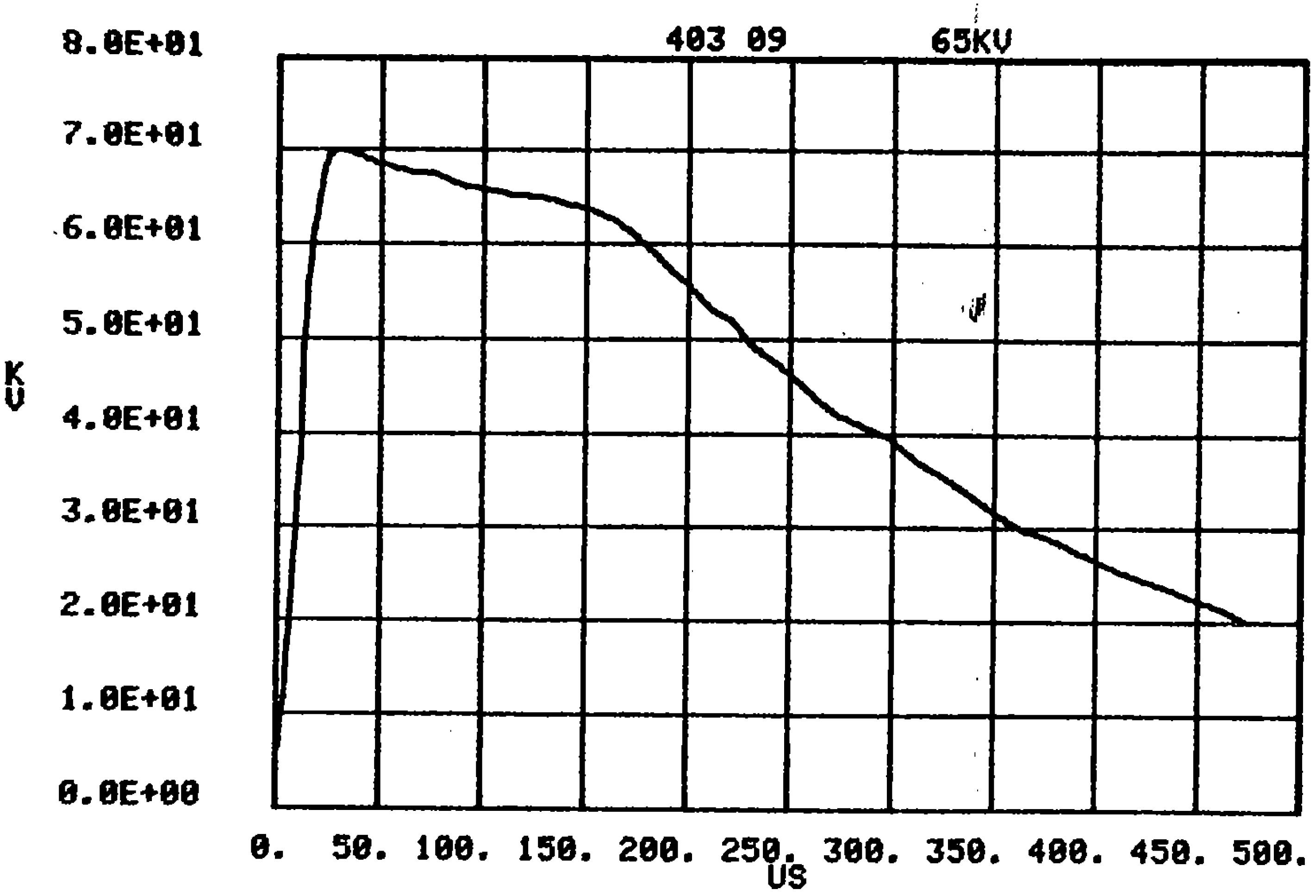

Figure B.55. 403A, .01, .5, .1, 350 sand-mix; V_o.

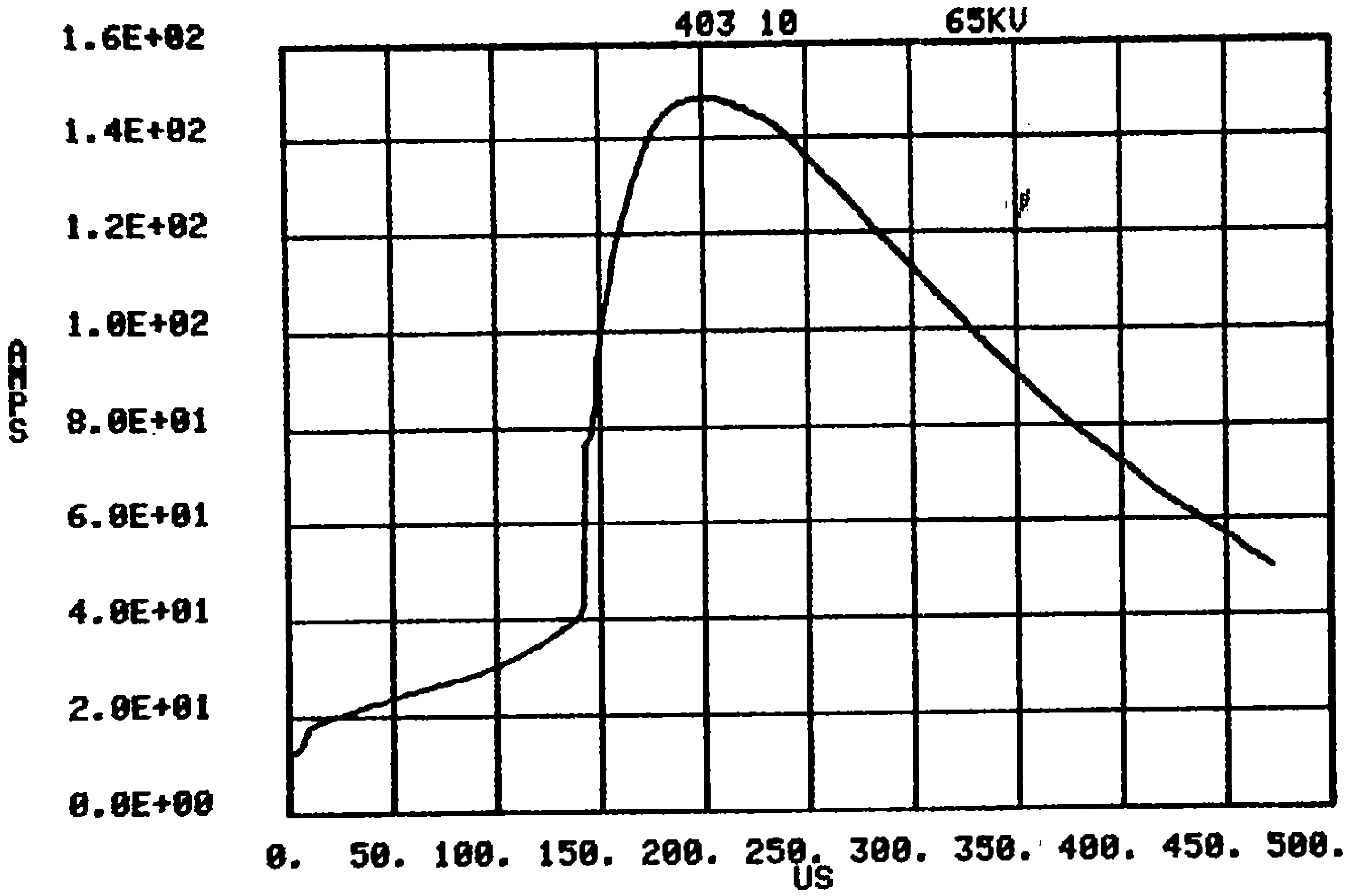

Figure B.56. 403A, .01, .5, .1, 350 sand-mix; I.

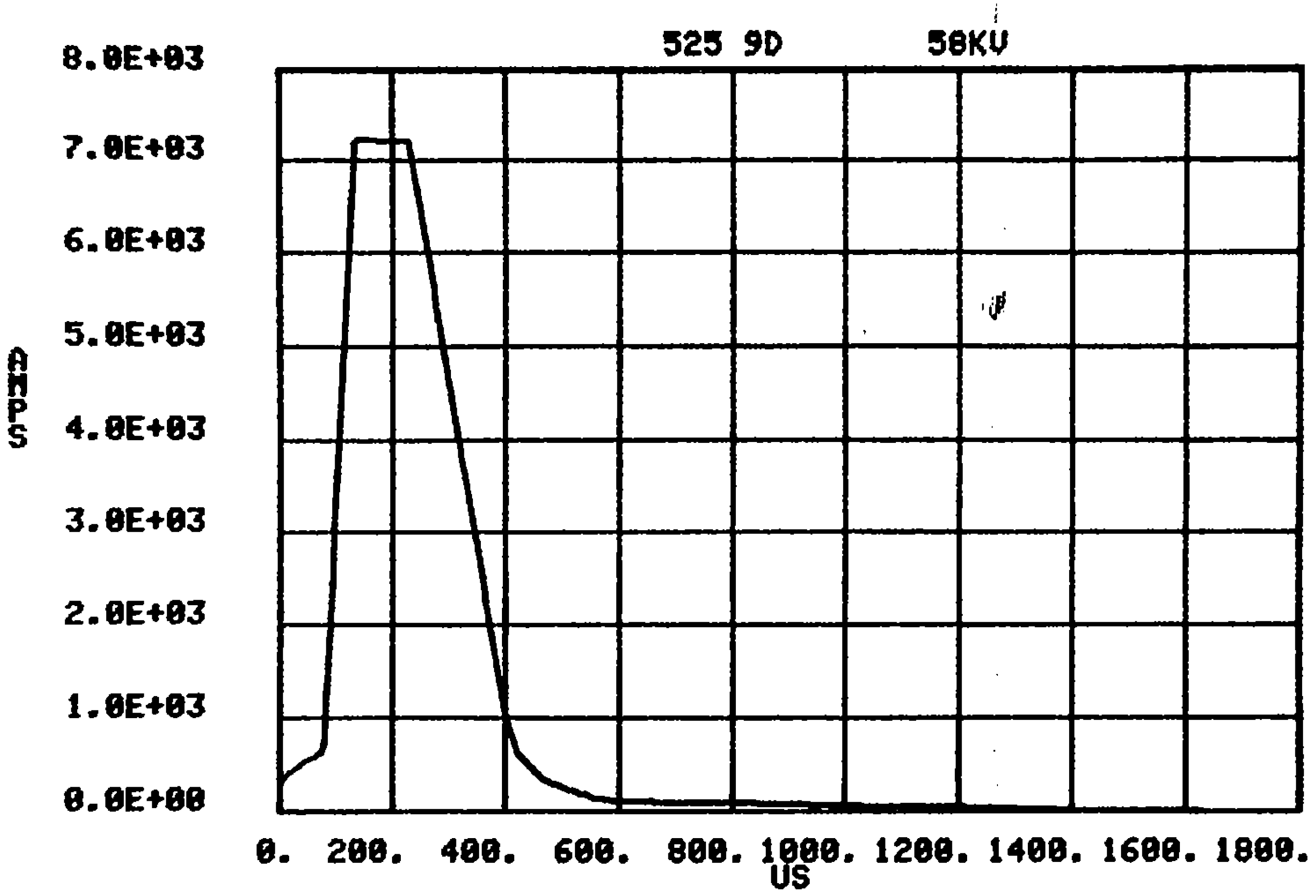

Figure B.57. 525B, .01, 1.0, 1.0, 300 sand-mix; I.

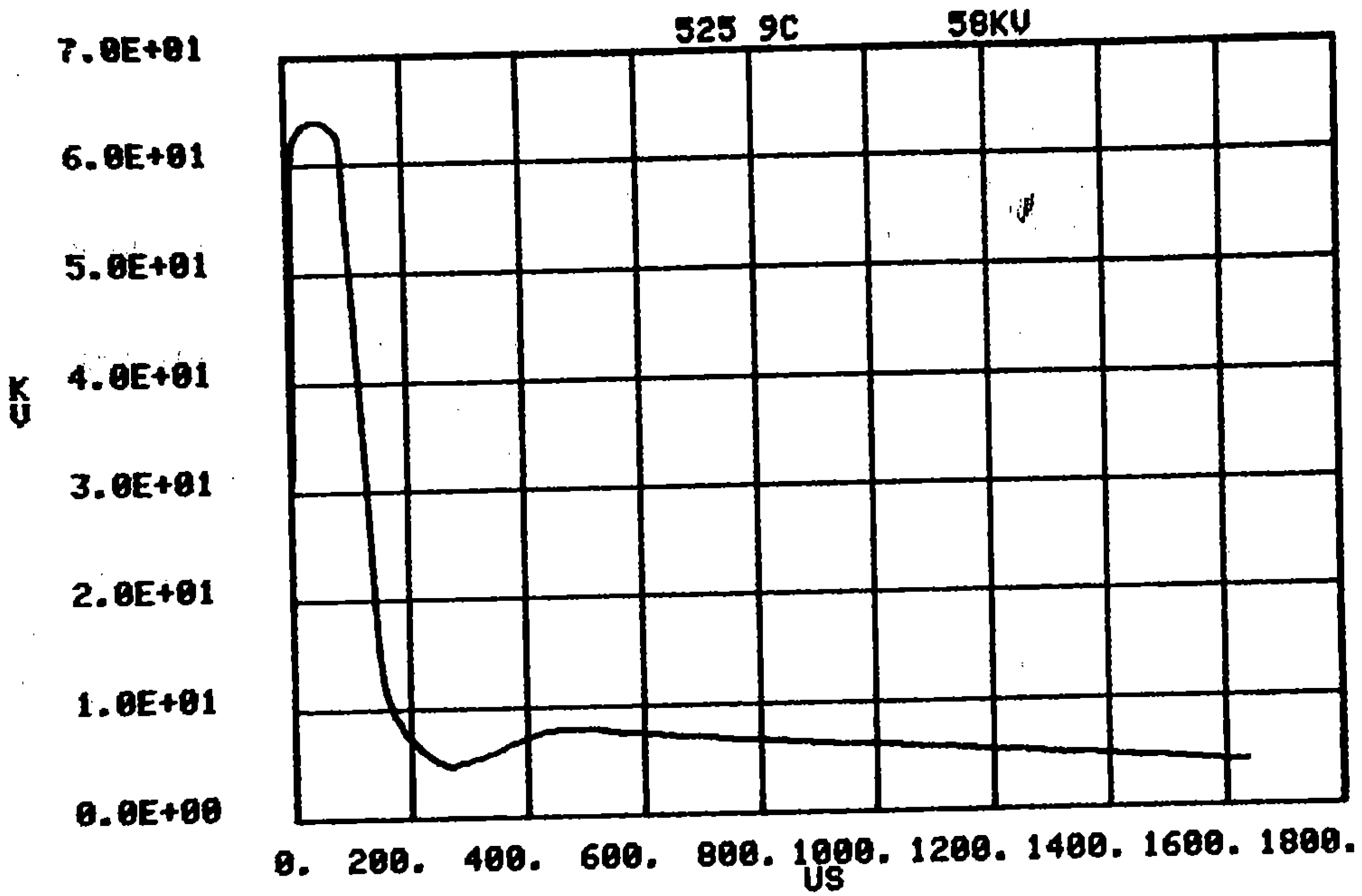

Figure B.58. 525B, .01, 1.0, 1.0, 300 sand-mix; V_o.

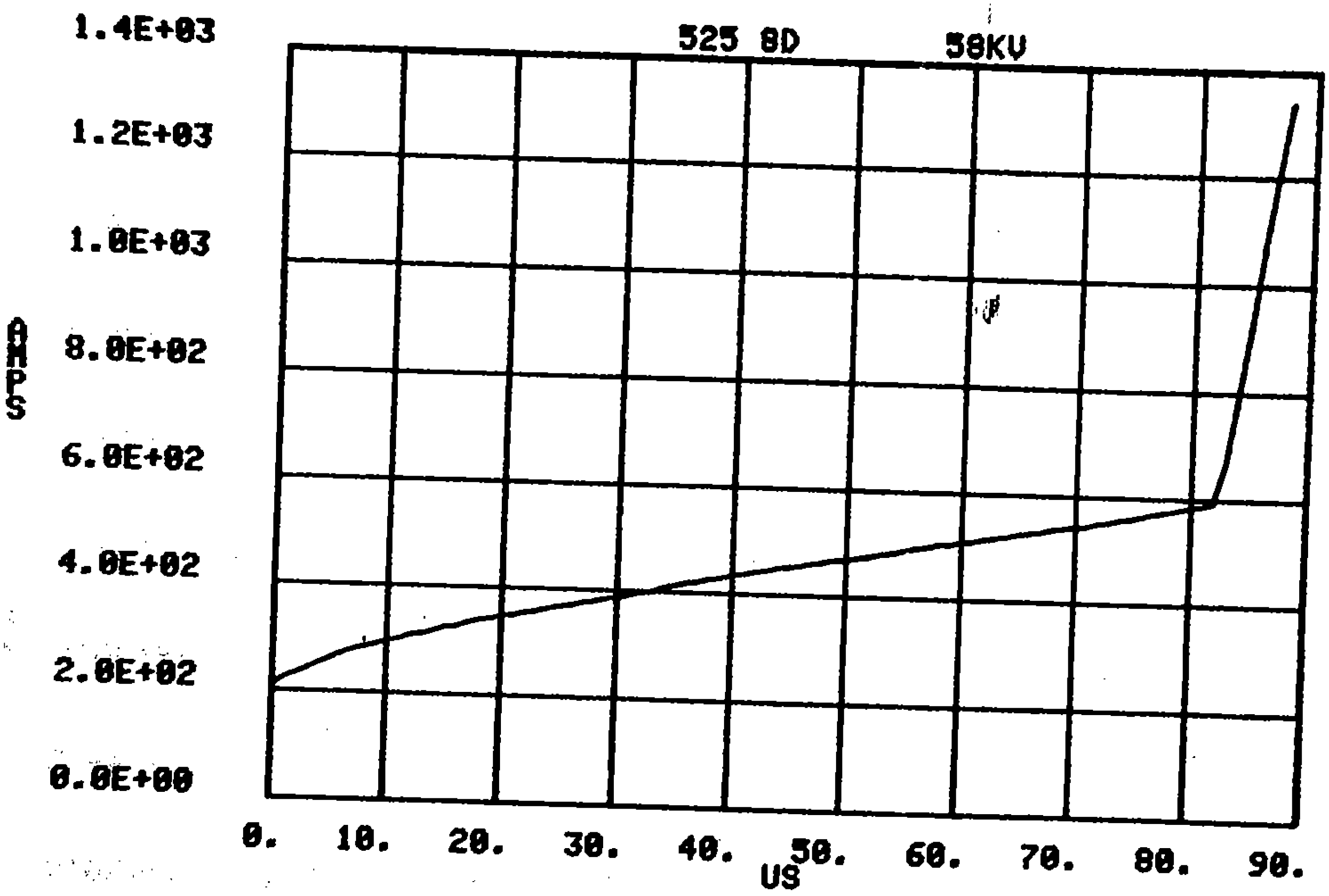

Figure B.59. 525B, .01, 1.0, 1.0, 300 sand-mix; I.

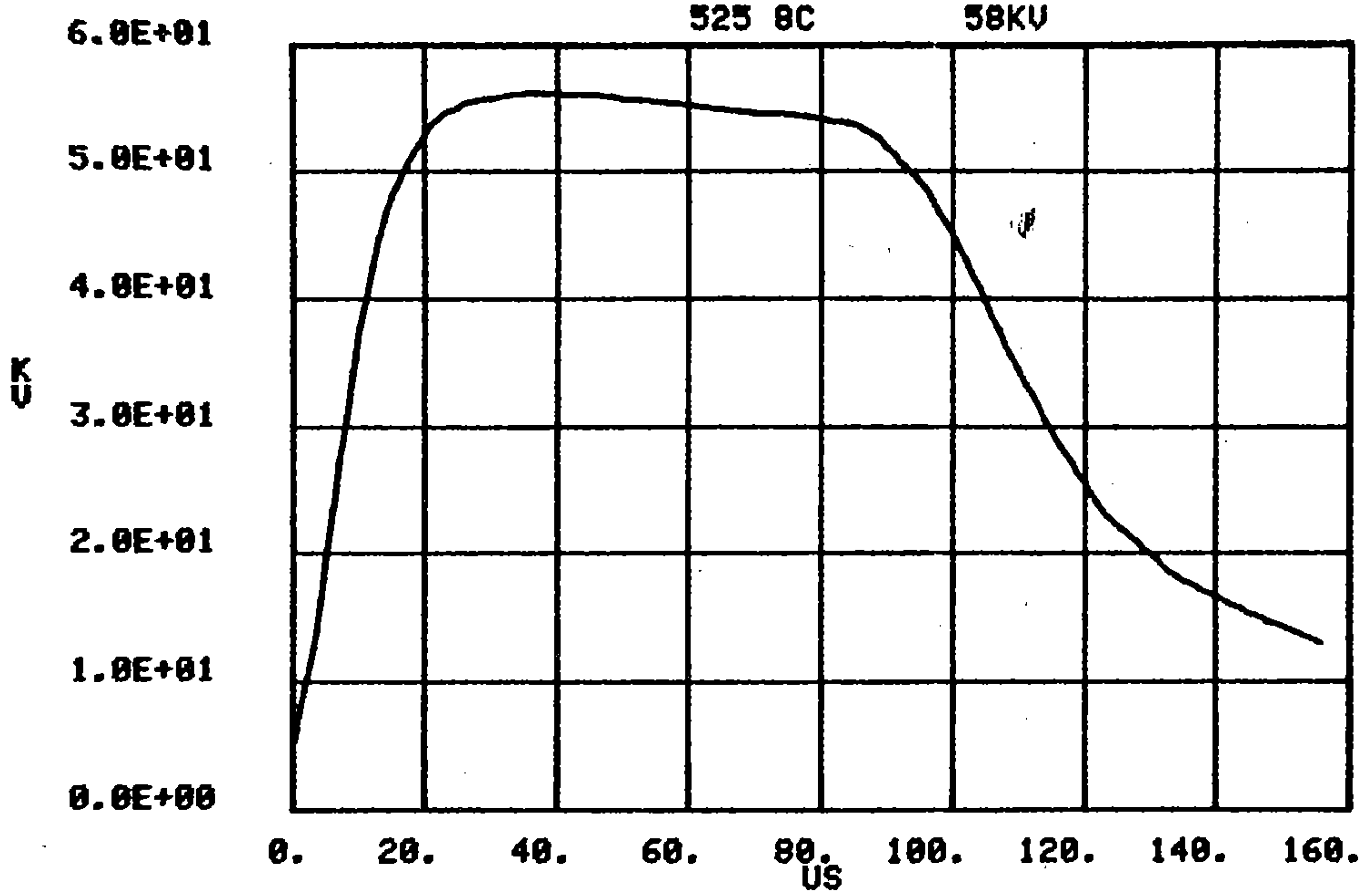

Figure B.60. 525B, .01, 1.0, 1.0, 300 sand-mix; I.

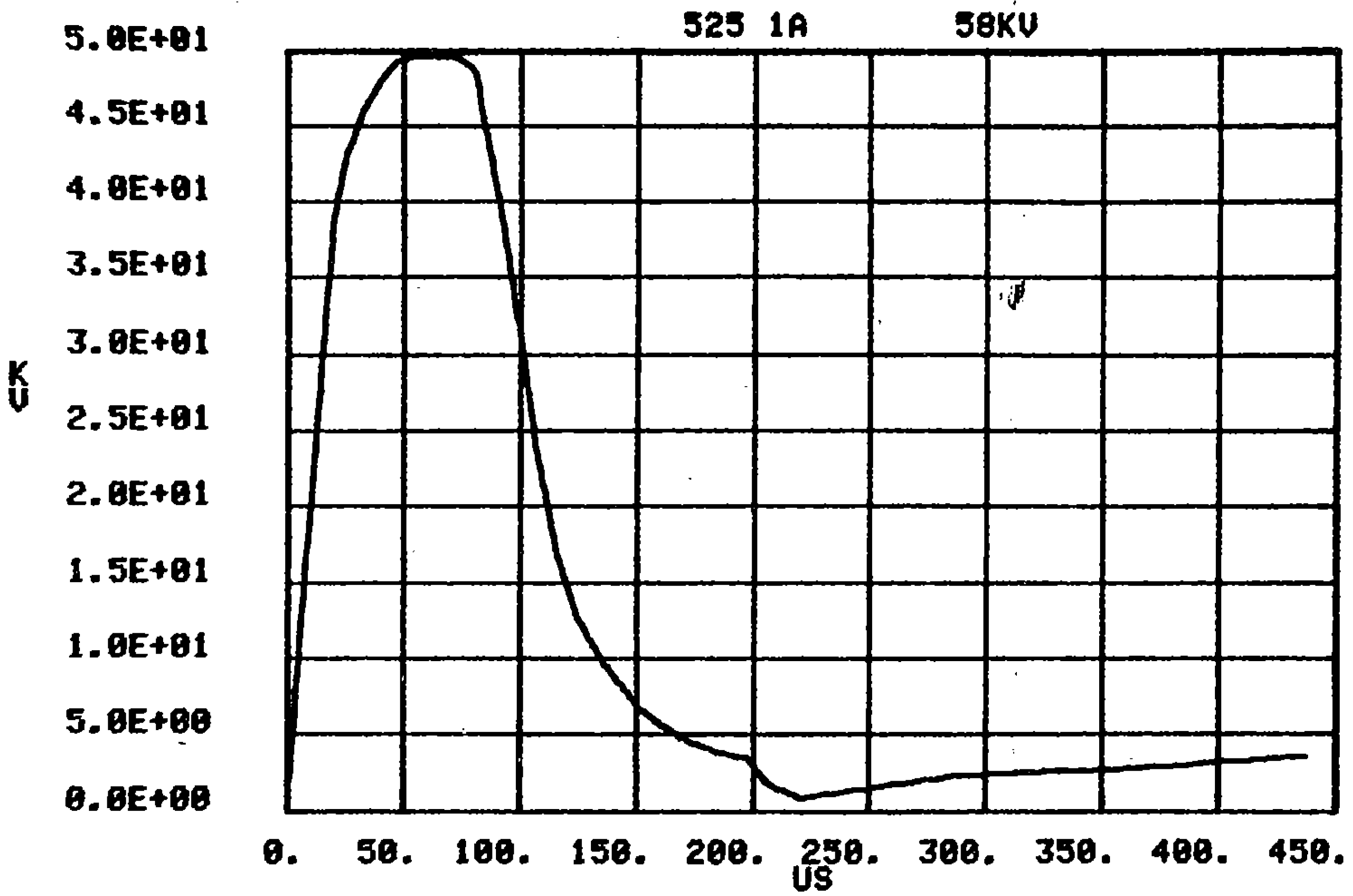

Figure B.61. 525B, .01, 1.0, 1.0, 300 sand-mix; V at r, θ = .51 m, 0° (bottom).

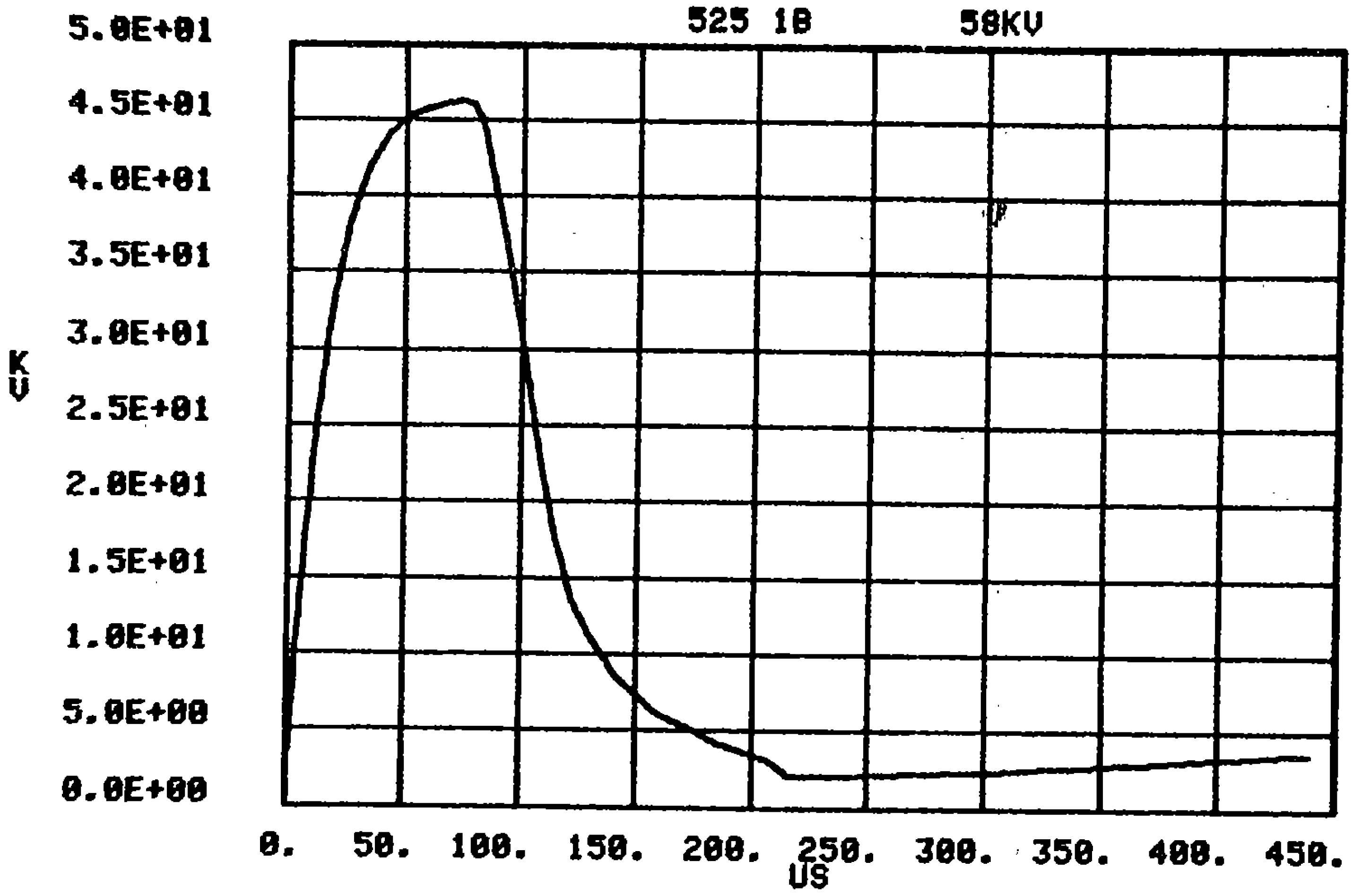

Figure B.62. 525B, .01, 1.0, 1.0, 300 sand-mix; V at r,θ = .10 m, 0° (bottom).

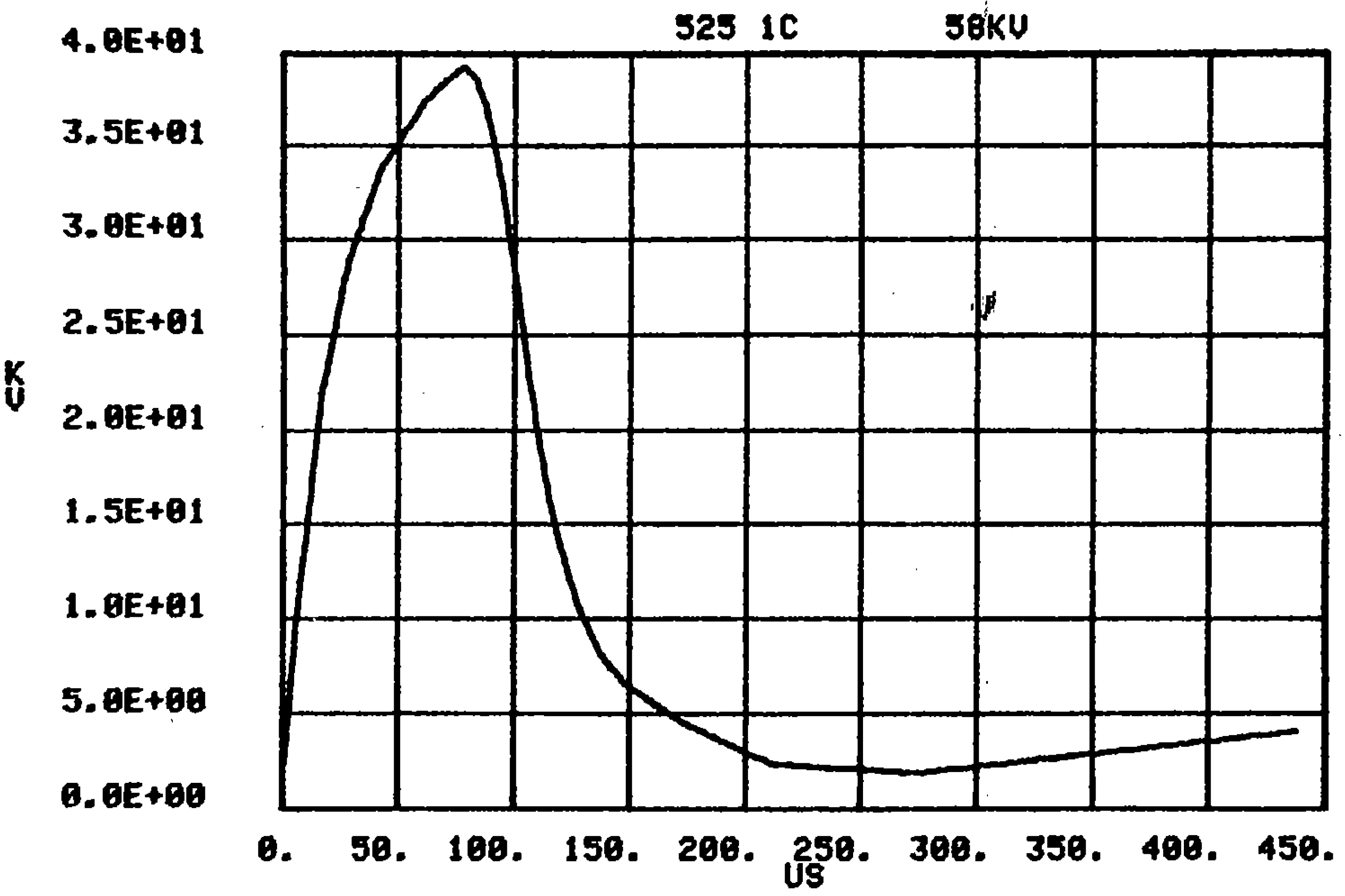

Figure B.63. 525B, .01, 1.0, 1.0, 300 sand-mix; V at r,θ = .18 m, 0° (bottom).

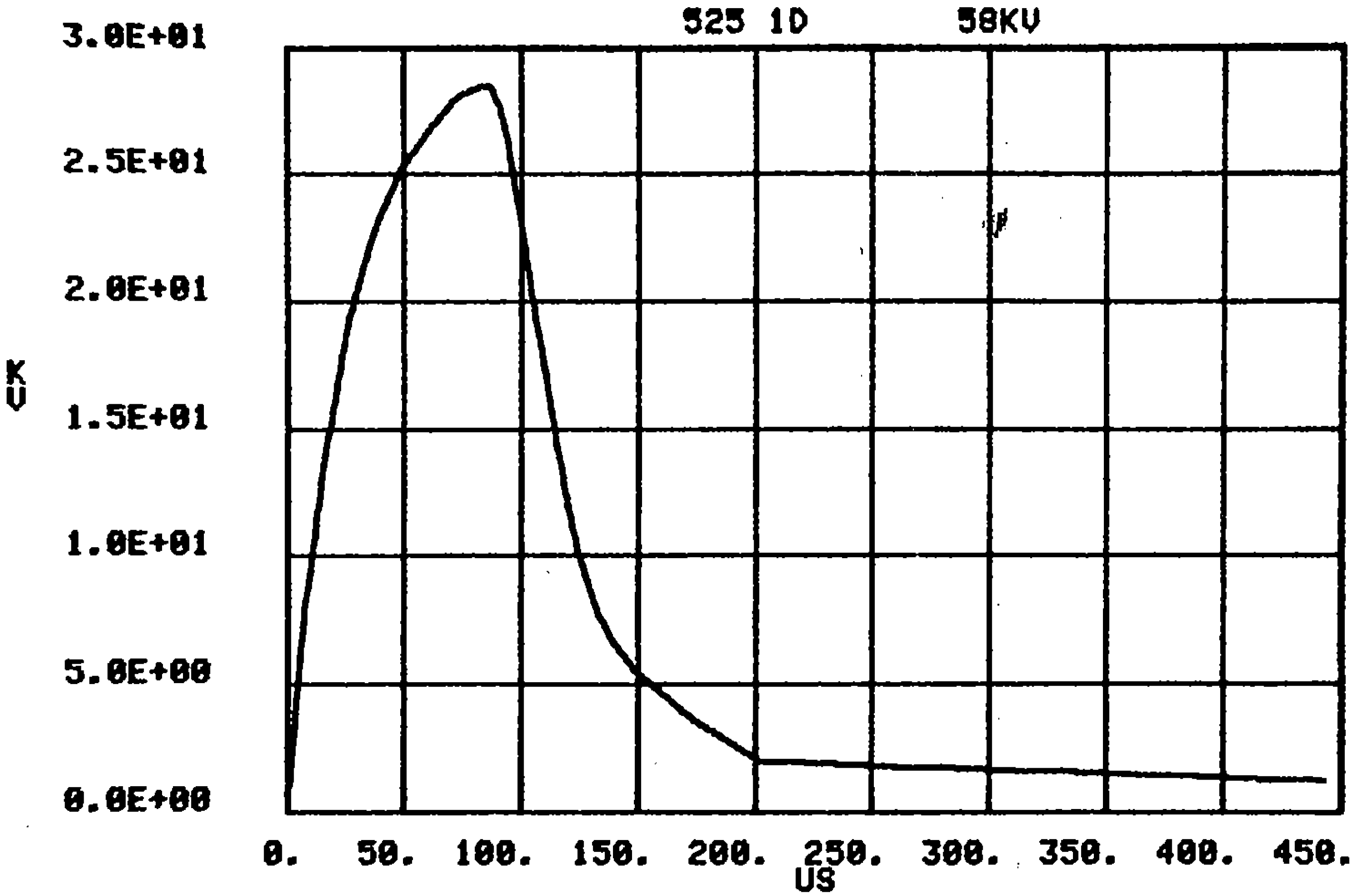

Figure B.64. 525B, .01, 1.0, 1.0, 300 sand-mix; V at r,θ = .30 m, 0° (bottom).

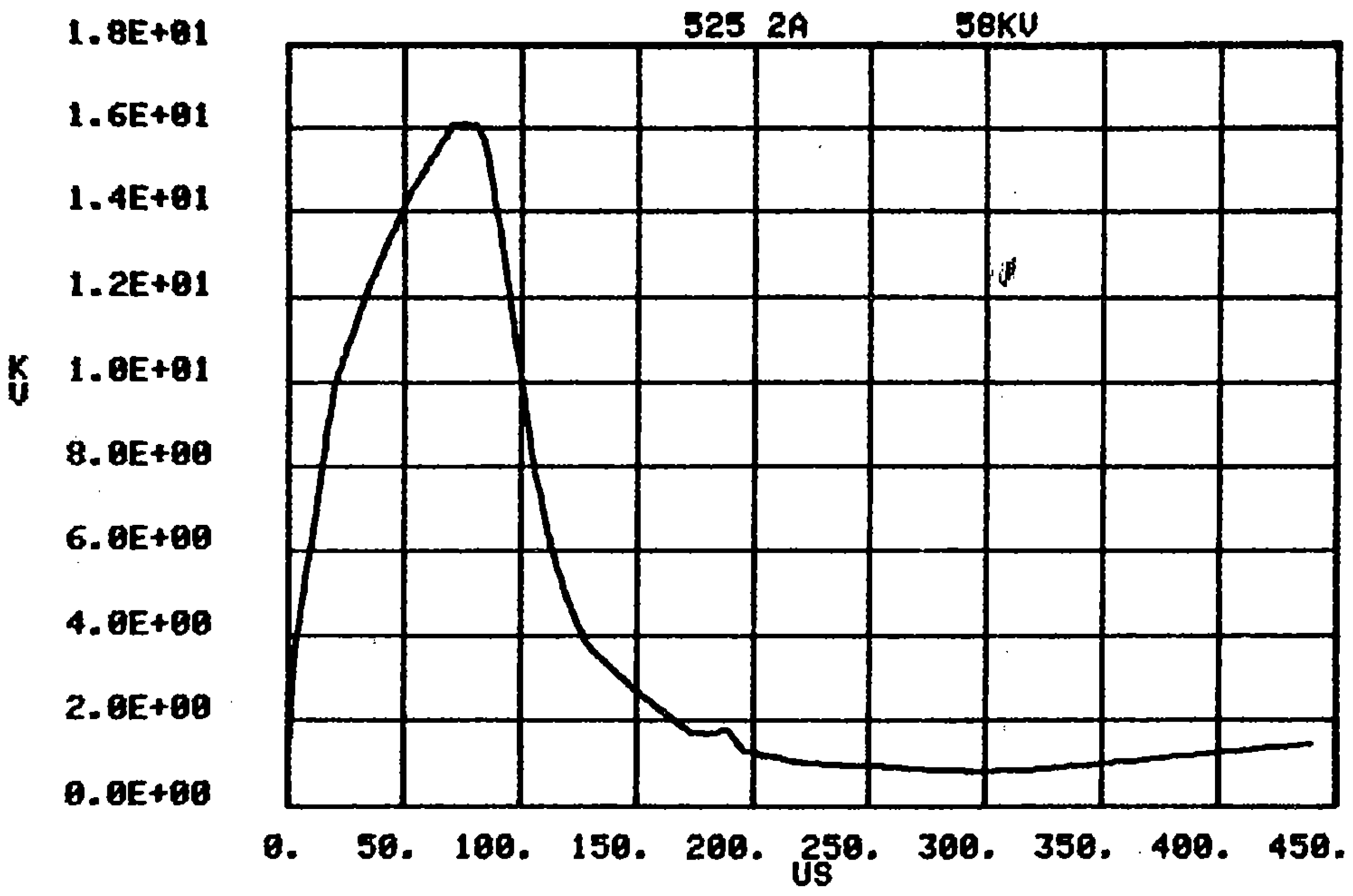

Figure B.65. 525B, .01, 1.0, 1.0, 300 sand-mix; V at r,θ = .51 m, 0° (bottom).

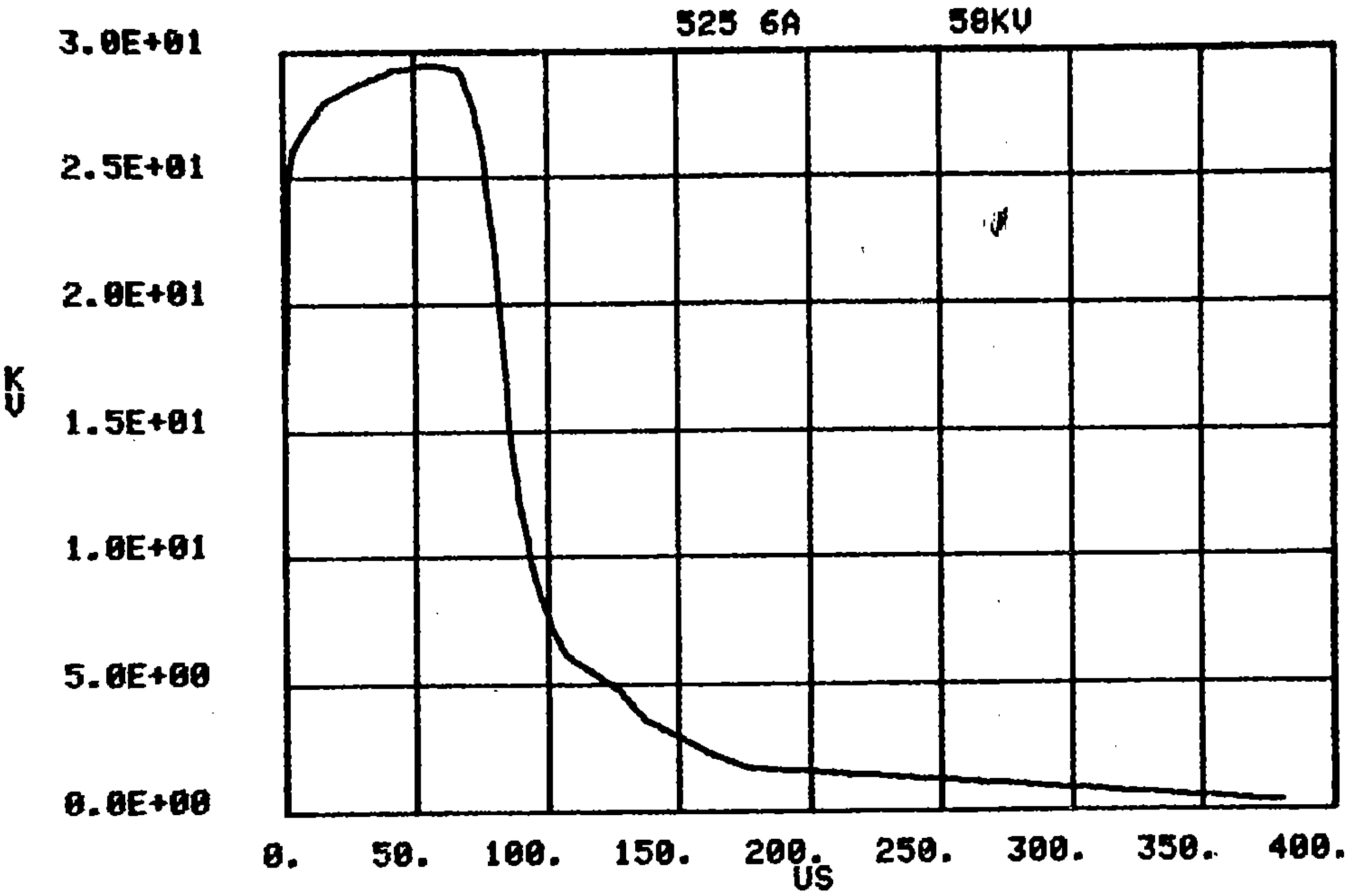

Figure B.66. 525B, .01, 1.0, 1.0, 300 sand-mix; V at r,θ = .15 m, 261 (top).

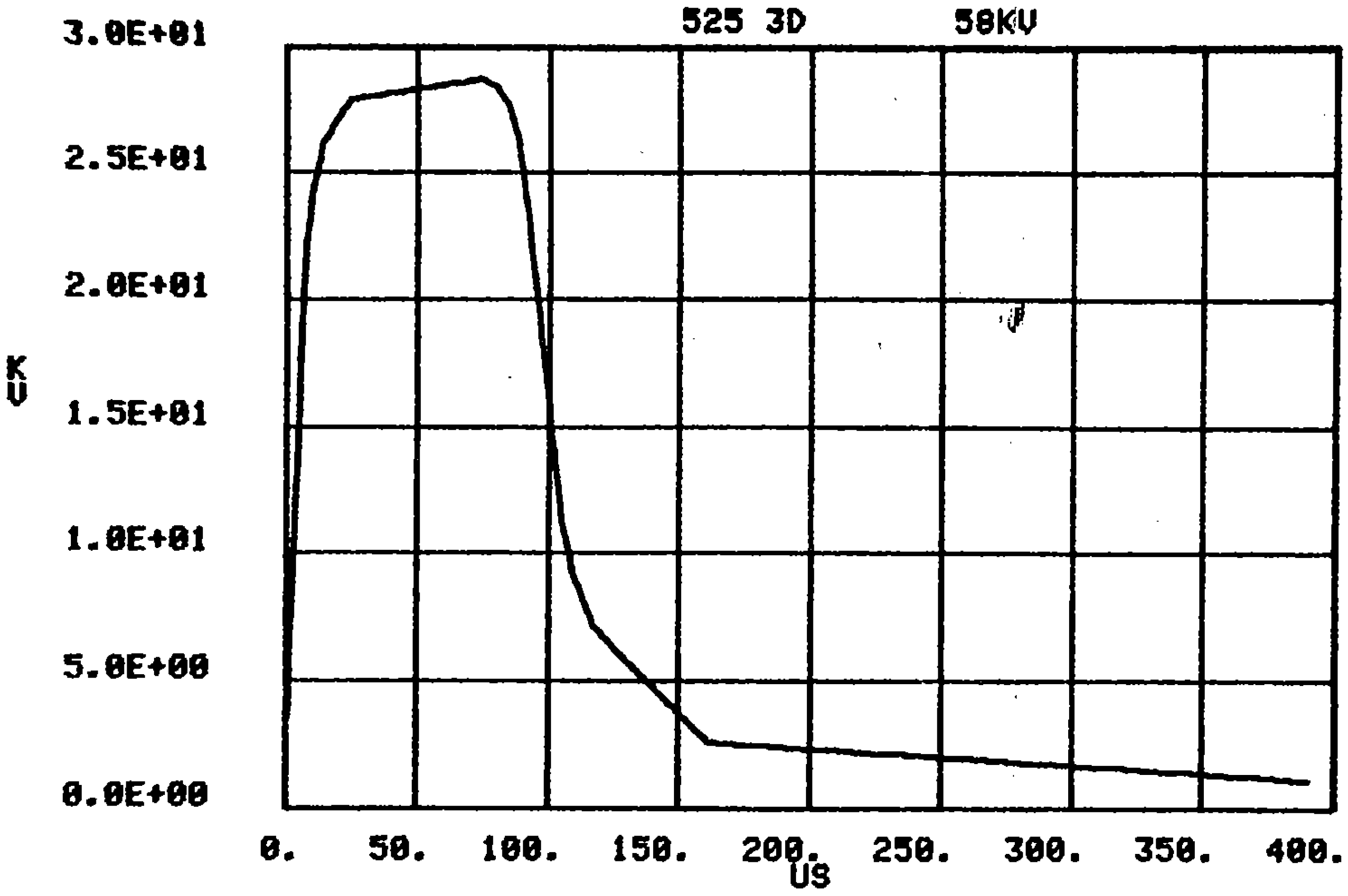

Figure B.67. 525B, .01, 1.0, 1.0, 300 sand-mix; V at r,θ = .15 m, 272 (top).

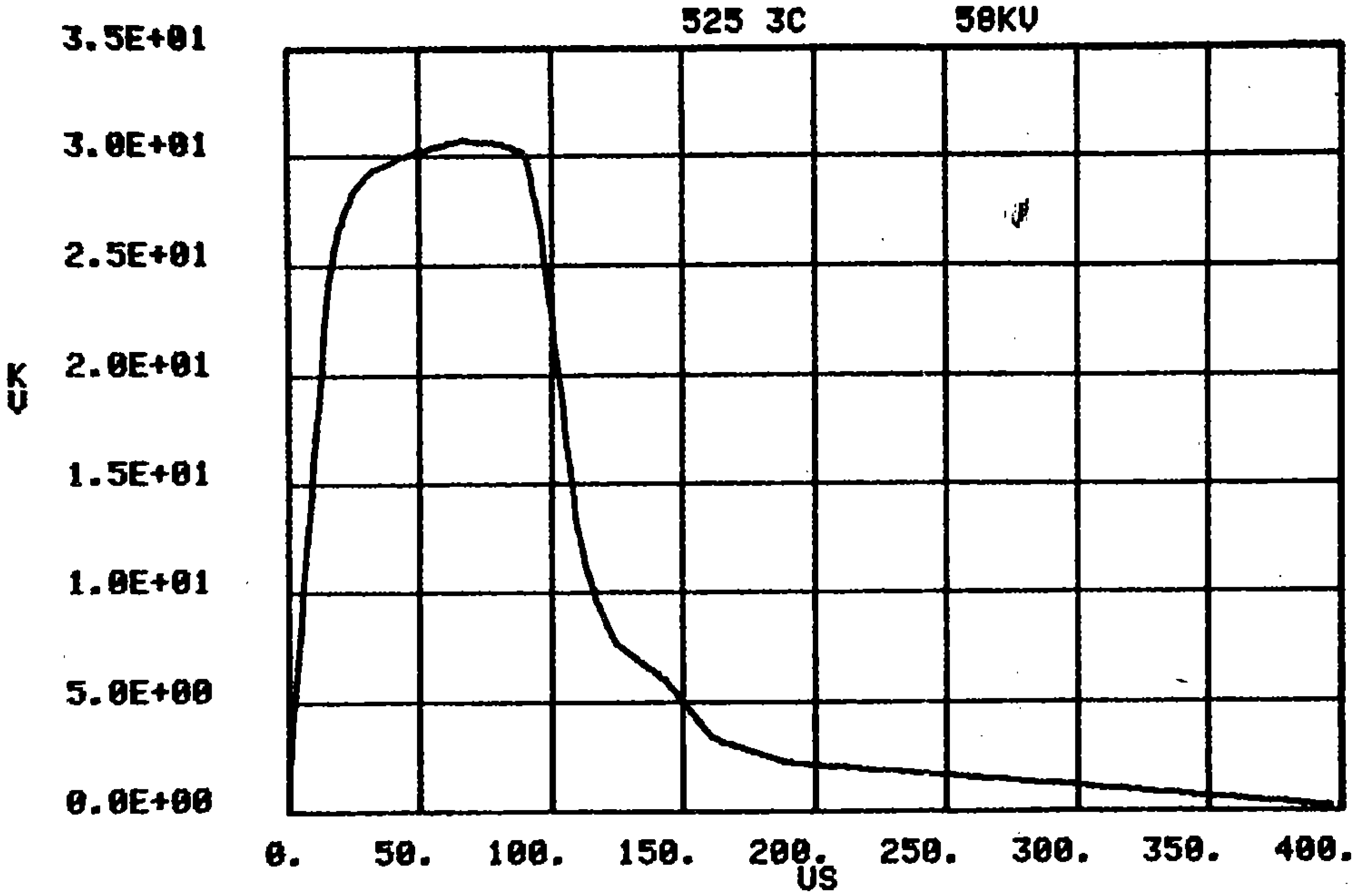

Figure B.68. 525B, .01, 1.0, 1.0, 300 sand-mix; V at r,θ = .15 m, 283 (top).

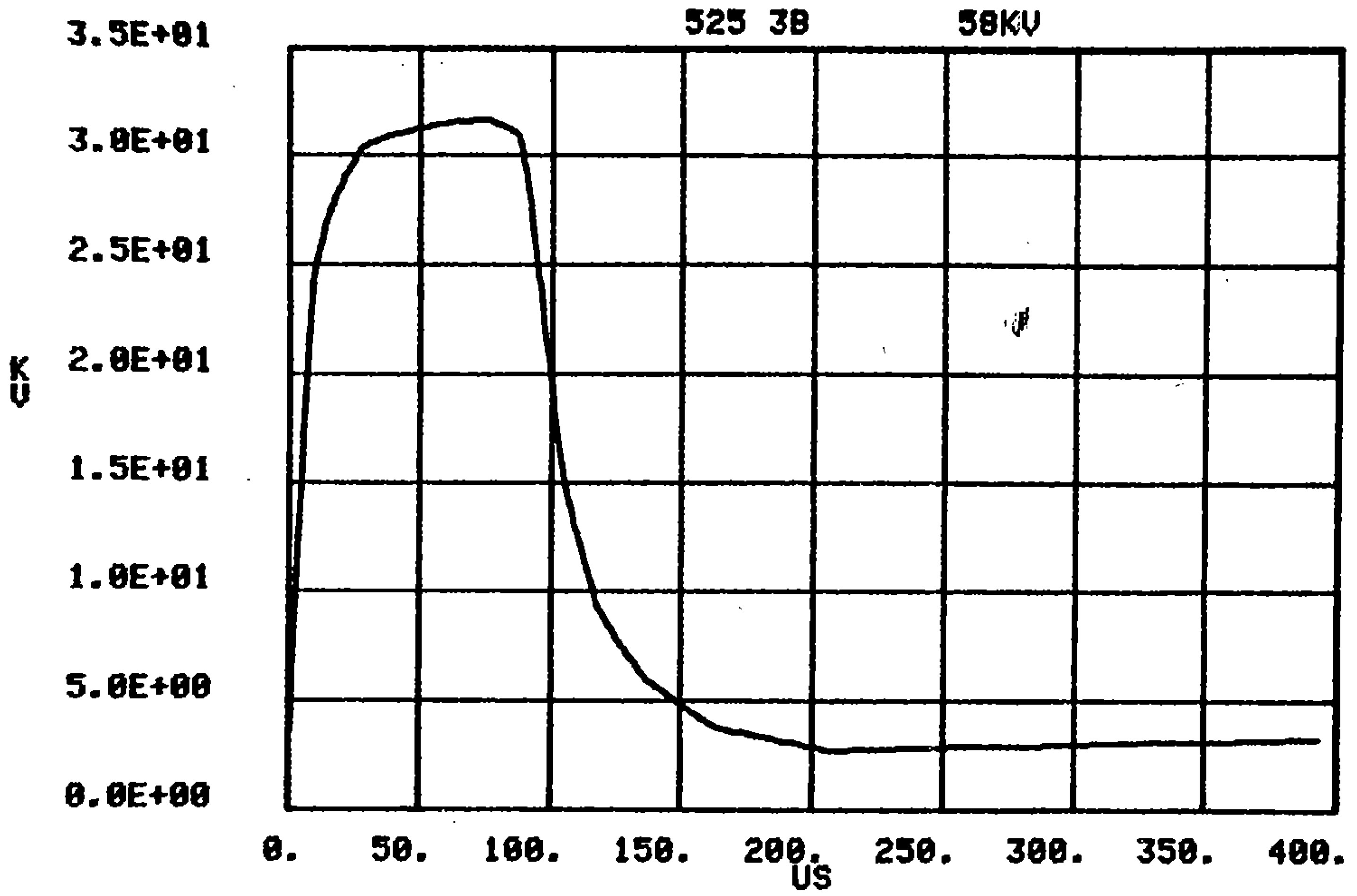

Figure B.69. 525B, .01, 1.0, 1.0, 300 sand-mix; V at r,θ = .15 m, 294 (top).

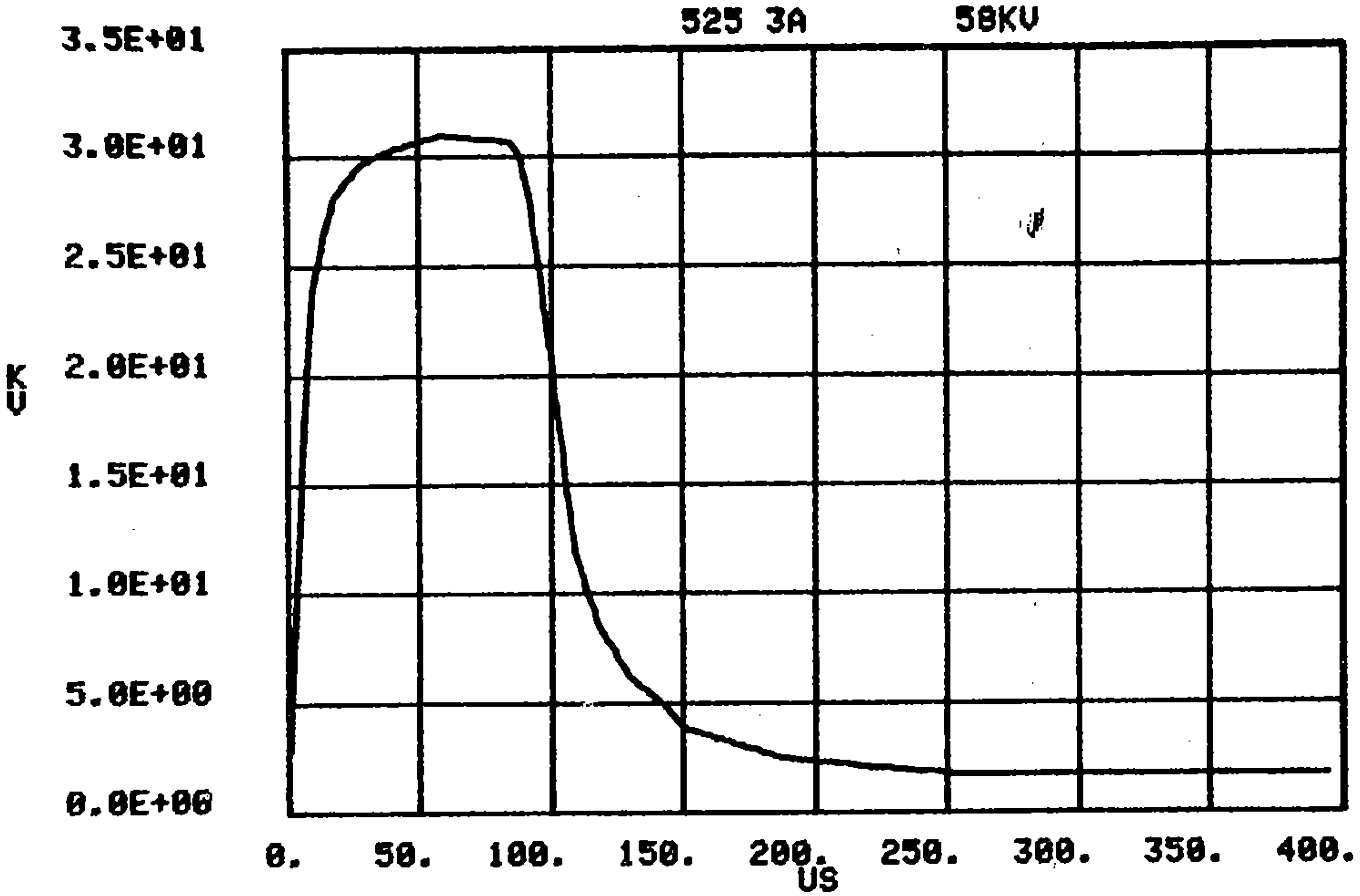

Figure B.70. 525B, .01, 1.0, 1.0, 300 sand-mix; V at r,θ = .15 m, 305 (top).

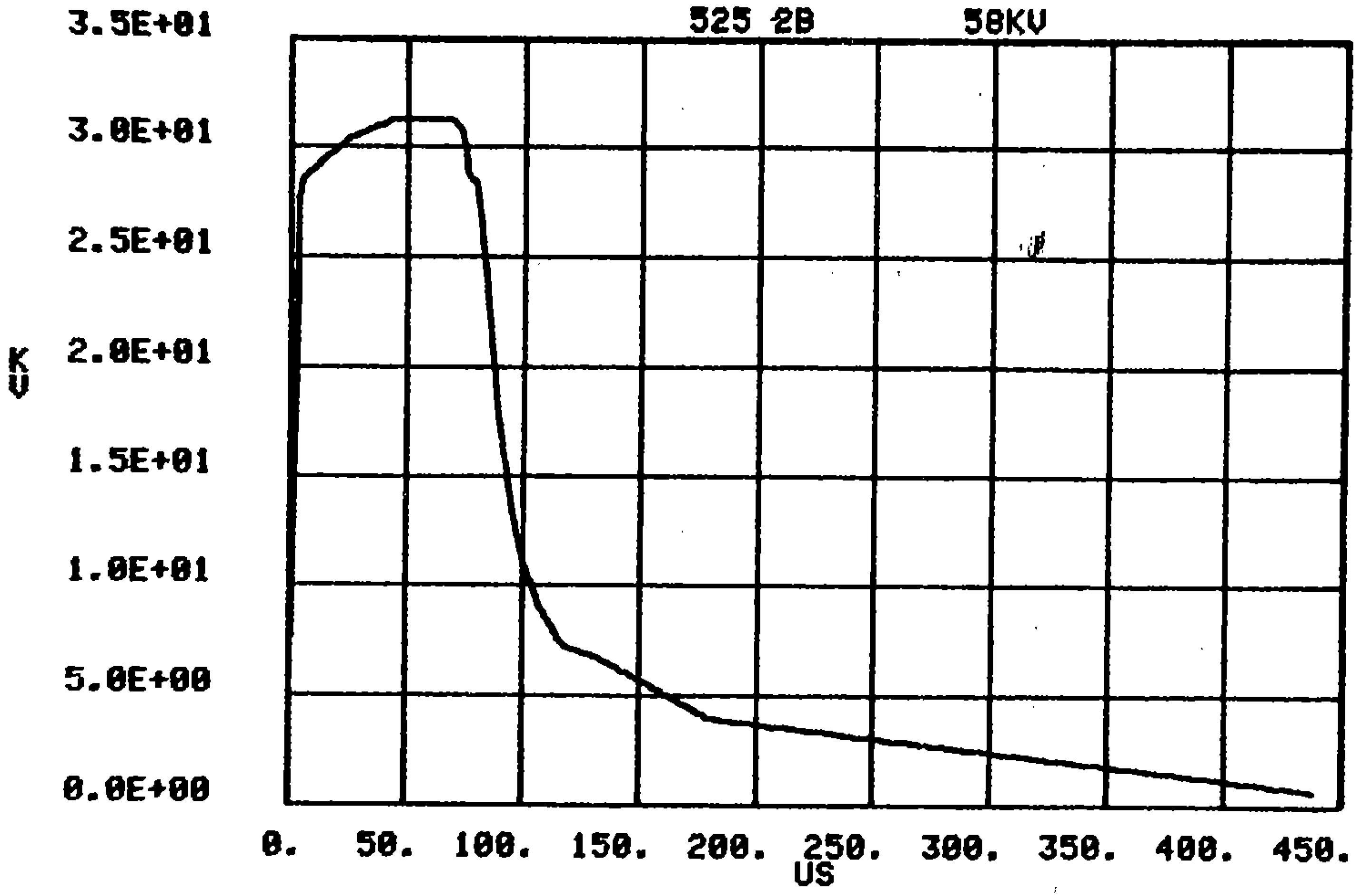

Figure B.71. 525B, .01, 1.0, 1.0, 300 sand-mix; V at r,θ = .15 m, 316 (top).

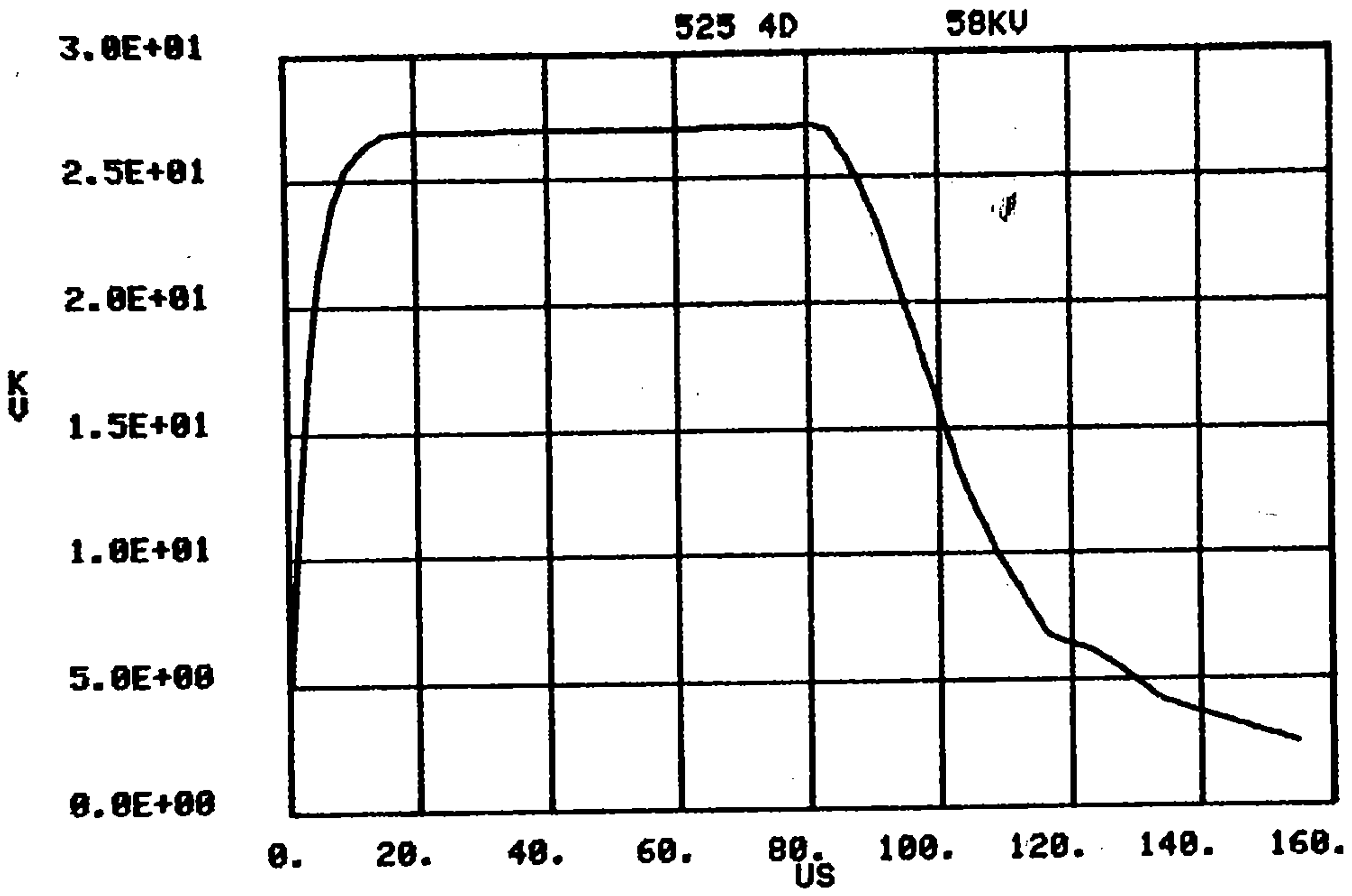

Figure B.72. 525B, .01, 1.0, 1.0, 300 sand-mix; V at r,θ = .15 m, 327 (top).

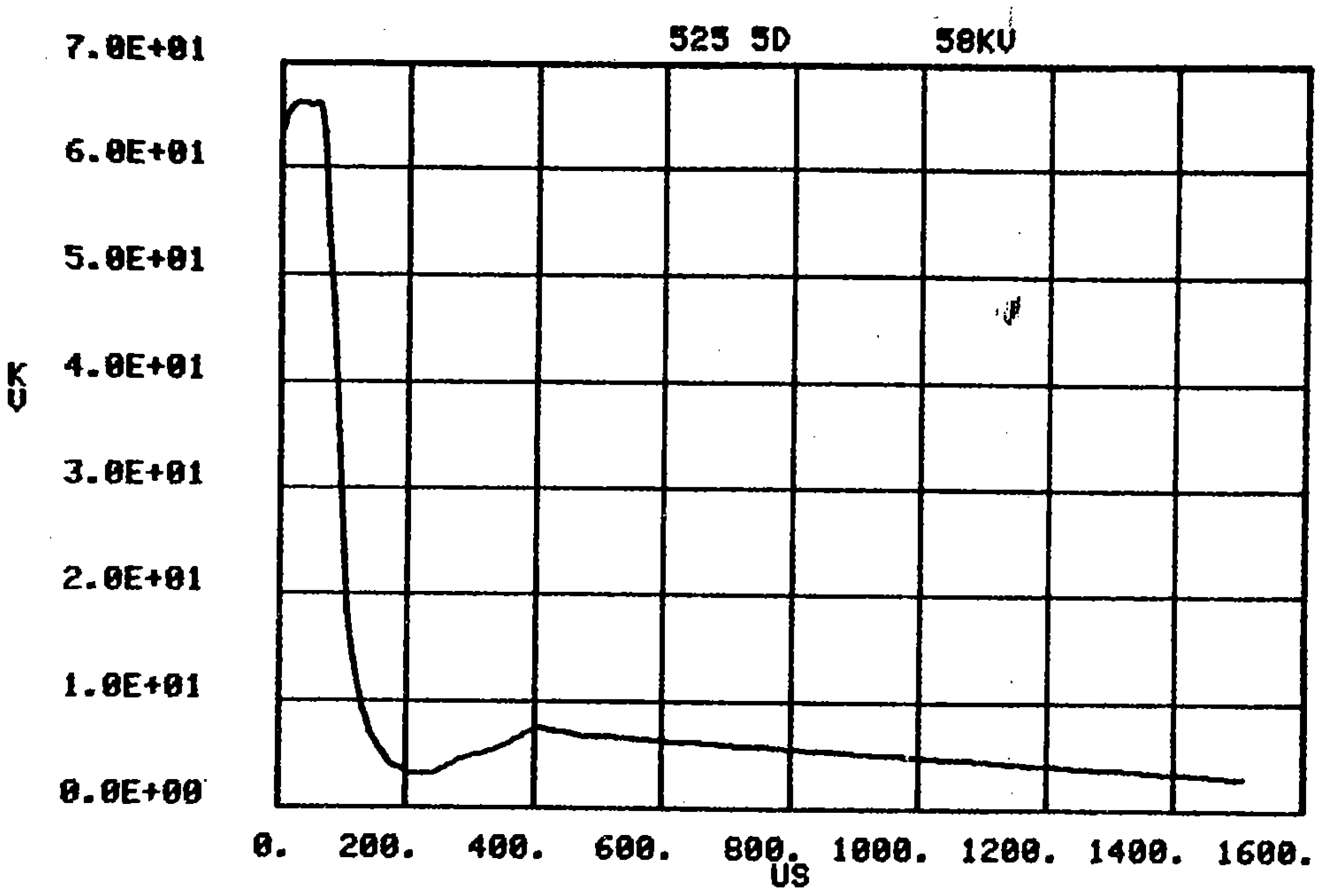

Figure B.73. 525B, .01, 1.0, 1.0, 300 sand-mix; V at r,θ = .15 m, 327 (top).

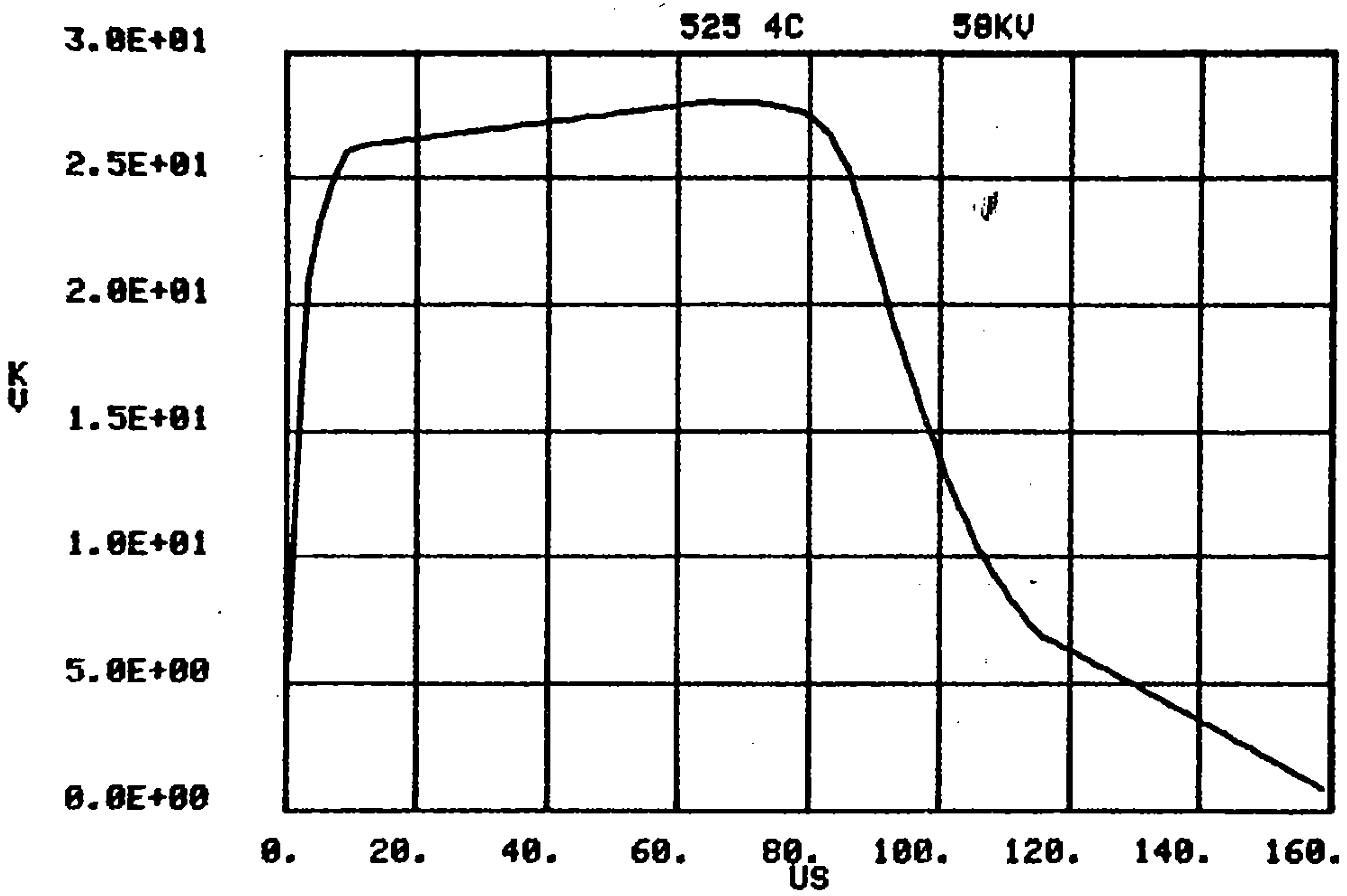

Figure B.74. 525B, .01, 1.0, 1.0, 300 sand-mix; V at r,θ = .15 m, 338 (top).

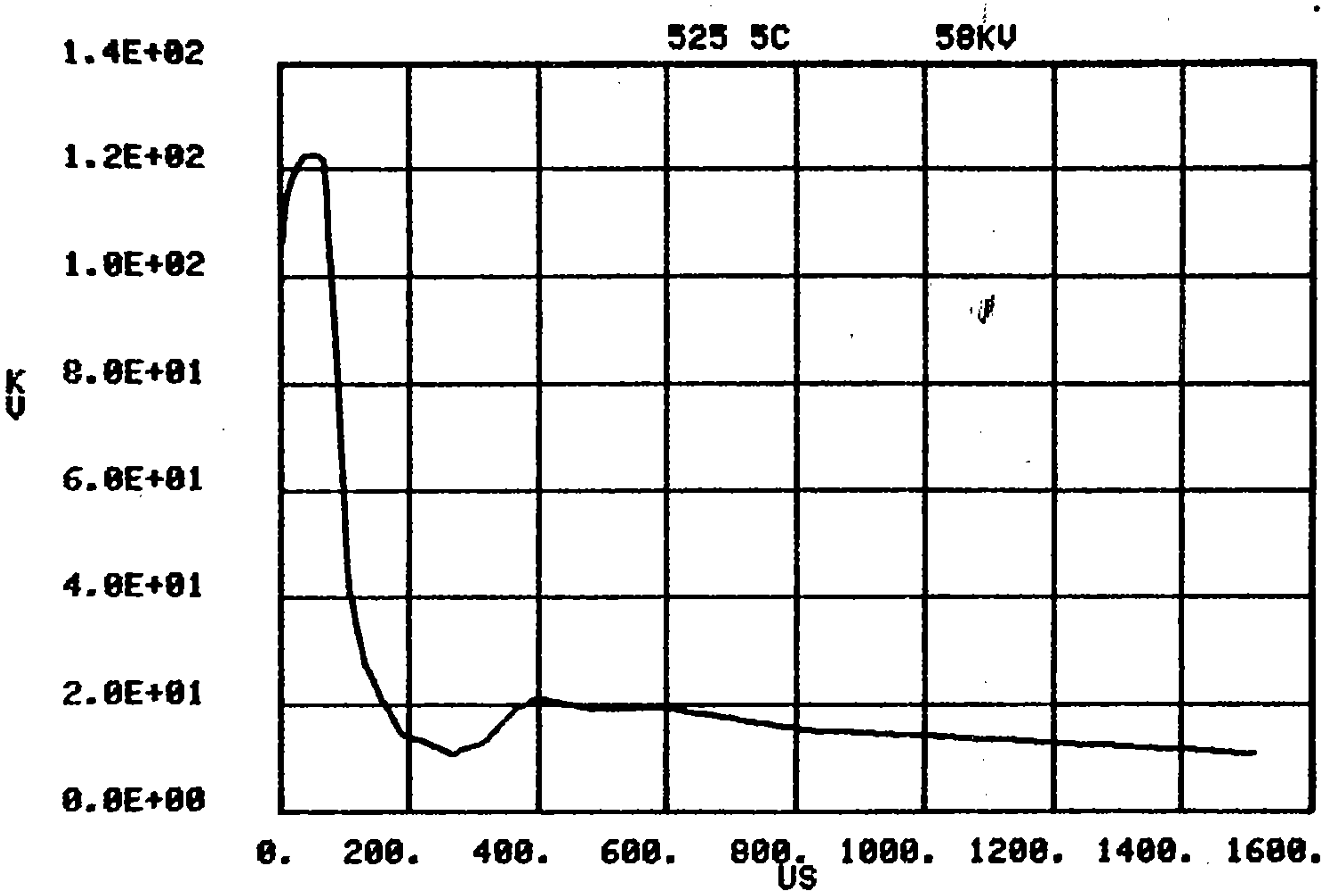

Figure B.75. 525B, .01, 1.0, 1.0, 300 sand-mix; V at r,θ = .15 m, 338 (top).

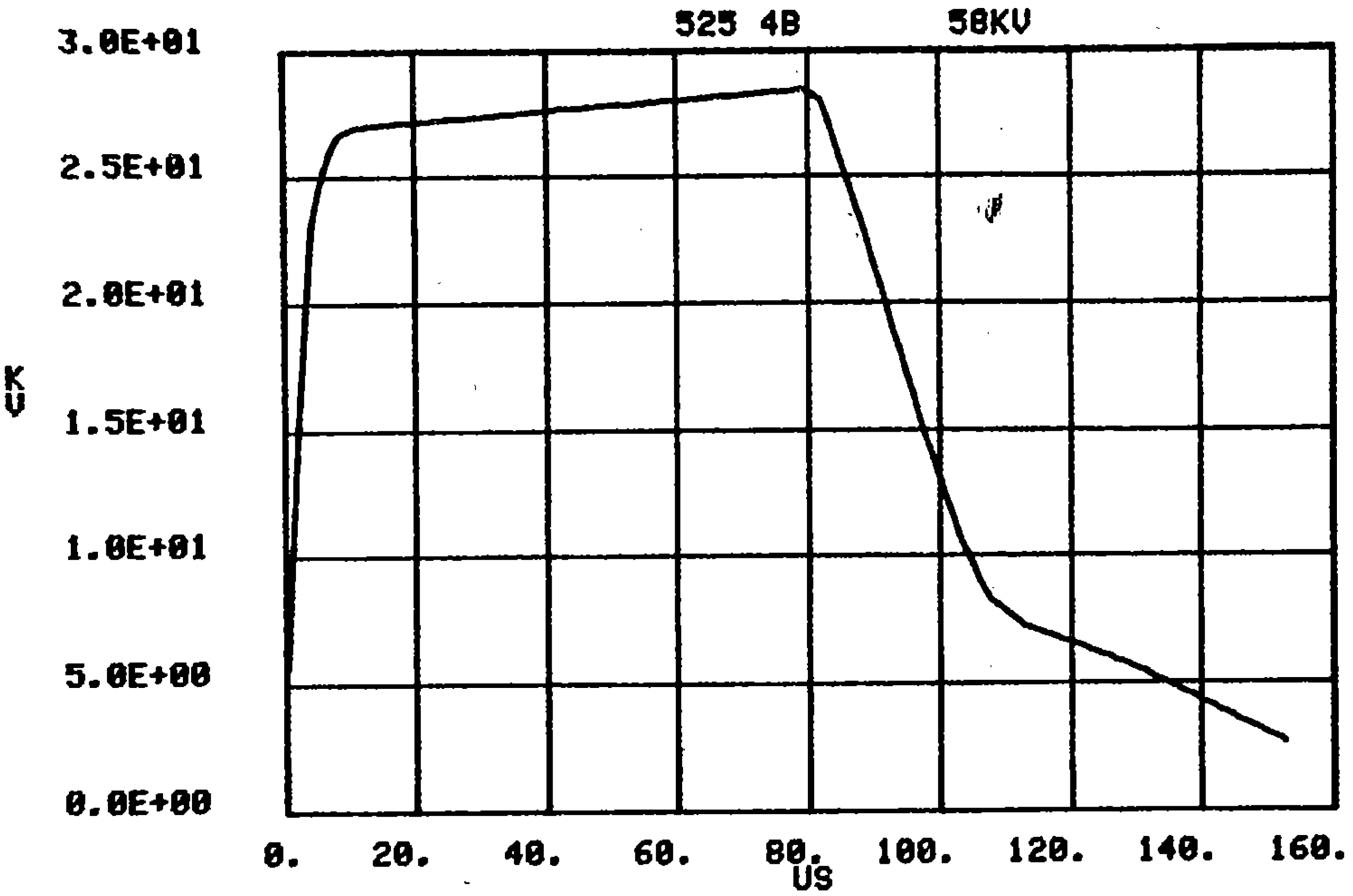

Figure B.76. 525B, .01, 1.0, 1.0, 300 sand-mix; V at r,θ = .15 m, 349 (top).

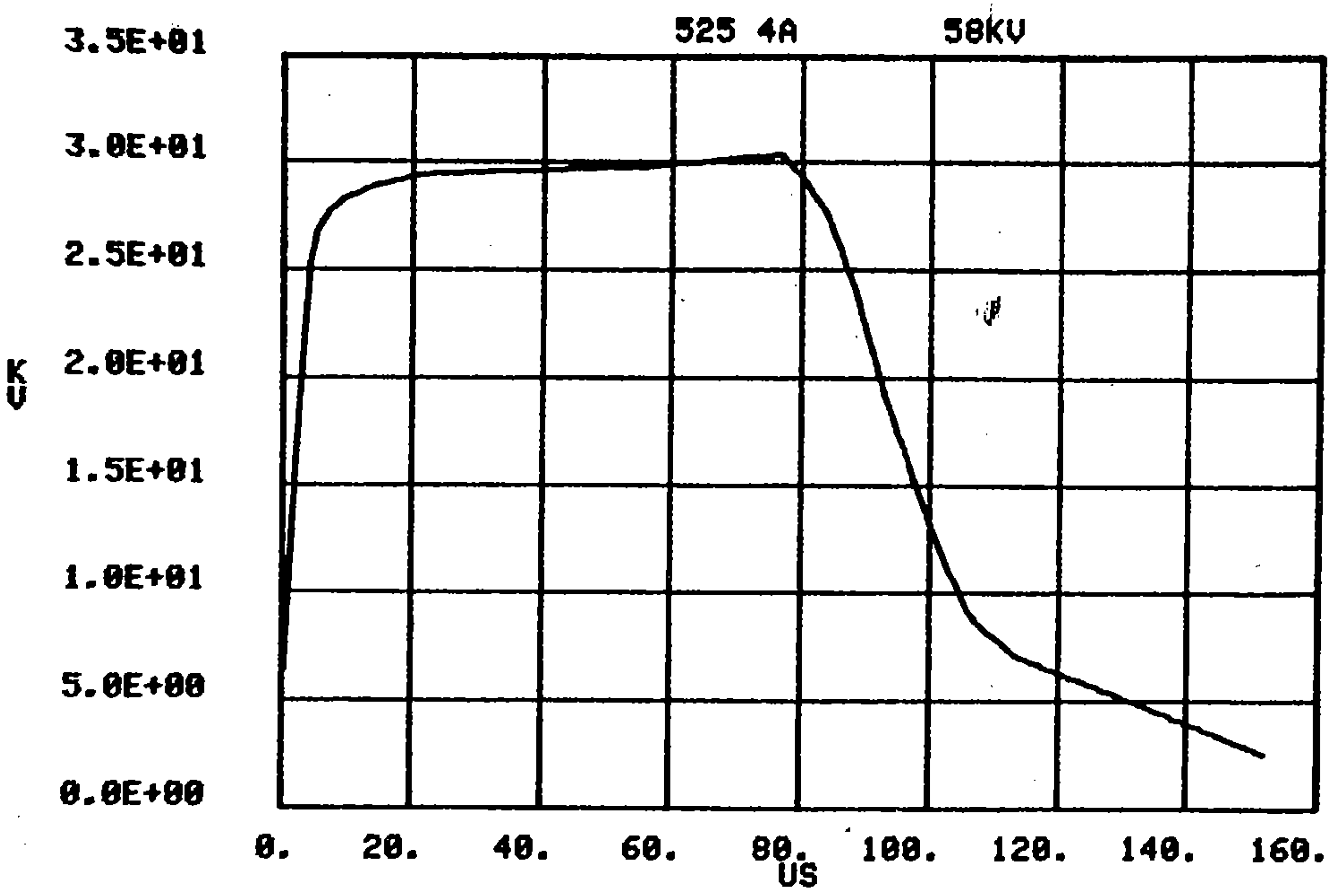

Figure B.77. 525B, .01, 1.0, 1.0, 300 sand-mix; V at r,θ = .15 m, 0 (top).

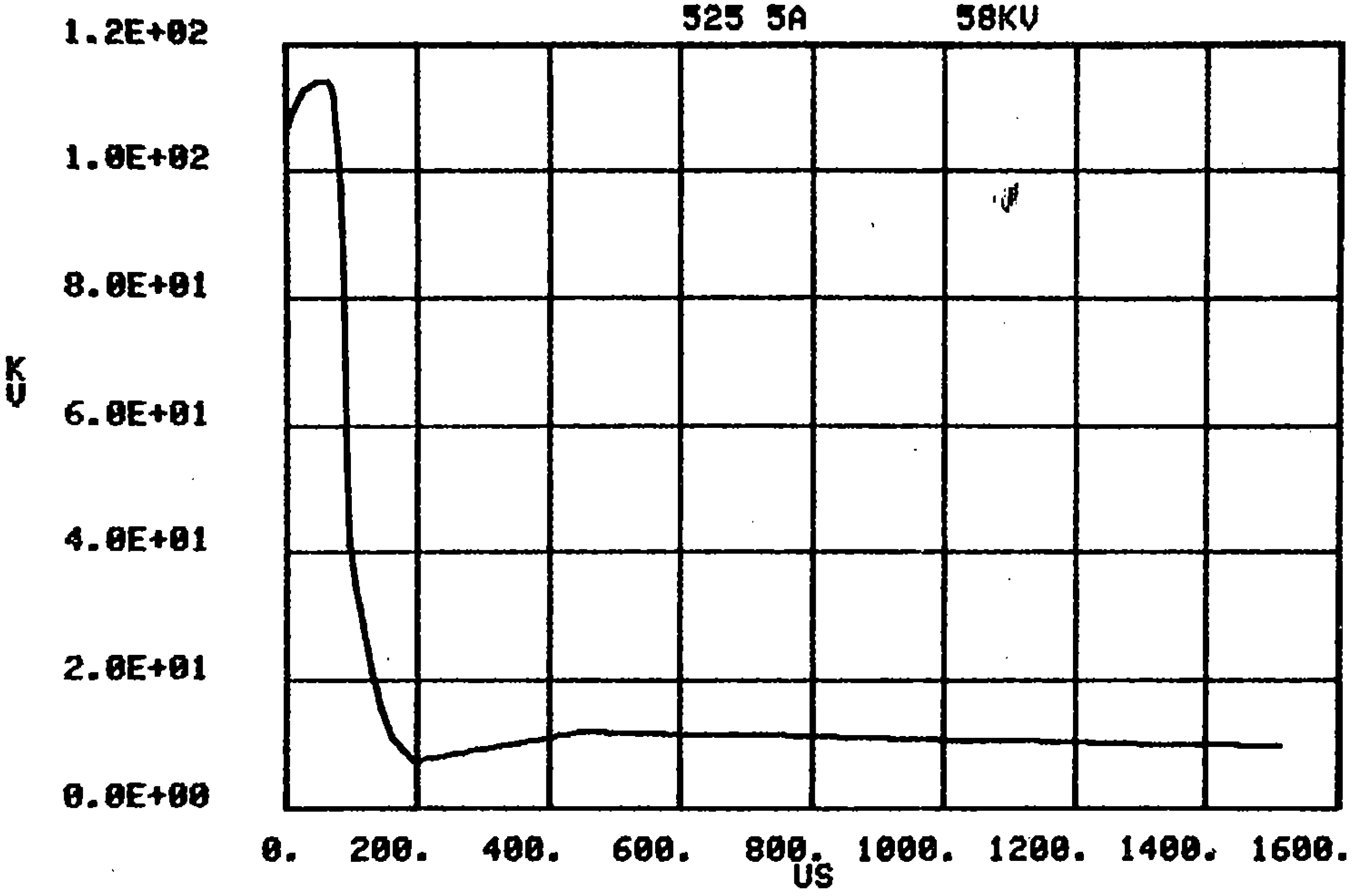

Figure B.78. 525B, .01, 1.0, 1.0, 300 sand-mix; V at r,θ = .15 m, 0 (top).

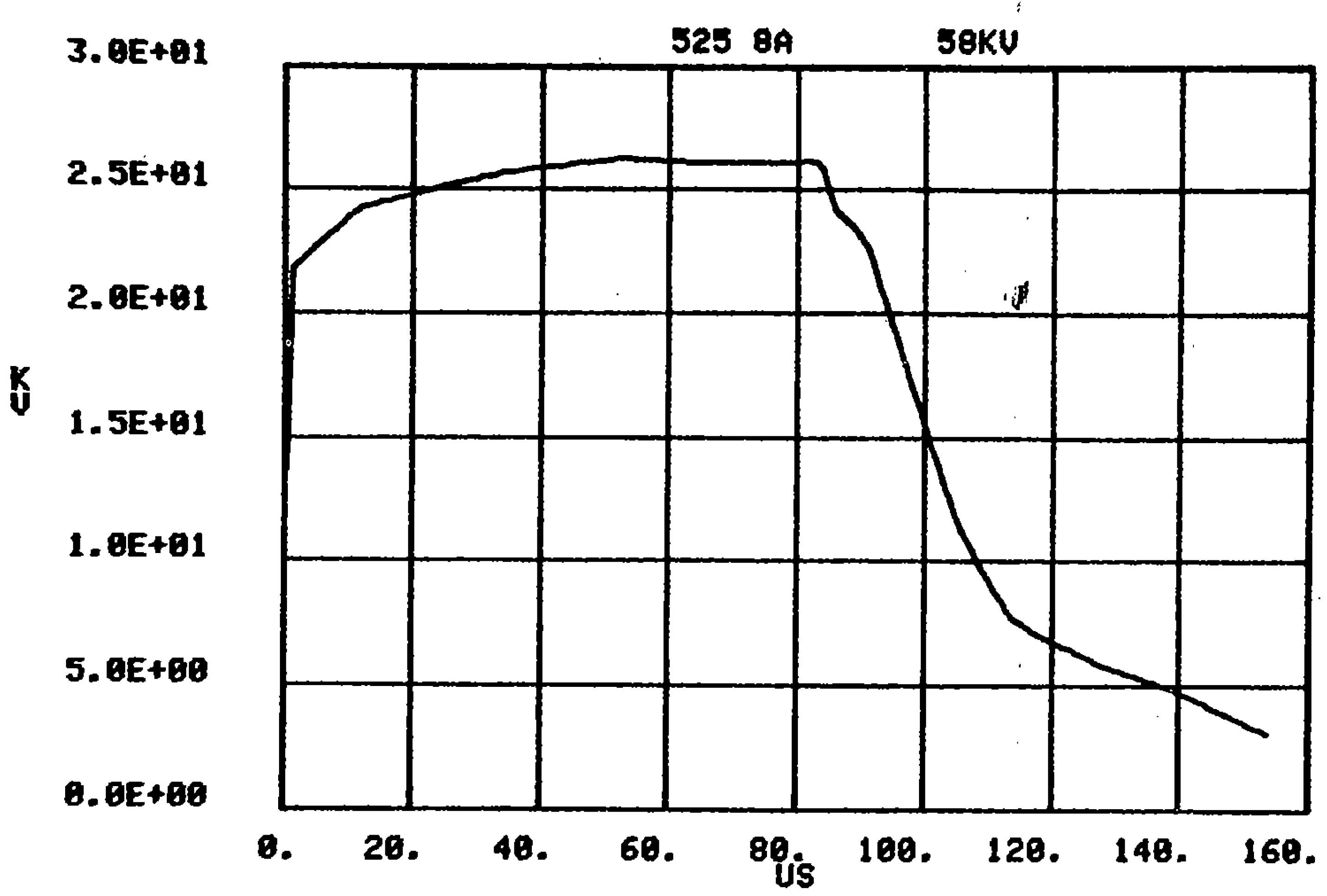

Figure B.79. 525B, .01, 1.0, 1.0, 300 sand-mix; V at r,θ = .15 m, 11 (top).

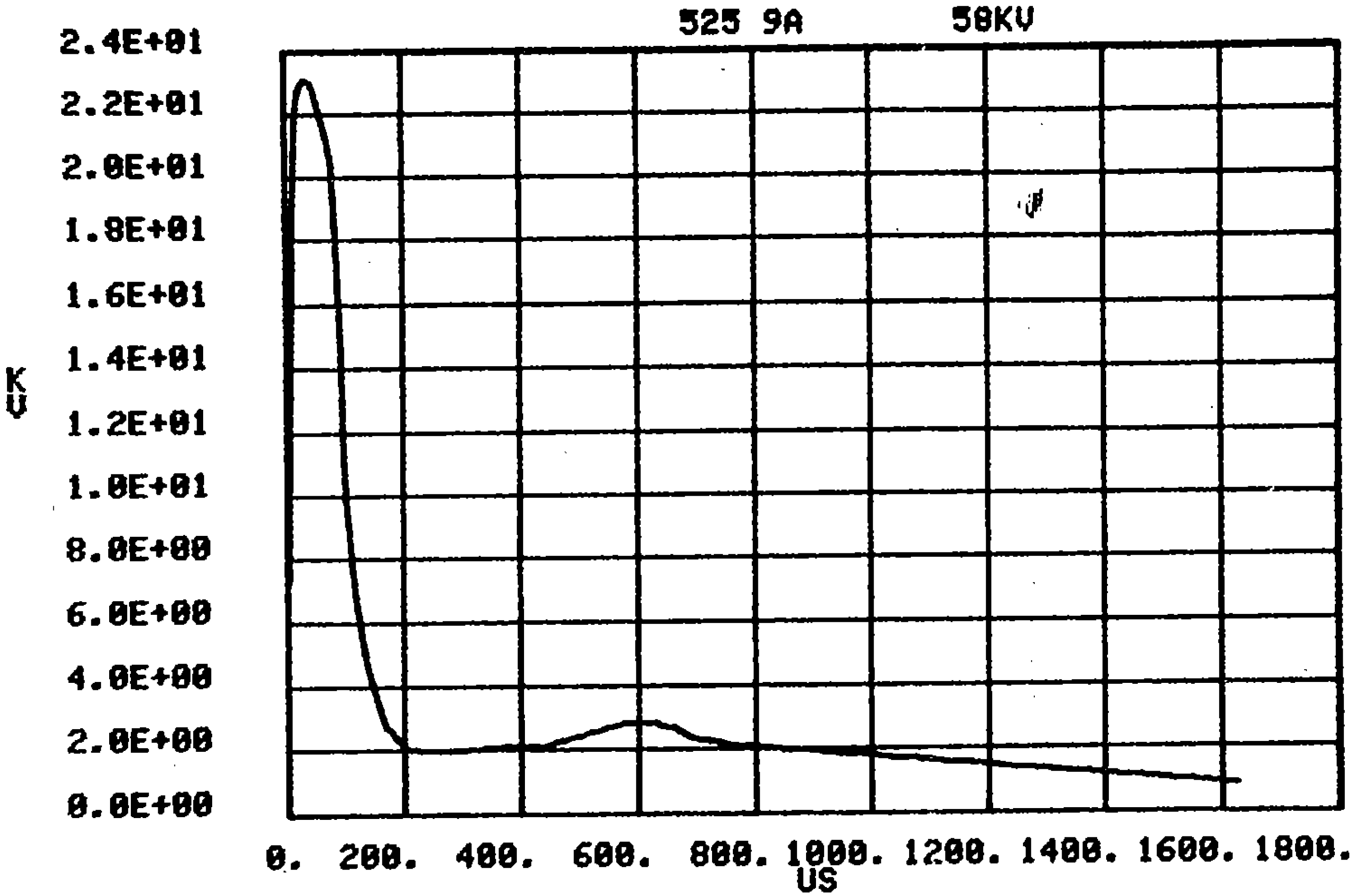

Figure B.80. 525B, .01, 1.0, 1.0, 300 sand-mix; V at r,θ = .15 m, 11 (top).

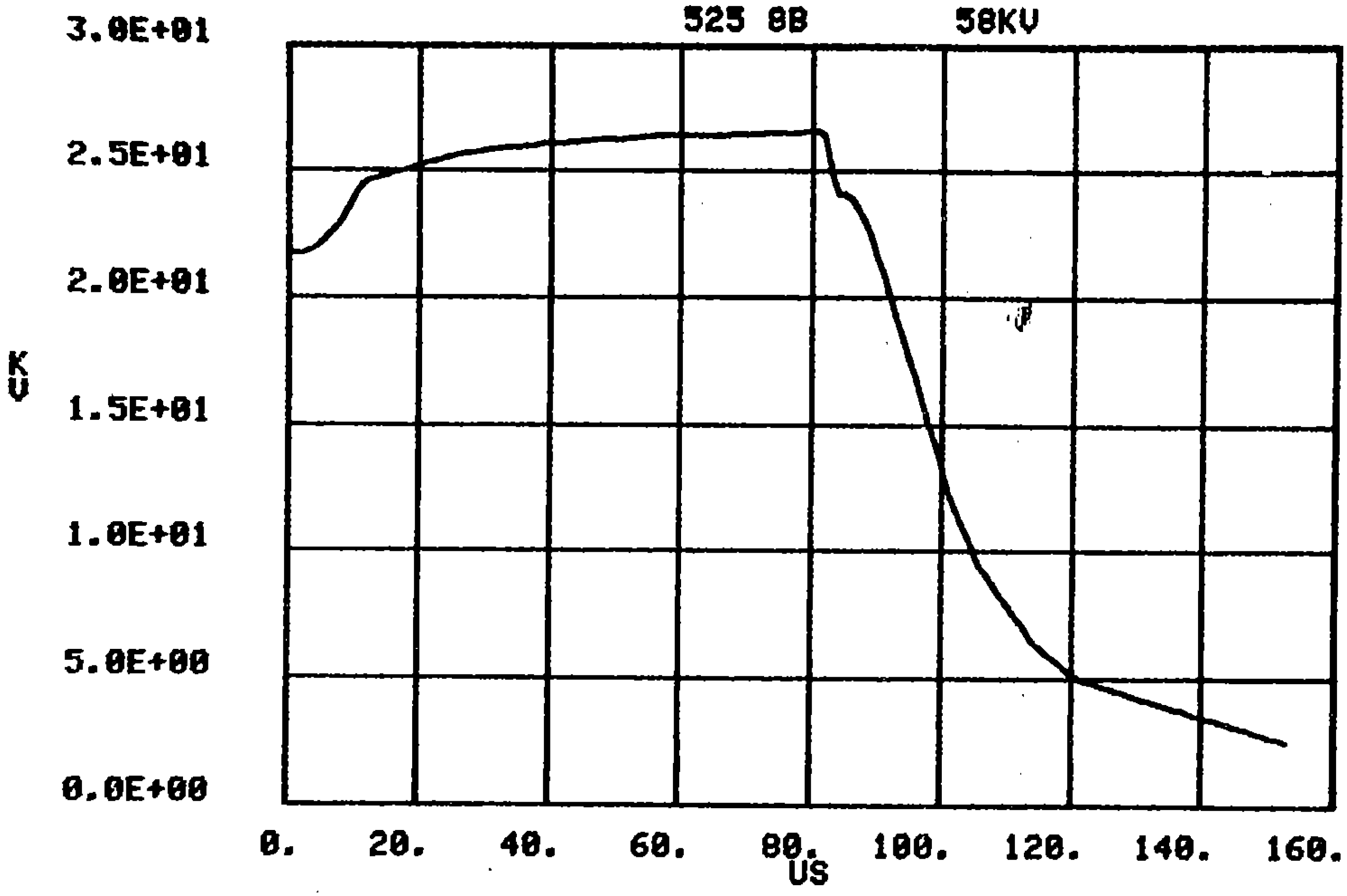

Figure B.81. 525B, .01, 1.0, 1.0, 300 sand-mix; V at r,θ = .15 m, 22 (top).

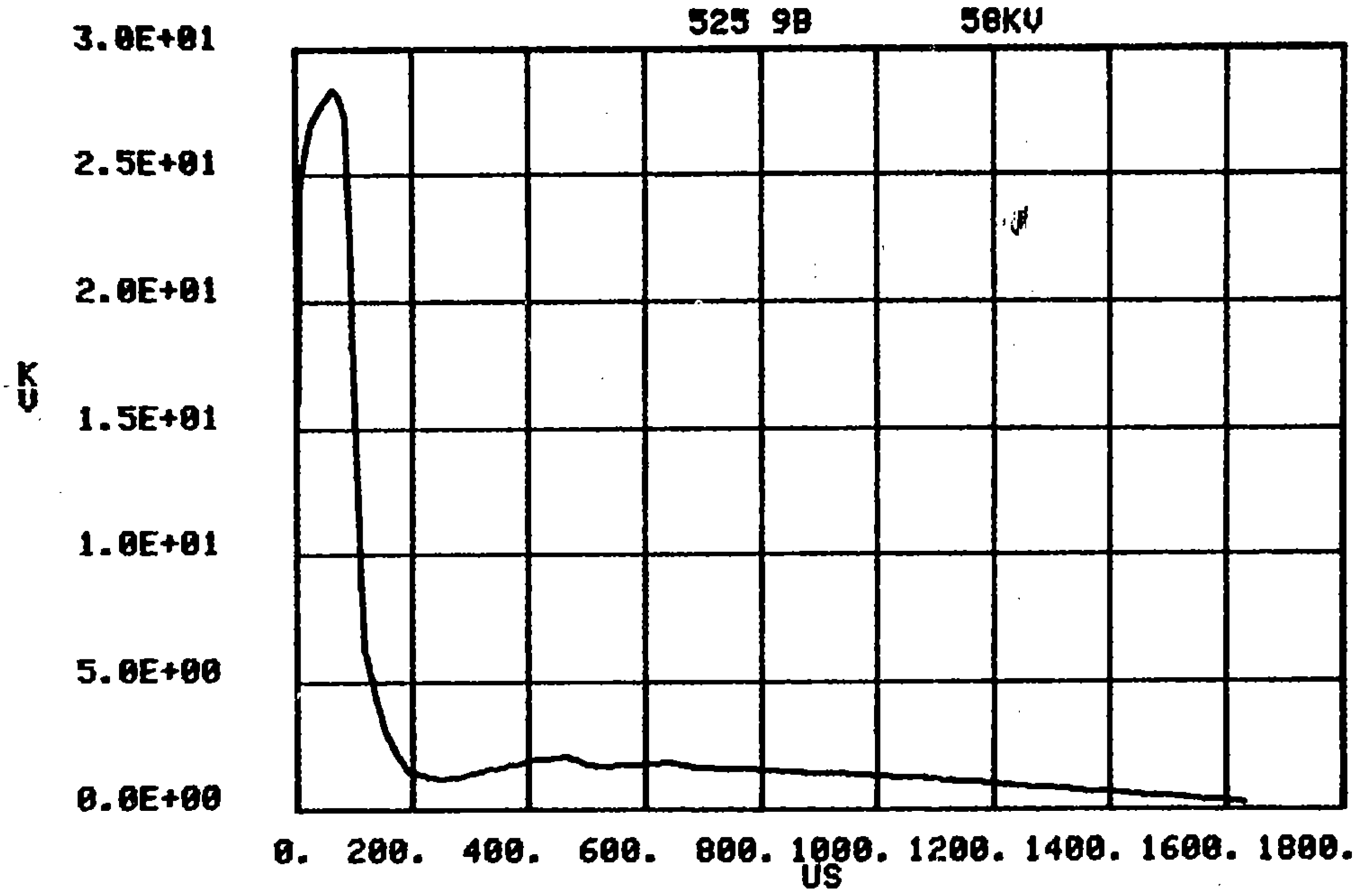

Figure B.82. 525B, .01, 1.0, 1.0, 300 sand-mix; V at r,θ = .15 m, 22 (top).

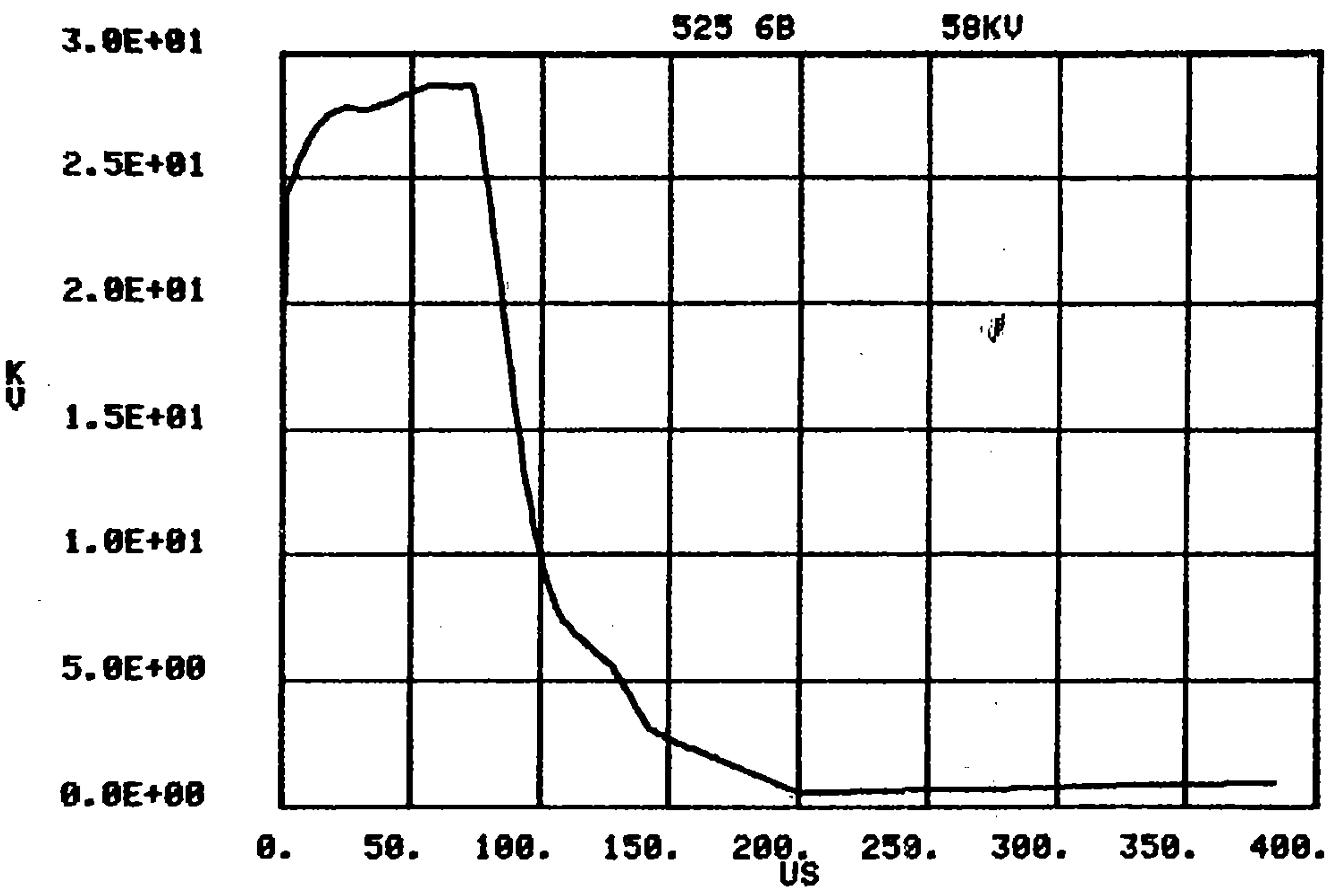

Figure B.83. 525B, .01, 1.0, 1.0, 300 sand-mix; V at r,θ = .15 m, 33 (top).

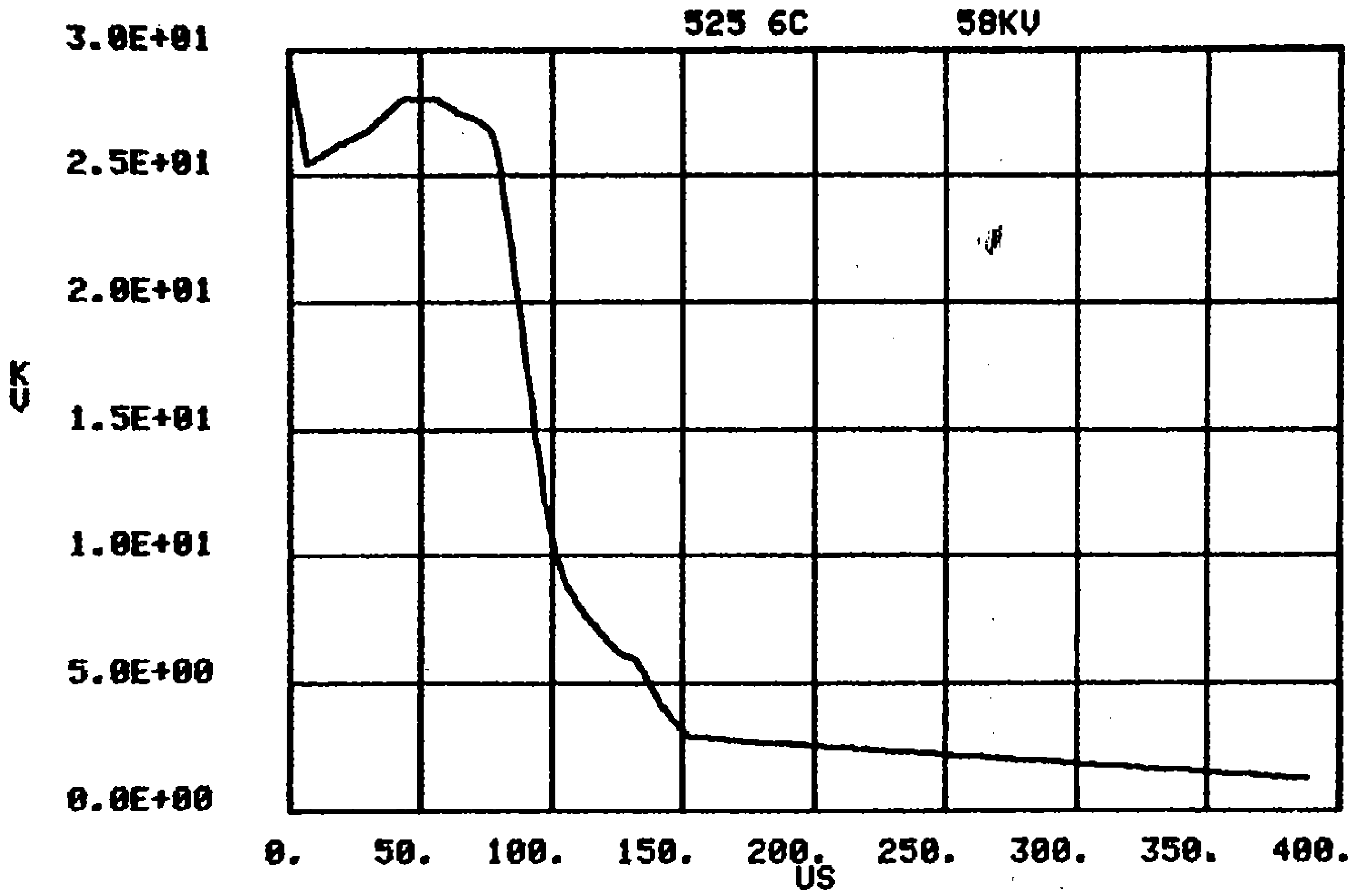

Figure B.84. 525B, .01, 1.0, 1.0, 300 sand-mix; V at r,θ = .15 m, 44 (top).

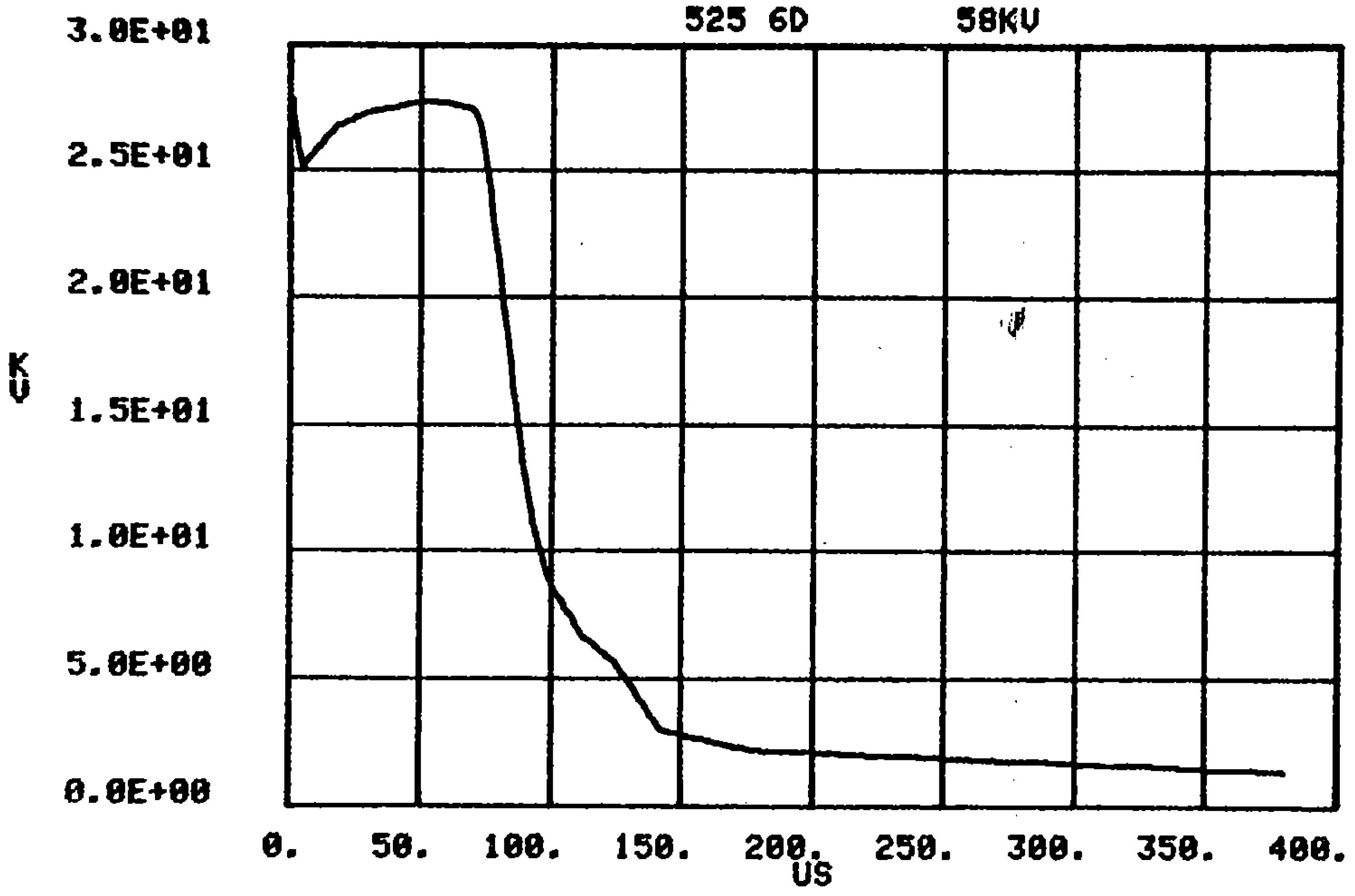

Figure B.85. 525B, .01, 1.0, 1.0, 300 sand-mix; V at r,θ = .15 m, 55 (top).

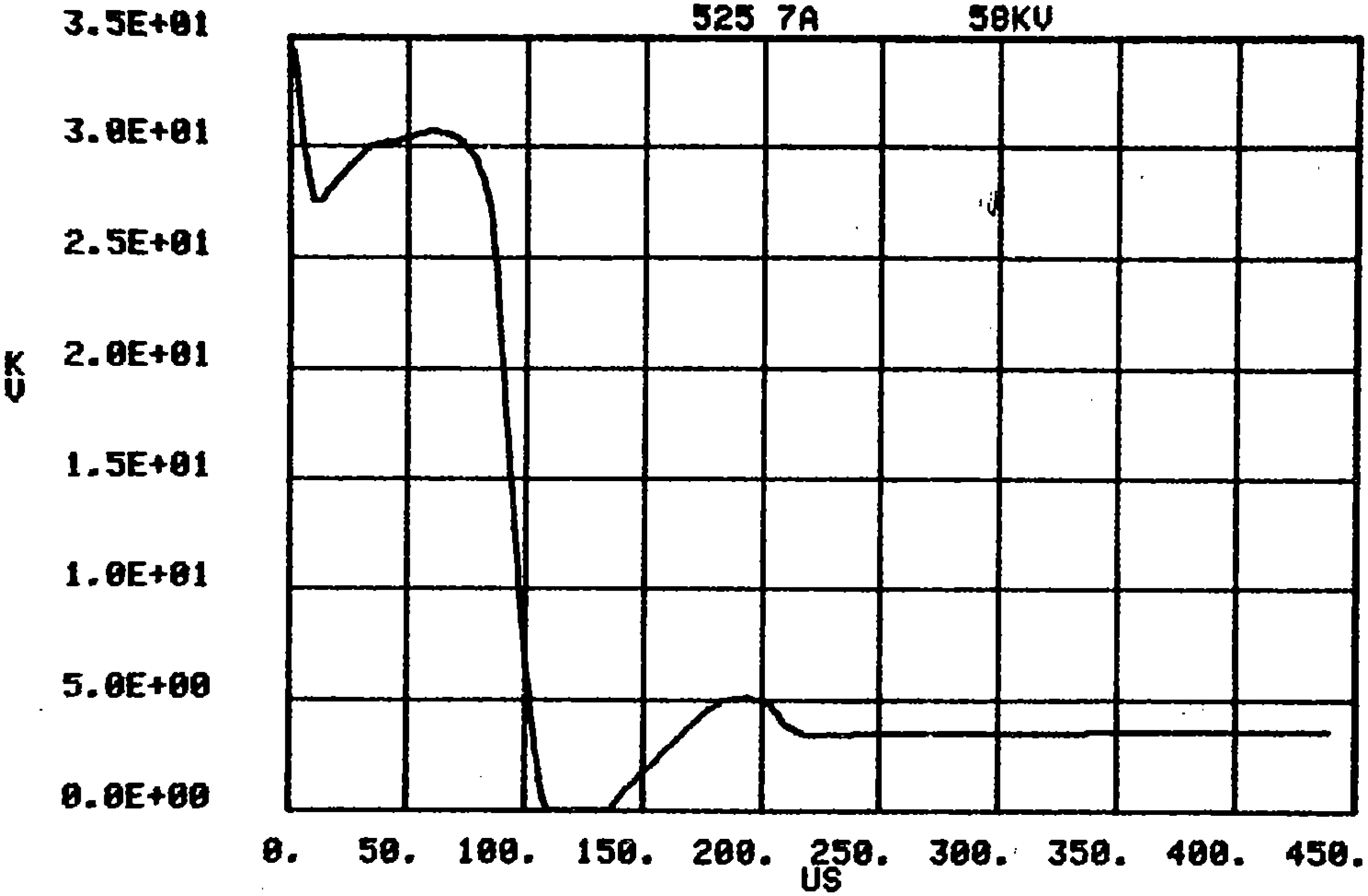

Figure B.86. 525B, .01, 1.0, 1.0, 300 sand-mix; V at r,θ = .15 m, 66 (top).

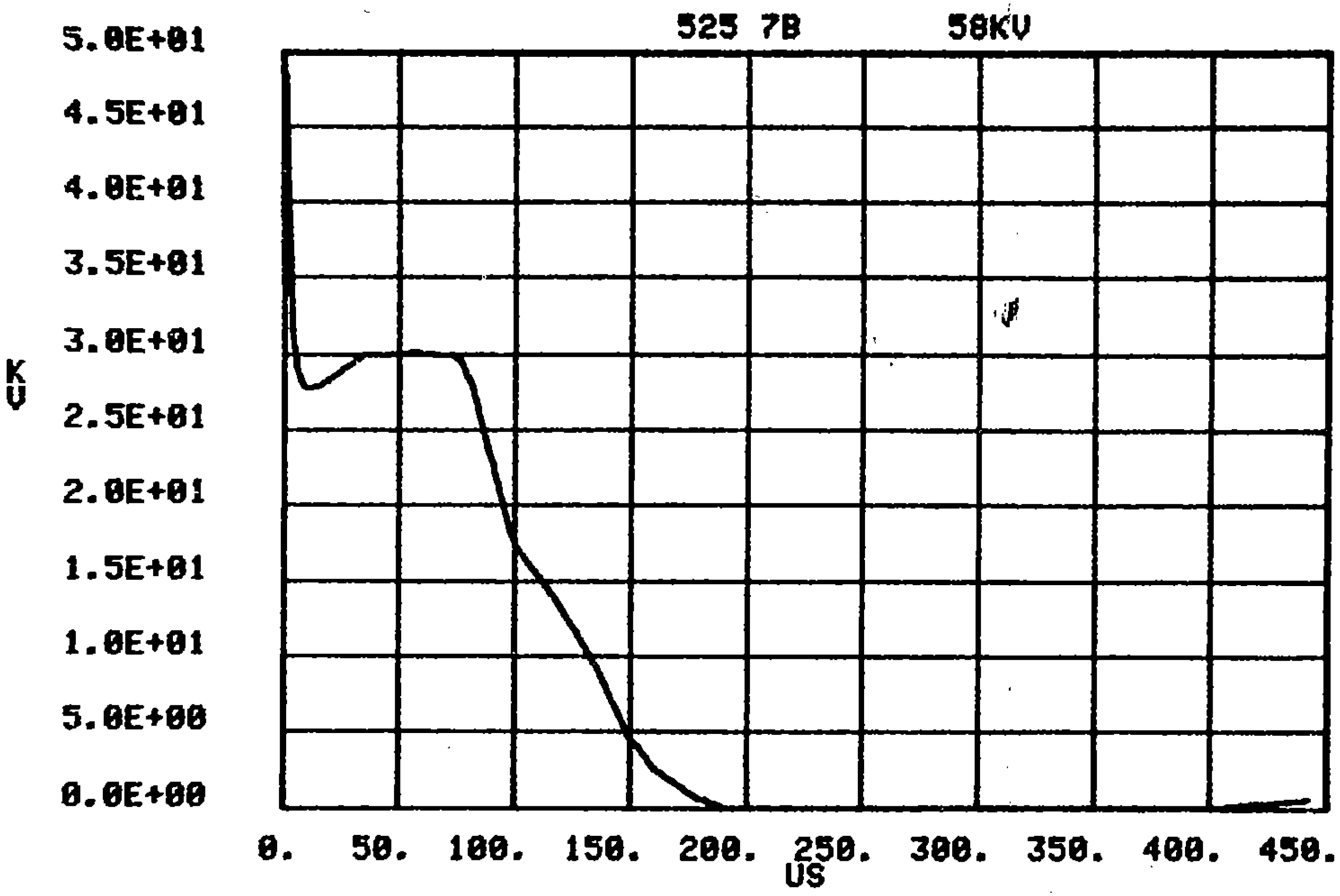

Figure B.87. 525B., .01, 1.0, 1.0, 300 sand-mix; V at r,θ = .15 m, 77 (top).

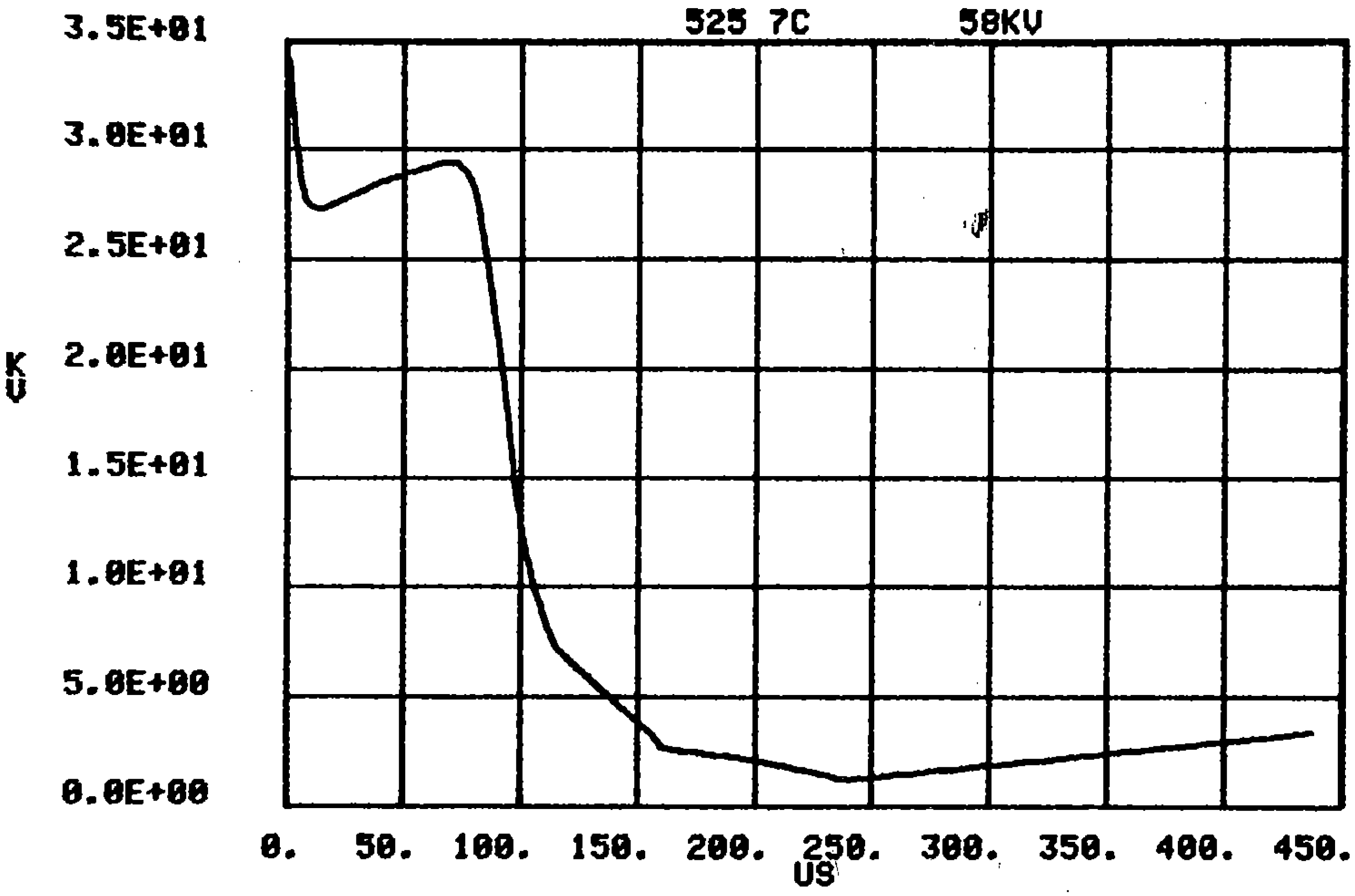

Figure B.88. 525B., .01, 1.0, 1.0, 300 sand-mix; V at r,θ = .15 m, 88, (top).

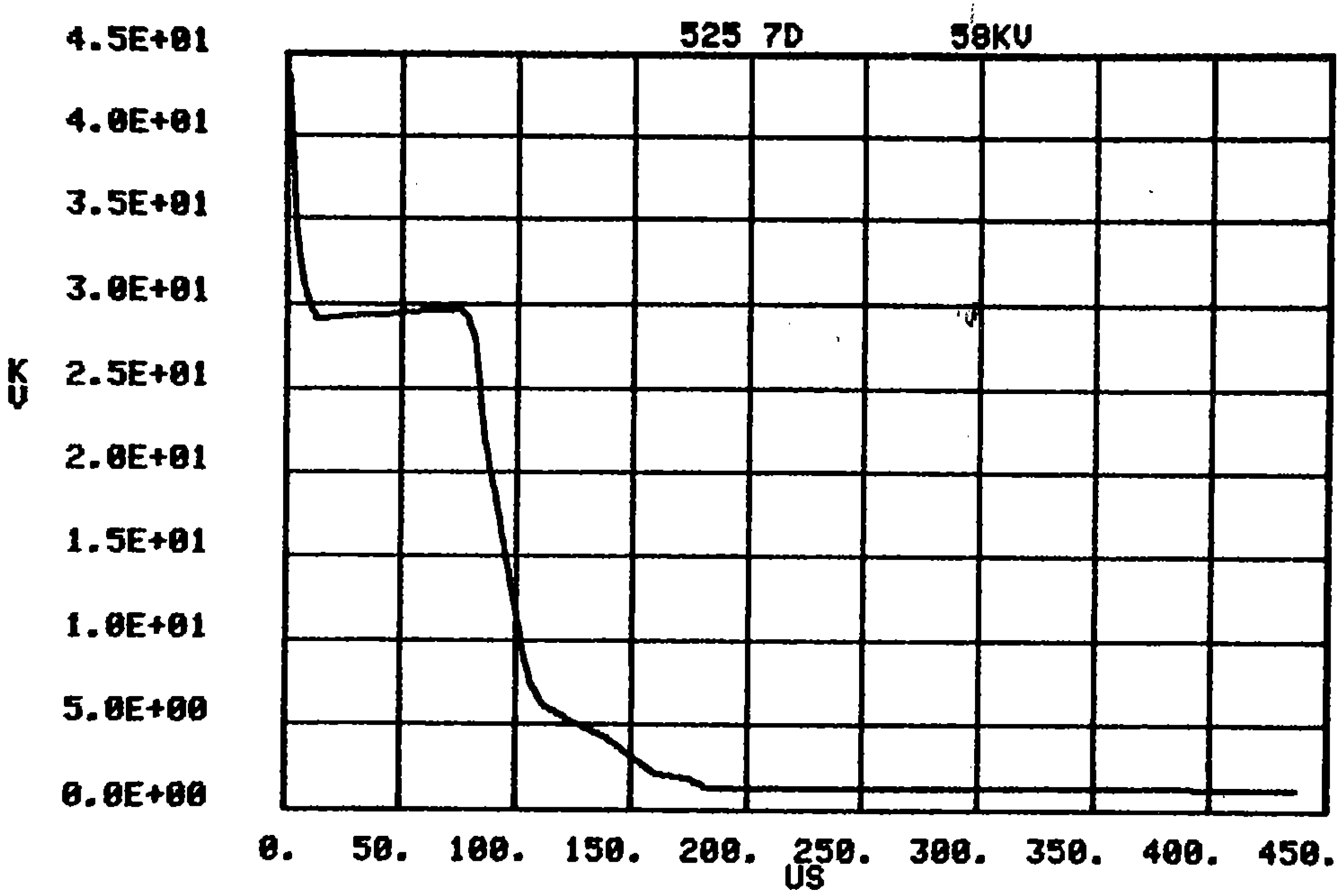

Figure B.89. 525B., .01, 1.0, 1.0, 300 sand-mix; V at r,θ = .15 m,99 (top).

References

1. Mallon, C., R. Denson, R.E. Leadon, and T.M. Flanagan, "Electrical Breakdown Characteristics of Soil Samples", Theoretical Note 316 JAYCOR, San Diego, CA, Jan. 12, 1981.

2. Van Lint, V.A.J., and J.W. Erler, "Buried Conductor Studies", Theoretical Note 347, Mission Research Corp., San Diego, CA, Dec., 1981,

3. Mallon, C., R. Denson, T.M. Flanagan, and R.E. Leadon, "Electrical Breakdown Characteristics in 0.8 and 1.0 Meter Soil Samples", Theoretical Note 318, JAYCOR San Diego, CA, 19 April 1982.

4. Leadon, R.E., T.M. Flanagan, C.E. Mallon, and R. Denson, "Nonlinear Electrical Studies on Buried Conductors", Theoretical Note 348, JAYCOR, San Diego, CA, June 8, 1982.

5. Petropoulos, G.M., J. IEE, Pt. II, 95, 59, 1948.

6. Bellaschi, P.L., Trans. Am. Inst. Elec. Engr., 60, 123, March, 1941.

7. Bellaschi, P.L., R.E. Armington, and A.E. Snowden, Trans. Am. Inst. Elec. Engr. 61, 349, 1942.

8. Sunde, E.W., Earth Conduction Effects in Transmission Systems, D. Van Nostrand Co., 1949.

9. Liew, B.E. and M. Darveniza, Proc. IEE (Australia) 121, 123, February 1974.

10. Snowden, D.P., J.W. Erler, J.L. Gilbert, and C.L. Longmire, "Soil Breakdown Modeling Studies", Theoretical Note 349, Mission Research Corporation, November 1982.

11. Carlile, R.N., "A Geometrical Instability in a Soil Filled Coaxial Structure", EMP Theoretical Notes, No. 313, April 17, 1981.

12. Private communication, Charles Mallon, JAYCOR.

13. Archie, G. E., Transactions of the AIME, 146, 54, (1942).

14. Winsauer, W. D., H. M. Shearin, Jr., R. H. Masson, and M. Williams, Bull. of American Assn. of Petroleum Geologists, 36, 253, Feb., 1952.

15. Jackson, P. D., Taylor-Smith, D., and P. N. Stanford, Geophysics, 43, 1250, (1978).

16. Richards, L. A., ed., Diagnosis and Improvement of Saline and Alkalai Soils, U.S. Department of Agriculture, Agriculture Handbook No. 60, 1954.

17. Blatt, H., Middleton, G., and R. Murray, Origin of Sedimentary Rocks, Prentice-Hall, Inc., Englewood Cliffs, New Jersey, 1980.

18. Middleton, H.E., C.S. Slater, and H.G. Byers, "The Physical and Chemical Characteristics of the Soils from the Erosion Experiment Stations- Second Report", U.S. Dept. of Agriculture Technical Bulletin 430, p. 1, August, 1934.

19. Tagg, G. F., Earth Resistances, G. Newnes Co., London, 1964.

20. Ingram, J., Research, 14, 20, 1961.

☆U.S. GOVERNMENT PRINTING OFFICE:1983—776-131 / 1003